Universitat Autònoma de Barcelona

PhD Thesis

Suspended Micro- and NanoTools for Cell Biology

Sara Durán Ibáñez

Under the supervision of:
Dr. José Antonio Plaza Plaza

University Tutor:
Dr. Julián Alonso Chamarro

PhD Program in Chemistry
Chemistry Department - Science Faculty

2014

CSIC Consejo Superior de Investigaciones Científicas

Report submitted to aspire to the Doctor degree by:

Sara Durán Ibánez

Checked and accepted by:

Dr. José Antonio Plaza Plaza
Thesis Supervisor

Dr. Julián Alonso Chamarro
University Tutor

Cerdanyola del Vallès. September 26, 2014

Das Leben ist wie ein Fahrrad.
Man muss sich vorwärts bewegen,
um das Gleichgewicht nicht zu verlieren.

Albert Einstein

Acknowledgements

Después de cinco anos ha llegado ese momento que parecía que no llegaría nunca, el de recopilar en esta tesis doctoral todo lo aprendido. Conforme iba redactando este manuscrito he ido recordando a cada una de las personas que me han acompanado a lo largo de estos anos y que sin ellas la realización de esta tesis no hubiera sido posible. Por ello me gustaría agradecer su ayuda,

A mi director de tesis, el Dr. José Antonio Plaza, por ensenarme tantísimas cosas, por sus ideas, por su paciencia en algunas ocasiones, por confiar desde un principio en mí y por darme la oportunidad de venir desde Valencia a vivir esta increíble aventura. Al Dr. Jaume Esteve, por interesarse siempre en mi trabajo dentro del grupo de Micro y NanoHerramientas, por estar siempre dispuesto a escuchar y a aportar su conocimiento. Y al Dr. Julián Alonso, por aceptar ser mi tutor dentro del Departamento de Química en la Universidad Autónoma de Barcelona.

Al grupo de Lluisa Pérez, del Departamento de Farmacología y Química Terapéutica de la Universitat de Barcelona, en especial a Lluisa y a Oriol Penon, por las funcionalizaciones químicas de los chips, por estar siempre dispuestos a cualquier prueba que hiciera falta y por sus ganas de trabajar. Ha sido un placer trabajar con vosotros. Al grupo de Carme Nogués, del Departamento de Biología Celular, Fisiología e Inmunología de la Universitat de Autònoma de Barcelona, es especial a Sergi Novo y Tània Patino, por las pruebas biológicas de los chips y por conseguir las imágenes más impresionantes de nuestros dispositivos dentro de embriones y células. Algunas de las imágenes más impresionantes de esta tesis son obra suya. A Álvaro San Paulo y Marta Fernández, en su momento del Instituto de Microelectrónica de Barcelona (IMB-CNM, CSIC), pero ambos ya fuera del centro, por el crecimiento de nanohilos en nuestros chips. Marta, no hay por ahí nanohilos más bonitos que los tuyos. A Susana Castel y Manuel Reina del Departamento de Biología Celular de la Universitat

de Barcelona, por sus pruebas biológicas de los chips con nanohilos. A Rafael Pérez del Real del Instituto de Ciencia de Materiales de Madrid (ICMM, CSIC), por las caracterizaciones magnéticas de los códigos de cobalto-níquel y por estar siempre dispuesto a echarnos una mano.

A Marta Duch por estar siempre siempre ahí, por encontrar huecos en su apretadísima agenda para ayudarme con los códigos y partículas, por recibirme siempre con una sonrisa cuando llegaba a su despacho con algún problema ya fuera personal o laboral, por las horas en el laboratorio de microsistemas, por las infinitas horas de SEM y por las conversaciones frikis sobre juego de tronos!

A Rodrigo Gómez por su infinita ayuda, por tener siempre la respuesta para todo, por el consultorio psicológico que tiene en su despacho y por animarme siempre.

A Marta Gerbolés por nuestras conversaciones en microsistemas, a Núria Torres por las charlas matutinas en el autobús de la Renfe, a Javier Sánchez por estar siempre dispuesto a ayudar con la corrección de runes y a Consuelo Guardiola por todos sus consejos.

A Roberto Robaina por sus conversaciones sin fin, por sus tremendos dramas , por sus historias cubanas y por ayudarme tanto en los primeros anos de la tesis. Sin él esos anos hubieran sido mucho más difíciles. A Pili Alcaine por los buenísimos ratos delante de la vitrina del electroplating en los que nos contábamos la vida, por las visitas entre despachos, por los viajes entre Zaragoza y Barcelona, por escucharme tanto tantísimo y darme tan buenos consejos. Te debo una visita sí o sí!

A Carolina Vargas y a Laura Evangelio, por su ayuda en estos últimos meses, sin vuestro apoyo, vuestra ayuda y vuestros ánimos el sprint final hubiera sido muchísimo más duro. A Abhinav Kadambi, por sus historias sobre la India, sobre el yoga, sobre la actitud frente a la vida y por mantener la calma cuando los experimentos no salían ni a la de mil. That s science! A mis excompis de despacho, Sergi Sánchez y Libertad Solé, por los buenos ratos de platanicos y chocolates. A Eva Fernández, por su apoyo en los primeros anos de tesis, cuando salíamos a comer y nos dábamos cuenta de que el cielo seguía siendo azul por muy mal que estuvieran yendo los experimentos y por nuestras conversaciones filosóficas sobre la felicidad y como conseguirla.

A Sara del Cerro, por tantísimos anos juntas, por nuestras conversaciones infinitas que siempre me saben a poco, por notar su apoyo en todo momento aun estando a cientos de km, por conocerme mejor que yo misma y por entenderme como nadie. A Vanesa Sanchis, por nuestras llamadas semanales para ver cómo han ido las cosas, por nuestros desayunos y comidas en todas nuestras visitas a Valencia, por hacerme sentir como si nunca me hubiera ido, por escucharme tanto, por darme tan buenos consejos y estar siempre ahí. A Concha Martínez, por pensar tanto en nosotros y llenarnos la nevera hasta los topes, sobre todo con tuppers de su receta especial de macarrones que sabe que tanto me gustan!

A Eduardo Solano, por dónde empiezo? Gracias por las comidas en letras, gracias por los cafelicos de vainilla, gracias por los fuets del pueblo, gracias por su infinita paciencia, gracias por tener la respuesta a cualquier problema que me surgiera y si no la tenía apanárselas para averiguarla, gracias por haberme escuchado tantas veces y por sus buenísimos consejos. Sin su ayuda hubiera tardado 10 anos más en acabar la tesis.

A Antonio José Durán, porque aun estando en otro continente siento que está aquí a mi lado. Que me conoce y me entiende tan bien. Gracias por nuestras conversaciones sobre el futuro, por nuestras risas por chorradas que a nadie más le hacen gracia, por los viajes de reunificación familiar a USA y por nuestros planes del puesto de mojitos frente al mar.

A Antonio Durán y a María José Ibánez, los pares, por estar siempre ahí, por hacerme sentir como una reina cada vez que estamos juntos, por su alegría cada vez que nos encontramos los viernes que vamos a Valencia y su apoyo cada vez que nos vamos los domingos. Por hacerme sentir que están aquí al lado aunque no sea así, por decirme que no sea tan llorona y que tire para adelante y por sus sabios consejos. Ya sabéis que la familia no se separa, sólo se expande.

A José Miguel Sánchez, por estar siempre a mi lado, por acompanarme cada día, por tu paciencia, por tu alegría, por tus consejos, por tu amor, por tu paz, por ayudarme tanto con la tesis, por lo apanados que somos, por que estando contigo estoy en casa, por nuestros planes amenos, por hacerme vivir el lado bonitista de la vida, por animarme siempre, por nuestros bailes, por venirte a Barcelona conmigo, por ser el amor de mi vida y por tantas y tantas cosas que podría seguir escribiendo la vida entera. Sin ti no lo hubiera conseguido.

Motivation

This thesis is dedicated to exploring the capability of designing and fabricating suspended silicon-based micro and nanotools with the main objective of being applied in cell biology.

This study rises due to the need of obtaining even more smaller devices for even more specific applications. Up to date, the provided systems obtained by the Micro and Nanotechnologies were based in Cell-on-a-Chip systems. Conversely and thanks to recent advances in miniaturization technologies, many researchers are focusing their efforts on manufacturing devices small enough to be applied for the study of single living cells. As individual cell studies to evaluate their behavior against different stimuli in an individual way are a topic of interest in nanomedicine.

For this reason and to support this line of research, in this thesis we provide multiple examples of Chip-on-a-Cell strategies, where we explore the possibility of obtaining diverse suspended devices under the cell scale. This means that a full range of applications at micro and nanoscale have been opened. The presented tools are promising in several applications, for instance, chemical mono and multi-functionalizations for sensing and acting directly in cell mediums, extra- and intracellular labeling and tracking of single living cells and embryos or these devices even allow us the study of the behavior of micro and nanomaterials in cell mediums at such scales. Summarizing, the work that is developed in this thesis provides proper tools to continue studying and exploring the wonderful and complicated world of living cells.

Finantial Support

This PhD work was financed by the Spanish Government through the projects MINAHE3 (TEC2008-06883-C03-01) and MINAHE4 (TEC2011-29140-C03). I would also like to thank the *Ministerio de Ciencia e Innovación* from the Spanish Government for my predoctoral grant (BES-2009-020415).

Contents

Abstract

This thesis presents the design, technological development, characterization and chemical and biological validations of five types of micro and nanodevices which are focused on being functional tools for cell biology.

This research is possible thanks to the recent advances in Micro and Nanotechnologies, where the application of miniaturization techniques at cell scale is already a reality. Therefore and taking advantage of the silicon microtechnologies, and this thesis is a clear example, we are able to obtain a large variety of Chip-on-a-Cell systems, where our devices are small enough to label and track living embryos or even sense and operate in single cells in an extra- and intracellular way. Furthermore, one of the most relevant new features of the micro and nanotools presented in this thesis is the capability of being suspended, meaning that these devices can be released from the silicon wafer and directly interact with cells in their same medium.

These micro and nanotools present different shapes, sizes, materials and specific functionalities, as the combination of these features or even the incorporation of nanostructured parts in a single device can let us obtain multi-tasking devices.

Summarizing, the extensive capabilities of the presented micro and nanotools imply a broad number of applications in cell biology.

Objectives

The main objective of this PhD is to develop silicon-based suspended micro and nanotools using micro and nanotechnologies for several bioapplications. With this aim, the following specific objectives have been proposed:

1. Design micro and nanodevices with dimensions under the cell scale with several shapes, sizes and materials.
2. Develop the technological processes for the fabrication of micro and nanodevices at wafer level combining different microelectronic technologies.
3. Develop the releasing techniques for the obtaining of suspended micro and nanodevices.
4. Characterize the suspended micro and nanodevices through several techniques.
5. Validate the suspended micro and nanodevices for advanced applications in cell biology.

Structure of the thesis

The thesis has been organized as follows:

An introduction about the state of the art in advances in the study and operation through different techniques in living cells is given in **Chapter 1**.

The presentation of the fabricated micro and nanotools performed during this thesis begins in **Chapter 2**, where the design, technological development, characterization and validation of Polysilicon Barcodes as chemically functionalized extracellular biolabels to identify and track living embryos is described.

Going one step forward and with the main objective of incorporating even more sophisticated features in our devices, **Chapter 3** describes the design, technological development, characterization and validation of Cobalt and Nickel Magnetic Barcodes for micro-labeling and sorting.

Deepening in the study of obtaining multitasking chips, **Chapter 4** describes the design, technological development, characterization and validation of Polysilicon-Chromium-Gold Chips as bi-functional multi-material platforms for intracellular biosensing.

The incorporation of silicon nanowires to our microtools, allow us to perform a new and revolutionary line of devices. The first of these devices is presented in **Chapter 5**, where the design, technological development, characterization and validation of Nanowire Silicon Chips as nano-patterned devices for intracellular applications is described.

And lastly, the capabilities of the polysilicon labels with the advantages of silicon nanowires are combined in only one device. **Chapter 6** describes the design, technological development, characterization and validation of Nanowire Silicon Barcodes

as physical extracellular bio-labels to identify and track living embryos.

Eventually, the work developed during this PhD project allows the extraction of several conclusions presented in **Chapter 7**.

Chapter 1

General Introduction

Contents

1.1 Micro and Nanoparticle Suspensions for Cell Biology

1.1.1 Introduction

The use of micro and nanomaterials has been used for centuries, however, recent advances in micro and nanosciences are focused on obtaining even more sophisticated particles for applications in cell biology, biomedical research, diagnostics and therapy. As the multimodality (or now so-called theranostics, diagnostic capabilities combined with therapeutic actions) is the key feature of micro and nanoparticle applications.[1]

Due to the nature of this thesis, the applications of micro and nanoparticles explained here will be focused in cell biology. As the understanding of how living cells live and develop is the first step to manipulate more complicated biosystems for advanced applications in nanomedicine.

The ability of particles to sense or operate somehow in populations of cells for future bioapplications resides in the fact that they can be added within a cell culture and subsequently be adhered or absorbed by the cell population (Figure 1.1). In this section, a short overview of the progress achieved in the development of some of the most studied bioapplications of micro and nanoparticle suspensions is presented.

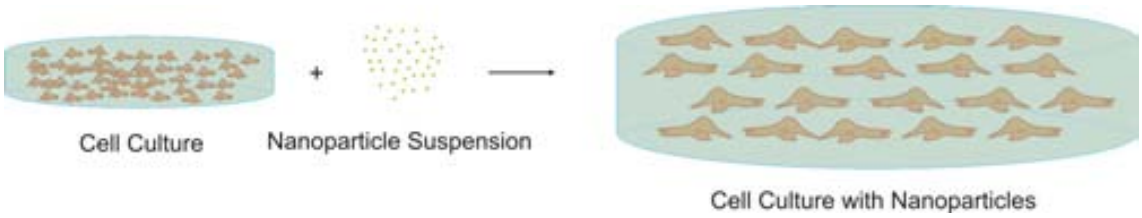

Figure 1.1: **Use of micro and nanoparticles within populations of living cells.** Micro and Nanoparticles can be added directly to the cell culture and adsorbed by the cell population.

1.1.2 Cell Labeling and Tracking

Cellular labeling and tracking using micro and nanoparticles are one of the most studied applications and have made the most advanced progress, attracted the greatest interest and also reached certain stage of commercialization. Numerous reports have appeared describing the use of several types of particles with different sizes and shapes to label cells, as these differences permit their visualization into the cells. Nanoparticles inside cells are not only useful to study and track living cells but also to study cell division and metastasis because of their stability and color emission.[2] In this section two of the most used particles for cell labeling and tracking are described.

i Gold Nanoparticles

Gold nanoparticles have fascinated scientists since the middle ages and have been used for a long time before the prefix *nano* emerged as colorants in glass windows and pottery due to their vibrant colors.[3] The colloidal chemistry resurged to popularity in the 1850s when Faraday first synthesized a pure gold colloid. From the first moment, gold nanoparticles have been in the focus of the nanochemistry due to their biocompatible nature and their potential biomedical applications. As this kind of nanoparticles possess unique size- and shape-dependence optical properties, large surface area, biocompatibility and high stability.[4]

Recently, gold nanoparticles have been regarded with interest in the nanomedicine field due to their numerous applications as agents for cell labelling and tracking.[5] For instance, gold nanoparticles can be conjugated with a specific antibody and used to target biomarkers overexpressed in breast cancer cells,[6] or they scatter strongly in the near-infrared region, being capable of detecting head and neck cancer cells.[7] Furthermore, the gold core is inert so, gold nanoparticles, although penetrating the cells, are mainly not cytotoxic.[8]

ii Quantum Dots

Over the past decade quantum dots (QDs) have emerged as a premier biological labeling tool due to their unique photophysical properties.[4] A quantum dot is a nanocrystal made of semiconductor materials that are small enough to exhibit quantum mechanical properties. Electronic characteristics of a quantum dot are closely related to its size and shape, as the band gap in a quantum dot determines the frequency range of emitted light and is inversely related to its size. Consequently, the color of emitted light shifts from red to blue when the size of the quantum dot is made smaller. The techniques to obtain quantum dots are cheap and surface modifications and functionalizations can be implemented.[9] In fact, the use of quantum dots for highly sensitive cellular imaging has seen major advances over the past decade. One of the most relevant achievements of the quantum dots is the acquisition of many consecutive focal-plane images that can be reconstructed into a high-resolution three-dimensional image, this ability can be applied, for example, to the advanced study of cell structures (Figure 1.2).[2, 10] Or even they allow the real-time tracking of molecules and cells over extended periods of time.[11]

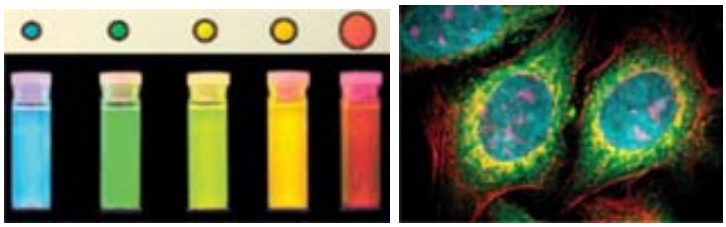

(a) (b)

Figure 1.2: **Cellular multicolor imaging using quantum dots**. a) The fluorescent emission (from red to blue) of QDs with different sizes excited by a hand-held UV lamp (λex = 365 nm). b) The multicolocr imaging of fixed human epithelial cells using five different color QDs. Cyan corresponds to 655-QDs labeling the nucleus, magenta 605-QDs labeling Ki-67 protein, orange 525-QDs labeling mitochondria, green 565-QDs labeling microtubules, and red 705-QDs labeling actin filaments.[2]

1.1.3 Cell sorting

Another application of particles in cell biology is cell sorting. Cell sorting is the ability to separate cells into intracellular or extracellular according to their properties. Intracellular processes can include DNA, RNA and protein molecule interactions, whereas extracellular physical properties include size, shape and surface protein expressions. A high suitable cell sorting is important, as cells are basic structural and functional units of all living organisms, so the ability to isolate and sort different cell types within organs and tissues has led to many established principles in medicine and physiology.

Currently there are several methods for cell sorting. However, in this case only those which are involved with particle suspensions are described in this section, such as magnetic cell selection and fluorescent cell sorting.

i Magnetic Nanoparticles

Magnetic nanoparticles offer some attractive possibilities in cell biology as their most important properties are nontoxicity, biocompatiblilty and injectability.[12] Magnetic nanoparticles can also be attracted to a high magnetic flux density, being possible to manipulate cells labeled with magnetic nanoparticles using magnets. This action *at a distance*, combined with the intrinsic penetrability of magnetic fields into human tissue, opens up applications, such as magnetic separation, drug delivery and hyperthermia treatments.[13] Magnetic separation has been successfully applied to many aspects of biomedical and biological research, as it has been proved to be a highly sensitive technique for the selection of rare tumour cells from blood and is especially well-suited to the separation of target cells.[14] Ferric oxide is the main constituent of magnetic particles, although metals such as cobalt and nickel are also used (Figure 1.3).

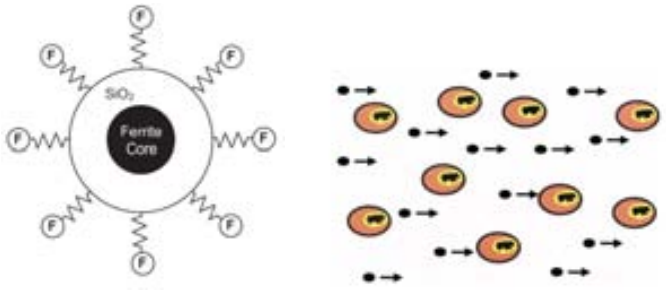

(a) (b)

Figure 1.3: **Magnetic Nanoparticles for Cell Sorting**. a) Schematic diagram of a functionalized magnetic nanoparticle showing a core/shell structure with a shell of silica, $SiCl_2$, and functional groups attached to the shell.[13] b) Magnetic loading principle. Magnetic nanoparticles (small dots) are forced to move through a cell mixture by application of a magnetic gradient thereby increasing cell-nanoparticle collisions.[14]

ii Fluorescence Nanoparticles

Fluorescence generates very intense signals that allow detection in very short data acquisition times with straightforward analysis.[15, 16] In fact, fluorescence-encoded particles can be rapidly processed by using methods that detect fluorescence in single cells or tissues such as confocal laser scanning microscopy,[17] fluorescence-activated cell-sorting or by advanced imaging techniques to detect fluorescence in small animals.[18] Thus, such fluorescently encoded particles offer a sensitive, rapid and cost-effective solution for cell sorting and diagnostic applications.[15]

For instance, quantum dots are ideal candidates as fluorescent tags for cell separation capabilities, due to their broad absorption spectra, their narrow emission band (which allows the use of a single light source for exciting at once various quantum dots emitting at different wavelengths), their high fluorescence quantum yield and their robustness (see section 1.1.2 - ii).[19]

1.1.4 Cell Biosensing

i Noble Metal Nanoparticles

In the last decade the use of micro and nanomaterials has been having a great impact in biosensing.[20] In particular, the unique properties of noble metal nanoparticles have allowed the development of new biosensing platforms with enhanced capabilities in the specific detection of bioanalytes.[20] Noble metal nanoparticles show unique physicochemical properties that allied with their unique spectral and optical properties, allow us to apply them in many bioapplications, such as nanobiosensors for disease diagnosis, nanoprobes for *in vivo* sensing/imaging, cell tracking and therapy monitoring.[21–23]

They can measure between 1 to 100 nm in diameter, have different shapes and can be composed of one or more inorganic compounds, such as noble metals, heavy metals, iron, etc. The majority of them exhibit size-related properties that differ significantly from those observed in bulk materials. Noble metal nanoparticles, in particular gold and silver, are among the most extensively studied nanomaterials for biosensing applications and have led to the development of innumerous techniques and methods.[20]

In addition, gold nanoparticles have a number of physical properties that make them appealing for medical applications (see section 1.1.2 - i), where this array of features has led to applications in approaches, such as concurrent diagnosis and therapy.[24]

1.1.5 Drug Delivery

Another one of the most studied applications of micro and nanoparticles is drug delivery, which refers to approaches and technologies for transporting a pharmaceutical compound in the body as needed to safely achieve its desired therapeutic effect. In addition, site-specific drug delivery is an important area of research that is anticipated to increase the efficacy of the drug and reduce potential side effects. Recently, targeted nanoparticles have been used to direct another particles to specific tissues, minimizing toxicity and improving oral bioavailability, unfavorable pharmacokinetics, drug effect in the target tissue and the stability of therapeutic

agents against decomposition.[19] In this section three of the most used micro and nanoparticles for drug delivery are shortly described.

i Polymeric Nanoparticles

Polymeric nanoparticles are nanosized carriers made of natural or synthetic polymers with applications in several fields such as energy and materials science.[25] However, their drug delivery capabilities is one of their most relevant applications.[25–27] For instance, polymeric nanoparticles have been shown to be promising carriers due to their potential both in encapsulating drugs, hence protecting them from excretion and metabolism and in delivering active agents across the blood - brain barrier without inflicting any damage to the barrier.[26] These nanoparticles will act as a kind of nanocapsules forming a thin polymeric envelope, thus, they can be considered as a reservoir system. The drug can be loaded in the solid state, in solution or chemically linked to the nanoparticle surface.[26] Some advantages of polymeric nanoparticles as drug delivery systems are that they increase the stability of any volatile pharmaceutical agents, easily and cheaply, that they offer a significant improvement over traditional oral and intravenous methods of administration and they deliver a higher concentration of pharmaceutical agent to a desired location (Figure 1.4a).[27, 28]

ii Mesoporous Silica Nanoparticles

Another type of nanoparticles which is being considered as an efficient carrier for intracellular drug delivery is the mesoporous silica nanoparticles. The ability to functionalize the surface of these nanocarriers with other nanoparticles, polymers or even proteins allows us to use these nanoparticles as a kind of reservoir for the controlled release of various cargos inside a specific cell.[29] The most recent reports on the toxicity of mesoporous silica nanoparticles *in vitro* have shown promising results.[29] However, much more work needs to be performed to demonstrate the biocompatibility of mesoporous silica nanoparticles *in vivo* (Figure 1.4b).[29]

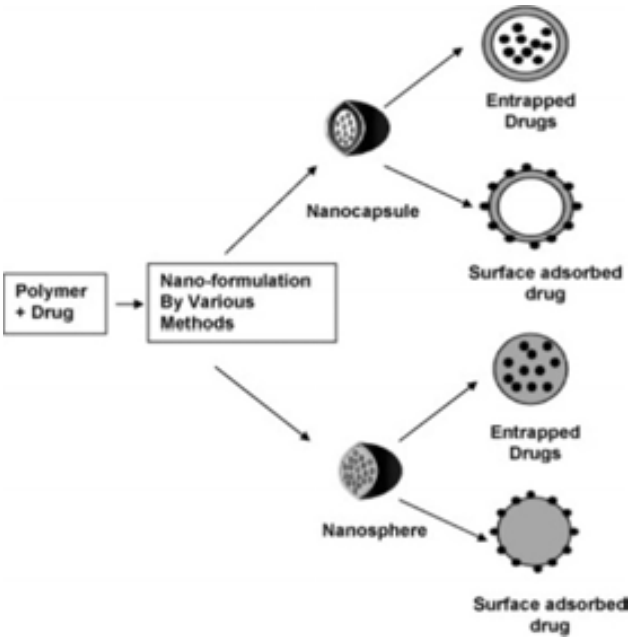

(a)

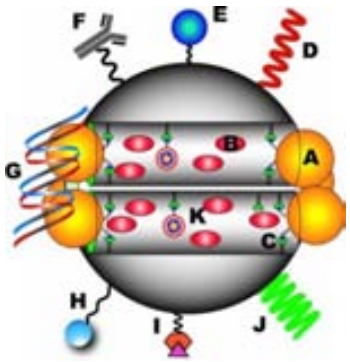

(b)

Figure 1.4: **Nanoparticles for intracellular drug delivery**. a) Polymeric nanoparticles are classified as nanocapsule and nanosphere. The drug molecules are either entrapped inside or adsorbed on the surface.[27, 30] b) Mesoporous silica nanoparticles (MSNs) as a platform for drug delivery. A) Nanoparticles attached to MSNs as functional gatekeepers. B) Hydrophobic/hydrophilic guest molecules entrapped in the interior of the nanochannels. C) Stimuli-responsive linkers, which chemically attach MSNs and gatekeepers. D) Grafting with a protecting polymer, shields the MSN surface from interacting with opsonizing proteins. E) Bioimaging agents such as magnetic nanoparticles, quantum dots, or fluorophores. F) Targeting ligands such as antibodies. G) Complexation with plasmid DNA. H) Additional ligands such as cell-penetrating peptides. I) Incorporation of a diagnostic label. J) Stimuli-responsive polymers. K) Attachment of functional groups that could modify the metabolism of cells.[29]

iii Silicon Microparticles

Nano-structured delivery systems are also emerging as powerful tools for the systemic delivery of therapeutic molecules and imaging agents for different biomedical applications, from cancer[31] to cardiovascular diseases.[32] These delivery systems can be loaded with a multitude of drug molecules and contrast agents to simultaneously provide therapeutic and imaging capabilities. For instance, vascular endothelial cells are capable of rapidly internalizing silicon microparticles by phagocytosis (Figure 1.5).[33]

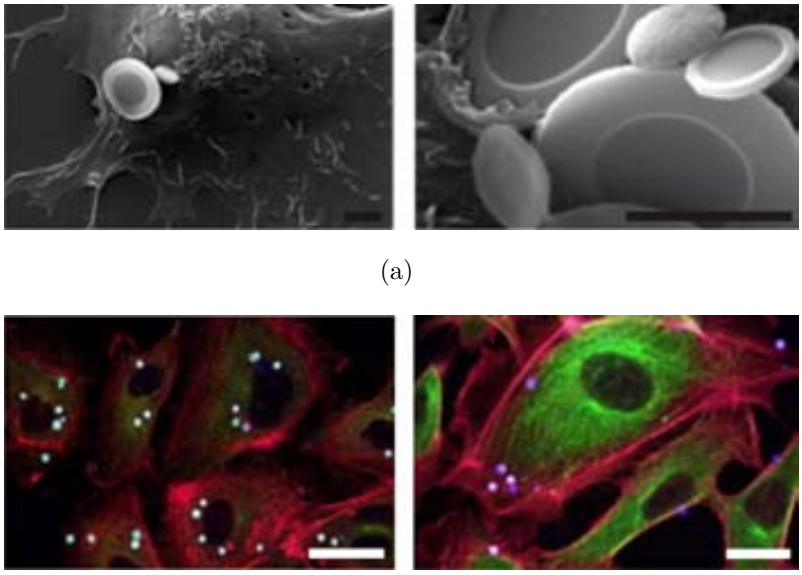

(a)

(b)

Figure 1.5: **Extracellular oxidized silicon microparticles as drug delivery systems.** a, b) Scanning electron and confocal microscopy images of human umbilical vein endothelial cells with a mixture of oxidized silicon microparticles, respectively. Black scale bars = 2 μm. White scale bars = 25 μm.[33]

Loading nanoparticles into porous silicon matrices provides tuning at multiple levels. Tunable parameters include particle geometry and surface modification, as well as tunable rates of degradation based on silicon porosity. As modulation of particle geometry, surface chemistry, and porosity allows silicon particles to be optimized for more specific applications.

1.1.6 Advantages and Disadvantages of Micro and Nanoparticle Suspensions in Cell Biology

Most benefits of micro and nanosciences depend on the fact that it is possible to tailor the essential structures of micro and nanomaterials to achieve specific properties. Hence, these materials can effectively be made to be stronger, lighter, more durable or more reactive, among many other traits. There already exist over 800 everyday commercial products that rely on micro and nanoscale materials.

We can find particles in a huge ammount of applications. For instance, in many computing and communications systems. Furthermore, the difficulty of meeting the world s energy demand is compounded by the growing need to protect our environment. For this reason, many scientists are looking into ways to develop clean, affordable and renewable energy sources. There are many eco-friendly applications for micro and nanoparticles, such as cleaning water from polluted water sources in both large-scale and portable applications and ones that detect and clean up environmental contaminants. And last but not least, micro and nanoparticles have the real potential to revolutionize a wide array of medical and biotechnology tools (as I explained in the last sections) and procedures so that they are more personalized, portable, cheaper, safer and easier to administer.

However, after analyzing the bioapplications of the best known micro and nanoparticles carefully, the possible drawbacks of some types of particles should also be analyzed. Micro and Nanomaterials have the potential to revolutionize biosciences because of their ability to affect organs and tissues at molecular and cellular levels. However, current micro and nanomaterial research is focused mainly on the particle applications, whereas side effects associated with their uses are not taken into consideration during the obtaining process.[34] For instance, nanoparticles possess different physicochemical properties that their bulk analogues due to their extremely small size and large surface area. For this reason, nanomaterials should be evaluated separately for toxicity and adverse health effects, as possible toxic health effects of these particles associated with human exposure are still unknown.[35] In fact, toxicity issues related to nanomaterials used in bioapplications are often ignored.[36, 37]

Thus, along with the development of novel nanoparticles, experts in related scientific fields are calling for a simultaneous assessment of the toxicological and

environmental effects of nanoparticles.[38] Recent *in vivo* and *in vitro* studies have suggested that inhalation and dermal absorption of some nanomaterials may have adverse health effects[38] and the use of medical products containing nanomaterials may lead to chronic health risks (Figure 1.6).[35] Doubtless, micro and nanosciences will have a profound impact on a wide range of applications and therefore on many aspects of human life. Although one major challenge is the lack of information on the possible adverse health effects caused by exposure to different micro and nanomaterials. Development of safety guidelines by governments including manufacturing, monitoring of worker exposure, ambient release of micro and nanoparticles and risk evaluations is mandatory to promote them for bioapplications.[35]

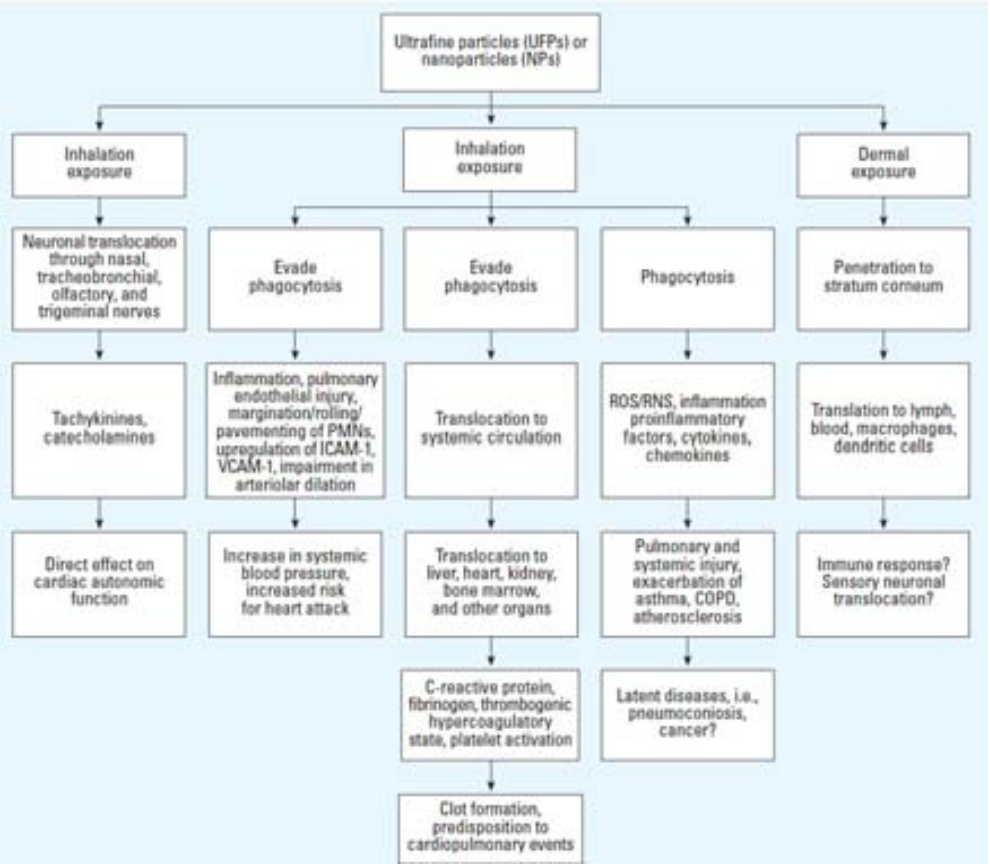

Figure 1.6: **Hypothetical schema of potential interactions of nanoparticles with the human body.** Abbreviations: ICAM-1, intracellular adhesion molecule-1; PMNs, polymorphonuclear leukocytes; RNS, reactive nitrogen species; VCAM-1, vascular adhesion molecule-1. Schema also shows suspected interactions (indicated by a question mark) leading to sequences of events that may cause cardiovascular and pulmonary morbidity and mortality.[35]

1.2 Micro and Nanochips for Cell Biology

1.2.1 Introduction

Due to the health concern (see section 1.1.6), the use of some types of micro and nanoparticles has been minimized and the task to identify substitute benign nanoparticles has become a focus in bioapplications.[39] On the other hand, the different sizes and shapes of the particle suspensions are carefully analyzed because of the well-known dependence between the shape of the particles and their specific uses. However, while much effort has gone into creating and understanding the resulting properties for synthetized particles, achieving an optimized control over the nature of the particles is still a challenge to overcome.[4]

Conversely, microelectronics industry has much to say on solving these fundamental issues, as progresses in microelectronics allow the fabrication of low cost systems, with complex structures, easy-to-operate and at a high level of design control.[40, 41] In addition, the interface between microsystems and biosystems is emerging as one of the broadest and most dynamic areas of science and technology, bringing together biology, chemistry, physics, engineering, biotechnology and medicine. Thus, the combination of these diverse areas of research promises to yield revolutionary advances in healthcare, medicine and life sciences.[42]

In this section, microelectronic systems focused on the study of living cells are analyzed. As the understanding of how living cells live and develop is the first step to manipulate more complicated biosystems for advanced applications in life sciences.

There are several types of microdevices focused on the study of living cells. For instance, Cell-on-a-Chip systems, where populations of cells can be directly cultured on a single chip to study their way of life or how a specific parameter can affect the whole cell culture (Figure 1.7a). Or even microchips with an integrated nanostructure have been developed, where they can sense or operate over a single cell (still in the culture) in an invasive or non-invasive way (Figure 1.7b). In this section, a comprehensive overview of the progress achieved in the microsystems development for cell biology is presented.

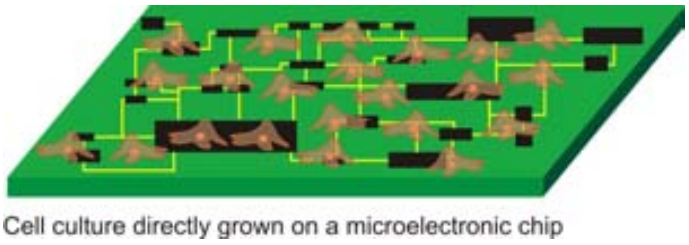

(a)

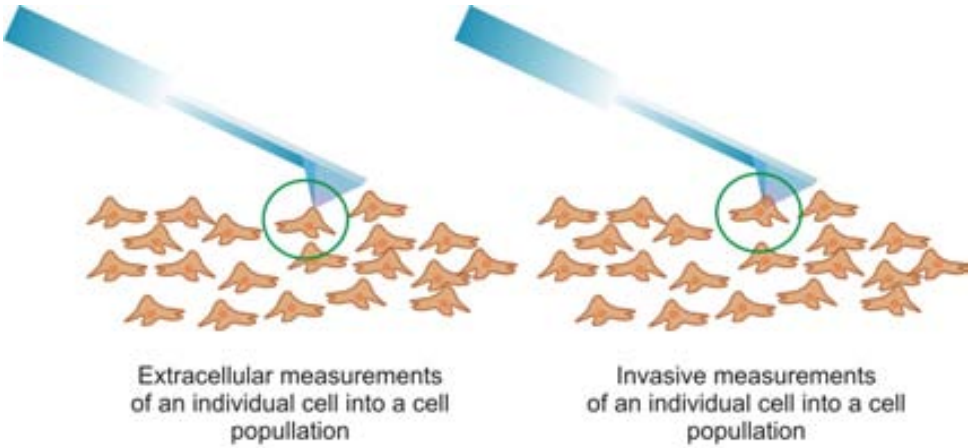

(b)

Figure 1.7: **Different uses of microelectronic systems for the study and operation of cell populations**. a) A population of cells can be directly grown over a microelectronic chip for its study over different stimuli. b) Non-invasive and invasive measurements through microchips with an integrated nanostructure over a single cell inside a cell population.

1.2.2 Cells-on-a-Chip Microsystems

Cell-on-a-chip systems have recently become a research hotspot because of their numerous advantages, such as miniaturization, control of the microenvironment, increased sensitivity, non-invasiveness, real-time analysis and reduced costs.[43] In addition, these chips have been applied in many fields, such as biomedicine and cell biology.[41]

Much cell-based microsystem research takes place under a lab-on-a-chip or micro-total-analysis-system (μTAS) framework that seeks to create microsystems incorporating several steps of an assay into a single system.[44] This makes microtechnology an excellent tool in the fundamental study of cell biology. For instance, microelectronics allows experiments that cannot be performed simply by miniaturizing and mechanizing conventional laboratory procedures (Figure 1.8).[45] This is possible because microtechnology provides new opportunities for understanding biochemical and mechanical processes responsible for changes, for instance, in cell behavior.[46]

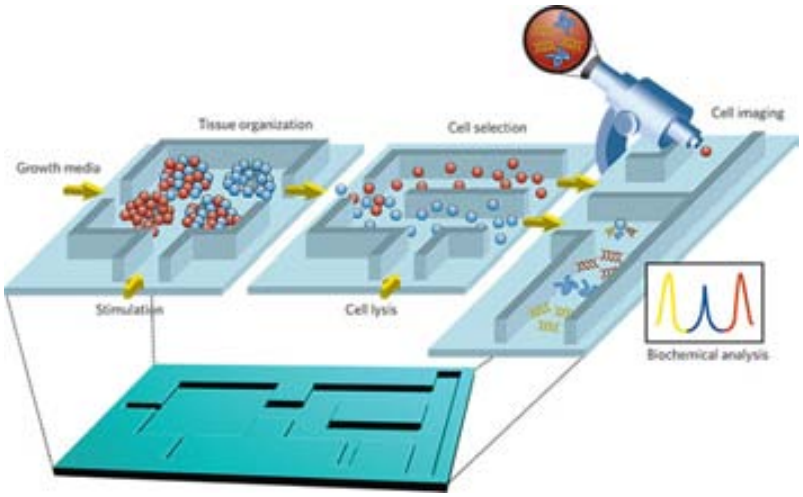

Figure 1.8: **Example of a lab-on-a-chip system.** Microsystems can incorporate numerous techniques for the analysis of living cells. As indicated by the yellow arrows, the different components of the chip can be connected with each other to form an integrated system, realizing multiple functionalities on a single chip.[45]

1.2.3 Microchips with an Integrated Nanostructure

The integration of nanostructures (smaller than cells) in microsytems (bigger than cells) through microtechnology processes is becoming a tendency for microchip applications in cell biology, as this methodology offers the possibility to directly sense a specific parameter or operate of an indivual cell membrane.

Processes can also be achieve in an non-invasive and invasive way, where a portion of the nanostructure (attached to the microchip) touches or is inserted into the cell, for instance, to inject some specific molecules directly into a single cell for biosensing, diagnosis or intracellular drug delivery. However, we should take into account that these applications will act on an indidual cell but this cell will be still into its cell population.

As a destacable example, nanoscale field-effect transistors (FET) as localized bioprobes, where a so-called tip is situated on the top of a microchip, are shown in figure 1.9. This nanoprobe (once inserted into the cell) exhibited conductance and demonstrated high pH sensitivity.[47]

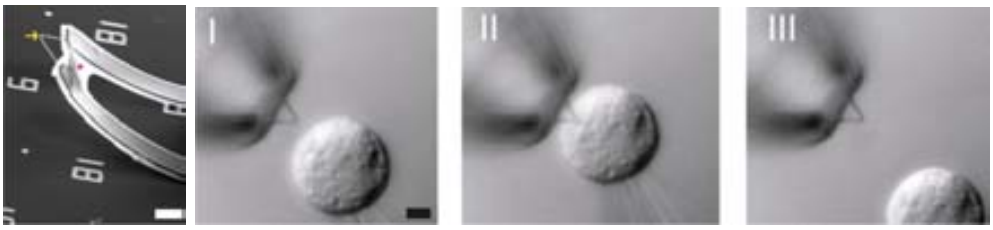

(a) (b)

Figure 1.9: **Example of a microchip with an integrated nanostructure**. a) Scanning electron microscopy image of a nanostructured device. The yellow arrow and pink star mark a nanoscale FET and SU-8 (a commonly negative photoresist which is used as flexible device support), respectively. b) Differential interference contrast microscopy images of the nanoprobe as the cell approaches (I), contacts (II) and internalizes (III). Scale bars = 5 μm.[47]

1.2.4 Nanostructured Platforms

Inside of the microelectronic systems the nanostructured devices are one of the most potential tools for cell biology, as the similarity in sizes of synthetic and natural nanostructures makes them an obvious choice. Integrated microdevices with nanosized parts are emerging as general platforms and offer a huge potential to develop different devices for wide range of applications.[42]

Although so many nanostructured platforms have been developed, this section will be focused on one of the most used nanostructures for cell biology application, the nanowire.[42] As the potential of using vertical nanowires for biological applications has been, and still is, an area gaining increasing attention and interest.

As relevant examples, nanowires have been used for delivering biomolecules into living cells (Figure 1.10a, b),[48, 49] or as efficient capturer of circulating tumor cells (Figure 1.10c).[50, 51] Nanowire devices have been also proved to transduce chemical and biological binding events into electronics for a highly sophisticated interface for biological information[52–55] or even silicon nanowires may be coupled to a variety of molecules, such as antibodies and DNA plasmids (Figure 1.10d).[48, 52, 56]

Furthermore, many post-fabrication modifications can be made to tailor the nanowires to improve their possible applications or even increase their biocompatibility. For instance, cytotoxic copper oxide nanowires can be encapsulated in a harmless silicon oxide coating[53] or cell attachment to the various materials can be improved to increase the wettability of the surface.[57]

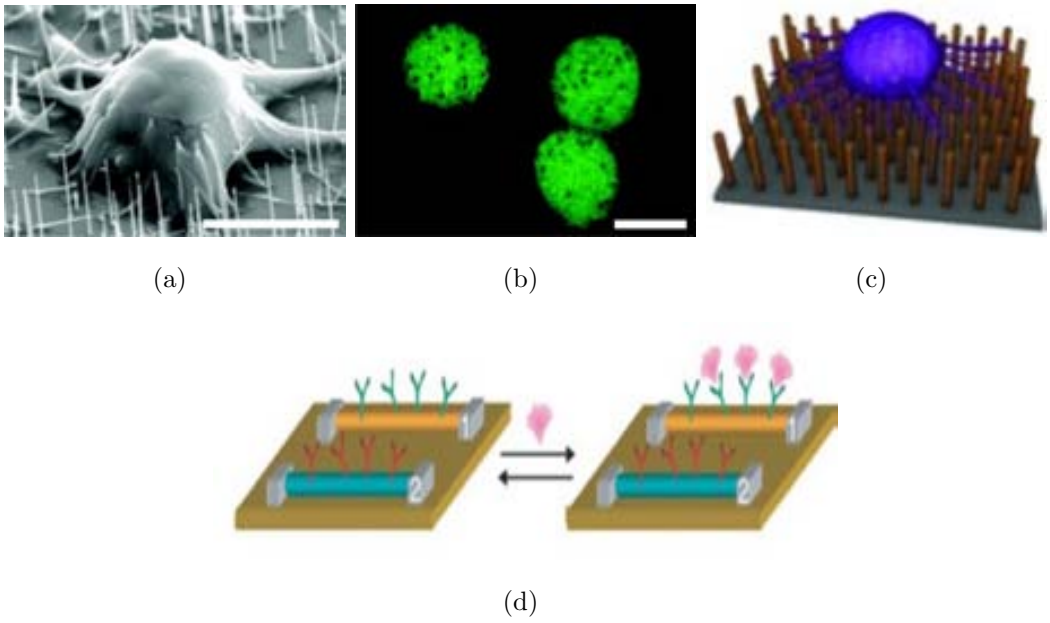

(a) (b) (c)

(d)

Figure 1.10: **Potential applications of nanowire platforms in cell biology**. a, b) A scanning electron and confocal microscopy images of mouse embryonic cells penetrated with silicon nanowires, respectively.[49] c) Conceptual illustration of a new-generation nanomaterial-based platform for cell-affinity assays capable of capturing circulating tumor cells[50] d) Schematic showing two nanowire devices within an array, where the nanowires are modified with different (green and red) antibody receptors. A cancer marker protein (pink), which binds specifically to its receptor, will produce a conductance change of the surface charge of the protein only on nanowire-1.[52] Scale bars = 10 μm.

1.2.5 Chemical Functionalized Systems

Going one step further and combining the functional features of chemically obtained macro, micro and nanomolecules with the countless applications of the microelectronic systems explained during the last sections, highly precise microelectronic chips for bioapplications can be obtained.

One of the most currently used methods to immobilize biomolecules to solid substrates (for instance, a microchip) is the formation of an organic layer that will act as linker, the so-called self-assembled monolayer. Self-assembled monolayers (SAMs) have been deeply studied and investigated in the last decade because of their high range of applications in many different areas such as nanotechnology, chemical surface

sciences, biotechnology, chemical engineering or electronics.[5] SAMs are molecular assemblies formed on metallic or inorganic surfaces by chemisorption between the substrate and a functional head group (Figure 1.11).[58] The activity and the utility of SAMs depend on the molecule that will be immobilized into the SAM using the reactivity between the functional group of the SAM and the desired molecule.[59] The selectivity offered by biomolecules liked to the solid surface through this method, such as antibodies, proteins, nucleic acids and enzymes or even organized systems like whole cells can be profitably used for molecular recognition.

Well-defined functional surfaces can be achieve by the formation of SAMs through the covalent interactions of thiols, disulphides, sulphides and other related molecules (head group) with the surfaces of noble metals, particularly gold, as well as silicon and platinum (solid surfaces).[4] The monolayer produced by self-assembly allows high flexibility with respect to several applications depending upon their terminal functionality (functional group) or by varying the chain length (alkyl chain). SAMs are also used as model substrates in biological studies because of their well-defined structure, controlled surface properties and biocompatibility.[5] SAM formation allows also the possibility of changing surface properties or to add new characteristics to the materials.

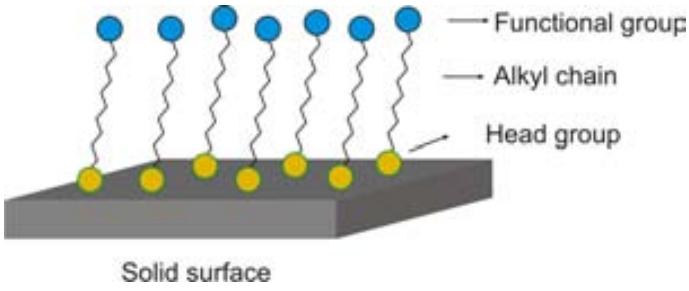

Figure 1.11: **Fragments of a functional self-assembled monolayer.** The head group is responsible for the anchoring of the molecules onto the solid surface. The alkyl chain has a significant influence on the ordering of the SAM and provides the stability of the monolayer. The functional end group introduces chemical functionality into the monolayer system and is important for the overall properties of surfaces because it allows the immobilization of the desired active molecule.[5, 60]

1.3 Suspended Micro and NanoTools: Single Cell Analysis

1.3.1 Introduction

As it can be seen in the last sections, even more sophisticated systems are being devised for applications in cell biology.

At this point, our group (*Micro and Nanotools of the IMB-CNM, CSIC*) had the idea of combining the countless possibilities of the chemistry (nanoparticles and self-assembled monolayers) with the potential applications of the microelectronic systems (multi-functional and nanostructured devices) along with the microelectronics miniaturization capabilities to develop suspended micro and nanotools, with dimensions under the cell scale, for single cell applications. These chips will be the base of a new line of Chip-on-a-Cell systems.

In contrast to the microsystems presented during the last sections (see 1.2), the suspended micro and nanotools possess the ability of having dimensions below the cell scale, what means that these devices can be adhered or internalized within a single cell allowing, in a revolutionary way, the single living cell study (Figure 1.12). To achieve this purpose we need to shrink the devices in factor below 1.000.000.000, as these dimensions are the typical ones of the microchips, i. e., from the millimetre to the micrometre.

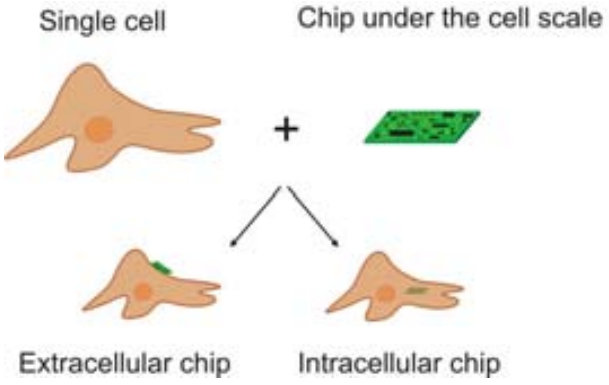

Figure 1.12: **A single cell analysis thanks to the suspended micro and nanotools**. Single cell analysis by extra and intracellular micro and nanotools.

Furthermore, with this type of tools we have also the possibility of analyzing a single cell inside its own cell culture, simply adding the suspended chips directly over the cell population (Figure 1.13). In contrast to the single cell analysis explained in section 1.2.1, where microchips with an integrated nanostructure is used to analyze a unique single cell at once into its cell population, here we can achieve a complete single cell analysis, as every single cell will carry an attached or internalized chip.

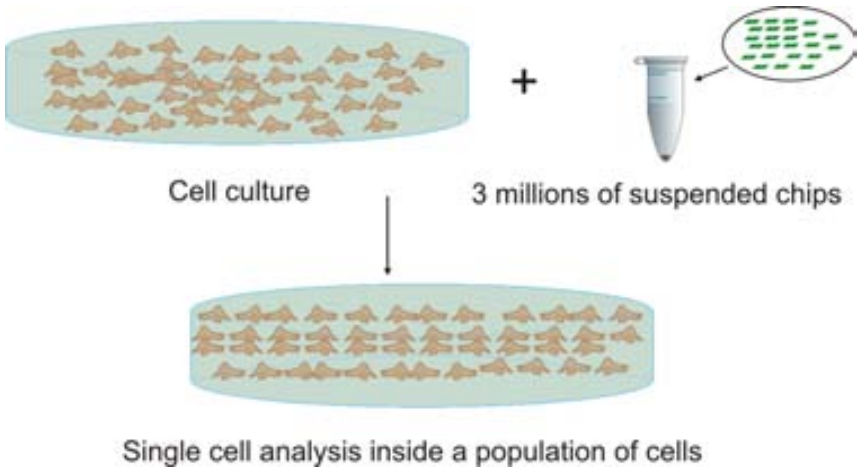

Figure 1.13: **Single cell analysis inside a cell population thanks to the suspended micro and nanotools**.

Thus, we can obtain new tools under the cell scale which can sense and control bioparameters in an extra and intracellular way. In fact, single cell analysis is the new frontier in biological studies and has the potential to transform biological systems through new discoveries.[61]

Taking into account the wide range of possibilities that devices under the cell scale can provide, our group has tried to innovate with the design and fabrication of suspended micro and nanotools for several applications in cell biology, such as bio-labelling and tracking, bio-sensing and in the near future bio-theragnostics, combining intracellular diagnosis and therapy.

Traditionally, our devices were made mainly of one material, polycrystalline silicon, which is widely used in microelectronics and with versatile applications. However, the main objective of this thesis will be, starting from mono-material devices composed only of polysilicon, incorporate more and more sophisticated features to our tools.

1.3.2 Previous Tools Fabricated in the Micro and NanoTools Group

i Using Polysilicon as a Main Material

Polycrystalline silicon (best known as polysilicon) is a silicon material consisting of small crystals, also known as crystallites, which give the material its typical metal flake effect, unlike single crystal silicon, which has one single, continuous and unbroken crystal, as its structure contains no grain boundaries.

Polysilicon has been long used as the conducting gate material in complementary metal-oxide-semiconductor (CMOS) processing technology. For this technology polysilicon is deposited using low-pressure chemical-vapor deposition (LPCVD) reactors at high temperatures, where the wafer (substrate) is exposed to one or more volatile precursors, which react and decompose on the substrate surface to produce the desired deposit, in our case, polysilicon. Reduced pressures tend to reduce unwanted gas-phase reactions and improve film uniformity across the wafer. A uniform deposition from several microns to a few nanometers can be obtained with this method, which is a fundamental requirement for the obtaining of micro and nanometric tools (Figure 1.14).

(a) (b)

Figure 1.14: **Examples of different polysilicon samples**. a) Some polycrystalline silicon rods. b) Polysilicon wafers.

Eventually, polysilicon can be used for bioapplications in life sciences for two major reasons, its large available knowledge based on this material and its well-known biocompatibility in cell cultures.[62]

ii Polysilicon Chips as Intracellular Biosensors

Intracellular chips with the advantages of microelectromechanical systems (controlled shape and size, versatility and mass-production) but small enough to be internalized inside living cells were succesfully achieved by our group (Figure 1.15a and b).

Human macrophages were chosen as a cellular model to determine if these polysilicon chips could be introduced inside the cells by phagocytosis, as macrophages have an inherent phagocytic capacity and can engulf large pathogens and microparticles up to 20 μm. Cytotoxicity was also analyzed and no significant differences between the cells with internalized chips and the cell group were observed.[63]

Inside this line of research, our group went one step forward. To assess if cells are healthy and alive after polysilicon chip internalization a vital dye fluorescein diacetate (CFDA) and time-lapse microscopy were used. In this case HeLa cells were used to achieve the experiments. Interaction of CFDA with active intracellular esterases hydrolyzes the acetate groups, producing fluorescein emission, which can be observed under a fluorescent light. Alive chip-containing HeLa cells display green fluorescence (Figure 1.15c and d).[64]

As it can be seen, polysilicon microchips provide endless possibilities to the design of innovative devices for intracellular applications. For instance, they enable characterization and quantification at the level of single cells and single molecules, *in vivo* real-time monitoring of cellular events and specific targeting of living cells, among others.[63, 64]

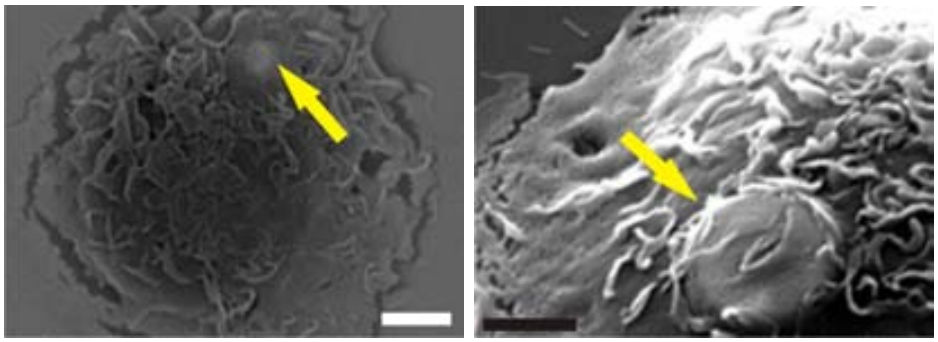

(a) (b)

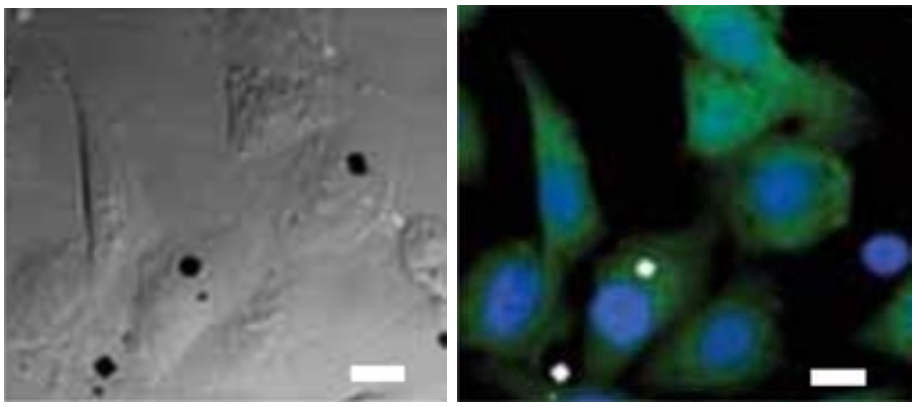

(c) (d)

Figure 1.15: **Micro and NanoTools group polysilicon microchips.** a, b) Scanning electron microscopy images showing a phagocited polysilicon microchip. Yellow arrows point to microchips.[63] c, d) Optical and confocal image of intracellular chips internalized in HeLa cells, respectively. White scale bars = 10 μm. Black scale bar = 2 μm[64]

.

iii Intracellular Polysilicon Barcodes for Cell Identification

We encounter many products and brands every day. We recognize the ones that we know or want by looking for an associated logo or the name of the product. This information is present on the label of the product and helps us to identify it, know some warning, instructions of use or any relevant information of the product. When we go to the micro and nano-scale objects, identification is a problem. We therefore need labels to prevent confusion.

Barcodes are representations of data (related to an object) attached to the object of interest. They were originally designed for optical readability by machines. These barcodes were initially one-dimensional and later two-dimensional. The use of barcodes as a technology for research applications at the microscale is not new. For instance, there have been some demonstrations of metallic barcode studies (Figure 1.16).[65–70] Novel applications of barcoded particles are reported every week as researchers find creative ways of utilizing the efficiency and flexibility made possible by encoded microparticles.

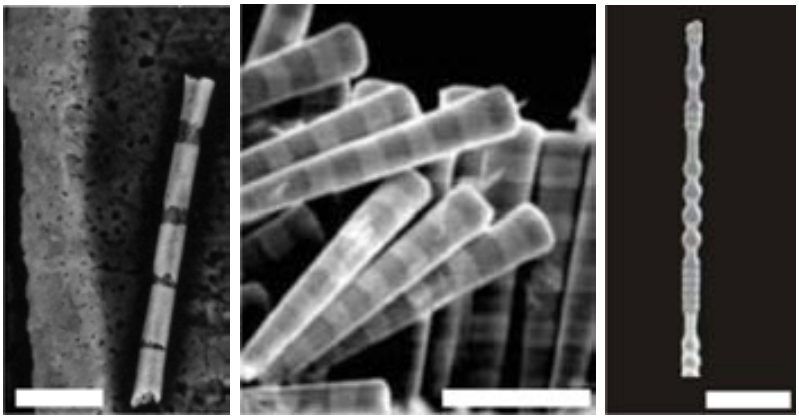

(a) (b) (c)

Figure 1.16: **Examples of metallic codes.** a) SEM image of an Au-Ag nanorod. Scale bar = 1 μm.[65] b) Conical metallic barcoded wires. Scale bar = 3 μm.[69] c) Diameter-modulated gold barcodes wires. Scale bar = 10 μm.[70]

In case of fertility clinics, there have been documented mix-ups due to mistakes in proper identification of the correct parental gametes.[71] These mix-ups are followed by long standing legal suits with too much economic damage and mental agony to the parties involved. To prevent such mix-ups, research ideas for biotagging using microbarcodes as labels was recently developed by our group, Micro and NanoTools group. Firstly, our group developed a polysilicon barcode sufficiently small to be introduced into a living cell, yet visible and readily identifiable under an optical microscope. Human macrophages were used as a cell line due to their ability to engulf the devices. The utility of the barcodes for cell tracking was successfully demonstrated by following individual cells for up to ten days in culture and recording their locomotion (Figure 1.17a).[62]

Later, polysilicon microbarcodes were modified with specific ligands in order to be selectively attached to chemical residues located at the plasma membrane and thus to be applied to study individual cells in culture. Barcodes were modified by adsorption and covalent attachment with either wheat germ agglutinin (WGA) or a generic immunoglobulin G (IgG), both labeled with a fluorophore organic molecule. The WGA lectin would enable the attachment of the devices to any cell type whereas the IgG would be representative of an antibody to a specific membrane receptor in a selected cell type, taking into account that all antibodies share the same basicstructure. Fluorescence imaging and statistical analysis were carried out to demonstrate the covalent attachment of the ligand to the surface of the microdevice. Vero cells in culture were labeled with the covalently modified barcodes and successfully tracked for up to 1 week without observing any alteration in the viability of the cells (Figure 1.17b).[72]

Eventually, and with the idea of solving the documented mix-ups in fertility clinics,[71] the microinjection of polysilicon barcodes in the perivitelline space of mouse embryos has been achieved by our group. The obtained results presented demonstrated the feasibility of this direct embryo labeling system and constituted the starting point in the development of such systems Figure 1.17c.)[73]

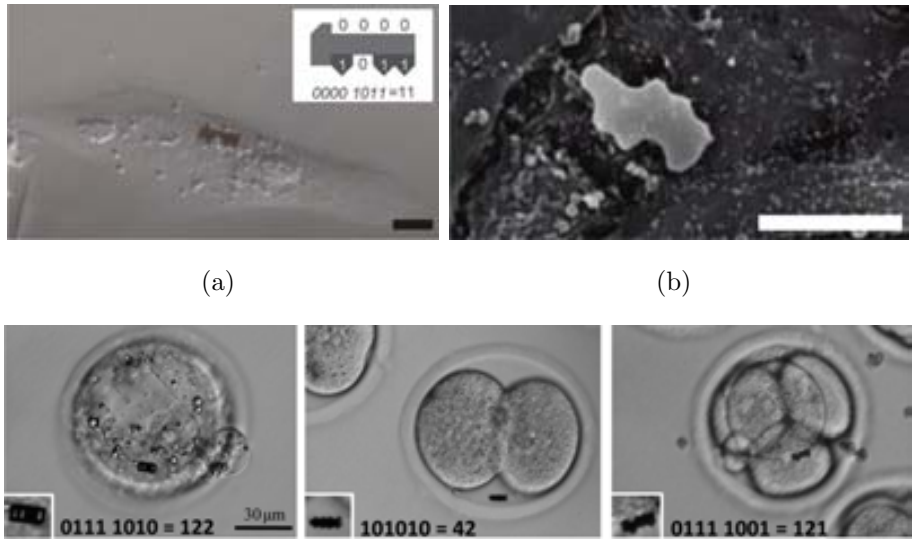

Figure 1.17: **Micro and NanoTools group polysilicon barcodes.** a) Inverted light microscopy image of a macrophage with an intracellular polysilicon barcode.[62] b) A scanning electron microscopy image of a Vero cell with an extracellular, previosuly functionalized, barcode. Scale bars = 10 μm[72] c) Optical images of *in vitro* tagged embryos with different types of polysilicon barcodes. Scale bars = 30 μm.[73]

1.3.3 Beyond Polysilicon

Along this chapter the almost infinite different uses of micro and nanoparticle suspensions and electronic microdevices, over or under the cell scale, for bioapplications have been presented. However, the advances in fields such as micro and nanotechnologies, nanomedicine or cell biology do not end up here. Throughout the last years the main objective of this PhD work has been going one step forward and design and develop a revolutionary new line of micro and nanotools beyond polysilicon. It means, that new barcode designs, multi-materials chips, magnetic devices and nanostructured chips have been developed.

i Suspended Chemically Functionalized Polysilicon Tools as Extracellular Embryo Labels

Taking the idea of the polysilicon microbarcodes as intracellular and extracellular cell labels (successfully obtained by our group) a brand new design of functional-

ized polysilicon barcodes for extracellular embryo labeling and tracking has been developed.

ii Suspended CoNi Tools as Magnetic Labels

We go one step forward and propose a new technology to obtain magnetic microbarcodes, made of cobalt and nickel alloys, such that they satisfy the same technological and optical requirements of polysilicon barcodes but in addition to having magnetic properties for magnetic micro-labeling and sorting.

iii Suspended Multi-Material Tools as Intracellular Biosensors

Implementing the idea of a polysilicon chip and with the main objective of incorporating even more functional features in our devices, several different combinations of materials in only one device have been tested to achieve further robust and versatile devices. Thus, polysilicon-chromium-gold chips as multi-material platforms for intracellular multi-functionalization has been developed.

iv Suspended Silicon Nanowire Tools as Nanostructured Intracellular Platforms

With the main purpose of integrating nanostructured materials into our traditional polysilicon chips, cutting-edge intracellular silicon nanowire chips has been developed for future intracellular applications, such as biosensing, diagnosis and drug delivery.

v Suspended Silicon Nanowire Tools as Extracellular Embryo Labels

Eventually, the capabilities of the polysilicon labels with the advantages of incorporating silicon nanowires on the surface of a single tool have been combined in a brand new tool and nanowire silicon barcodes as physical extracellular bio-labels to identify and track living embryos have been developed.

Bibliography

[1] R. Arvizo and P. Bhattacharya, Resham Mukherjee, Gold nanoparticles: Opportunities and Challenges in Nanomedicine, *Expert Opinion on Drug Delivery*, vol. 7, no. 6, pp. 753 763, 2011. (cited on page(s) 29)

[2] J. Gao and B. Xu, Applications of nanomaterials inside cells, *Nano Today*, vol. 4, pp. 37 51, Feb. 2009. (cited on page(s) 30, 31, 200)

[3] I. Dror, D. Baram, and B. Berkowitz, Use of nanosized catalysts for transformation of chloro-organic pollutants., *Environmental science & technology*, vol. 39, pp. 1283 1290, Mar. 2005. (cited on page(s) 30)

[4] M. Hepel and C.-J. Zhong, eds., *Biomolecule Nanoparticle Hybrid Systems for Bioanalysis and Nanomedicine*, vol. 1. New York: Hepel2012, acs sympos ed., 2012. (cited on page(s) 30, 31, 40, 46)

[5] O. Penon, M. Rodrigues, and L. Pérez-García, Supramolecular chemistry for Nanomedicine, *Recent Advances in Pharmaceutical Sciences III*, vol. 661, no. 2, pp. 1 22, 2013. (cited on page(s) 30, 46)

[6] H. Park, S. Lee, L. Chen, E. K. Lee, S. Y. Shin, Y. H. Lee, S. W. Son, C. H. Oh, J. M. Song, S. H. Kang, and J. Choo, SERS imaging of HER2-overexpressed MCF7 cells using antibody-conjugated gold nanorods, *Physical chemistry chemical physics*, vol. 11, pp. 7348 7349, Sept. 2009. (cited on page(s) 30)

[7] X. Huang, I. H. El-Sayed, W. Qian, and M. a. El-Sayed, Cancer cell imaging and photothermal therapy in the near-infrared region by using gold nanorods., *Journal of the American Chemical Society*, vol. 128, pp. 2115 2120, Feb. 2006. (cited on page(s) 30)

[8] C. M. Goodman, C. D. McCusker, T. Yilmaz, and V. M. Rotello, Toxicity of gold nanoparticles functionalized with cationic and anionic side chains., *Bioconjugate chemistry*, vol. 15, no. 4, pp. 897 900, 2004. (cited on page(s) 30)

[9] M. Cieplak, Quantum dots as probes in biology, *Journal of Physics: Condensed Matter*, vol. 25, p. 190301, May 2013. (cited on page(s) 31)

[10] F. Tokumasu, R. M. Fairhurst, G. R. Ostera, N. J. Brittain, J. Hwang, T. E. Wellems, and J. a. Dvorak, Band 3 modifications in Plasmodium falciparum-infected AA and CC erythrocytes assayed by autocorrelation analysis using quantum dots., *Journal of cell science*, vol. 118, pp. 6498 6504, Mar. 2005. (cited on page(s) 31)

[11] M. Dahan, S. Lévi, C. Luccardini, P. Rostaing, B. Riveau, and A. Triller, Diffusion dynamics of glycine receptors revealed by single-quantum dot tracking., *Science*, vol. 302, pp. 442 445, Oct. 2003. (cited on page(s) 31)

[12] A. Ito, M. Shinkai, H. Honda, and T. Kobayashi, Medical application of functionalized magnetic nanoparticles., *Journal of bioscience and bioengineering*, vol. 100, pp. 1 11, July 2005. (cited on page(s) 32)

[13] Q. A. Pankhurst, J. Connolly, S. K. Jones, and J. Dobson, Applications of magnetic nanoparticles in biomedicine, *Journal of Physics D: Applied Physics*, vol. 36, pp. 167 181, 2003. (cited on page(s) 32, 33)

[14] P. A. Liberti, C. G. Rao, and L. W. M. M. Terstappen, Optimization of ferrofuids and protocols for the enrichment of breast tumor cells in blood, *Journal of Magnetism and MagneticMaterials*, vol. 225, pp. 301 307, 2001. (cited on page(s) 32, 33)

[15] L. Rodriguez-Lorenzo, K. Fytianos, F. Blank, C. von Garnier, B. Rothen-Rutishauser, and A. Petri-Fink, Fluorescence-encoded gold nanoparticles: library design and modulation of cellular uptake into dendritic cells., *Small*, vol. 10, pp. 1341 1350, Apr. 2014. (cited on page(s) 33)

[16] M. Han, X. Gao, J. Z. Su, and S. Nie, Quantum-dot-tagged microbeads for multiplexed optical coding of biomolecules., *Nature Biotechnology*, vol. 19, pp. 631 635, July 2001. (cited on page(s) 33, 69, 200)

[17] D. N. Heo, D. H. Yang, H.-J. Moon, J. B. Lee, M. S. Bae, S. C. Lee, W. J. Lee, I.-C. Sun, and I. K. Kwon, Gold nanoparticles surface-functionalized with paclitaxel drug and biotin receptor as theranostic agents for cancer therapy., *Biomaterials*, vol. 33, pp. 856 866, Jan. 2012. (cited on page(s) 33)

[18] X. Michalet, F. F. Pinaud, L. A. Bentolila, J. M. Tsay, S. Doose, J. J. Li, G. Sundaresan, A. M. Wu, S. S. Gambhir, and S. Weiss, NIH Public Access, *Science*, vol. 307, no. 5709, pp. 538 544, 2005. (cited on page(s) 33)

[19] M. De, P. S. Ghosh, and V. M. Rotello, Applications of Nanoparticles in Biology, *Advanced Materials*, vol. 20, pp. 4225 4241, Nov. 2008. (cited on page(s) 33, 35)

[20] G. Doria, J. a. Conde, B. Veigas, L. Giestas, C. Almeida, M. Assunçao, J. a. Rosa, and P. V. Baptista, Noble metal nanoparticles for biosensing applications., *Sensors*, vol. 12, pp. 1657 1687, Jan. 2012. (cited on page(s) 34)

[21] K. K. Jain, Applications of nanobiotechnology in clinical diagnostics., *Clinical chemistry*, vol. 53, pp. 2002 2009, Nov. 2007. (cited on page(s) 34)

[22] K. K. Jain, Nanomedicine: application of nanobiotechnology in medical practice., *Medical principles and practice*, vol. 17, pp. 89 101, Jan. 2008. (cited on page(s) 34)

[23] W. Zhao, J. M. Karp, M. Ferrari, and R. Serda, Bioengineering nanotechnology: towards the clinic., *Nanotechnology*, vol. 22, pp. 490201 490202, Dec. 2011. (cited on page(s) 34)

[24] A. J. Mieszawska, W. J. M. Mulder, Z. a. Fayad, and D. P. Cormode, Multifunctional gold nanoparticles for diagnosis and therapy of disease., *Molecular pharmaceutics*, vol. 10, pp. 831 847, Mar. 2013. (cited on page(s) 34)

[25] J. Zhao and V. Castranova, Toxicology of nanomaterials used in nanomedicine., *Journal of toxicology and environmental health. Part B, Critical reviews*, vol. 14, pp. 593 632, Jan. 2011. (cited on page(s) 35)

[26] B. Neha, B. Ganesh, and K. Preeti, Drug Delivery to the Brain using Polymeric Nanoparticles. A Review, *International Journal of Pharmaceutical and Life Sciences*, vol. 2, no. 3, pp. 107 132, 2013. (cited on page(s) 35)

[27] A. Kumari, S. K. Yadav, and S. C. Yadav, Biodegradable polymeric nanoparticles based drug delivery systems., *Colloids and surfaces. B, Biointerfaces*, vol. 75, pp. 1 18, Jan. 2010. (cited on page(s) 35, 36)

[28] C. Pinto Reis, R. J. Neufeld, A. J. Ribeiro, and F. Veiga, Nanoencapsulation I. Methods for preparation of drug-loaded polymeric nanoparticles., *Nanomedicine : nanotechnology, biology, and medicine*, vol. 2, pp. 8 21, Mar. 2006. (cited on page(s) 35)

[29] J. L. Vivero-Escoto, I. I. Slowing, B. G. Trewyn, and V. S.-Y. Lin, Mesoporous Silica Nanoparticles for Intracellular Controlled Drug Delivery, *Small*, vol. 6, pp. 1952 1967, Sept. 2010. (cited on page(s) 35, 36)

[30] Waree Tiyaboonchai, Chitosan nanoparticles: a promising system in novel drug delivery., *Naresuan University Journal*, vol. 11, pp. 51 56, Nov. 2003. (cited on page(s) 36)

[31] M. Ferrari, Cancer nanotechnology: opportunities and challenges., *Nature reviews. Cancer*, vol. 5, pp. 161 171, Mar. 2005. (cited on page(s) 37)

[32] E. Tasciotti, X. Liu, R. Bhavane, K. Plant, A. D. Leonard, B. K. Price, M. M.-C. Cheng, P. Decuzzi, J. M. Tour, F. Robertson, and M. Ferrari, Mesoporous silicon particles as a multistage delivery system for imaging and therapeutic applications., *Nature nanotechnology*, vol. 3, pp. 151 157, Mar. 2008. (cited on page(s) 37)

[33] R. E. Serda, J. Gu, R. C. Bhavane, X. Liu, C. Chiappini, P. Decuzzi, and M. Ferrari, Biomaterials The association of silicon microparticles with endothelial cells in drug delivery to the vasculature, *Biomaterials*, vol. 30, no. 13, pp. 2440 2448, 2009. (cited on page(s) 37, 129)

[34] I. Linkov, F. K. Satterstrom, and L. M. Corey, Nanotoxicology and nanomedicine: making hard decisions., *Nanomedicine : nanotechnology, biology, and medicine*, vol. 4, pp. 167 171, June 2008. (cited on page(s) 38)

[35] M. R. Gwinn and V. Vallyathan, Nanoparticles: Health Effects-Pros and Cons, *Environmental Health Perspectives*, vol. 114, no. 12, pp. 1818 1825, 2006. (cited on page(s) 38, 39)

[36] V. E. Kagan, H. Bayir, and A. A. Shvedova, Nanomedicine and nanotoxicology: two sides of the same coin., *Nanomedicine : nanotechnology, biology, and medicine*, vol. 1, pp. 313 316, Dec. 2005. (cited on page(s) 38)

[37] S. M. Moghimi, A. C. Hunter, and J. C. Murray, Nanomedicine: current status and future prospects., *FASEB journal*, vol. 19, pp. 311 330, Mar. 2005. (cited on page(s) 38)

[38] A. Seaton and K. Donaldson, Nanoscience, nanotoxicology, and the need to think small., *Lancet*, vol. 365, no. 9463, pp. 923 924, 2005. (cited on page(s) 39)

[39] Y. Piao, A. Burns, J. Kim, U. Wiesner, and T. Hyeon, Designed Fabrication of Silica-Based Nanostructured Particle Systems for Nanomedicine Applications, *Advanced Functional Materials*, vol. 18, pp. 3745 3758, Dec. 2008. (cited on page(s) 40)

[40] K. R. Kam and T. A. Desai, Nano- and microfabrication for overcoming drug delivery challenges, *Journal of Materials Chemistry B.*, vol. 1, pp. 1878 1884, 2013. (cited on page(s) 40, 129)

[41] E. Primiceri, M. S. Chiriacò, R. Rinaldi, and G. Maruccio, Cell chips as new tools for cell biology results, perspectives and opportunities., *Lab on a chip*, vol. 13, pp. 3789 3802, Oct. 2013. (cited on page(s) 40, 42)

[42] F. Patolsky, G. Zheng, and C. M. Lieber, Nanowire sensors for medicine and the life sciences., *Nanomedicine*, vol. 1, pp. 51 65, June 2006. (cited on page(s) 40, 44)

[43] N. Li, A. Tourovskaia, and A. Folch, Biology on a Chip: Microfabrication for Studying the Behavior of Cultured Cells, *Critical Reviews in Biomedical Engineering*, vol. 31, no. 0, pp. 423 488, 2013. (cited on page(s) 42)

[44] A. MANZ, N. GRABER, and H. M. WIDMER, Miniaturized Total Chemical Analysis Systems : a Novel Concept for Chemical Sensing, *Sensors and Actuators, B*, pp. 244 248, 1990. (cited on page(s) 42)

[45] J. El-Ali, P. K. Sorger, and K. F. Jensen, Cells on chips, *Nature*, vol. 442, pp. 403 411, July 2006. (cited on page(s) 42, 129, 161)

[46] S. Britland, P. Clark, P. Connolly, and G. Moores, Micropatterned substratum adhesiveness: a model for morphogenetic cues controlling cell behavior., *Experimental cell research*, vol. 198, pp. 124 129, Jan. 1992. (cited on page(s) 42)

[47] B. Tian, T. Cohen-Karni, Q. Qing, X. Duan, P. Xie, and C. M. Lieber, Three-dimensional, flexible nanoscale field-effect transistors as localized bioprobes, *Science*, vol. 329, pp. 830 834, Aug. 2010. (cited on page(s) 43, 161)

[48] A. K. Shalek, J. T. Robinson, E. S. Karp, J. S. Lee, D. R. Ahn, M. H. Yoon, A. Sutton, M. Jorgolli, R. S. Gertner, T. S. Gujral, G. MacBeath, E. G. Yang, and H. Park, Vertical silicon nanowires as a universal platform for delivering biomolecules into living cells, *PNAS*, vol. 107, pp. 1870 1875, Feb. 2010. (cited on page(s) 44, 129, 161, 162, 176, 189)

[49] W. Kim, J. K. Ng, M. E. Kunitake, B. R. Conklin, and P. Yang, Interfacing silicon nanowires with mammalian cells, *Journal of the American Chemical Society*, vol. 129, pp. 7228 7229, June 2007. (cited on page(s) 44, 45, 161, 162, 189, 201)

[50] S. Hou, H. Zhao, L. Zhao, Q. Shen, K. S. Wei, D. Y. Suh, A. Nakao, M. A. Garcia, M. Song, T. Lee, B. Xiong, S. C. Luo, H. R. Tseng, and H. H. Yu, Capture and stimulated release of circulating tumor cells on polymer-grafted silicon nanostructures, *Advanced Materials*, vol. 25, pp. 1547 1551, Mar. 2013. (cited on page(s) 44, 45, 162)

[51] S. Wang, H. Wang, J. Jiao, K.-J. Chen, G. E. Owens, K.-i. Kamei, J. Sun, D. J. Sherman, C. P. Behrenbruch, H. Wu, and H.-R. Tseng, Three-dimensional nanostructured substrates toward efficient capture of circulating tumor cells, *Angewandte Chemie*, vol. 48, pp. 8970 8973, Jan. 2009. (cited on page(s) 44, 162, 186)

[52] G. Zheng, F. Patolsky, Y. Cui, W. U. Wang, and C. M. Lieber, Multiplexed electrical detection of cancer markers with nanowire sensor arrays, *Nature Biotechnology*, vol. 23, pp. 1294 1301, Oct. 2005. (cited on page(s) 44, 45, 162)

[53] F. Mumm, K. M. Beckwith, S. Bonde, K. L. Martinez, and P. Sikorski, A transparent nanowire-based cell impalement device suitable for detailed cell-nanowire interaction studies, *Small*, vol. 9, pp. 263 272, Jan. 2013. (cited on page(s) 44, 162, 176, 189)

[54] L. De Vico, M. H. Sorensen, L. Iversen, D. M. Rogers, B. S. Sorensen, M. Brandbyge, J. Nygard, K. L. Martinez, and J. H. Jensen, Quantifying signal changes in nano-wire based biosensors, *Nanoscale*, vol. 3, pp. 706 717, Mar. 2011. (cited on page(s) 44, 162)

[55] N. S. Ramgir, Y. Yang, and M. Zacharias, Nanowire-based sensors, *Small*, vol. 6, pp. 1705 1722, Aug. 2010. (cited on page(s) 44, 162)

[56] A. K. Shalek, J. T. Gaublomme, L. Wang, N. Yosef, N. Chevrier, M. S. Andersen, J. T. Robinson, N. Pochet, D. Neuberg, R. S. Gertner, I. Amit, J. R. Brown, N. Hacohen, A. Regev, C. J. Wu, and H. Park, Nanowire-mediated delivery enables functional interrogation of primary immune cells: application to the analysis of chronic lymphocytic leukemia., *Nano Letters*, vol. 12, pp. 6498 6504, Dec. 2012. (cited on page(s) 44)

[57] K. J. Cha, J. M. Hong, D.-W. Cho, and D. S. Kim, Enhanced osteogenic fate and function of MC3T3-E1 cells on nanoengineered polystyrene surfaces with nanopillar and nanopore arrays., *Biofabrication*, vol. 5, p. 025007, June 2013. (cited on page(s) 44)

[58] A. Ulman, Formation and Structure of Self-Assembled Monolayers., *Chemical reviews*, vol. 96, pp. 1533 1554, June 1996. (cited on page(s) 46)

[59] M. Kohn, Immobilization strategies for small molecule, peptide and protein microarrays., *Journal of peptide science*, vol. 15, pp. 393 397, June 2009. (cited on page(s) 46)

[60] L. S. Wong, F. Khan, and J. Micklefield, Selective covalent protein immobilization: strategies and applications., *Chemical Reviews*, vol. 109, pp. 4025 53, Sept. 2009. (cited on page(s) 46, 147)

[61] D. Wang and S. Bodovitz, Single cell analysis: the new frontier in omics ., *Trends in biotechnology*, vol. 28, pp. 281 290, June 2010. (cited on page(s) 48)

[62] E. Fernández-Rosas, R. Gómez-Martínez, E. Ibanez, L. Barrios, M. Duch, J. Esteve, C. Nogués, and J. A. Plaza, Intracellular polysilicon barcodes for cell tracking, *Small*, vol. 5, pp. 2433 2439, Nov. 2009. (cited on page(s) 49, 53, 54, 69, 97, 129, 161, 178)

[63] E. Fernández-Rosas, R. Gómez-Martínez, E. Ibanez, L. Barrios, M. Duch, J. Esteve, J. A. Plaza, and C. Nogués, Internalization and cytotoxicity analysis of silicon-based microparticles in macrophages and embryos, *Biomedical Microdevices*, vol. 12, pp. 371 379, June 2010. (cited on page(s) 50, 51, 70, 84, 97, 130, 132, 183)

[64] R. Gómez-Martínez, P. Vázquez, M. Duch, A. Muriano, D. Pinacho, N. Sanvicens, F. Sánchez-Baeza, P. Boya, E. J. de la Rosa, J. Esteve, T. Suárez, and J. A. Plaza, Intracellular silicon chips in living cells, *Small*, vol. 6, pp. 499 502, Feb. 2010. (cited on page(s) 50, 51, 130, 132, 161, 165, 176, 178, 179)

[65] S. R. Nicewarner-Pena, R. G. Freeman, B. D. Reiss, L. He, D. J. Pena, I. D. Walton, R. Cromer, C. D. Keating, and M. J. Natan, Submicrometer metallic barcodes., *Science*, vol. 294, pp. 137 141, Oct. 2001. (cited on page(s) 52, 69, 200)

[66] D. J. Lockhart and M. O. Trulson, Multiplex metallica Molecular tag made of small metal rods may enable parallel and, *Nature Biotechnology*, vol. 19, pp. 1122 1123, 2001. (cited on page(s) 52, 69, 200)

[67] S. E. Brunker, K. B. Cederquist, and C. D. Keating, Metallic barcodes for multiplexed bioassays., *Nanomedicine*, vol. 2, pp. 695 710, Oct. 2007. (cited on page(s) 52, 69, 200)

[68] N. H. Finkel, X. Lou, C. Wang, and L. He, Barcoding the microworld, *Analytical Chemistry*, pp. 352 359, 2004. (cited on page(s) 52, 69)

[69] R. J. True, M. K. Taylor, G. S. Chakarova, and I. D. Walton, Microfabricated templates for the electrodeposition of metallic barcodes for use in multiplexed bioassays, *Proceedings of the 26th Annual Conference of the IEEE EMBS*, vol. 4, pp. 2619 2622, 2004. (cited on page(s) 52)

[70] S. Matthias, J. Schilling, K. Nielsch, F. Muller, R. B. Wehrspohn, and U. Gosele, Monodisperse Diameter-Modulated Gold Microwires, *Advance materials*, vol. 14, no. 22, pp. 1618 1621, 2002. (cited on page(s) 52)

[71] M. Spriggs, IVF mixup: white couple have black babies, *Journal of Medical Ethics*, vol. 29, pp. 65 65, Apr. 2003. (cited on page(s) 53, 70)

[72] E. Fernández-Rosas, A. Baldi, E. Ibanez, L. Barrios, S. Novo, J. Esteve, J. A. Plaza, M. Duch, R. Gómez-Martínez, O. Castell, C. Nogués, and C. Fernández-Sánchez, Chemical functionalization of polysilicon microparticles for single-cell studies, *Langmuir*, vol. 27, pp. 8302 8308, July 2011. (cited on page(s) 53, 54, 69, 72, 97)

[73] S. Novo, L. Barrios, J. Santaló, R. Gómez-Martínez, M. Duch, J. Esteve, J. A. Plaza, C. Nogués, and E. Ibánez, A novel embryo identification system by direct tagging of mouse embryos using silicon-based barcodes, *Human Reproduction*, vol. 26, pp. 96 105, Jan. 2011. (cited on page(s) 53, 54, 70, 72, 73, 84, 97, 200, 201, 215)

Chapter 2

Polysilicon Barcodes for Extracellular Tagging of Living Embryos

Contents

2.1 Abstract

This thesis begins with the presentation of the first type of our micro and nanotools, a novel device entirely made of polysilicon, with amazing identification capabilities and completely inside the microscale. In this chapter I describe the design, technological development, characterization and possible applications of polysilicon barcodes. Firstly, a barcode template is designed with 256-varieties of codifications, making possible hundreds of micro-identifications. Microbarcode fabrication is based on photolithographic processes, where in addition, different parameters such as different ething processes and ething times are studied to obtain the most robust and versatile barcodes possible. The characterization of the polysilicon barcodes is performed by scanning electron and atomic force microscopies. Subsequently and with the main objective of demonstrating the promising applications of our tool in surface chemistry and cell biology, a functionalization process on the barcode surface and an embryo tagging process are described. Eventually, the validation tests of the polysilicon barcodes as extracellular labels of living embryos are performed quantifying the retention rates of the devices to the outer membrane of mouse embryos.

2.2 Introduction

Historically, the study of cell behavior under different conditions has been reported for many researchers worldwide. In order to achieve this purpose, diverse types of codification systems have been designed with the clear aim of labeling and identifying living cells. For instance, quantum dots,[1] magnetic nanoparticles[2, 3] or poly(dimethylsiloxane) (PDMS) particles[4] have been used. But in general, these materials are complex and could be harmful for living cells. In addition, these kinds of encoders have been envisaged to follow cell populations. On the contrary, there have been many demonstrations of metallic barcode studies in molecular interaction[5–8] and in cellular identification and tracking .[9, 10]

However, an increasing demand of studying or labeling a unique embryo has become a crucial area in life sciences. For example, the increasingly high number of patients undergoing assisted reproductive technologies (ART) treatments worldwide[11] prevents the performance of totally individualized clinical and laboratory procedures,

causing ever more frequently misleading sample identifications.[12–14] For this reason and to achieve a single embryo labeling and tracking, a simple and robust system of codification should be performed. The selected codes must be designed into the micrometer scale and be made of a biocompatible material in order to ensure cell viability. Furthermore, the number of identifiable labels must be large enough to identify a sufficient number of cells to perform biological studies.

Thanks to the recent advances in microelectromechanical (MEMS) and nanoelectromechanical systems (NEMS), the miniaturization of their devices at cell scale is already a reality. Therefore and taking advantage of the silicon microtechnologies, nowadays we are able to design and fabricate a type of polysilicon barcode small enough to label a single cell or embryo, which is biocompatible and can be identified under an optical microscope.[15]

Tagging of mouse embryos by the microinjection of barcodes in the perivitelline space has already been achieved in our group (Micro and Nanotools group, IMB-CNM, CSIC)[15] but the direct contact between the embryo membrane and the barcode implicit for an internalized tagging is a limitation, as in case the embryo is subsequently transferred to a recipient female the microbarcodes could interfere with its implantation on the uterine wall.

For this reason, in the present work tag externalization is targeted in order to avoid possible damages to the processes occurring inside the embryo and simplifying the attachment protocol, as the microinjection is not needed. To achieve it, specific adhesion of biofunctionalized barcodes to the Zona Pellucida (ZP), the cover that surrounds oocytes and embryos, is performed using one of the most currently used methods to immobilize biomolecules to substrates, the formation of a self-assembled monolayer (SAM) that will act as a linker between the living embryo and the polysilicon barcode. In addition, a lectin (WGA) bonded to SAM is used because of its capacity to recognize specific carbohydrates present on the surface of most cells. Furthermore, no effect of the attached biofunctionalized barcodes on the developmental potential of the tagged embryos is observed, as expected according to our previous studies.[15, 16]

Thus, the present interdisciplinary research involves the design, technological development and characterization of polysilicon microbarcodes, the covalent biofunctionalization of polysilicon surfaces through a synthetic protein (WGA) and lastly the adhesion of the fabricated barcodes to the ZP of mouse embryos (Figure 2.1).

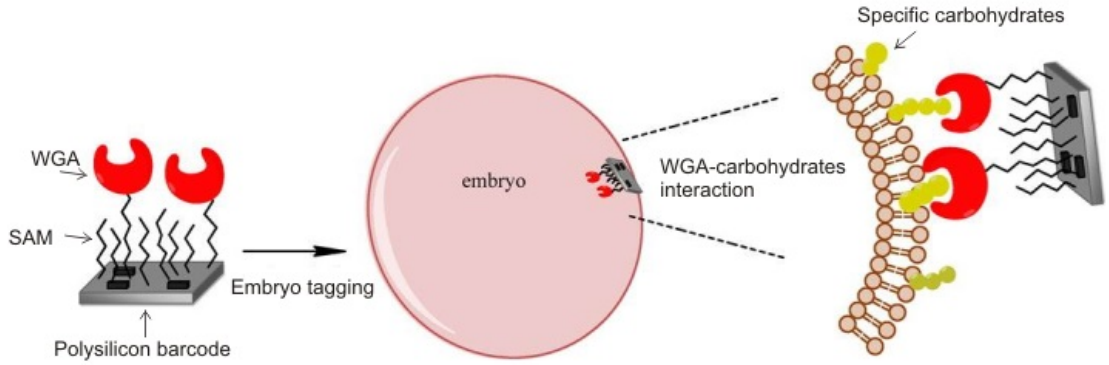

Figure 2.1: **Proposed schematic representation of the process followed to label and track a living embryo**. A polysilicon barcode is functionalized with a self-assembled monolayer as a linker and lectin (WGA) as carbohydrate-binding protein. Then, the selected lectin recognizes specific carbohydrates present on the embryo membrane to achieve a highly selected and robust bonding.[17]

2.3 Design of Polysilicon Barcodes as bio-labels to identify and track living embryos

2.3.1 Previous designs of Polysilicon Barcodes

During the last years the group of Micro and Nanotools of the IMB-CNM (CSIC) have designed a completed line of different polysilicon barcodes as cell and embryo labels. For instance, 3D-silicon barcodes[18] (Figure 2.2, type A), encoded microbarcodes[10] (Figure 2.2, type B) and vertical-card barcodes (Figure 2.2, type C) have been fabricated, being very successful to date.[15]

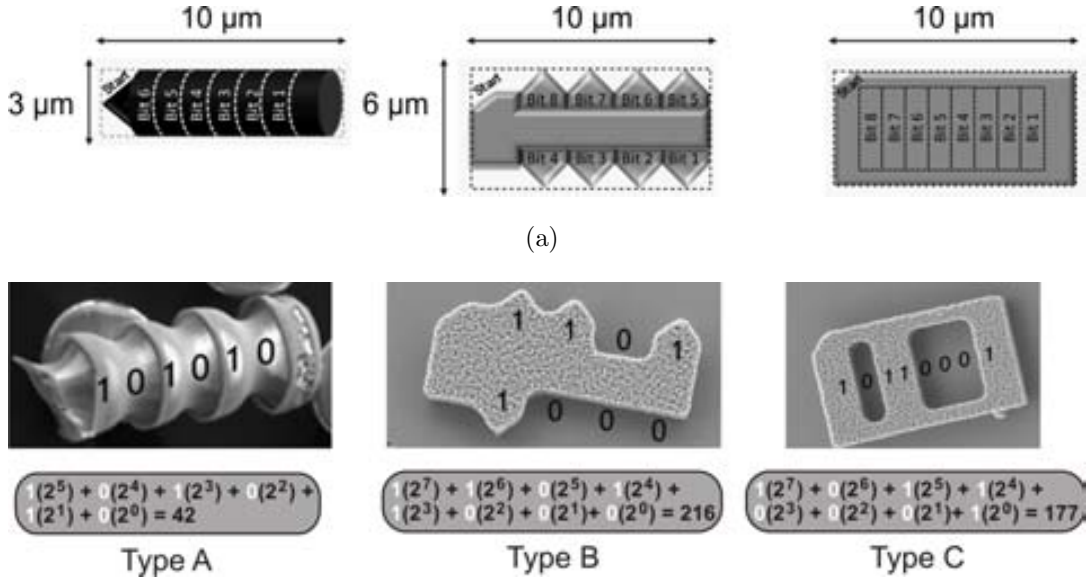

Figure 2.2: **Design and dimensions of previous polysilicon-based barcodes**. a) Schematic representation of the different types of barcodes, 3D-silicon barcodes (type A), encoded microbarcodes (type B) and vertical-card barcodes (type C) showing shape, dimensions, number of bits and the start point (top left corner). b) Scanning electron microscopy (SEM) images of some representative barcodes, where the binary code number is indicated. The corresponding conversion of the binary code into a decimal number is detailed in the box below each image.[15]

However, a novel line of polysilicon barcodes, with a horizontal-card shape, was devised in orden to improve their design and capabilities.

2.3.2 New Polysilicon Barcodes

A new and revolutionary design was performed to try to improve the small limitations that the old designs had. Such us poor visibility, fragile shapes or low number of codificacions.

The new horizontal-card barcode (Type D) is a two-dimensional tool based on a horizontal representation defined by rectangular bits. The external dimensions of the barcodes were fixed to 10.0 μm length, 6.0 μm width, and 1.0 μm thickness, in order to make them easily identifiable under an optical microscope. A barcode consist of a matrix of 2 rows and 4 columns of individual bits (Figure 2.3a). Thus, the total 8 bits represent 256 combinations of different values in a base-2 number system (Figure 2.3b). Bit lateral dimensions were fixed to 2.0 μm length, 1.5 μm width, and 1.0 μm thickness. A solid-bit represented symbol 1 (Bit = 1) and a hole-bit represented symbol 0 (Bit = 0). A start mark in the top left corner was designed in order to expedite the correct reading of data.

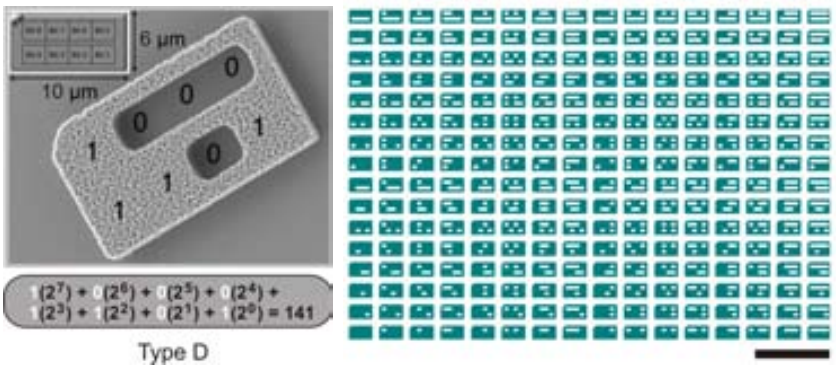

(a) (b)

Figure 2.3: **Design, dimensions and different combinations of new polysilicon barcodes**. a) Scanning electron microscopy image of a representative barcode, where the binary code number is indicated. Inset image shows a schematic representation of the horizontal-card polysilicon barcode (Type D) showing shape, dimensions, number of bits and the start point (top left corner). The corresponding conversion of the binary code into a decimal number is detailed in the box below the image.[15] b) Schematic representation of the full range, from 0 to 255 designs, of the polysilicon barcodes. The series starts from top right and ends at the bottom left. Scale bar = 30 μm.

2.4 Technological development of Polysilicon Barcodes

2.4.1 Preliminar trial of the technological development of Polysilicon Barcodes

The polysilicon barcodes were fabricated on 100 mm p-type silicon wafers (Figure 2.4a). A 1 μm-thick silicon oxide layer was thermally grown to be used as sacrificial layer (Figure 2.4b). Next, a 1 μm-thick low-pressure chemical vapor deposition (LPCVD) polysilicon layer was deposited as the device layer (Figure 2.4c). In this case, the polysilicon deposition occurred at both sides of the wafer, the front and the back side, as this effect is determined by the equipment. The devices were patterned by a photolithographic step (Figure 2.4d and e) and by a posterior polysilicon dry etching process at the front side (Figure 2.4f). Then, the photoresist was removed (Figure 2.4g). The barcodes were released by 40-minute etching in vapors of 49% HF out of the silicon oxide sacrificial layer (Figure 2.4h). Finally, the barcodes were suspended by ultrasounds (MiniSpin Plus) in 96% ethanol, centrifuged, and collected at 14 000 rpm for 5 minutes.

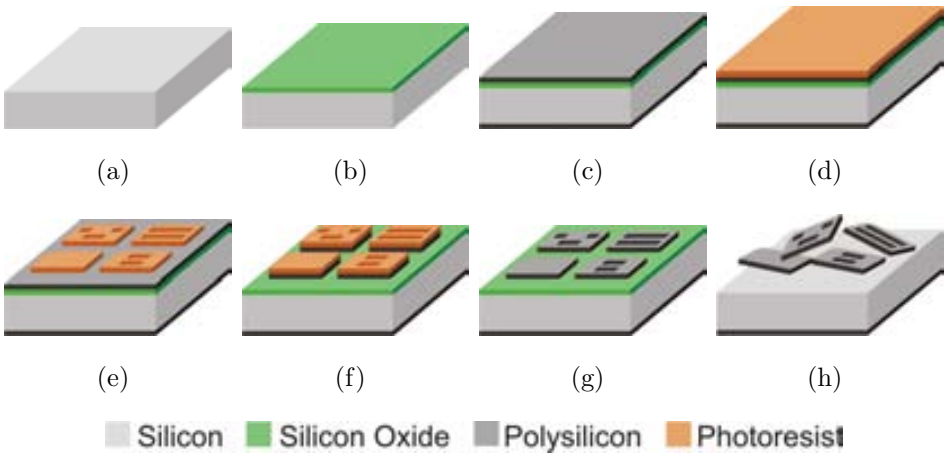

Figure 2.4: **Preliminar fabrication process of the polysilicon barcodes.** a) Silicon wafer as initial substrate, b) silicon oxide sacrificial layer, c) polysilicon device layer, d) covering of the wafer with photoresist, e) photolitographic step, f) polysilicon patterning, g) photoresist removal and h) device release of the sacrificial layer.

Although defined polysilicon barcodes were obtained a huge amount of big pieces of wafer was also observed during the characterization (Figure 2.5). Possibly, remains of the back side polysilicon layer were detached from the wafer and contaminated the samples. With this kind of mixture (silicon-waste pieces and released barcodes) it was impossible to obtain extraordinary clean samples (a must in microtechnology techniques) and consequently the released barcodes could not be used in the functionalization techniques.

In order to solve this issue, an extra polysilicon etching process was performed only at the back side of the wafer, while the front side was protected with a layer of photoresist. Thus, the front polysilicon layer, from which the polysilicon barcodes were later obtained, was kept in perfect conditions. This treatment will be applied in all technologies showed in this thesis, in order to obtain released tools as clean as possible.

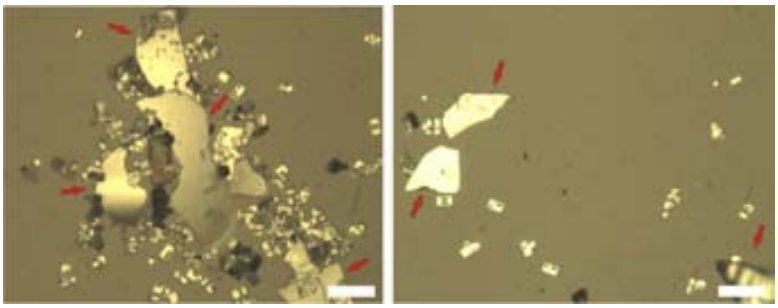

(a)

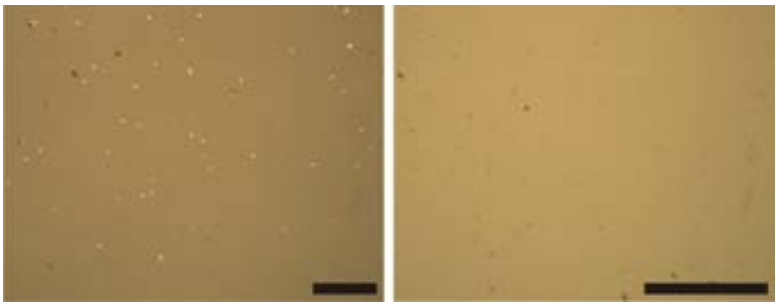

(b)

Figure 2.5: **Optical images before and after the extra polysilicon etching process.** a) Optical images before the back side polysilicon etching process. In the images several wafer pieces can be clearly observed, most likely belonging to the back side polysilicon layer (red arrows). b) Optical images of perfectly clean samples after the etching treatment. White scale bars = 30 μm. Black scale bars = 200 μm

2.4.2 Optimized technological development of Polysilicon Barcodes

The barcodes were manufactured using semiconductor microtechnologies based on photolithographic processes to obtain reproducible devices.

The polysilicon barcodes were fabricated on 100 mm p-type silicon wafers (Figure 2.6a). A 1 μm-thick silicon oxide layer was thermally grown to be used as sacrificial layer (Figure 2.6b).

Next, a 1 μm-thick low-pressure chemical vapor deposition (LPCVD) polysilicon layer was deposited as the device layer (Figure 2.6c). An extra polysilicon etching process was performed only at the back side of the wafer, in order to avoid the polysilicon layer detachment. The front side of the wafer was protected with photoresist until the finalization of the etching process. After that the photoresist was removed from the front side.

The devices were patterned by a photolithographic step (Figure 2.6d and e) and by a posterior polysilicon dry etching process at the front side (Figure 2.6f). Polysilicon etching stopped at the silicon oxide layer. Vertical profile and uniformity of the etching were required due to the small dimensions of the devices.

Then, the photoresist was removed (Figure 2.6g). The barcodes were released by 15 and 40 minute etching in vapors of 49% HF out of the silicon oxide sacrificial layer (Figure 2.6h). Different times of 49% HF etching were used in order to study this influence on the roughness of the polysilicon barcodes and subsequently in the functionalization process. Finally, the barcodes were suspended by ultrasounds (MiniSpin Plus) in 96% ethanol, centrifuged, and collected at 14 000 rpm for 5 minutes (Figure 2.6i).

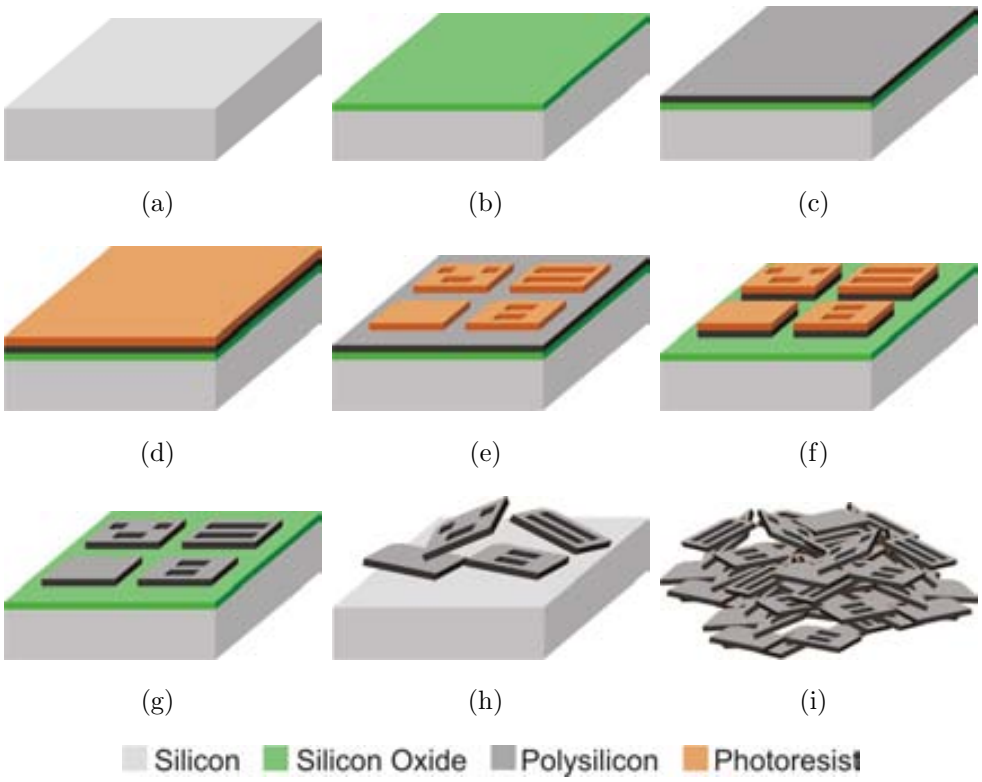

Figure 2.6: **Fabrication process of new polysilicon barcodes.** a) Silicon wafer as initial substrate, b) thermal growth of a silicon oxide sacrificial layer, c) deposition of the polysilicon device layer, d) covering of the wafer with photoresist by spin coating, e) photolitographic step, f) polysilicon patterning by dry etching, g) photoresist removed, h) devices released by 49% HF etching of the sacrificial layer, and finally, i) centrifugation and collection of the barcodes.

2.5 Characterization of fabricated Polysilicon Barcodes

Scanning electron microscopy was used to characterize the fabricated devices. Images of the 255-, 105-, 153- and 0-barcodes, still on the wafer, it can be seen in figure 2.7a, b, c and d, respectively. Several released barcodes after the 49% HF etching it can be also observed in figure 2.7e and f. The fabricated barcodes maintain perfectly their well-defined shape and homogenous surface even after their wafer release.

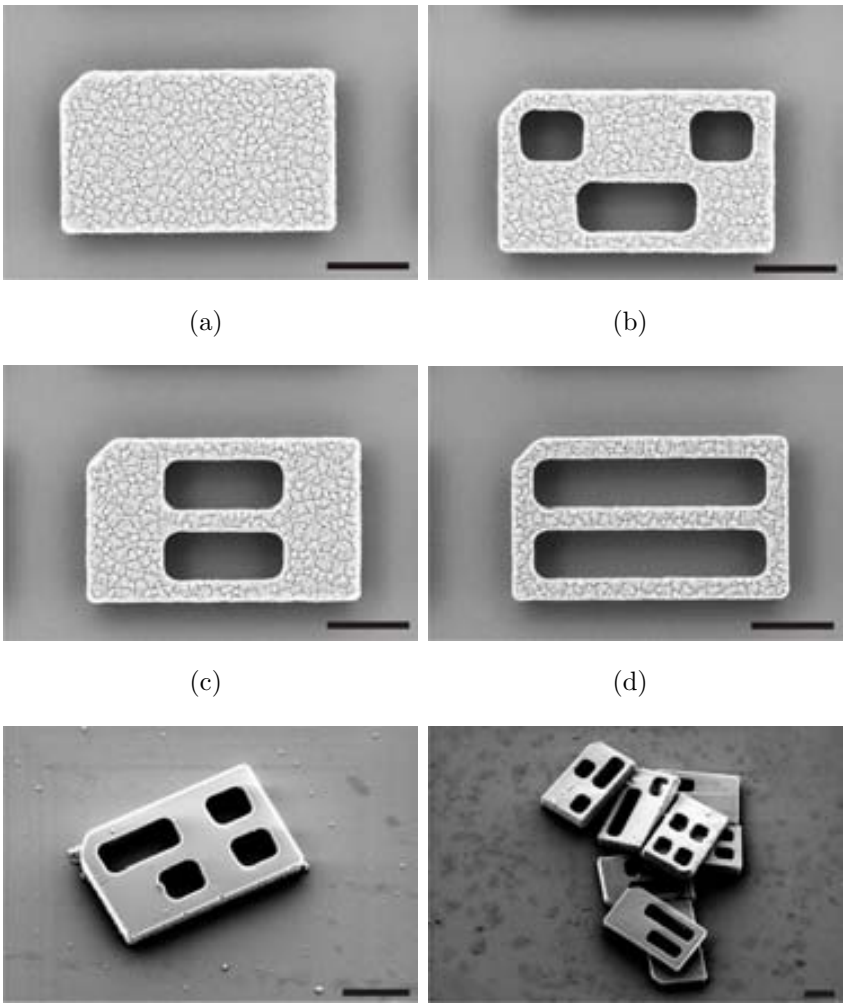

Figure 2.7: **Fabrication results of polysilicon barcodes**. Scanning electron microscope images of the a) 255-, b) 105-, c) 153- and d) 0-barcodes. f) 42-barcode after their wafer release and g) a view of different barcodes. Scale bars = 3 μm.

2.6 Chemical and biological studies: Biofunctionalization and embryo tagging of Polysilicon Barcodes

2.6.1 Biofunctionalization of Polysilicon Barcodes through lectin immobilization using self-assembled monolayers

(Performed by Department of Pharmacology and Therapeutical Chemistry, Universitat de Barcelona)

In order to prove the extraordinary capabilities of the polysilicon barcodes as extracellular labels, firstly we performed several chemical tests to demonstrate that our devices can be used as functionalization platforms in surface chemistry. Protein biofunctionalization of polysilicon barcodes is achieved in three steps: Surface activation, silane immobilization and protein immobilization. The followed process is shown below:

1. *Silicon surface activation*: Hydroxylation of the polysilicon barcode surfaces using an oxidant treatment was carried out at room temperature. The samples were submerged in a prepared mixture of H_2SO_4:H_2O_2 (piranha solution), at a volume ratio of 7:3 for 1 h, and then rinsed with water. Cleaned substrates were submerged in an alkaline mixture of NH_4OH and distilled H_2O for 30 min, and then rinsed abundantly with water and dried in a stream of nitrogen gas (Figure 2.8a).

2. *SAM formation using solution chemistry*: Silanization of the hydroxylated silicon oxide surface was carried out. The hydroxylated substrates were submerged in a solution of CH_3COOH, absolute ethanol and 11-(triethoxysilyl)undecanal (TESUD) (CHO-SAM) (Figure 2.8b). After the deposition time, the wafers were rinsed with absolute ethanol and dried with nitrogen. Finally, the substrates were located in a vacuum oven for 30 min at 80°C.

3. *Protein immobilization*: The terminal aldehyde groups reacted with the wheat germ agglutinin (WGA) amine groups under reductive conditions by adding a solution of WGA in PBS (either 15, 25, or 35 μg/mL) to the previously aldehyde covered surfaces, in the presence of a PBS solution of $NaBH_3CN$, and the mixture was kept at 4°C overnight (Figure 2.8c). Next, to cover the unreacted active groups on the surface, a PBS solution of 2-(2-aminoethoxy)ethanol was added as chemical blocker. After 20 min, the surface was rinsed with PBS abundantly, to eliminate unspecific protein adsorption.

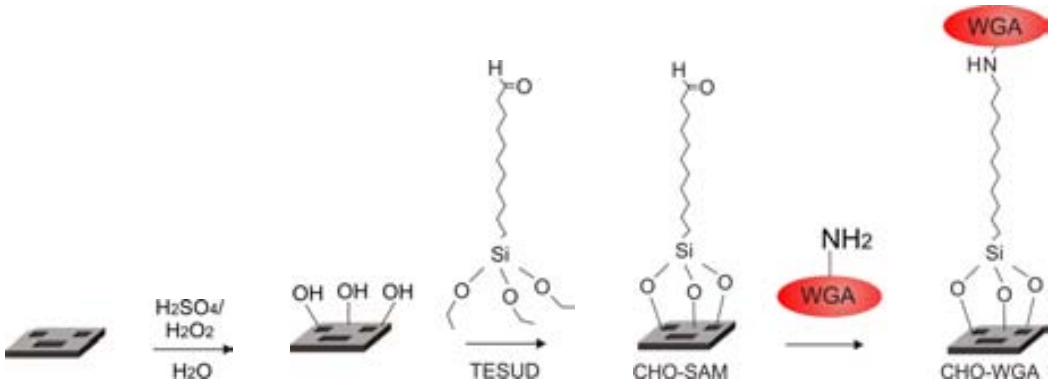

Figure 2.8: **Stepwise formation of the WGA-SAM on polysilicon surfaces**. a) Hydroxylation of the polysilicon barcode surfaces. b) Silanization of the hydroxylated silicon oxide surfaces. c) Immobilization of the WGA.

2.6.2 Study of the roughness effect on the functionalization effectiveness of Polysilicon Barcodes

Atomic force microscopy (ICON AFM, BRUKER) was used to study the influence of HF wet etching process duration on the roughness of the polysilicon barcodes and consequently in the functionalization process of the barcodes. This aspect was assessed by measuring first the maximum roughness of unreleased barcodes directly from the wafer (Figure 2.9a) and comparing these values with the roughness of released barcodes that had been exposed to 49% HF vapors for either 15 or 40 min. This was achieved when a 2 μL-drop of released barcodes was deposited in the AFM equipment and the roughness of a selected barcode was estimated. Roughness of the released barcodes was measured before chemical treatment (Figure 2.9b), after hydroxylation (Figure 2.9c), as well as after aldehyde treatment (CHO-SAM) (Figure 2.9d).

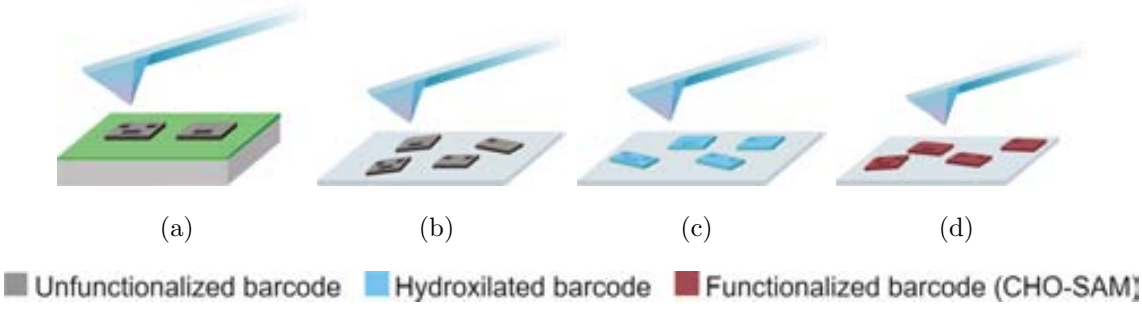

Figure 2.9: **Schematic representation of the polysilicon barcode roughness measurements through atomic force microscopy**. AFM roughness measurements of a) a barcode on a silicon wafer, b) a released barcode, c) a released hydroxylated barcode and d) a released hydroxylated and biofunctionalized barcode.

The results of the study are included in the graph of figure 2.10a, and indicate that roughness increases proportionally with etching time (time of exposure to 49% HF vapors), with values of ca. 8.5 nm when etching took 15 min, and of ca. 14.6 nm when etching was 40 min. However, this difference is not significant after hydroxylation or functionalization of the barcodes, for which roughness has smaller values, indicating a dense packing of functional groups on the polysilicon barcode surface after chemical treatment. Figure 2.10b and c show images of different barcodes released after 15 or 40 min etching, respectively. It can also be observed in scanning electron microscopy

images that barcodes with shorter wet etchings (15 min) (Figure 2.10b) present smoother and more homogenous polysilicon surfaces in contrast with those polysilicon barcodes with longer wet etchings (40 min) (Figure 2.10c). This might mean that barcodes with higher roughness values and consequently with higher exposed areas present better conditions as functionalization surfaces.

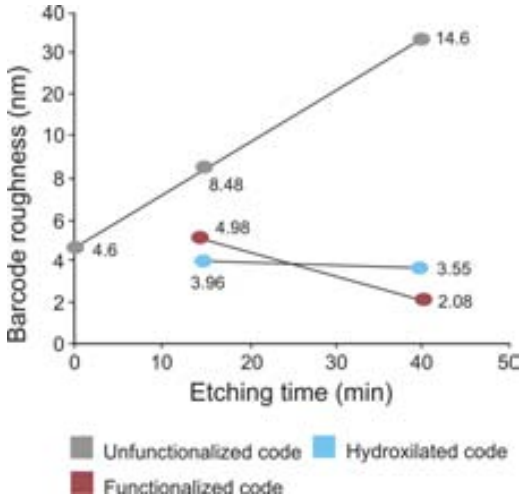

(a)

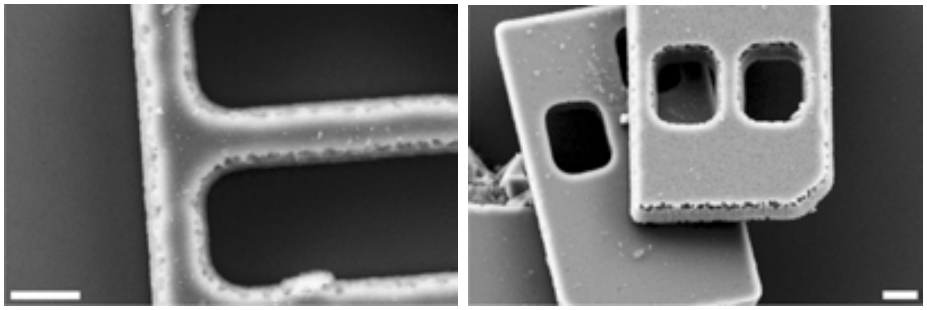

(b) (c)

Figure 2.10: **Roughness dependence on the etching process duration**. a) Graph corresponds to the roughness value tendency vs. exposure time of the devices in vapors of 49% HF. Barcode SEM images correspond to b) 15 min and c) 40 min etching time. Scale bars = 1 μm.

2.6.3 Embryo culture and embryo-viability tests

(Performed by Department of Cellular Biology, Physiology and Immunology, Universitat Autònoma de Barcelona)

Several biological experiments were also performed with the main objective of demonstrating the promising applications of our tools in cell biology. The embryo tagging system is achieved in four steps: Collection of mouse embryos, *in vitro* mouse embryo tagging, *in vitro* development and full-term development of barcode-tagged embryos.

1. *Collection of mouse embryos:* Mouse females were used as embryo donors. Ovulation induction was induced by intraperitoneal injection of pregnant mare serum gonadotrophin. After 48 h, a second injection of human chorionic gonadotrophin was administered and the females were mated with mouse males. Pronuclear embryos were collected 25 h after and incubated in HEPES-buffered potassium simplex optimized medium (H-KSOM). Denuded embryos were washed twice in fresh H-KSOM, and embryos with two pronuclei and a good morphology were incubated at 37°C in a 5% CO_2 atmosphere until tagging.

2. *In vitro mouse embryo tagging:* A drop of PBS containing biofunctionalized barcodes was placed in a dish and groups of 10 barcodes were transferred to separate drops of H-KSOM (Figure 2.11a). Each embryo was then rolled over the barcodes by means of a mouth-controlled aspiration system, until the 10 barcodes were attached to its ZP (Figure 2.11b and c). It is noted that the mere contact between the barcodes and mouse ZP surface was enough to allow their attachment. Finally, each tagged embryo was cultured at 37°C in a 5% CO_2 atmosphere for 96 - 120 h in parallel to a group of control non-tagged embryos. Cultured embryos were monitored every 24 h to assess their developmental progression.

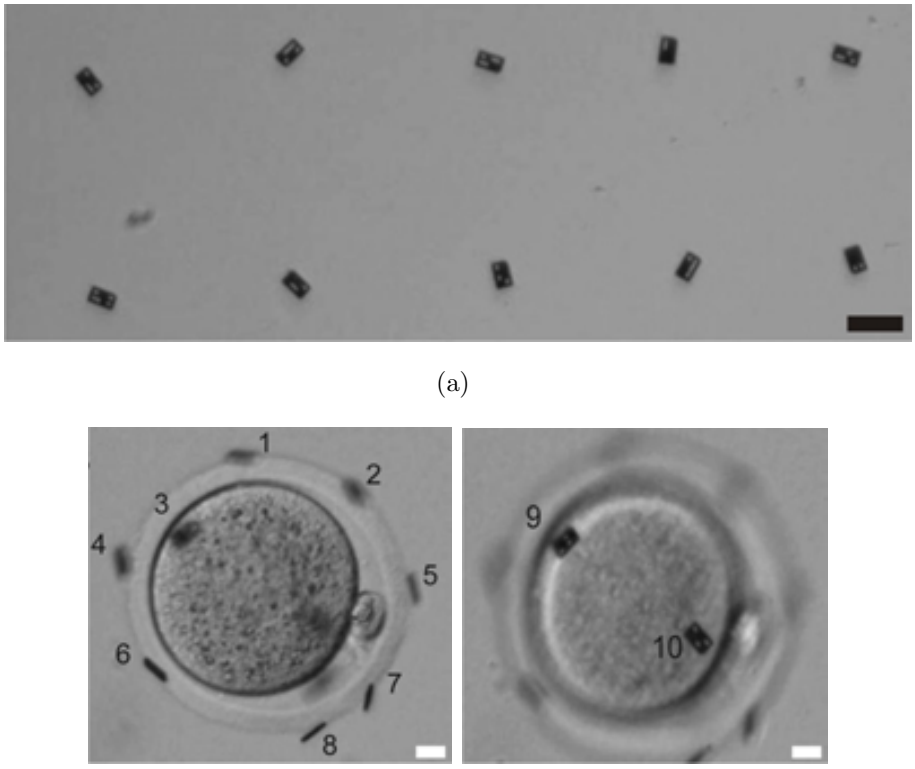

(a)

(b) (c)

Figure 2.11: **Embryo tagging by the attachment of WGA-biofunctionalized polysilicon barcodes to mouse Zona Pellucida outer surface**. Optical images of (a) a group of 10 barcodes strategically distributed, and b and c) two different focal planes of the same embryo with a total of 10 barcodes attached to the outer surface of its ZP. Black scale bar = 20 μm. White scale bars = 10 μm.[20]

3. *In vitro development of barcode-tagged mouse embryos:* To test the non-toxicity of polysilicon barcodes, tagged embryos were allowed to develop *in vitro* and were monitored every 24 h. After 96 h of *in vitro* culture 90% of the tagged embryos achieved the blastocyst stage (Figure 2.12). No effect of the attached WGA-biofunctionalized barcodes on the developmental potential of the tagged embryos up to the blastocyst stage was observed, as expected according to our previous studies.[15, 16] Eventually, embryos that reached the blastocyst stage by 96 h were kept in culture for an additional 24 h to assess the fate of the barcodes after embryo hatching. And as expected, all the barcodes remained attached to the ZP and a barcode release rate of 100% was achieved in the hatched embryos (Figure 6.2a and b).

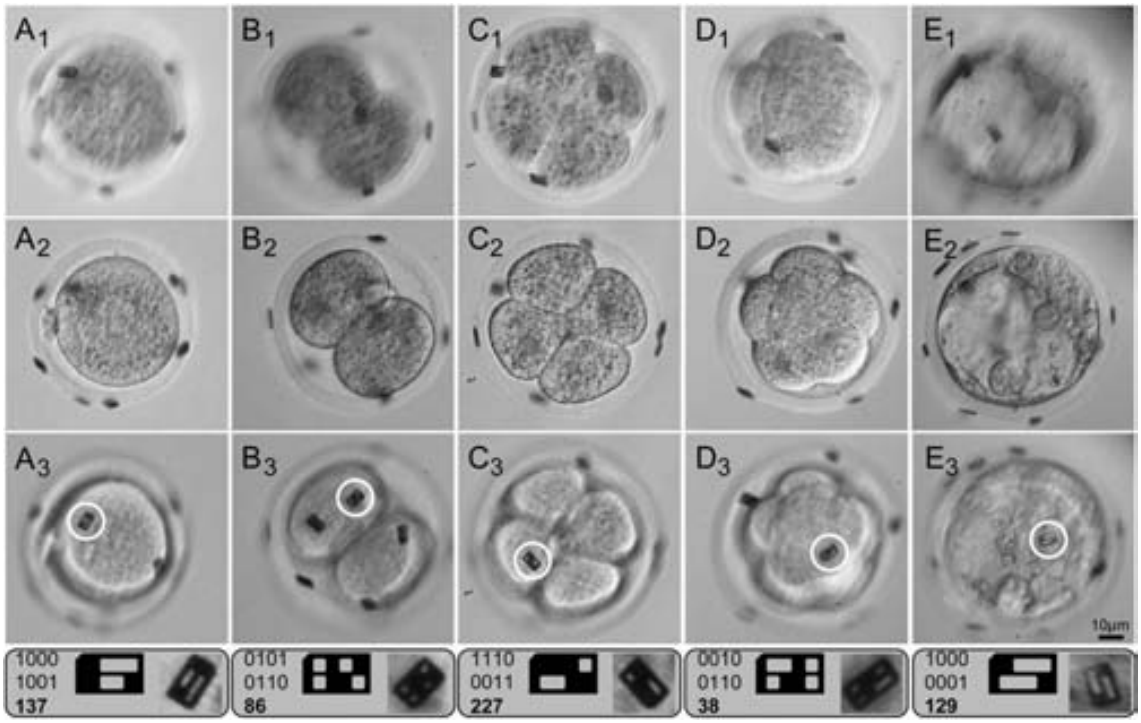

Figure 2.12: ***In vitro* development of tagged embryos**. Three different focal planes of 1-cell (A1 A3), 2-cell (B1 B3), 4-cell (C1 C3), compacting 8-cell (D1 D3) embryos and a hatching blastocyst (E1 E3) with barcodes attached to their ZP. Identification was performed simply by adjusting the focus of the inverted microscope until a barcode properly oriented for reading was found (white circles). A magnified image of the readable barcode, its diagrammatic representation and the corresponding conversion of the binary code to the decimal system (in bold) are detailed in the box below each image series.[20]

4. *Embryo transfer and full-term development of barcode-tagged embryos:* After 24 h in culture, a group of 2-cell stage *in vitro* tagged embryos and a group of control non-tagged embryos were separately transferred into recipient females. After embryo transfer, females were kept in individual cages and were allowed to deliver naturally. The *in vivo* development of the tagged embryos was assessed and compared with that of a group of control non-tagged embryos. Surprisingly, full-term development of the tagged embryos (74.3%) turned out to be significantly higher than that of the control non-tagged ones (57.4%). On the other hand, all females and their offspring were apparently healthy and all the obtained pups showed an apparently normal development. The fate of the barcodes in the female body is unknown and, because of their small size,

their localization inside the reproductive track by histological studies would not be possible. As barcodes are not biodegradable, one can hypothesize that when the ZP is degraded[22] the barcodes are released into the uterus and they might be eventually removed from the female body after parturition.[23]

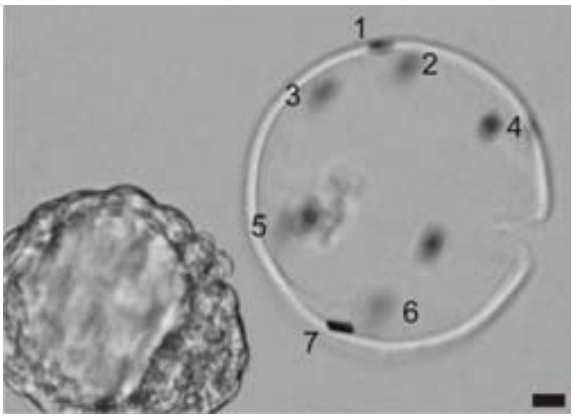

(a)

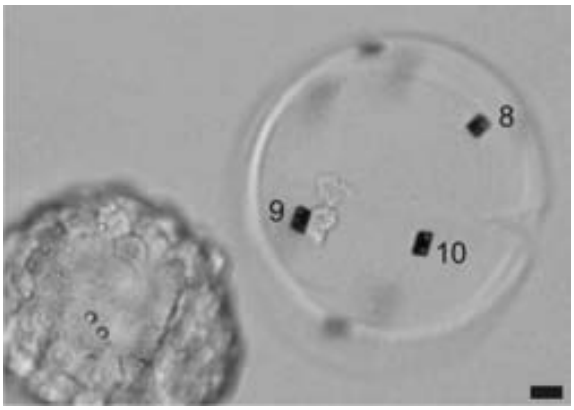

(b)

Figure 2.13: **Barcode release after blastocyst hatching**. Two different focal planes (a and b) of a hatched blastocyst free of barcodes and of the corresponding empty ZP with the 10 barcodes attached to its outer surface. Scale bars = 10 μm.[20]

2.7 Validation of the Polysilicon Barcodes as embryo labels: Retention studies

Eventually, validation tests of the polysilicon barcodes as extracellular labels of living embryos were performed quantifying the retention rates of the devices to the outer membrane of mouse embryos.

Protein concentration and polysilicon surface roughness values were analyzed and proved to be crucial for a successful adhesion (Figure 2.14).

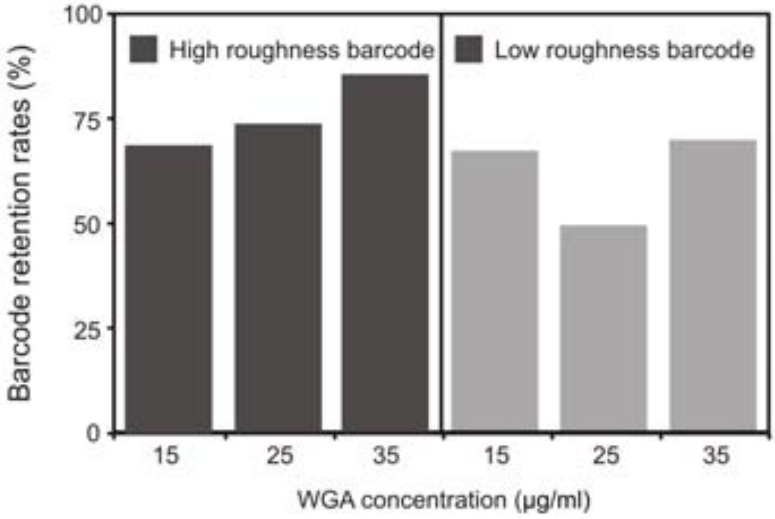

Figure 2.14: **Influence of WGA concentration and surface roughness of polysilicon barcodes on the embryo retention**. 40- and 15 min-etching polysilicon barcodes functionalized with three different concentrations of WGA retention rates are compared.[17]

Higher roughness barcodes (after 40 min-etching) functionalized as CHO-SAM, were used to assess whether protein concentration influenced the biofunctionalization efficiency. The highest retention rate after 96 h of culture was obtained with a WGA concentration of 35 μg/mL (84.9%), which was significantly higher than for 25 μg/mL (73.4%) and 15 μg/mL (68.6%) concentrations. Lower roughness barcodes (after 15 min etching) were functionalized with the same concentrations of WGA as higher roughness barcodes. In contrast to the results with higher roughness barcodes, no differences were observed in barcode retention rates among the three WGA concentrations used. Thus, the same retention rate was achieved with the

lowest (15 μg/mL: 67.2%) and the highest (35 μg/mL: 69.8%) WGA concentration used. The comparison between higher roughness and lower roughness barcodes showed that retention rates of higher roughness barcodes biofunctionalized with 25 and 35 μg/mL of WGA were significantly higher than those of lower roughness barcodes biofunctionalized at the same concentrations, i.e., higher surface roughness is a positive factor influencing biofunctionalization. These results are extremely important, because they proved the efficiency of the biofunctionality.

2.8 Conclusions

In this chapter, a highly interdisciplinary research to obtain a new embryo tagging system is presented. This line of research involves the design, technological development and characterization of polysilicon microbarcodes as extracellular labels to identify and track living embryos.

Two-dimensional polysilicon barcodes were designed with 10.0 μm length, 6.0 μm width and 1.0 μm thickness as external dimensions and 256 combinations of different values were obtained. Taking advantage of the silicon microtechnologies and after a preliminar trial a successful fabrication was performed. The obtained barcodes maintained perfectly their shape and presented a homogenous and high robust surface even after their wafer release. Two different times of 49% HF wet etching were carried out with the intention of checking this influence over polysilicon roughness and subsequently in biofunctionalization and embryo retention rates.

Chemical tests were performed in order to prove the efficiency of the polysilicon barcodes as functionalization platforms for surface chemistry. A methodology for covalent immobilization of lectins on polysilicon substrates was described. Then, biological tests were also carried out with the objective of demonstrating the non-toxicity of the polysilicon barcodes. A *in vitro* culture of tagged embryos (taking advantage of the biofunctionalized surface of the barcode) was performed. It should be noted that the simple contact between the barcodes and the ZP was enough to allow their attachment. No viability effects on the development of *in vitro* tagged embryos were observed. Even *in vivo* experiments were carried out, where the obtained pups showed an apparently normal development. Lastly, to test the validity of our devices as extracellular labels for living embryos, retention studies of the devices to the outer membrane of mouse embryos were carried out. The obtained results clearly validate this embryo tagging system.

Therefore, as it can be seen in this chapter the successful design and technological development of polysilicon barcodes have allowed us the application of our devices in fields as surface chemistry and cell biology. So that, a novel direct embryo-tagging system by biofunctionalized polysilicon barcodes is successfully presented.

Bibliography

[1] M. Han, X. Gao, J. Z. Su, and S. Nie, Quantum-dot-tagged microbeads for multiplexed optical coding of biomolecules., *Nature Biotechnology*, vol. 19, pp. 631 635, July 2001. (cited on page(s) 33, 69, 200)

[2] W. J. Rogers, C. H. Meyer, and C. M. Kramer, Technology insight: in vivo cell tracking by use of MRI., *Nature clinical practice. Cardiovascular medicine*, vol. 3, pp. 554 562, Oct. 2006. (cited on page(s) 69, 200)

[3] C. Wilhelm and F. Gazeau, Universal cell labelling with anionic magnetic nanoparticles., *Biomaterials*, vol. 29, pp. 3161 3174, Aug. 2008. (cited on page(s) 69)

[4] D. Dendukuri, D. C. Pregibon, J. Collins, T. A. Hatton, and P. S. Doyle, Continuous-flow lithography for high-throughput microparticle synthesis., *Nature materials*, vol. 5, pp. 365 369, May 2006. (cited on page(s) 69)

[5] S. R. Nicewarner-Pena, R. G. Freeman, B. D. Reiss, L. He, D. J. Pena, I. D. Walton, R. Cromer, C. D. Keating, and M. J. Natan, Submicrometer metallic barcodes., *Science*, vol. 294, pp. 137 141, Oct. 2001. (cited on page(s) 52, 69, 200)

[6] D. J. Lockhart and M. O. Trulson, Multiplex metallica Molecular tag made of small metal rods may enable parallel and, *Nature Biotechnology*, vol. 19, pp. 1122 1123, 2001. (cited on page(s) 52, 69, 200)

[7] S. E. Brunker, K. B. Cederquist, and C. D. Keating, Metallic barcodes for multiplexed bioassays., *Nanomedicine*, vol. 2, pp. 695 710, Oct. 2007. (cited on page(s) 52, 69, 200)

[8] N. H. Finkel, X. Lou, C. Wang, and L. He, Barcoding the microworld, *Analytical Chemistry*, pp. 352 359, 2004. (cited on page(s) 52, 69)

[9] E. Fernández-Rosas, R. Gómez-Martínez, E. Ibanez, L. Barrios, M. Duch, J. Esteve, C. Nogués, and J. A. Plaza, Intracellular polysilicon barcodes for cell tracking, *Small*, vol. 5, pp. 2433 2439, Nov. 2009. (cited on page(s) 49, 53, 54, 69, 97, 129, 161, 178)

[10] E. Fernández-Rosas, A. Baldi, E. Ibanez, L. Barrios, S. Novo, J. Esteve, J. A. Plaza, M. Duch, R. Gómez-Martínez, O. Castell, C. Nogués, and C. Fernández-Sánchez, Chemical functionalization of polysilicon microparticles for single-cell studies, *Langmuir*, vol. 27, pp. 8302 8308, July 2011. (cited on page(s) 53, 54, 69, 72, 97)

[11] V. C. Wright, J. Chang, G. Jeng, and M. Macaluso, Assisted reproductive technology surveillance, *Morbidity and mortality weekly report*, vol. 61, pp. 1 23, Nov. 2012. (cited on page(s) 69)

[12] R. Liebler, Are you my parent? Are you my child? The role of genetics and race in defining relationships after reproductive technological mistakes., *DePaul journal of health care law*, vol. 5, pp. 15 56, Jan. 2002. (cited on page(s) 70)

[13] M. Spriggs, IVF mixup: white couple have black babies, *Journal of Medical Ethics*, vol. 29, pp. 65 65, Apr. 2003. (cited on page(s) 53, 70)

[14] L. Bender, 'To err is human . ART mix-ups: A labor-based, relational proposal, 2006. (cited on page(s) 70)

[15] S. Novo, L. Barrios, J. Santaló, R. Gómez-Martínez, M. Duch, J. Esteve, J. A. Plaza, C. Nogués, and E. Ibánez, A novel embryo identification system by direct tagging of mouse embryos using silicon-based barcodes, *Human Reproduction*, vol. 26, pp. 96 105, Jan. 2011. (cited on page(s) 53, 54, 70, 72, 73, 84, 97, 200, 201, 215)

[16] E. Fernández-Rosas, R. Gómez-Martínez, E. Ibanez, L. Barrios, M. Duch, J. Esteve, J. A. Plaza, and C. Nogués, Internalization and cytotoxicity analysis of silicon-based microparticles in macrophages and embryos, *Biomedical Microdevices*, vol. 12, pp. 371 379, June 2010. (cited on page(s) 50, 51, 70, 84, 97, 130, 132, 183)

[17] O. Penon, S. Novo, S. Durán, E. Ibanez, C. Nogués, J. Samitier, M. Duch, J. A. Plaza, and L. Pérez-García, Efficient biofunctionalization of polysilicon barcodes for adhesion to the zona pellucida of mouse embryos, *Bioconjugate chemistry*, vol. 23, pp. 2392 2402, Dec. 2012. (cited on page(s) 71, 87, 132, 161, 178, 201)

[18] R. Gómez-Martínez, A. Sánchez, M. Duch, J. Esteve, and J. Plaza, DRIE based technology for 3D silicon barcodes fabrication, *Sensors and Actuators B: Chemical*, vol. 154, pp. 181 184, June 2011. (cited on page(s) 72)

[19] O. Penon, D. Siapkas, S. Novo, S. Durán, G. Oncins, A. Errachid, L. Barrios, C. Nogués, M. Duch, J. A. Plaza, and L. Pérez-García, Optimized immobilization of lectins using self-assembled monolayers on polysilicon encoded materials for cell tagging, *Colloids and Surfaces B: Biointerfaces*, vol. 116, pp. 104 113, Apr. 2014. (cited on page(s) 130, 201)

[20] S. Novo, O. Penon, L. Barrios, C. Nogués, J. Santaló, S. Durán, R. Gómez-Matínez, J. Samitier, J. A. Plaza, L. Pérez-García, and E. Ibánez, Direct embryo tagging and identification system by attachment of biofunctionalized polysilicon barcodes to the zona pellucida of mouse embryos, *Human Reproduction*, vol. 28, pp. 1519 1527, June 2013. (cited on page(s) 84, 85, 86, 97, 130, 201, 215, 227)

[21] S. Novo, R. Morató, O. Penon, and S. Duran, Identification of bovine embryos cultured in groups by attachment of barcodes to the zona pellucida, *Reproduction, Fertility and Development*, vol. 25, no. 1, pp. 218 219, 2013. (cited on page(s) 97, 130, 201, 215, 227)

[22] S. P. Lin, R. K. Lee, and Y. J. Tsai, In vivo hatching phenomenon of mouse blastocysts during implantation, *Journal of assisted reproduction and genetics*, vol. 18, pp. 341 345, June 2001. (cited on page(s) 86)

[23] L. A. Salamonsen, Review Tissue injury and repair in the female human reproductive tract, *Reproduction*, vol. 125, pp. 301 311, 2003. (cited on page(s) 86)

Chapter 3

Cobalt and Nickel Magnetic Barcodes for micro-labeling and sorting

Contents

3.1 Abstract

In this chapter we go one step forward and propose a new technology to obtain magnetic microbarcodes, made of cobalt and nickel alloys, such that they satisfy the same technological and optical requirements of polysilicon barcodes (see Chapter 2) but in addition to having magnetic properties. In this case microbarcode fabrication is based on photolithographic processes in combination with an electroplating method to grow magnetic cobalt and nickel alloys (CoNi) as main device materials. The optimal parameters of a highly precise electrodeposition bath, such time and temperature, are studied to obtain robust and versatile magnetic barcodes. Different characterization tests are also performed on the barcodes. For instance, confocal and scanning electron microscopies are used to characterize the design, shape and integrity of the fabricated devices, analysis using energy-dispersive X-ray (EDX) spectroscopy and X-ray fluorescence (XRF) are performed to determinate the material composition and finally a vibrating sample magnetometer (VSM) is used to define the magnetic properties of the obtained barcodes. The magnetic capabilities of these kinds of devices enable their manipulation by applying magnetic fields, which does not apply to polysilicon barcodes. Therefore, in the future we will be able to label, sort and, what is more important, manipulate different types of microobjects, such as devices, molecules, biological entities or living cells.

3.2 Introduction

As stated in the former chapter (Chapter 2), in the Micro and Nano Tools group at IMB-CNM (CSIC) we have developed different types of barcodes, entirely made of polysilicon, to label and track living cells and embryos.[1–7] In those cases the main material of the barcodes was polysilicon, which is a high suitable material for such applications due to its large knowledge developed by the Integrated Circuit (IC) research, high strength and Young s modulus[8] and biocompatibility.[5] Or what is most important about using polysilicon, a uniform deposition (from a few nanometers to several microns) and the ability of patterning polysilicon layers with micrometric or submicrometric dimensions (using dry-etching techniques and photolithographic processes). On the other hand, many researches worldwide are focusing their efforts on

obtaining synthesized magnetic nanoparticles with a huge number of applications.[9–14] Hence, we envisioned that it would also be possible to combine the functional features of both approaches, i. e. on one hand we have the microtechnology capabilities, such as the possibility of fabricating millions of reproducible devices, a complete control over the size and shape of the devices or the ability to achieve a low-cost fabrication; and on the other hand, the magnetic material capabilities, allowing us the manipulation of magnetic devices by applying magnetic fields.

For this reason, a novel design and technological development using a photolithographic based technology combined with a specific electroplating process to obtain micron and submicron sized magnetic devices is presented. Electroplating is one of the many methods to deposit and eventually integrate magnetic materials into microtechnology processes.[15] Besides being a cost effective technique, the whole process can be thermoregulated, requires low energy, can achieve high deposition rates and can handle complex geometries.[15] The electroplating set up is also easy to maintain and what is most important the properties of the deposit can be adapted by modifying the solution concentrations.

In this chapter we are focused on obtaining a novel type of barcode made of cobalt and nickel alloys, so we will be able to manipulate our devices and subsequently the attached microobjects by applying magnetic fields. Cobalt and nickel alloys are soft magnetic material and can be electrodeposited using the hydrated chloride salts of Ni and Co to achieve magnetic layers.[16] Soft magnetic materials are commonly used in microtechnology processes and can be easily electrodeposited, so are ideal for magnetism based MEMS applications. Later, for CoNi alloys to be made into microbarcodes, we need to perform a micromachined surface so that an inverted barcode pattern is obtained and can be used as a high suitable mold.

Therefore, a forward step is taken and a new generation of magnetic microbarcodes for label, sort and manipulate different types of microobjects is presented.

3.3 Start up and optimization of the CoNi electroplating setup

3.3.1 CoNi electroplating bath

Firstly, we should start up the electroplating setup and optimize the parameters and conditions for a high suitable electroplating bath. Hence, an appropriate chloride bath was needed to deposit CoNi alloys onto a specific substrate. The electrolyte bath solution was made up using hydrated nickel chloride, hydrated cobalt chloride, boric acid and saccharine. The required concentration was achieved using the following optimised values shown in Table 3.1.[17]

Boric acid acted as a weak pH buffer and maintained the pH in the range of 3 3.5 and also improved the quality of the deposit, as deposits may be cracked and burnt at low boric acid concentrations.[18] Saccharine was a de-stressing agent which helps to homogenize the CoNi deposition, as saccharine has been found to obtain a smooth alloy deposition.[19] As boric acid and saccharine were highly insoluble, the solution had to be left for magnetic stirring overnight.

Compound	Concentration	Mass (g)
$NiCl_2{\cdot}H_2O$	0.9 M	21.36
$CoCl_2{\cdot}H_2O$	0.2 M	4.76
H_3BO_3	30 g/l	3
Saccharine	0.7 g/l	0.07

Table 3.1: **Chemical composition of the electroplating bath**.[17]

3.3.2 CoNi electroplating setup

The electroplating setup requires an extremely accurate thermoregulation, as CoNi thickness not only depends on the applied time, but also it is dependent on the applied temperature. In fact, previous CoNi electroplating experiments failed, due to a non-extremely accurate control of the temperature. For this reason a highly precise thermostatic bath (Magnetic stirrer and heater, Lab-Mix 35, Fisher Scientific®)

was acquired by the group with the only purpose of manufacturing CoNi magnetic devices (Figure 3.1a).

So the electroplating setup includes a thermostatic bath which has the capability of regulating the bath temperature in an extremely precise way, a temperature probe which indicates the temperature at all times and a modified made-to-order beaker lid with provisions for inserting the reference, counter and the working electrodes.

The electrodeposition process was performed in a three-electrode cell. The reference electrode is an Ag/AgCl electrode, counter electrode is made of Ni and working electrode is a wafer piece. The electrodes and the wafer piece (where the CoNi alloy is going to be deposited) were connected to the Autolab equipment (Potentiostat/Galvanostat Autolab 302N) which regulates the voltage and time of deposition. The Autolab equipment requires a computer system for operation (Figure 3.1b).

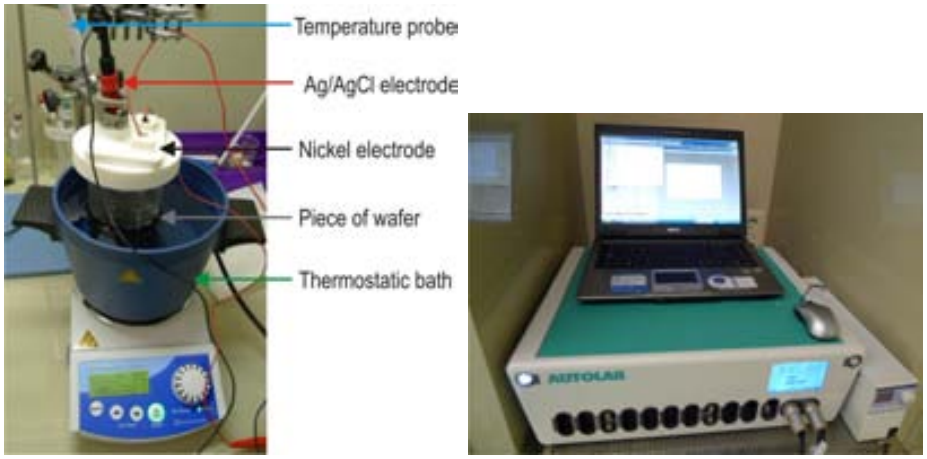

(a) (b)

Figure 3.1: **Experimental setup for the CoNi electroplating process.** Setup showing (a) the electroplating bath with electrodes connected to the (b) Autolab equipment.

3.4 Smooth CoNi microchips

3.4.1 Technological development of smooth CoNi microchips

Titanium and nickel smooth microchips were fabricated to be electrodeposited in the CoNi bath in order to find the most optimized deposition parameters before the fabrication of the CoNi barcodes. A 1 μm-thick silicon oxide layer was deposited on a 100 mm p-type silicon wafer to be used as a sacrificial layer (Figure 3.2a and b). Later, 50 nm-thick titanium and nickel layers were deposited as seed layers (Figure 3.2c and d, respectively), as we needed a conductive sample to obtain the electrodeposited CoNi layers.[17]

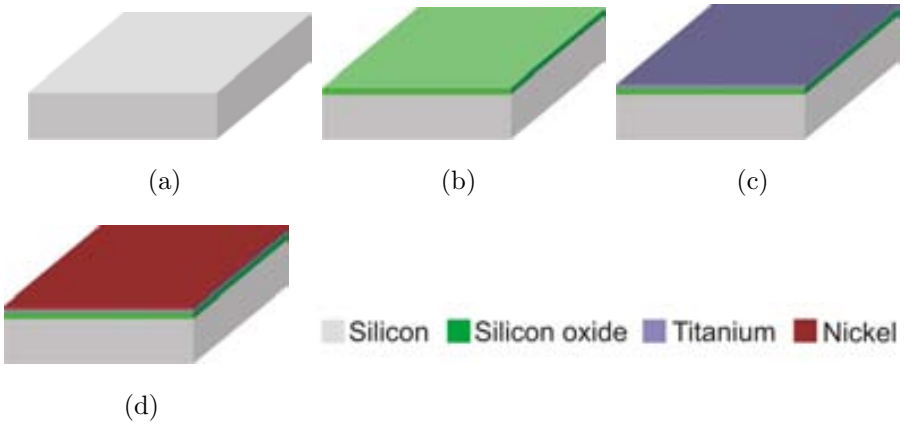

Figure 3.2: **Fabrication of smooth Ti and Ni microchips.** a, b) Silicon oxide as a sacrificial layer was deposited on a silicon substrate. c, d) 50 nm-thick titanium and nickel layers were deposited as seed layers for the CoNi electrodeposition.

Parameters tested for an optimal deposition were temperature and time. A piece of KaptonTM tape, a very good electrical insulator, was used to mask a part of every chip prior to the electroplating process for posterior deposited thickness determination (Figure 3.3a and b), as by measuring the step profile using confocal microscopy, we can determine the thickness of the deposited alloy. The deposition was performed for different time periods (100 s, 200 s, 300 s, 450 s and 600 s) and different temperatures (45°C, 55°C and 65°C) in the electrolyte bath using an Autolab equipment (Figure 3.3c). The voltage range between the counter electrode and the wafer piece was maintained at -0.8 V for all depositions.[17] After deposition, the KaptonTM® tapes were removed from each sample in order to find the step

profile and hence, the thickness of the deposited material using confocal microscopy (3D Optical profiler Microscopy Pl-μ Sensofar) was measured (Figure 3.3d).

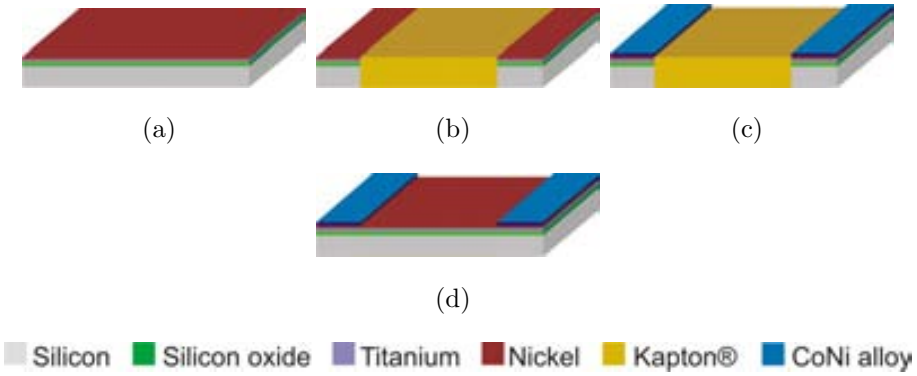

Figure 3.3: **Measurement of the electrodeposited CoNi step profile in CoNi smooth microchips.** a) Starting from a titanium and nickel microchip (b) we attached a piece of KaptonTM on the front side of the chip. c) Later, a CoNi electroplating process was carried out at different times and temperatures. This methodology results in a uniform deposition only on those sides where the KaptonTM is not present, as direct contact with the Ti and Ni seed layers is necessary to grow the CoNi alloy. d) Lastly, we carefully removed the KaptonTM and measured the obtained step between the titanium and nickel layers and the CoNi alloy using confocal microscopy.

3.4.2 Characterization of smooth CoNi microchips

Two characterization processes were performed in order to validate the electrodeposition setup as a reliable and robust method. Firstly, we have represented the obtained values of current (extrated from the Autolab) in dependende with time and temperature during the CoNi electrodeposition on Ti and Ni microchips. Thus, we could determinate the reliability of this process to mantain some constant parameters, such as temperature and current. As it can be seen in figure 3.4, 15 samples were prepared. Specifically, samples at 5 different times (100 s, 200 s, 300 s, 450 s and 600 s) and at 3 different temperatures (45^{o}C, 55^{o}C and 65^{o}C) were electrodeposited. In all cases, we obtained an almost constant tendency of the current with no temperature or time dependence. However, it is also worth mentioning that during the first few seconds of the deposition, as more conductive surface area is exposed for the deposition of Co

Ni, we observed an increasing deposition current. With progressing deposition time, after seeding is accomplished, the deposition current and thereby the deposition rate reach a constant level. This could be due to the decrease in the conducting area of exposure. In addition and apparently, there s a better control of the current stability at lower temperatures like 45^{o}C and 55^{o}C, in contrast with the obtained values for a temperature of 65^{o}C.

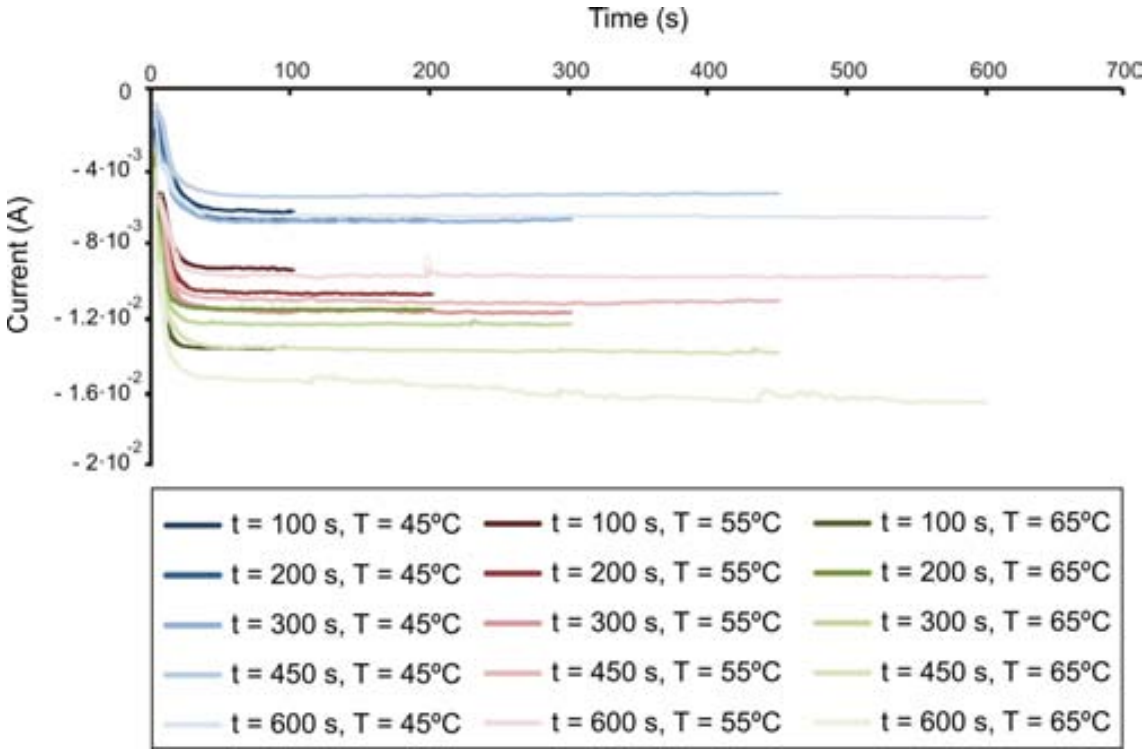

Figure 3.4: **Current tendency during the electroplating process for fabricating CoNi smooth microchips.** An almost constant tendency of the current was observed and no current dependence with the different applied times and temperatures was showed. During the first seconds of the deposition, an increasing deposition current was observed. While the deposition time was progressing, the deposition current reached a constant level due to a decrease in the exposured area.

Also, a confocal characterization was performed, as with this kind of microscopy we can easily measure the step (between the Ti and Ni layers and the CoNi alloy) that we obtained thanks to the KaptonTM use (Figure 3.3). It was noted that, as expected, for longer times of deposition, higher deposition was observed (Figure 3.5). The thickness of the layer is almost 1 μm closer to 100 s while it steadily becomes higher at longer times. As expected at 65°C, the deposition rate was faster

than 45°C, as the more the temperature increases the more the ion movement and the thickness of the layer grow. It can also be observed that for a 10°C increase in temperature, there is about 40% increase in the thickness of the deposit. Eventually, 55^{o}C temperature was chosen, as for us the obtained results at this temperature were the most satisfactory.

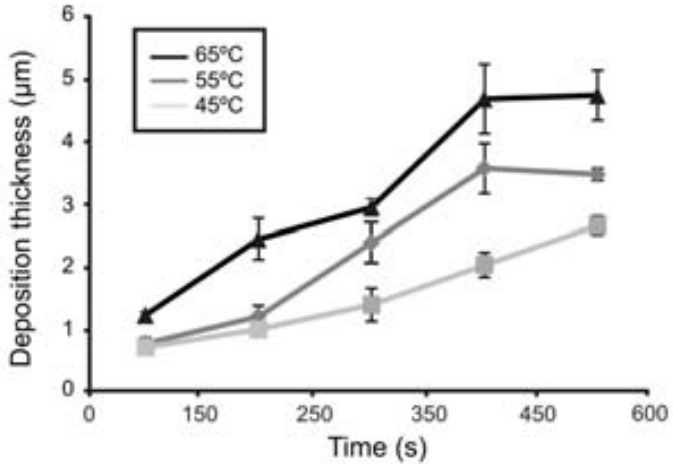

Figure 3.5: **Thickness of electrodeposited CoNi films vs. time of deposition.** The more the temperature and time during CoNi electrodeposition increased, the more the thickness of the layer grew.

3.5 Design of CoNi Barcodes as magnetic labels

After the electroplating setup was optimized, this methodology was applied for the obtaining of magnetic barcodes.

As noted in chapter 2, the design of barcode type D (horizontal-card barcode) is the most robust and the easiest to identify of the 4 barcode models designed by our group and is alone dealt with in the involved experiments in this chapter (see figure 2.3). For further information about the horizontal-card barcode design requirements, such as external and bit dimensions and the 256 combinations of different values, refer to section 2.3.2.

3.6 Technological development of CoNi Barcodes

3.6.1 Inverted barcode pattern fabrication

In order to fabricate our magnetic barcodes, it is necessary to design an inverted barcode photorerist pattern, as this kind of mold should be filled with the electrodeposited CoNi layer. For this reason and as this was the very first time we developed this kind of device, we had to design and order a brand new mask with the only purpose of manufacturing CoNi magnetic devices. Fabrication of the magnetic barcodes started with a 100 mm p-type silicon wafer (Figure 3.6a). A 1 μm-thick silicon oxide layer was deposited as a device layer (Figure 3.6b). 50 nm-thick Ti and Ni layers were deposited as seed layers to allow the deposition of the cobalt/nickel alloy (Figure 3.6c and d, respectively). 0.9 μm of photoresist was spun as inverted pattern on the wafer (Figure 3.6e). Finally, the photoresist was patterned by photolithography to define the devices (Figure 3.6f).

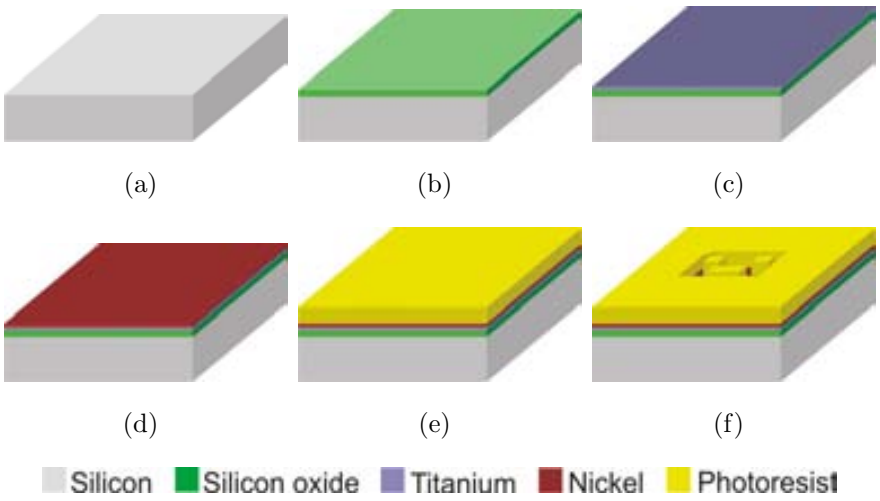

Figure 3.6: **Inverted barcode pattern fabrication.** a) Silicon substrate deposited with (b) silicon oxide layer followed by (c, d) titanium and nickel depositions as seed layers, respectively. e) Photoresist was spun. f) A photoresist patterning was performed by photolithography to define the devices.

In figure 3.7 it can be observed two scanning electron microscopy images of the inverted pattern. An almost perfectly defined shape of inverted barcodes was obtained by photolithographic processes, as the edges of the small bits were a little bit rounded.

This fact could be explained due to a non-perfectly defined photolithographic process. However, a valid inverted barcode pattern was obtained.

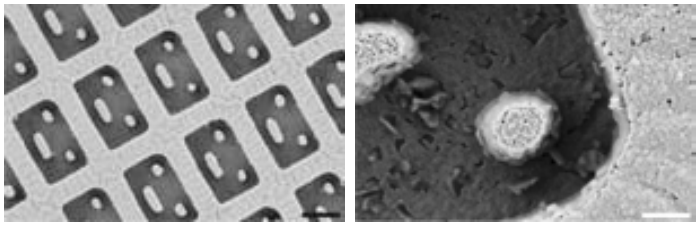

(a) (b)

Figure 3.7: **Characterization of the inverted barcode pattern.** a) Scanning electron microscope image of the inverted barcode pattern made of photoresist. b) A zoom image of the same pattern. Black scale bars = 5 μm. White scale bars = 1 μm.

3.6.2 CoNi electrodeposition upon inverted barcode patterns

The next steps of the CoNi barcode fabrication consisted on filling the gaps with the electrodeposited alloy and removing the patterned photoresist. Starting from a wafer with an inverted photoresist pattern on its surface (Figure 3.8a), an CoNi electroplating process was performed (at an optimal 55^{o}C temperature for various times of deposition, 50 s, 100 s, 200 s, 300 s, 450 s and 600 s) (Figure 3.8b). Then, the photoresist was removed by exposing it to acetone, isopropyl alcohol and washing it in water for 1 minute (Figure 3.8c).

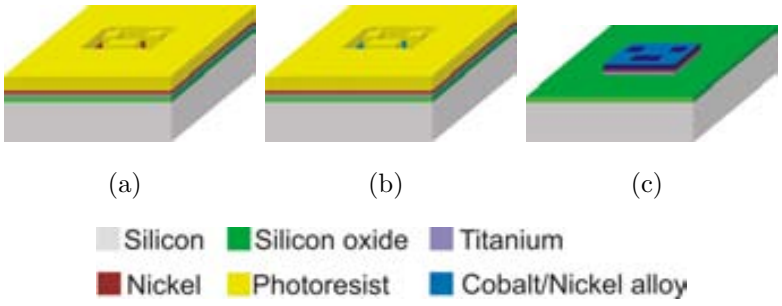

Figure 3.8: **CoNi electrodeposition upon the inverted barcode pattern.** a) Starting from a wafer with an inverted barcode pattern on its surface (b) a electroplating process at -0.8 V and 55^{o}C was performed at different times. c) Photoresist removal was carried out by exposing it to acetone and isopropyl alcohol.

3.7 Characterization of fabricated CoNi Barcodes

Firstly, and before the characterization through several microscopies, we represented the obtained values of current (as we did with the smooth CoNi samples, figure 3.4) in dependende with time during the CoNi electrodeposition on the barcode-patterned surfaces. Specifically, 2 types of barcode designs (BC105 and BC153) at 5 different times (100 s, 200 s, 300 s, 450 s and 600 s) and at 55^{o}C were electrodeposited. In both graphs (Figure 3.9) we could observed that during the first few seconds of the deposition, as more conductive surface area was exposed for the deposition of CoNi, an increasing deposition current was observed. With progressing deposition time, after seeding was accomplished, the deposition current and thereby the deposition rate reached a constant level.

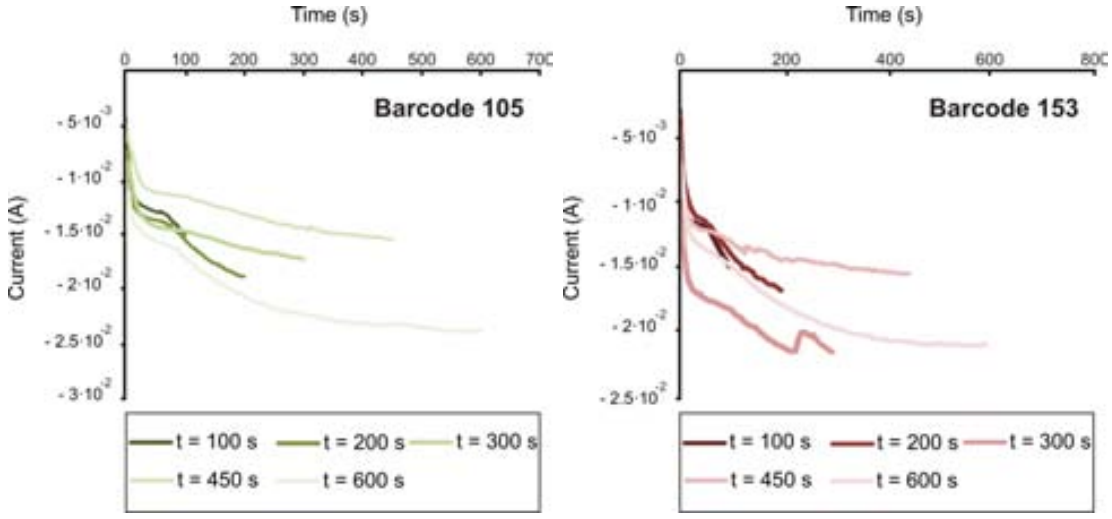

(a) (b)

Figure 3.9: **Current tendency during the electroplating process for fabricating the CoNi magnetic barcodes.** An almost constant tendency of the current was observed and no current dependence with the different applied times and temperatures was showed. During the first seconds of the deposition, an increasing deposition current was observed. While the deposition time was progressing, the deposition current reached a constant level due to a decrease in the exposured area.

3.7.1 Scanning electron microscopy

2 out of 256 types of barcodes were chosen for this work. Barcode-105 (BC105) is the 8-bit binary code *0110 1001* and barcode-153 (BC153) is the 8-bit binary code *1001 1001*. The barcodes after electrodeposition and photoresist removal were characterized by scanning electron microscopy (Carl Zeiss Auriga Microscope, Oxford Instruments IncaX-act, GmbH, Germany) as shown in figure 3.10.

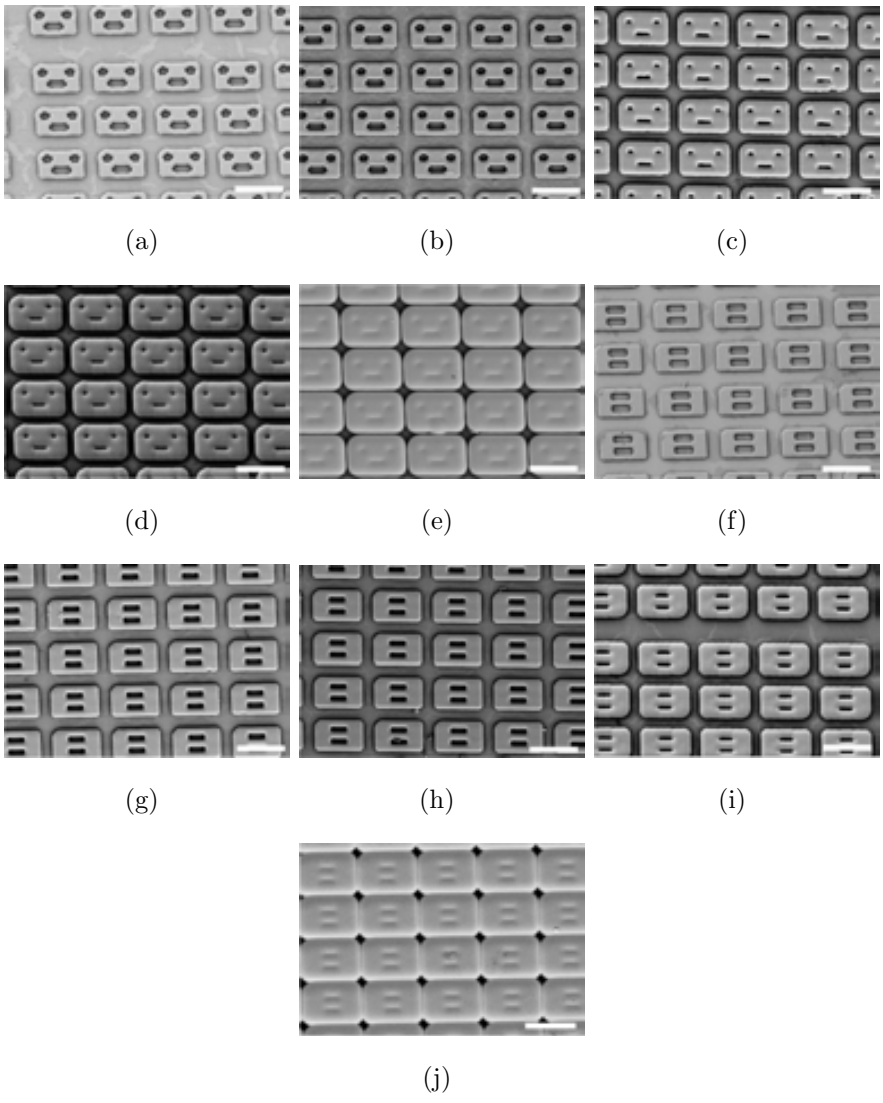

Figure 3.10: **Unreleased barcodes after CoNi electroplating process.** (a-e) Unreleased 105-barcodes after (a) 50 s, (b) 100 s, (c) 200 s, (d) 300 s and (e) 450 s of electrodeposition. (f-j) And unreleased 153-barcodes after (f) 50 s, (g) 100 s, (h) 200 s, (i) 300 s and (j) 450 s of electrodeposition. Scale bars = 10 m.

It was observed that barcodes deposited at 50 s did not have well defined shapes, as the boundaries of the undeposited regions in figure 3.10a and f were not complete. This fact could be related with a non-perfectly defined photolithographic process, as I mentioned above (see figure 3.7). At 100 s, the barcodes had well defined shapes (Figure 3.10b and g). At 200 s and above over-depositions were observed and the definition of shape is lost. It is clear from the SEM images that the deposition progresses to fill the gap between adjacent barcodes as the time progresses. Based on the shape constrain, 100 s was chosen as the optimal time parameter for deposition (Figure 3.11).

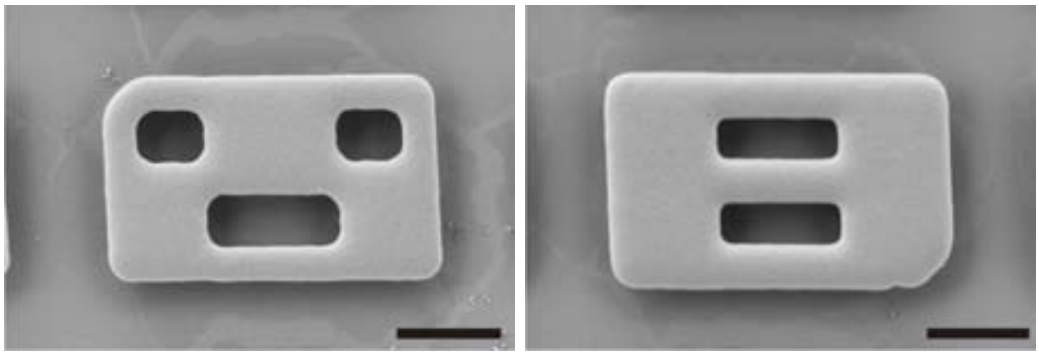

(a) (b)

Figure 3.11: **Optimized magnetic barcodes.** Unreleased barcodes after 100 s of CoNi electrodeposition. Image (a) corresponds to a 105-barcode and image (b) to a 153-barcode. Scale bars = 3 μm.

3.7.2 Confocal microscopy

The patterned substrates were measured for thickness with confocal microscopy (3D Optical profiler Microscopy - Pl- μ Sensofar) after deposition at various time intervals at 55^{o}C (Figure 3.12). Depositions at 50 s, 100 s, 200 s, 300 s, 450 s and 600 s were analyzed. And as expected, as time went by, the tendency of the thickness of the deposit was observed to grow. The thickness of the observed values was not exactly similar for both barcodes at the same time of deposition (Figure 3.13). This could be due to the slightly differences in the area exposed during electrodeposition, however both designs followed the same thickness tendency over time.

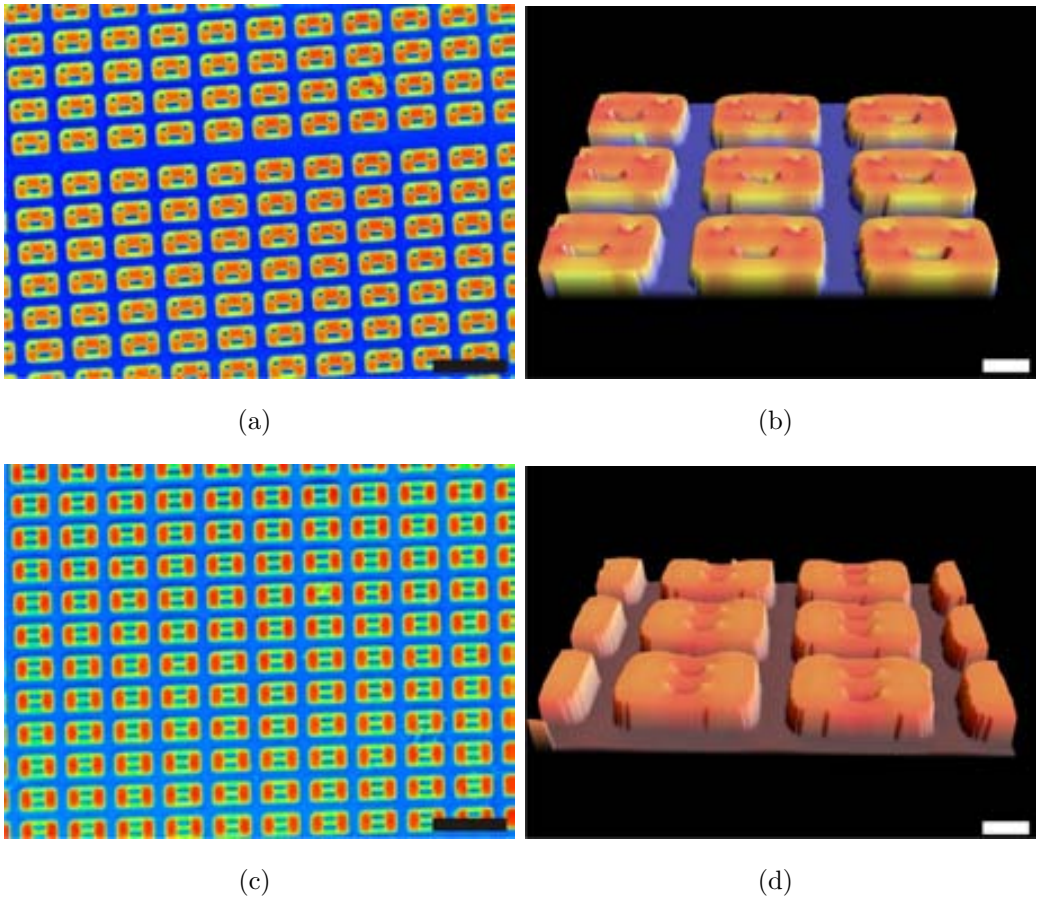

(a) (b)

(c) (d)

Figure 3.12: **Confocal characterization of the magnetic barcodes.** a) 2D confocal image of a 105-barcode wafer after 100 s of electroplating process and b) a 3D confocal image of the same wafer. c) 2D confocal image of a 153-barcode wafer after 100 s of electroplating process and d) a 3D confocal image of the same wafer. Black scale bars = 20 μm. White scale bars = 4 μm

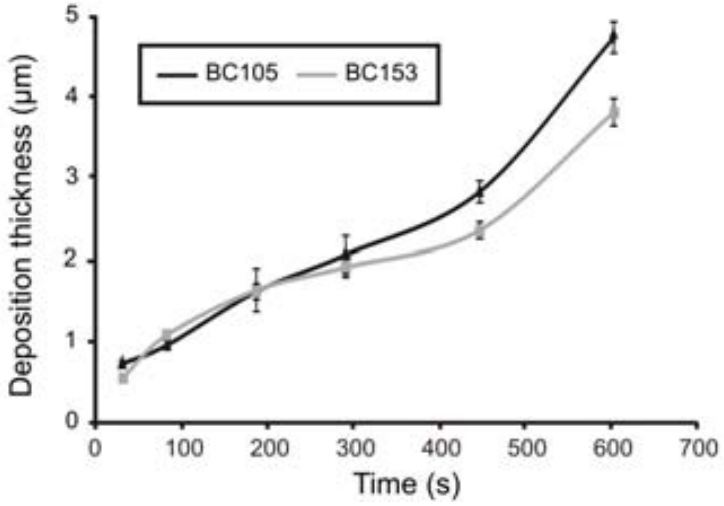

Figure 3.13: **Deposition thickness vs. time of deposition in CoNi barcode samples.** BC105 and BC153 designs followed the same tendency and only slight differences were observed due to the differences in the exposed area during electrodeposition. 50 s, 100 s, 200 s, 300 s, 450 s and 600 s time CoNi depositions were performed. Black line corresponds to *0110 1001*-barcode. Grey line corresponds to *1001 1001*-barcode.

3.7.3 Energy-dispersive X-ray spectroscopy

Material composition of the barcodes was analyzed by Energy-dispersive X-ray spectroscopy (PentaFET-Precision attached to the SEM equipment) and was found that the deposits of both BC105 and BC153 barcodes were composed of only CoNi without any kind of impurities (Figure 3.14a and b). The characteristic peaks of cobalt and nickel signals at 0.776 KeV and 0.851 KeV, respectively, can be clearly observed.

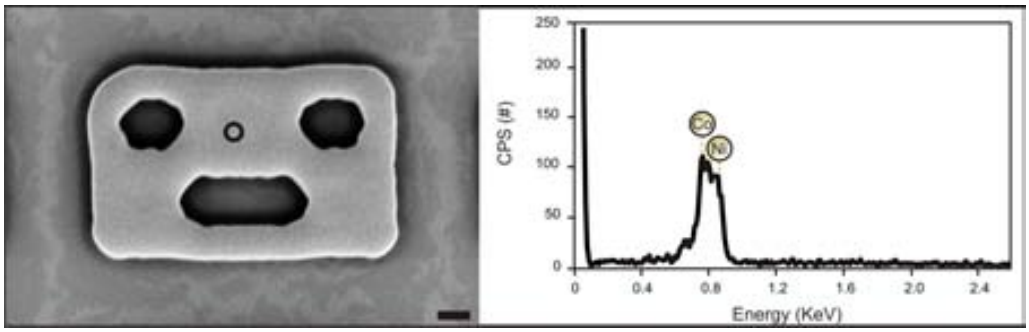

(a)

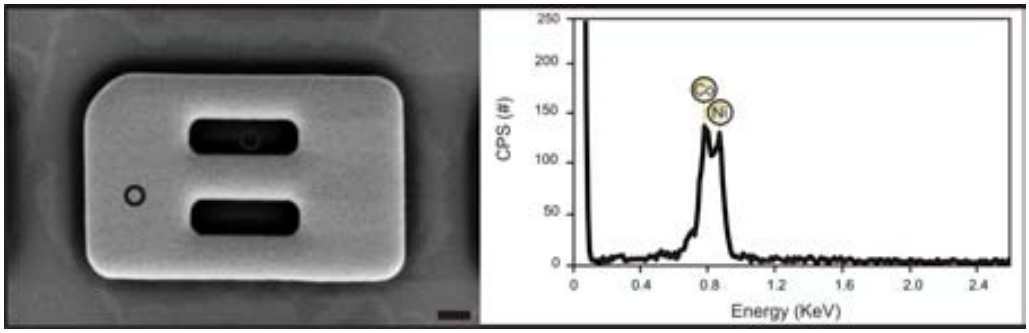

(b)

Figure 3.14: **Energy-dispersive X-ray spectroscopy analysis of the magnetic barcodes.** Unreleased a) BC105 and b) BC153 and theirs corresponding EDX plots confirming Co and Ni presence. Black circles represent points of inspections. Scale bars = 1 μm.

3.7.4 X-ray fluorescence

(Performed by Laboratori de Ciència i Tecnologia Electroquímica de Materials (LCTEM), Departament de Química física, Universitat de Barcelona)

X-ray fluorescence (XRF) (X-ray Fluorescence Fisher scope system XDAL with DCM 3D optical image profiler software) analysis for an advanced material identification was also carried out, as this technique is widely used for elemental and chemical analysis. In this case, XRF results for both designs (BC105 and BC153) showed a fairly constant cobalt and nickel composition ratio in the barcode deposits (Tables 3.2 and 3.3).

BC105		
	Co (%)	Ni (%)
Sample 1	46.9	53.1
Sample 2	47.4	52.6
Sample 3	48.6	51.4
Mean (%)	47.6	52.3

Table 3.2: **X-ray fluorescence analysis of the magnetic barcode 105.** BC105 barcode X-ray fluorescence analysis confirmed constant composition ratio for the deposited cobalt and nickel layers with any kind of impurities.

BC153		
	Co (%)	Ni (%)
Sample 1	42.7	57.3
Sample 2	43.7	56.3
Sample 3	43.1	56.8
Mean (%)	43.1	56.8

Table 3.3: **X-ray fluorescence analysis of the magnetic barcode 153.** BC153 barcode X-ray fluorescence analysis confirmed also a constant composition ratio for the deposited cobalt and nickel layers with any kind of impurities.

3.8 Sacrificial etching and release of CoNi Barcodes

3.8.1 Preliminary etching tests of CoNi Barcodes

Preliminary tests were performed before the optimal conditions for a suitable sacrificial etching process of CoNi barcodes were found.

1. Firstly, we combined the etching of the Ti and Ni seed layers (see next section for a detailed explanation) with the polysilicon barcode etching method (see section 2.4). Namely the barcodes were released with a 40-minute etching process in vapors of 49% HF out of the silicon oxide sacrificial layer. The barcodes were suspended by ultrasounds (MiniSpin Plus) in 96% ethanol, centrifuged, and collected at 14 000 rpm for 5 minutes. However, only a formless layer of CoNi was observed (Figure 3.15a). In this case, we attributed this fealure to a too long 49% HF exposure, as this acid in such concentration was too strong and damaged deeply the CoNi barcodes.

2. Secondly, we reproduced the same parameters of those in the first method, but avoiding the 49% HF ething, as we thought that the Ti and Ni etchings would be enough to release the CoNi barcodes. We were right, however, several broken barcodes were observed (Figure 3.15b). We attributed this fealure to a too aggressive centrifugation step. Another explanation for the broken barcodes was a non-perfectly defined photolithographic step. Hence, we had to choose carefully the pieces of the wafer which were going to be attacked.

3. In the last method, we decided to skip the centrifugation step as well and just approximate a magnet to the wafer to achieve the precipitation of the barcodes. Finally, the optimal conditions for the etching process of CoNi barcodes were found and are deeply explained in the next section.

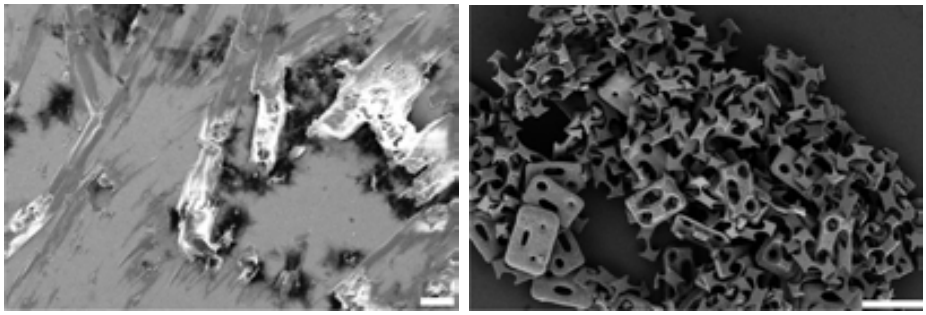

(a) (b)

Figure 3.15: **Failed magnetic barcodes obtained during the preliminary etching tests.** a) A formless layer of CoNi after a too long 49% HF sacrificial etching. b) Several broken barcodes after a too aggressive centrifugation step. Scale bars = 10 μm.

3.8.2 Optimized etching process and release of CoNi Barcodes

After several preliminary tests a high suitable etching process to obtain suspended CoNi barcodes were found.

The next step of the CoNi barcode fabrication after the electrodeposition process and the photoresist removal (See figure 3.8), is the sacrificial etching of the barcodes from the wafer in order to obtain completely suspended devices. CoNi barcodes were deposited on top of 50 nm-thick Ti and Ni seed layers, therefore the first step consisted of etching these two layers (Figure 3.16a).

The nickel etching bath contained a 1:4 mixture of 69% nitric acid (HNO_3) and double deionized-water. This mixture etched nickel at the rate of 200 nm/min. The wafer piece was placed in the nickel etching bath for 30 seconds, followed by a gentle wash in water.

The titanium etching bath was composed of a 1:1 mixture of 10% HF and polyethylene glycol (PEG). This mixture etched titanium at the rate of 50 nm/min. The wafer piece was place in the titanium etching bath for 1 minute (Figure 3.16b). The low concentration of HF in this mixture (in this case, 10%) was also enough to attack the SiO_2 of the sacrificial layer.

Eventually, we introduced the attacked wafer into a 5 ml-vial of 96% ethanol. It should be noted that the simple approach of a magnet to the vial with the suspended barcodes, was enough to allow their precipitation (Figure 3.16c).

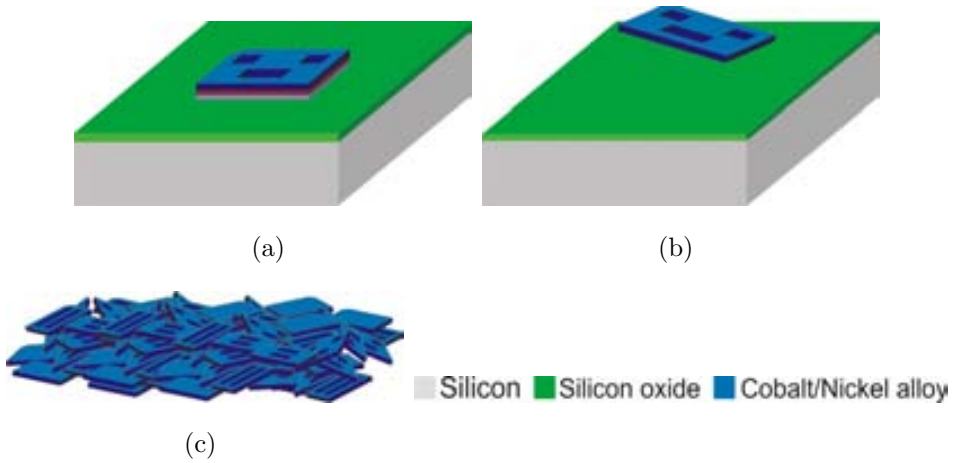

Figure 3.16: **Wafer release of the magnetic barcodes.** a) Starting from a wafer with the CoNi barcodes still attached on its surface, (b) we performed the device release through both Ti and Ni wet etchings. c) Lastly, the suspended CoNi barcodes after the immersion of the wafer into a vial with 96% ethanol was carried out approaching of a magnet to the vial.

3.9 Characterization of suspended CoNi Barcodes

Finally, suspended CoNi barcodes were obtained and observed under the scanning electron microscope after placing a 2μl-drop of devices in 96% ethanol on a clean silicon substrate (Ultrasonicator - Selecta 3000683).

In figure 3.17a a barcode looking upwards is presented. The acquired released barcodes showed an almost perfect and well-defined shape. Despite the rough surface obtained (Figure 3.17b), a homogenous and continuous CoNi layer was successfully deposited. A barcode looking downwards is also shown in figure 3.17c, in this case the released barcode presented bigger and deformed bits, in comparison with the non-released devices. This fact could be due to Ni and Ti wet etchings. As this part of the barcode was directly attacked by the acid solutions. A zoom image of the same barcode is showed in figure 3.17d.

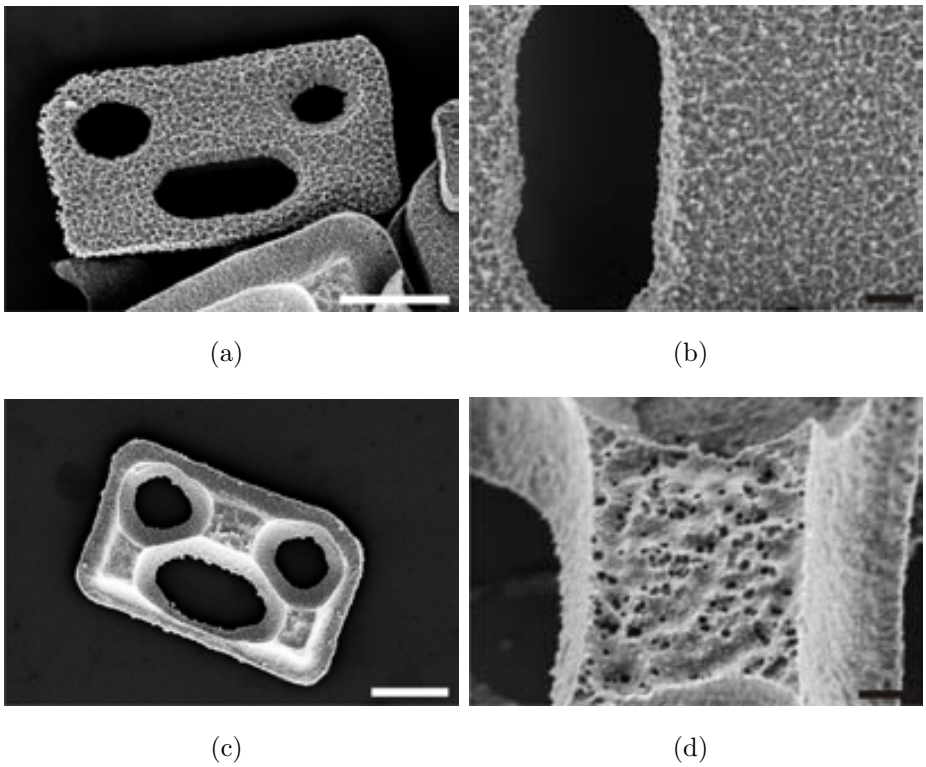

(a) (b)

(c) (d)

Figure 3.17: **Suspended magnetic barcodes after Ti and Ni wet etchings.** SEM images of a) a released barcode looking upwards on a silicon substrate, b) zoom image of the same barcode. c) A released barcode looking downwards and d) a zoom image of the same barcode. White scale bar = 3 μm. Black scale bar = 500 nm.

3.10 Validation of the CoNi Barcodes as magnetic labels

We also analyzed magnetically our barcodes. Firstly, a simple magnetic characterization of the devices was performed. We simply approached a magnet to our devices (still on the wafer) to easily characterize the magnetization of the cobalt and nickel layer. In figure 3.18 it can be clearly observed that the wafer is attracted to the magnet, and even changing the angle of the magnet the wafer still remained strongly attached to the magnet.

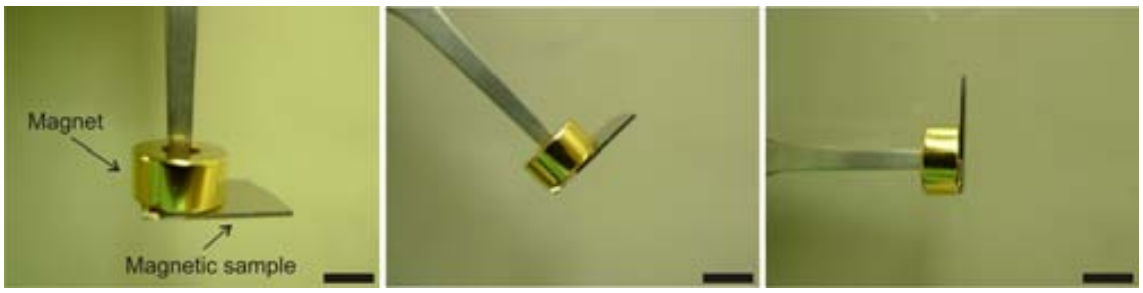

Figure 3.18: **Simple magnetic characterization of the unreleased CoNi barcodes.** Only approaching a magnet to the magnetic devices, the wafer is easily and strongly attached to it. Scale bar = 5 mm.

In addition, we also performed the characterization of the devices through a vibrating sample magnetometer (VSM) (Figure 3.19) (model EV7, LOT-Oriel) to define the magnetic properties of the obtained barcodes *(Performed by Instituto de Ciencia de Materiales de Madrid (ICMM-CSIC)*. The wafer was placed inside a uniform magnetic field to magnetize it. The sample was then physically vibrated sinusoidally through the use of a piezoelectric material. The corresponding voltage was induced in suitably located stationary pickup coils. This system uses an electromagent in order to apply an external magnetic field of 1.8 T.

Remanent magnetization and coercive field values were given by the obtained hysteresis loops (Figure 3.20). The remanence is a mesure of the remaining magnetization when the driving field is dropped to zero. While the coercivity is a measure of the reverse field needed to drive the magnetization to zero after the sample is saturated.

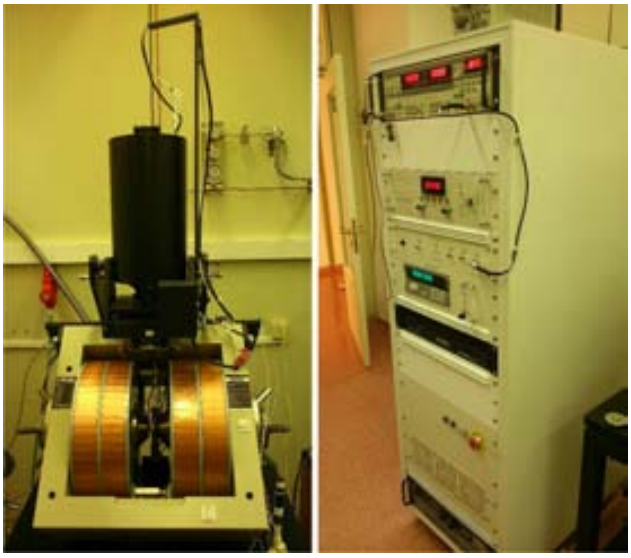

Figure 3.19: **A vibrating sample magnetometer.**

A magnetic characterization was performed on magnetic barcode wafers before and after the wet etching process of the Ti and Ni seed layers (see section 3.6.2) in order to discern if these layers affect somehow the magnetism of the CoNi barcodes. Both parallel and perpendicular magnetic fields were applied. It must be taken into account that the registered magnetization values belonged to all of the magnetic barcodes in the sample and not only to one of them.

Magnetic anisotropy (directional dependence of a material s magnetic properties) was observed in those samples where the Ti and Ni seed layers were still on the wafer (Figure 3.20a and b), thus the obtained hysteresis loops, when both parallel and perpendicular magnetic fields were applied, went to linearity. This means that the tendency of the curve is almost a horizontal line.

On the contrary, in figure (Figure 3.20c and d), the hysteresis loops after the wet etchings of the Ti and Ni layers, presented an almost perfect shape.

These obtained results also showed than the CoNi barcodes are perfect to be used as magnetic labels, as their coercive field (Hc $\sim$ 30-40 G) values are high enough not to be easily demagnetized, for instance, by the Earth s magnetic field (Hc = 0.5 G).

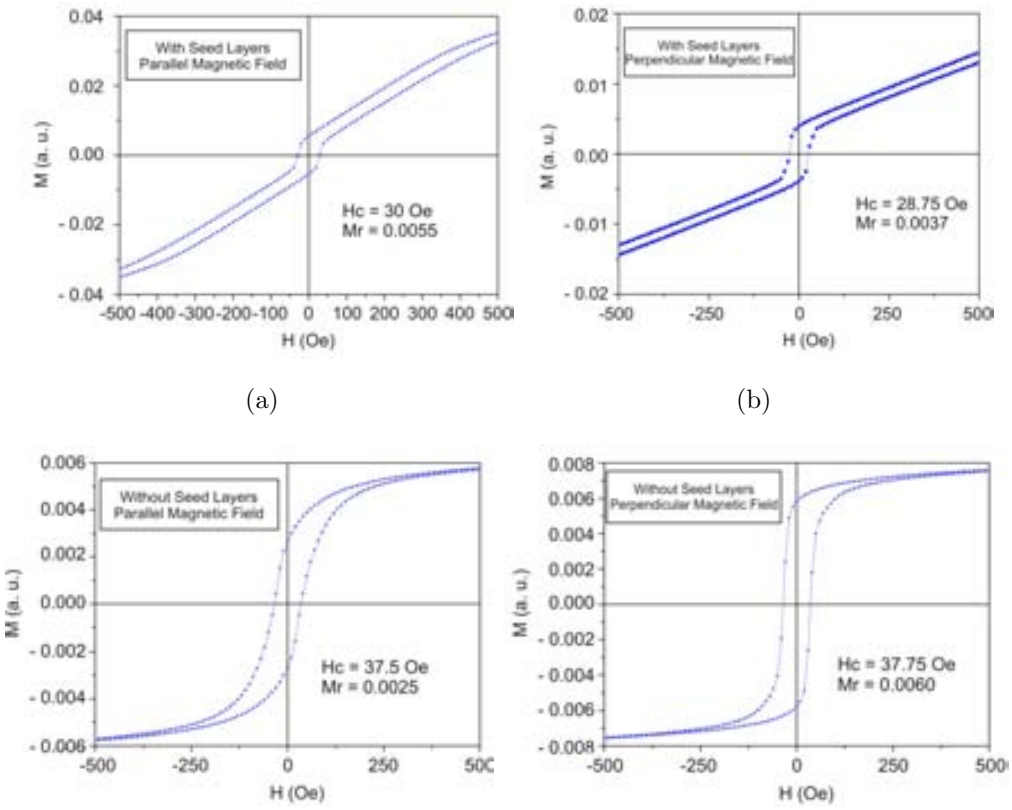

Figure 3.20: **Magnetic characterization of the CoNi barcodes by VSM.** Magnetic characterization of CoNi barcode wafer with (a, b) and without (c, d) the seed layers applying both parallel and perpendicular magnetic fields. Hc = Coercive field. Mr = Magnetic Remanence. Magnetic anisotropy was shown in those samples with the Ti and Ni seed layers still on the wafer. Conversely, after the Ti and Ni wet etchings the hysteresis loops of the CoNi barcodes presented a perfect shape. Hc = Coercive field. Mr = Magnetic Remanence.

3.11 Conclusions

Nowadays, an increasing demand for tracking small items has driven the exploration for novel methods of barcoding, and taking into account that microtechnology provides new opportunities for miniaturize devices, we have developed magnetic microbarcodes which allow the study of the microworld under optical microscopes and even the manipulation of the attached microobjects.

Firstly, the electrodeposition setup for CoNi thin films has been optimized. Based on the studies performed on the obtained thin films, a barcode fabrication strategy was formulated. Using microtechnology and electroplating processes, CoNi microbarcodes were fabricated. Several parameters such as time (50s, 100s, 200 s, 300 s, 450 s, 600 s) and temperature of deposition (45°C, 55°C, 65°C) were studied to obtain the optimal barcode thickness. Eventually, 55°C and 100 s were fixed as optimal conditions for the electrodepositon of barcodes. An extended material characterization (EDX and XPS) was performed and the obtained results showed us that our magnetic barcodes were composed of only CoNi materials without any kind of impurities, in addition to a fairly constant and uniform cobalt and nickel composition ratio. Several preliminary tests were performed before the optimal conditions for a suitable sacrificial etching process of CoNi barcodes were found. And different parameters such as type of etchants or the utilization or not of centrigugation were tested. Finally, almost well-defined barcodes were obtained.

In addition, we also performed the characterization of the devices through a vibrating sample magnetometer (VSM) to define the magnetic properties of the obtained barcodes. The obtained results showed that the CoNi barcodes are perfect to be used as magnetic labels, as their coercive fields values are high enough not to be easily demagnetizated.

In summary, not only do these magnetic devices satisfy the same technological and optical requirements that polysilicon barcodes, but also they have magnetic properties, which enable their manipulation by applying magnetic fields. These barcodes have promising applications into the microworld. Among others we hope to apply our magnetic devices in a magnetism-based microfluidic cell sorting technology in the future.

Bibliography

[1] S. Novo, L. Barrios, J. Santaló, R. Gómez-Martínez, M. Duch, J. Esteve, J. A. Plaza, C. Nogués, and E. Ibánez, A novel embryo identification system by direct tagging of mouse embryos using silicon-based barcodes, *Human Reproduction*, vol. 26, pp. 96 105, Jan. 2011. (cited on page(s) 53, 54, 70, 72, 73, 84, 97, 200, 201, 215)

[2] S. Novo, R. Morató, O. Penon, and S. Duran, Identification of bovine embryos cultured in groups by attachment of barcodes to the zona pellucida, *Reproduction, Fertility and Development*, vol. 25, no. 1, pp. 218 219, 2013. (cited on page(s) 97, 130, 201, 215, 227)

[3] S. Novo, O. Penon, L. Barrios, C. Nogués, J. Santaló, S. Durán, R. Gómez-Matínez, J. Samitier, J. A. Plaza, L. Pérez-García, and E. Ibánez, Direct embryo tagging and identification system by attachment of biofunctionalized polysilicon barcodes to the zona pellucida of mouse embryos, *Human Reproduction*, vol. 28, pp. 1519 1527, June 2013. (cited on page(s) 84, 85, 86, 97, 130, 201, 215, 227)

[4] S. Novo, C. Nogués, O. Penon, L. Barrios, J. Santaló, R. Gómez-Martínez, J. Esteve, A. Errachid, J. A. Plaza, L. Pérez-García, and E. Ibánez, Barcode tagging of human oocytes and embryos to prevent mix-ups in assisted reproduction technologies, *Human Reproduction*, vol. 29, pp. 18 28, Jan. 2014. (cited on page(s) 97, 130, 201, 215)

[5] E. Fernández-Rosas, R. Gómez-Martínez, E. Ibanez, L. Barrios, M. Duch, J. Esteve, C. Nogués, and J. A. Plaza, Intracellular polysilicon barcodes for cell tracking, *Small*, vol. 5, pp. 2433 2439, Nov. 2009. (cited on page(s) 49, 53, 54, 69, 97, 129, 161, 178)

[6] E. Fernández-Rosas, R. Gómez-Martínez, E. Ibanez, L. Barrios, M. Duch, J. Esteve, J. A. Plaza, and C. Nogués, Internalization and cytotoxicity analysis of silicon-based microparticles in macrophages and embryos, *Biomedical Microdevices*, vol. 12, pp. 371 379, June 2010. (cited on page(s) 50, 51, 70, 84, 97, 130, 132, 183)

[7] E. Fernández-Rosas, A. Baldi, E. Ibanez, L. Barrios, S. Novo, J. Esteve, J. A. Plaza, M. Duch, R. Gómez-Martínez, O. Castell, C. Nogués, and C. Fernández-Sánchez, Chemical functionalization of polysilicon microparticles for single-cell studies, *Langmuir*, vol. 27, pp. 8302 8308, July 2011. (cited on page(s) 53, 54, 69, 72, 97)

[8] H. Kahn, Mechanical Properties of Micromachined Structures, in *Nanotribology and Nanomechanics*, pp. 1297 1323, 2008. (cited on page(s) 97)

[9] G. Zhang, Y. Liu, C. Zhang, W. Hu, W. Xu, Z. Li, S. Liang, J. Cao, and Y. Wang, Aqueous immune magnetite nanoparticles for immunoassay, *Journal of Nanoparticle Research*, vol. 11, pp. 441 448, June 2008. (cited on page(s) 98)

[10] A. Fornara, P. Johansson, K. Petersson, S. Gustafsson, J. Qin, E. Olsson, D. Ilver, A. Krozer, M. Muhammed, and C. Johansson, Tailored Magnetic Nanoparticles for Direct and Sensitive Detection of Biomolecules in Biological Samples, *Nano Letters*, vol. 8, pp. 3423 3428, Oct. 2008. (cited on page(s) 98)

[11] R. Hao, R. Xing, Z. Xu, Y. Hou, S. Gao, and S. Sun, Synthesis, functionalization, and biomedical applications of multifunctional magnetic nanoparticles., *Advance materials*, vol. 22, pp. 2729 2742, July 2010. (cited on page(s) 98)

[12] H. Lee, A. M. Purdon, V. Chu, and R. M. Westervelt, Controlled Assembly of Magnetic Nanoparticles from Magnetotactic Bacteria Using Microelectromagnets Arrays, *Nano Letters*, vol. 4, pp. 995 998, May 2004. (cited on page(s) 98)

[13] M. Mahmoudi, S. Sant, B. Wang, S. Laurent, and T. Sen, Superparamagnetic iron oxide nanoparticles (SPIONs): development, surface modification and applications in chemotherapy., *Advanced drug delivery reviews*, vol. 63, no. 1-2, pp. 24 46, 2010. (cited on page(s) 98)

[14] P. Tartaj, P. Morales, S. Veintemillas-verdaguer, and T. Gonz, The preparation of magnetic nanoparticles for applications in biomedicine, *Journal of Physics*

D: Applied Physics, vol. 36, pp. 182 197, 2003. (cited on page(s) 98)

[15] N. V. Myung, D.-Y. Park, B.-Y. Yoo, and P. T. Sumodjo, Development of electroplated magnetic materials for MEMS, *Journal of Magnetism and Magnetic Materials*, vol. 265, pp. 189 198, Sept. 2003. (cited on page(s) 98)

[16] D. C. Jiles, T. T. Chang, D. R. Hougen, and R. Ranjan, Magnetic properties of nickel-copper and nickel-cobalt alloys, *Journal of Physique*, vol. 49, no. 12, pp. 3 4, 1988. (cited on page(s) 98)

[17] M. Duch, J. Esteve, E. Gómez, R. Pérez-Castillejos, and E. Vallés, Electrodeposited Co-Ni alloys for MEMS, *Journal of Micromechanics and Microengineering*, vol. 12, pp. 400 405, July 2002. (cited on page(s) 99, 101)

[18] M. Schlesinger and M. Paunovic, Modern Electroplating, in *Modern electroplating* (Wiley, ed.), no. November, 2011. (cited on page(s) 99)

[19] C. Xui and W. Chen, Saccharin Effects on Direct-Current Electroplating Nanocrystalline Ni Cu Alloys, *Journal of The Electrochemical Society*, vol. 155, no. 9, pp. 133 139, 2008. (cited on page(s) 99)

Chapter 4

Intracellular Polysilicon-Chromium-Gold Chips for orthogonal chemical functionalization

Contents

4.1 Abstract

In this chapter the new design and technological development of multimaterial chips, using polysilicon and gold as device layers, is presented. One of the main technological challenges is to overcome the low adherence between these two materials, especially because of their small contact-area, only 9 μm^2. Thus, in order to circumvent this difficulty a chromium adherent-layer is deposited in between. The advantage of having multiple material layers in one device is the potential to render multi-tasking chips, as once they are chemically multifunctionalized, we can provide the chip the ability of being multi-functional. Hence, and as a proof of concept, two different proteins, Wheat Germ Agglutinin (WGA) and Concanavalin (ConA), are immobilized on the chip surface through self-assembled monolayers using orthogonal chemistry. After fabrication, the devices following this design can be successfully internalized inside living macrophages without affecting their viability. The results of this work show a well-controlled fabrication, the multi-functional capabilities and no cell-toxicity of intracellular polysilicon-chromium-gold chips.

4.2 Introduction

Nowadays, semiconductor technologies are providing new tools, that extracellularly, can sense and control parameters in cell biology.[1, 2] Relevant examples can be found from chemical to physical applications, for instance, biosensors,[3] diagnosis devices,[4] drug delivery systems[5] or even devices for cell mechanics.[6] By going further and taking advantage of the miniaturization capabilities of micro- and nanotechnologies, researchers are focusing their efforts on manufacturing devices small enough to be internalized inside single living cells.[7, 8] However, to the date, the technological development for most valuable intracellular devices is currently under investigation by many researchers worldwide.[9, 10]

Following this line of research, the Micro and NanoTools group have previously demonstrated that microchips made of only one material, polysilicon, can be fabricated and internalized inside single living cells as intracellular barcodes[11] or as nanomechanical devices[12] always showing a low cellular toxicity. Conversely, the chemical functionalization of these devices opens up new opportunities as intracellular

sensors and actuators in cell biology. For instance, we reported that chemically functionalized silicon chips act as intracellular biomolecular sensors[13] or as extracellular tags which can be adhered to embryos at different development stages.[14–17]

Nano and micromaterials represent huge opportunities for developing new strategies to many scientific challenges.[18, 19] Spatially controlled functionalized surfaces are desirable, and, most of the times, patterning techniques rely mainly on lithographic methodologies: either microcontact printing, photolithography, applied on monomaterial surfaces.[20] Nevertheless, multiple chemical biofunctionalization in a single device, allowing the fabrication of multipurpose tools, still remains a challenge. A different approach consists of performing material selective surface modification, using a combination of orthogonal chemistry[21] on polymaterial substrates. This methodology has been successful using nanoparticles[22] and surfaces,[23, 24] although it presents limitations for protein patterning and it has not been well developed on microfabricated particles.[25]

In order to avoid the inconvenient of applying multi-functionalization procedures to a single-material chip, which could ruin the efficient control on the localization of the different biomolecules, chips composed of several materials are designed, that will then take advantage of orthogonal chemistry functionalization methodologies. Accordingly, microelectronic technologies are highly-suitable candidates for the fabrication of these multi-functional devices as they offer the possibility of depositing or growing many different materials as insulators, semiconductors and metals with high precision, well-known surface chemistry and many of them being biocompatible, generating a solid foundation for them to be used in cell biology applications.

In this chapter we report the technology for the fabrication of chips made from a combination of polysilicon and gold layers through common semiconductor techniques, orthogonally functionalized and bio-compatible (Figure 4.1). Polysilicon and gold, common materials in MEMS industry, are selected as device materials because of their well-known chemistry[14, 26–29] and biocompatibility.[30] In addition, gold has been used widely in chemical and biochemical sensors as a signal transducer based on its unique properties.[31] Nevertheless, one of the main issues in the applicability of gold thin films in microfabrication technology is their weak adhesion to silicon substrates.[32–34] For this reason, we also consider the deposition of a chromium interlayer between the gold and polysilicon layers, due to its efficient capabilities as a material-adherent.[32–35]

Consequently, the intracellular biocompatibility of chromium as such device material should be also evaluated. Thus, a technological development for the fabrication of chips entirely made of chromium and their corresponding cell viability tests are also presented. Then, orthogonal chemistry protocols, using self-assembled monolayers of thiol and silane derivatives, for gold and silicon selective bi-functionalization of a suspension of polysilicon-chromium-gold chips are also developed. Lastly, we investigate the capability of these devices of being cell-internalizable, as well as their biocompatibility inside living cells.

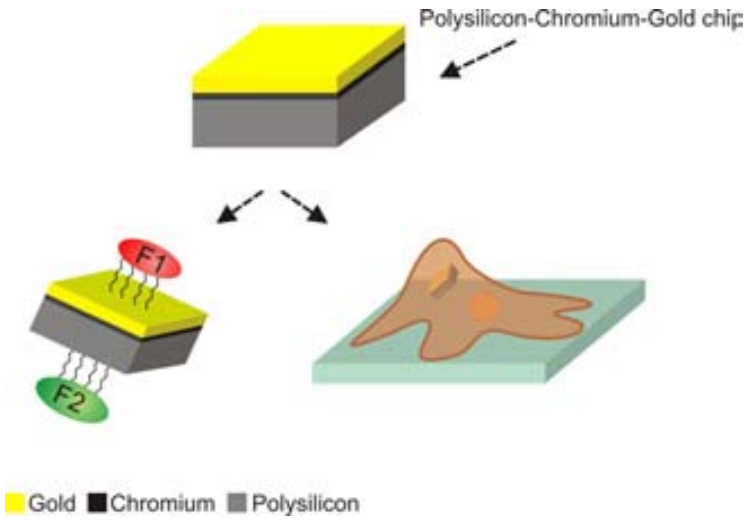

Figure 4.1: **Conceptual representation of chemically multifunctionalized polysilicon-chromium-gold chips for intracellular applications**. Polysilicon and gold layers can be selectively bi-functionalized with two different fluorescently labelled proteins, F1 and F2, giving them a highly specific double functionality. A chromium inter-layer is deposited in between as an efficient adherent layer. In addition, these chips can be internalized inside living cells.

4.3 Mono-Material Polysilicon chips

During the last years the group of Micro and Nanotools of the IMB-CNM (CSIC) have designed a completed line of different silicon microchips to be used as intracellular tools. For instance, 1.5 μm-thick silicon microparticles (Figure 4.2a),[30] 0.5 μm-thick rounded polysilicon microparticles (Figure 4.2b)[30] both of 3 μm in diameter and finally 0.5 μm-thick squared polysilicon microparticles with dimensions 3 μm x 3 μm (Figure 4.2c).[13, 36]

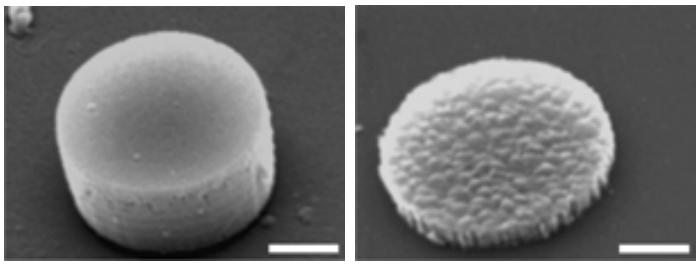

(a) (b)

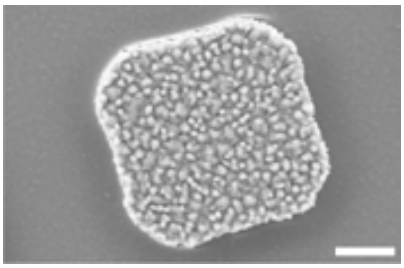

(c)

Figure 4.2: **Design of previous polysilicon-based microchips**. Scanning electron microscopy images of a) a 1.5 μm-thick silicon microparticle, b) a 0.5 μm-thick rounded polysilicon microparticle and c) a 0.5 μm-thick squared polysilicon microparticle. Scale bars = 1 μm.[13, 30, 36]

Despite of the successful results of the polysilicon microchips, a novel line of multi-material chips was devised in order to improve the uses and capabilities of this devices as intracellular tools.

4.4 Preliminary Multi-Material devices: Polysilicon-Gold Chips

4.4.1 Design of Polysilicon-Gold Chips

A preliminary design of a squared polysilicon-gold chip was performed in order to test if the fabrication of a multi-functional tool was possible. The external dimensions of the new chip were fixed to 3.0 μm length, 3.0 μm width and 500 nm thickness, where 400 nm was polysilicon and 100 nm gold (Figure 4.3).

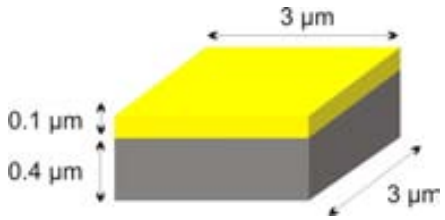

Figure 4.3: **Design and dimensions of preliminary polysilicon-gold chips**. Conceptual representation of a polysilicon-gold chip.

4.4.2 Technological development of Polysilicon-Gold Chips

Before the successfully fabrication of the polysilicon-chromium-gold chips. Several trials were performed in order to find the most suitable parameters of the technological development.

Thus, firstly a novel technology for the fabrication of polysilicon and gold chips was tested. The deposition of 1 μm-thick silicon oxide as a sacrificial layer on a silicon wafer began the fabrication (See figure 4.4a and b). A 400 nm-thick polysilicon layer was deposited (temperature 580°C, pressure 350 mTorr and a SiH_4 flow rate of 40 sccm) on the wafer as first device-layer (See figure 4.4c). A photolithographic step created a photoresist inverse pattern (See figure 4.4d). Next, a 100 nm-thick gold deposition layer was performed as the second device-layer (See figure 4.4e). A lift-off process was carried out in an acetone solution. The target material, in this case gold, remained only in the regions where the material had a direct contact with the polysilicon substrate (Figure 4.4f). A polysilicon dry etching using the gold as a mask material finally defined the chips (Figure 4.4g). And finally, an array of 3 μm

x 3 μm chips separated 3 μm was obtained. Lastly, the chips were released by a silicon oxide sacrificial etching in vapors of 49% HF for 40 minutes, suspended in 96% ethanol, centrifuged at 14000 g for 5 minutes (MiniSpin Plus) and collected in eppendorfs (See figure 4.4h).

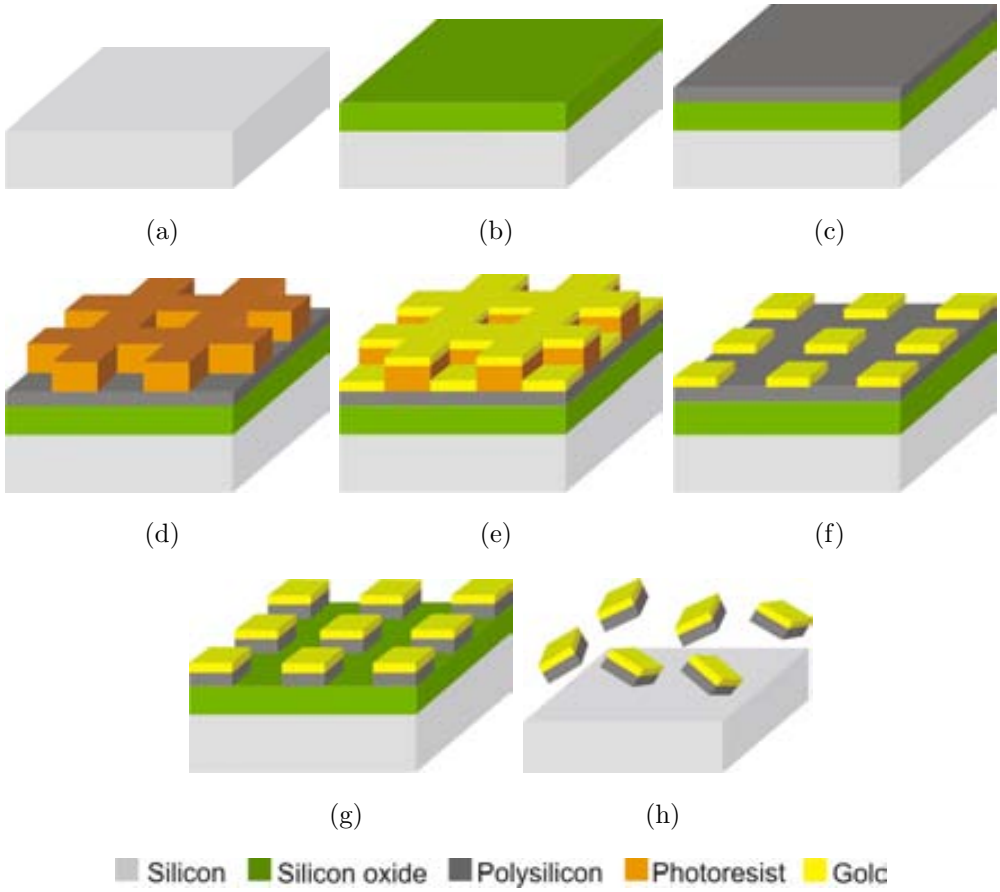

Figure 4.4: **Fabrication process of the polysilicon-gold chips**. a) Devices were fabricated starting from a silicon substrate. b) A 1 μm silicon oxide was deposited as a sacrificial layer and c) a 400 nm polysilicon layer were deposited as a device layer. d) 2 μm-thick photoresist layer was spun and exposed to UV light to define the devices. e) A 100 nm-thick gold layer was deposited as a second-device layer. Then, f) a lift-off process was performed. g) The polysilicon layer was pattern to define the chips. h) The polysilicon-gold devices were released in 49% HF vapors and suspended in ethanol.

4.4.3 Characterization of fabricated Polysilicon-Gold Chips

As it can be observed using scanning electron microscopy (Figure 4.5), the polysilicon etching was not properly performed at the wafer level.

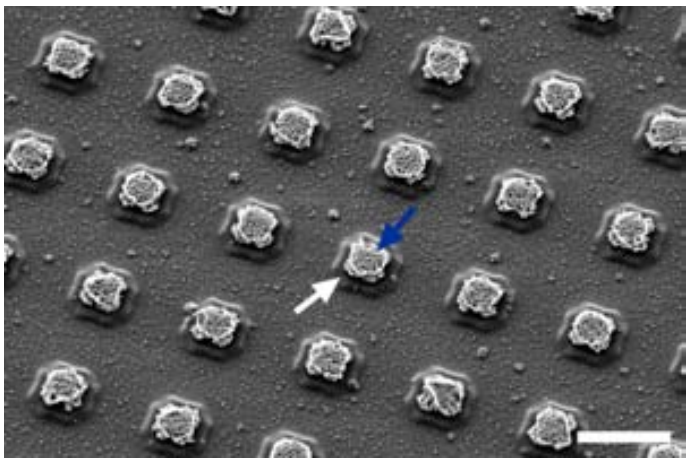

Figure 4.5: **Fabrication results of polysilicon-gold chips**. SEM image of the chips still adhered on the wafer. A ruined polysilicon patterning (white arrow) was obtained due to the non-defined edges of the gold layer (blue arrow). As this material should act as a mask during the polysilicon dry etching and homogenous gold edges were necessary to define the devices. Scale bar = 5 μm.

This could be related to the fact that a non-defined gold layer (blue arrow) was deposited because of the well-known bad and weak adherence between gold and silicon,[32–34] as gold has acted as a mask during the polysilicon dry etching and homogenous edges were necessary to clearly define the devices. All this means that non-robust devices have been obtained. In order to circumvent the difficulty of attaching gold layers to the polysilicon platforms, an intermediated adherent-layer should be deposited in between to improve the adhesion. For instance, titanium and chromium are common materials used as efficient adherents in microelectronics and microsystems technologies. However, in this case, titanium was not suitable due to its non-resistant capability to be etched by concentrated hydrofluoric acid, a key step in the release process of our devices. Therefore, chromium was selected as an adherent material because of its HF-resistance. As a result, metallic chromium cell viability should be evaluated first, as these chips are going to be used as a intracellular sensors and accordingly, chromium microchips were fabricated and their bio-compatibility was analyzed.

4.5 Chromium Chips

4.5.1 Design of Chromium Chips as efficient adherent interlayer

A design of a squared chromium chip was performed in order to test if the fabrication of a chromium chip was possible and to test its bio-compatibility inside living cells. The external dimensions of the new chip were fixed to 3.0 μm length, 3.0 μm width and 100 nm thickness (Figure 4.6).

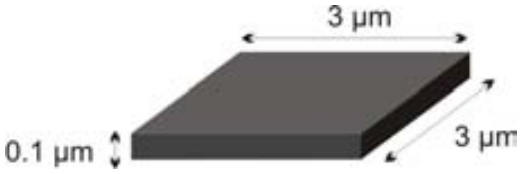

Figure 4.6: **Design and dimensions of chromium chips**. Conceptual representation of a chromium chips chip.

4.5.2 Technological development of Chromium Chips

Following a technological development similar to the one used with the polysilicon-gold chips, we performed a new fabrication process to develope mono-material chips entirely made of chromium.

The fabrication process was initiated by the deposition of 1 μm-thick silicon oxide sacrificial layer on a silicon wafer (Figure 4.7a and b). A photolithographic step defined an inverse photoresist pattern (Figure 4.7c and d). Next, a 100 nm-thick chromium deposition as a device layer was performed (Figure 4.7e). A lift-off process for 30 seconds was carried out to finally define the devices (Figure 4.7f).

Finally, chips were released by a sacrificial etching of the silicon oxide layer in vapors of 49% HF for 40 minutes, suspended in 96% ethanol, centrifuged at 14000 g for 5 minutes (MiniSpin Plus) and collected in eppendorfs (Figure 4.7g).

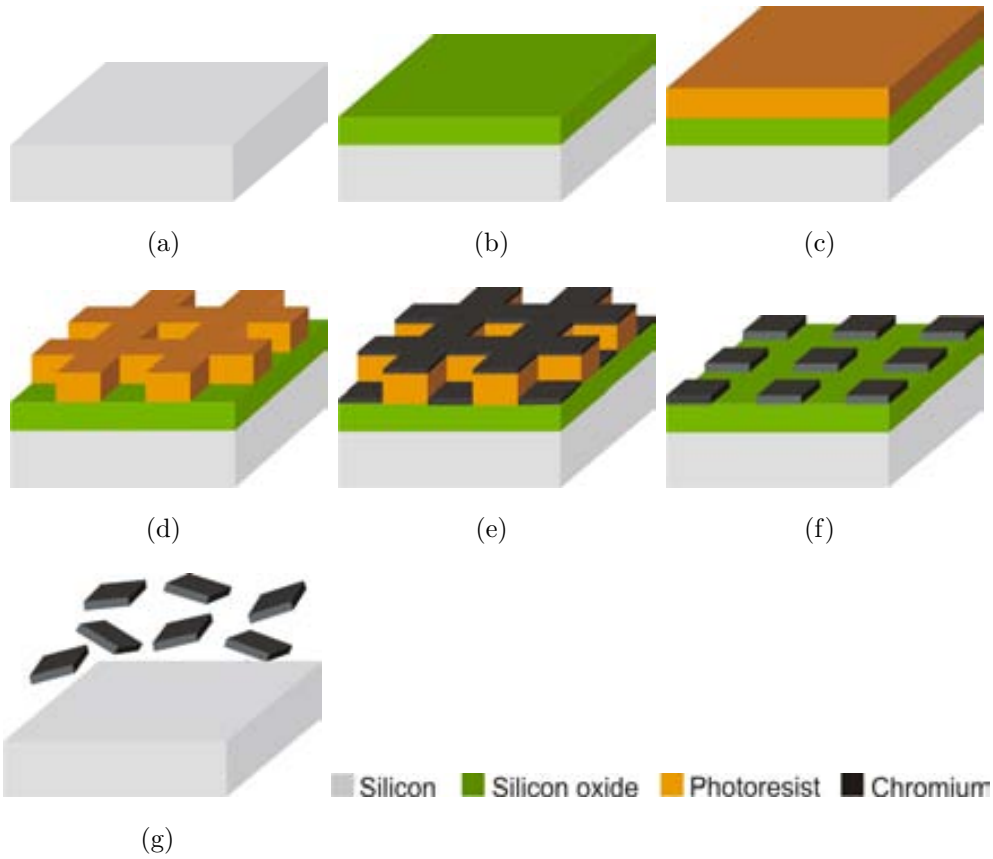

Figure 4.7: **Fabrication process of the chromium chips**. a) Starting from a silicon substrate chromium chips were fabricated. b) A 1 μm silicon oxide was deposited as a sacrificial layer and c) a 2 μm photoresist layer was spun over the surface. d) The photoresist layer was exposed to UV light to define the devices. e) A 100 nm-thick chromium layer was deposited by sputtering process and a f) lift-off process was performed. Finally, g) the chromium devices were released from the wafer in 49% HF vapors and suspended in ethanol.

4.5.3 Characterization of fabricated Chromium Chips

To characterize the chromium chips a combination of a scanning electron microscopy and energy dispersive-X-ray spectroscopy (EDX) methods was carried out. Devices were pipetted in a 2 μL-drop and deposited on a clean silicon substrate for inspection. After solvent evaporation the substrates were observed and characterize on a SEM (Carl Zeiss Auriga - Microscope GmbH, Germany). EDX analysis was also performed on pellets sections for a material identification. Images were captured by an Oxford Instruments IncaX-act SEM and the EDX spectrums were obtained using a PentaFET-Precision attached to the SEM equipment.

Figure 4.8a shows a SEM image of a silicon wafer with 100 nm-thick chromium chips on its surface, demonstrating that thin mono-material chromium chips can be successfully fabricated at the wafer level. Also, figure 4.8b shows several released chromium chips after the sacrificial etching; these devices showed high robustness, homogeneous surface and a perfectly defined shape, in despite of their small thickness.

In the EDX analysis included in Figure 4.8c, the characteristic peak of chromium signal at 0.573 KeV can be observed.

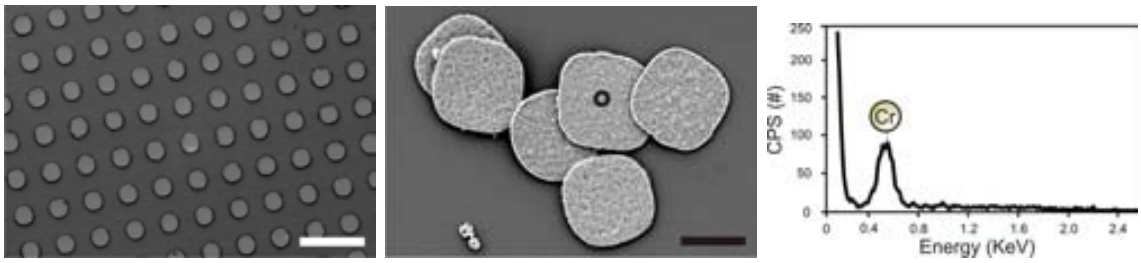

(a) (b) (c)

Figure 4.8: **Fabrication results of chromium chips**. a) SEM image of the chips before and b) after their release. Black encircled area points out where the EDX analysis was performed. c) EDX spectrum confirmed chromium presence. Chromium X-Ray signal can be observed at 0.573 KeV. White scale bar = 10 μm. Black scale bar = 2 μm.

4.5.4 Validation of Chromium Chips as bio-compatible adherent interlayer: Cell-viability tests

(Performed by Department of Cellular Biology, Physiology and Immunology, Universitat Autònoma de Barcelona)

To study chromium chips internalization, living macrophages were seeded in 24-well dishes at a density of 10^5 cells/well, the medium was replaced by fresh culture medium containing chips at a 2:1 chips/cell ratio. At days 1, 3 and 7, viability was assessed by a differential staining for live and dead cells using the LIVE/DEAD Viability/Cytotoxicity Kit for mammalian cells (L3224; Life Technologies).

Briefly, the kit consists of calcein acetomethoxy, which can diffuse through the cell membrane and is converted to highly green fluorescent calcein by intracellular esterases of living cells, and ethidium homodimer-1, which can only penetrate cells with a damaged plasma membrane reaching the nucleus and labeling the DNA of dead cells with red fluorescence. Labeled cells were analyzed under an inverted fluorescence microscope (Olympus IX71, Germany). For each treatment, three independent experiments were performed, counting 250 cells for each one. In addition and in parallel, at days 1, 3 and 7, after the addition of the chips, cells were fixed, dehydrated and dried by a 15 min treatment and observed under a scanning electron microscope (Carl Zeiss Merlin Microscope GmbH, Germany). To determine the localization of the chip (i.e., inside the cells or attached to their plasma membrane), cells were seeded at a density of 10^5 cells/dish on 35 mm diameter glass-bottom coverslip dishes (MatTek Corp, Ashland, MA). After 24 h, cells were stained with TR-WGA (10 μg/ml; Life Technologies) and counterstained with Hoescht 33258 (1 μg/ml; Sigma-Aldrich), to visualize the plasma membrane and the nucleus, respectively. Samples were then examined under a Confocal Laser Scanning Microscope (CLSM: Fluoview FV1000; Olympus Corp, Tokyo, Japan) using a 63 $\times$ oil immersion objective, where x-y-z sequential acquisition was achieved and orthogonal projections of the stacks were evaluated to determine the location of the chip within the cell. For the image analyses, the FV10-ASW Application Software (Ver. 01.07c; Olympus) was used. Statistical analyses were done using SPSS Statistics Ver. 19.0 software (IBM Oregon, USA).

Observation under optical light microscopy and confocal laser scanning microscopy (CLSM) showed that chromium chips were efficiently internalized by cells. Several macrophages with chromium chips can be observed in figure 4.9a, all of them, carrying or not a chip, showed green fluorescence (live cells) under the fluorescent microscope (Figure 4.9b). SEM studies confirmed the normal shape and membrane integrity of macrophages carrying a chromium chip (Figure 4.9c).

Some cells were analyzed by CLSM, where the orthogonal projections of the z-stack reconstruction of consecutive focal planes (0.5 μm each) confirmed the localization of the chips inside the cells (Figure 4.9d and e, respectively).

Finally, no statistically significant differences were found between macrophage cultures incubated with chromium chips during 1, 3 and 7 days and control cultures (Figure 4.9f), demonstrating that the exposure to chromium chips did not interfere in cell viability.

Thus, taken together these results we can conclude that our chips do not affect cell viability. This fact has been well documented by researchers worldwide, as health hazards associated with exposure to chromium are dependent on its oxidation state. For instance, the toxicity and carcinogenic properties of chromium (VI) are known for a long time.[37] However, water insoluble chromium metal (our case of study) is not considered as a toxic material.[38] Accordingly to these results, the use of chromium as adherent layer between polysilicon and gold was probed.

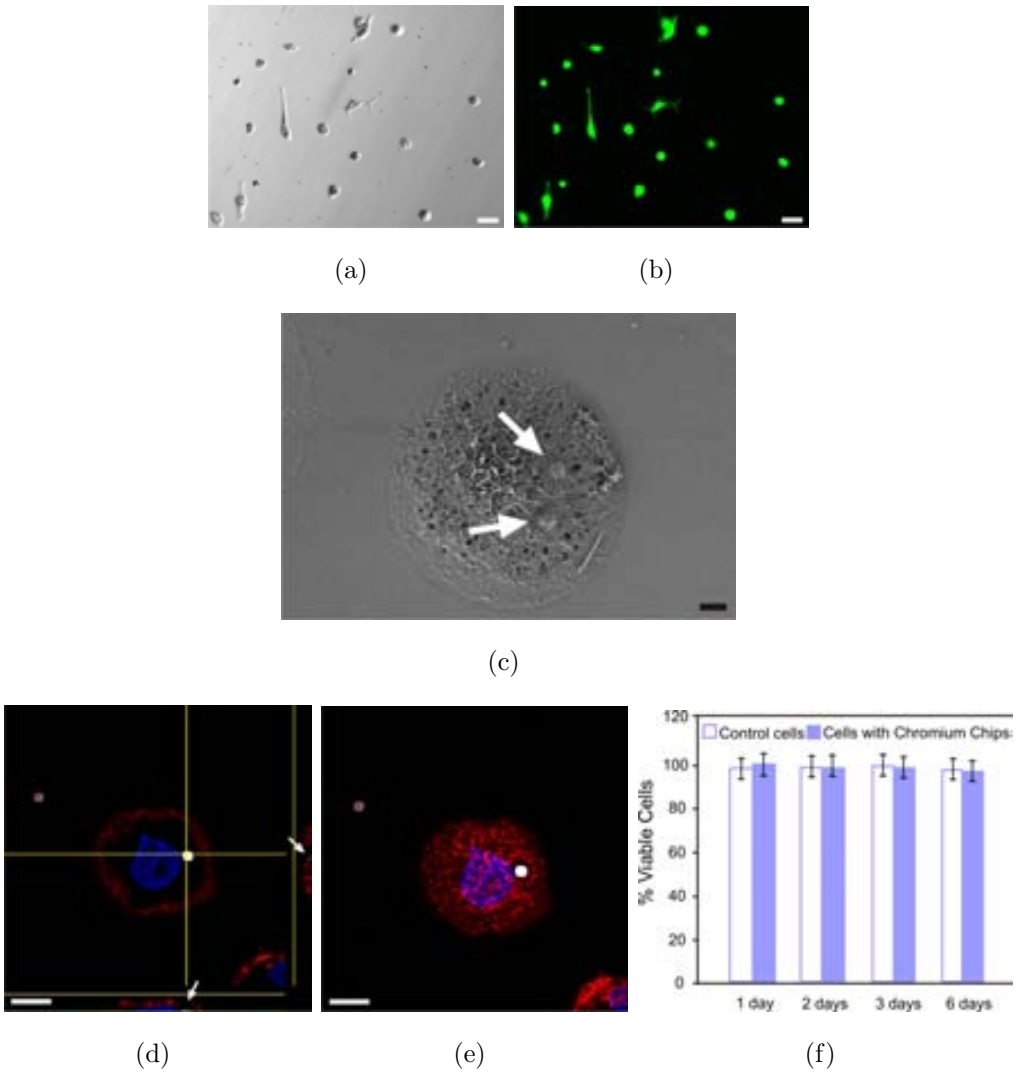

Figure 4.9: **Cell-viability assays with internalized chromium chips**. a) Inverted microscope images of macrophages incubated with chromium chips, nearly all the cells are in contact with a chip. b) The same image under the inverted fluorescence microscope shows that all cells are alive (green cells) and no dead cells (red cells) are observed, using calcein acetomethoxy and ethidium homodimer-1, respectively. Scale bars = 50 μm. c) SEM image of a cell with two internalized chromium chips. Arrows indicate zones where intracellular chips are situated. Scale bar = 5 μm. d) Orthogonal projection of the z-stack reconstructions of consecutive focal planes showing a culture cell with an internalized chip. Chips appear as white spots in confocal laser images due to the higher reflectivity of the polysilicon. White arrows indicate the internalized chip. e) Maximal confocal projection of the same cell taken with CLSM. Scale bars = 10 μm. f) Percentage of viable cells in the presence or absence (control) of chromium chips (Mean ± Standard error of the mean), n = 750.

4.6 Polysilicon-Chromium-Gold Chips

4.6.1 Design of Polysilicon-Chromium-Gold Chips for intracelullar bi-functionalization

A new and revolutionary design of multi-material chips was performed to improve the functional features of the traditional polysilicon chips. In this new design a combination of two main material layers (polysilicon and gold) along with an adherent interlayer (chromium) is presented. The new multi-material chip is a three-dimensional tool, where the external dimensions of the chips were fixed to 3.0 μm length, 3.0 μm width, and 530 nm thickness. The device is a so-called sandwich of polysilicon (400 nm), chromium (30 nm) and gold (100nm), as it can be observed in figure 4.10.

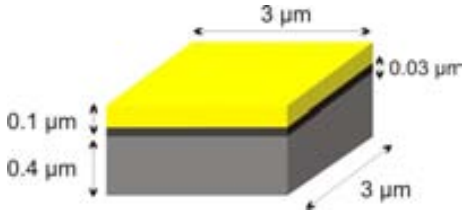

Figure 4.10: **Design and dimensions of new polysilicon-chromium-gold multi-material chips**. Conceptual representation of a polysilicon-chromium-gold chip.

4.6.2 Technological development of Polysilicon-Chromium-Gold Chips

After the bio-compatibility of Cr chips was confirmed, a novel technology for the fabrication of multi-material is presented. Starting from 100 mm p-type silicon wafer (Figure 4.11a), a 1 μm-thick silicon oxide sacrificial layer was deposited (Figure 4.11b). A 400 nm-thick polysilicon layer was performed (temperature 580°C, pressure 350 mTorr and a SiH_4 flow rate of 40 sccm) as a first device layer (Figure 4.11c). Then, a photolithographic step created a photoresist inverse pattern (Figure 4.11d). Then, 30 nm-thick chromium layer (Figure 4.11e) was deposited as adherent interlayer and, finally, a 100 nm-thick gold (Figure 4.11f) deposition defined the second device layer.

Next, a lift-off process was carried out in an acetone solution (Figure 4.11g). A polysilicon dry etching using the gold as a mask material defined the chips (Figure 4.11h). Chips were released by a sacrificial etching of the silicon oxide sacrificial layer in vapors of 49% HF for 40 minutes, suspended in 96% ethanol, centrifuged at 14000 g for 5 minutes (MiniSpin Plus®) (Figure 4.11i). Lastly, chips were collected in eppendorfs.

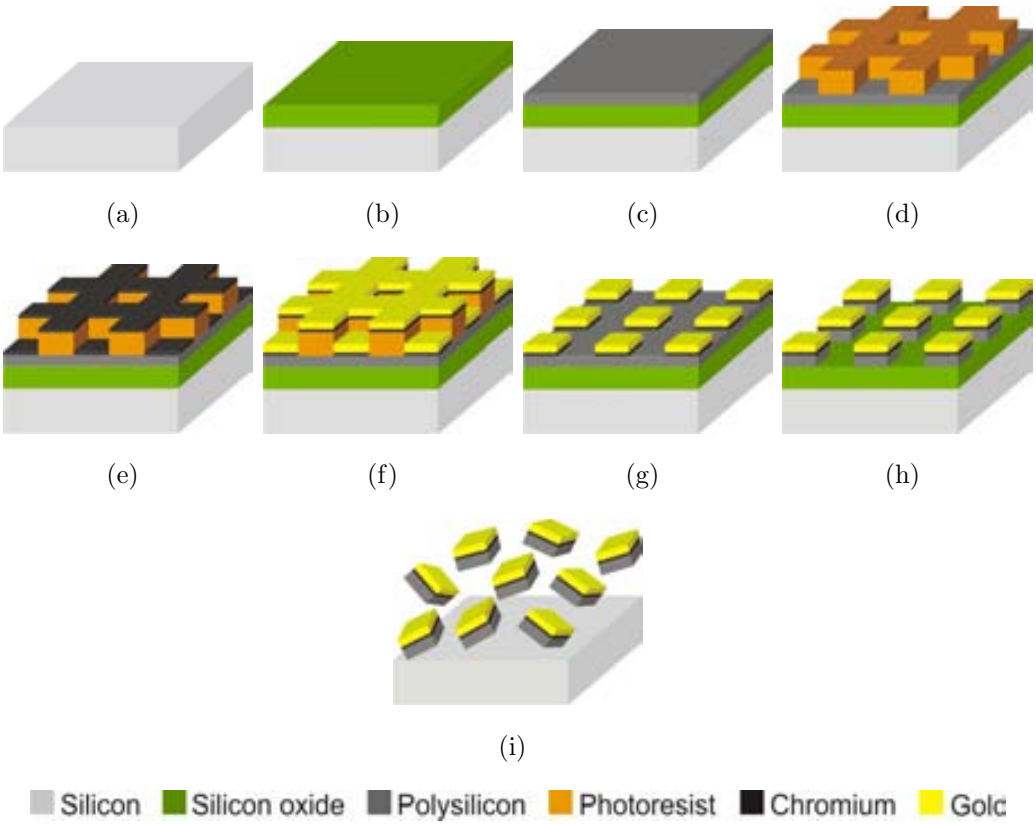

Figure 4.11: **Fabrication process of the polysilicon-chromium-gold chips**. a) Chips were fabricated using a silicon wafer as a starting material. b) A 1 m silicon oxide as a sacrificial layer and c) a 400 nm polysilicon as a first device-layer was deposited. d) A photoresist layer was spun and exposed to UV light to define the dimensions of the devices. e) A 30 nm-thick chromium and f) a 100 nm-thick gold layers were deposited by sputtering process as an adherent and second device-layer, respectively. g) A lift-off process was performed and h) the polysilicon layer was pattern using the chromium and gold layer as a masks. Finally, i) the polysilicon-chromium-gold chips were released in HF vapors and suspended in ethanol.

4.6.3 Characterization of fabricated Polysilicon-Chromium-Gold Chips

Finally, polysilicon-chromium-gold devices with a high versatility and robustness were manufactured.

A SEM image of these chips on the wafer (Figure 4.12a, inset is a zoom image) shows that, in this case, the polysilicon dry etching was perfectly performed, as the gold layer showed a homogenous defined shape. Here, the gold layer was deposited over the chromium layer achieving a good adhesion and ensuring a very robust device.

In figure 4.12b it can be seen the chips after their wafer release, showing their well-defined shape and homogenous surface. EDX analysis was also performed for thorough material identification. The black and red encircled areas in figure 4.12c show the point where the EDX analyses were carried out. The characteristic silicon and gold X-Ray signals were showed at 1.739 KeV and 2.120 KeV, respectively (Figure 4.12d). However, if the X-Ray beam fell on the polysilicon layer or on the gold layer, the chromium signal was not easily revealed, as their small thickness (only 30 nm) was probably masked by the silicon and gold higher signals. Nevertheless, if the EDX spot fell in the middle of the multi-material layer (Figure 4.12e) when the chip is tilted, we can easily recognize the chromium signal at 0.573 KeV, along with the silicon and gold signals at 1.739 KeV and 2.120 KeV, respectively (Figure 4.12f).

Accordingly to these results highly defined polysilicon- gold chips were manufactured using chromium as adherent layer.

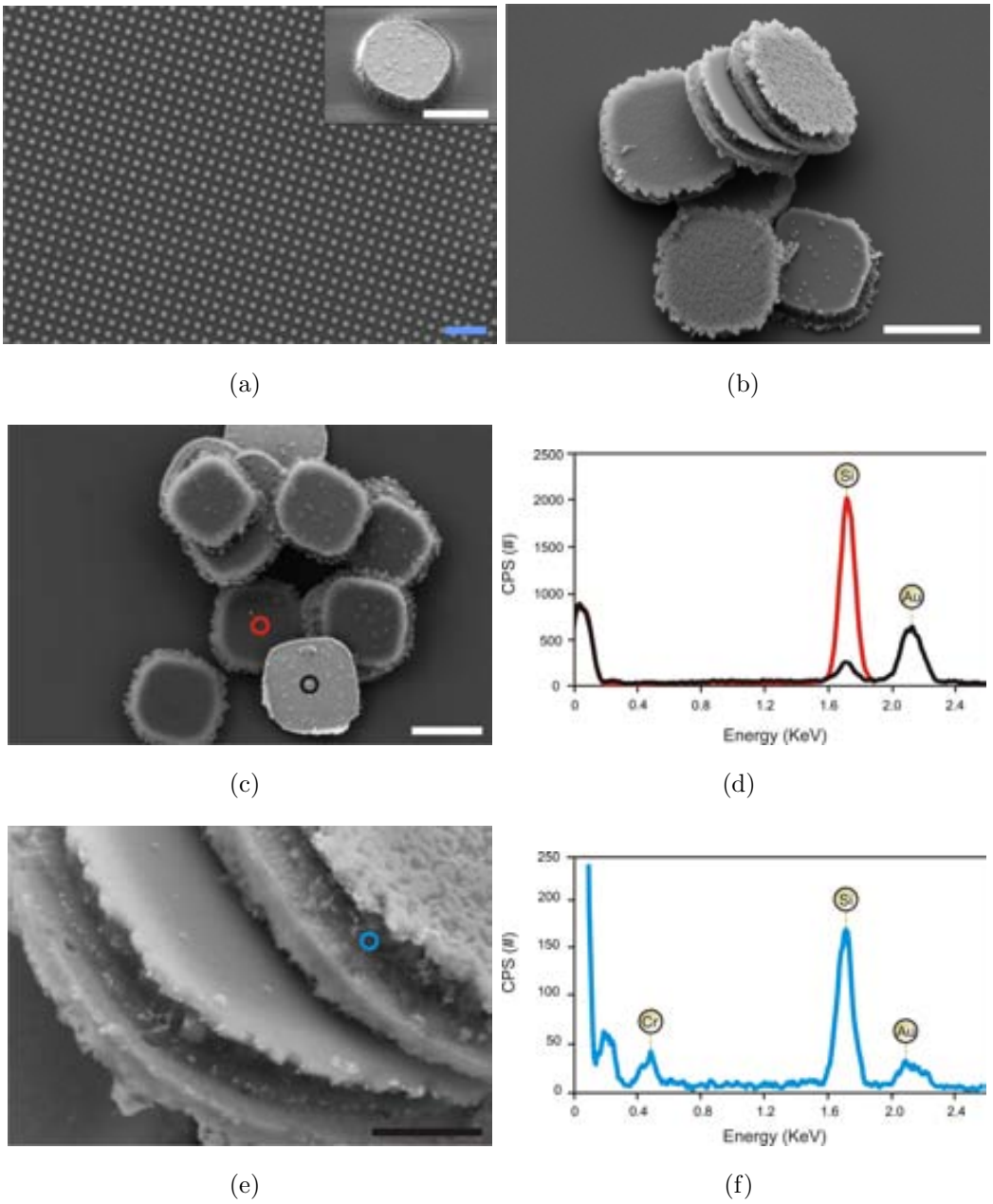

Figure 4.12: **Fabrication results of polysilicon-chromium-gold chips**. a) SEM image of the wafer before (inset is a zoom image) and b) after polyslicon-chromium-gold devices release. c) Released multi-material chips (black and red encircled areas indicate gold and polysilicon layers, respectively, and point out where the EDX analysis were performed). d) EDX spectrum confirmed polysilicon and gold presence. e) Tilted released multi-material chips (blue encircled area indicates chromium layer and where the EDX analysis was performed. f) EDX spectrum confirmed polysilicon, chromium and gold presence. Chromium, polysilicon and gold EDX signals can be observed at 0.573 KeV, 1.739 KeV and 2.120 KeV, respectively. White scale bar = 2 μm . Blue scale bar = 20 μm . Black scale bar = 500 nm.

4.6.4 Chemical studies: Orthogonal functionalization of suspended Polysilicon-Chromium-Gold Chips

(Performed by Department of Pharmacology and Therapeutical Chemistry, Universitat de Barcelona)

After a successful fabrication of multi-material chips, in this section a bi-functional procedure is showed.

Texas Red-WGA (wheat germ agglutinin) and Fluorescein-ConA (concanavalin) double functionalization proceeded following several steps:

1. *Polysilicon activation*: First, polysilicon was oxidized through piranha solution, H_2SO_4:H_2O_2 (7:3), (1 mL) for 1 hour. Next, chips were centrifuged (13000 rpm, 5 min) and they were washed adding Milli-Q water (1 mL x 3), replacing the supernatant in every centrifugation with clean water (Figure 4.13a and b).

2. *Mercaptoundecanoate-NHS SAM formation on gold*: chips were incubated with an ethanol solution of mercaptoundecanoate-NHS (1 mL, 8 mM) for 3 hours and consequently washed using centrifugation with ethanol (1 mL x 3) (Figure 4.13c).

3. *TR-WGA immobilization on the gold layer*: A phosphate buffered saline (PBS) solution of TR-WGA (1 mL, 35 μg/ml) was added to the chip suspension and was kept overnight at room temperature. After that, chips were washed using centrifugation with PBS (1 mL x 3) (Figure 4.13d).

4. *TESUD SAM formation on the polysilicon layer*: an ethanol solution of 11-(Triethoxysilyl) undecanal (TESUD) (1 mL, 135 mM) with an acetic buffer (pH = 5.2) was added to the chips suspension, and they were incubated for 3 hours at room temperature. Then, they were washed with ethanol using centrifugation (1 mL x 3) and finally dried with air (Figure 4.13e).

5. *F-ConA immobilization*: A PBS solution of F-ConA (1 mL, 35 μg/mL) incorporating sodium cyanoborohydride (100 μL, 5 mM) was added to the chips suspension and they were kept overnight at 4°C (Figure 4.13f). Finally, the biofunctionalized chips were washed using centrifugation with PBS (1 mL x 3) and they were kept in fresh water.

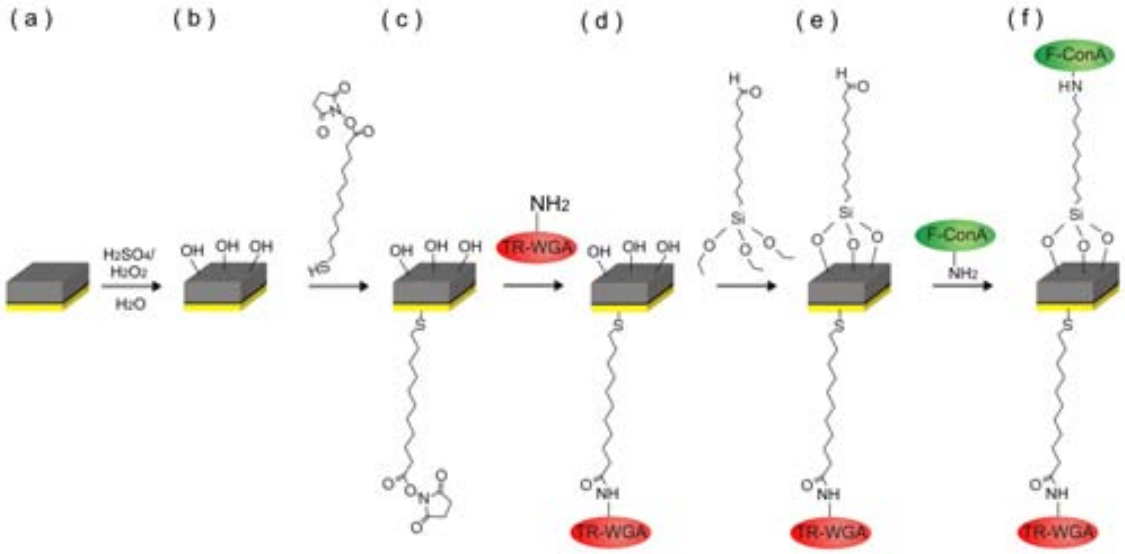

Figure 4.13: **Stepwise formation of double biofunctionalized chips**. a) Polysilicon-Chromium-Gold chip, b) polysilicon activation, c) mercaptoundecanoate-NHS SAM formation on gold, d) TR-WGA immobilization e) TESUD SAM formation on the polysilicon layer and f) F-ConA immobilization.

As probe of concept, multi-material polysilicon-chromium-gold chips were functionalized using orthogonal chemistry. The different chemical reactivity of the gold and the polysilicon substrates prompted us to combine the chemistry of thiols to coat the gold surface[39] and alcoxysilane derivatives[40] to functionalize the polysilicon side. Both the selected thiol and silanes self-assembled monolayers can be efficiently attached on surfaces, and incorporate functional groups capable of establishing covalent bonds with biomolecules, to furnish the microchips with robust multifunctionality. Furthermore, in order to prove the immobilization of different proteins and discard protein interaction defects as aggregation, two different fluorescently labelled lectins were immobilized[41] on the gold as well as on the polysilicon surfaces.

Lectins are proteins that are characteristic for their capacity to interact with different carbohydrates, playing an important role in cellular recognition.[42] Fluorescence microscopy was used to characterize the double biofunctionalized chips. Figure 4.14 shows several biofunctionalized chips in which their fluorescence emission is dependent on the fluorophores tagging the immobilized proteins (Texas-Red for WGA red or Fluorescein for ConA green). In addition, whether the chips show fluorescence or not depends on the functionalized substrate that is located in the

upper part of the standing microchip. It is clearly seen that if the gold substrate is at the top, red fluorescence is detected, whereas if the polysilicon side is at the top, the green fluorescence is observed (Figure 4.14a-c). Moreover, figure 4.14d-f show that the fluorescence emission can be also detected even when chips were partially overlap. Fluorescence images were obtained with a Leica DMIRB inverted fluorescence microscope.

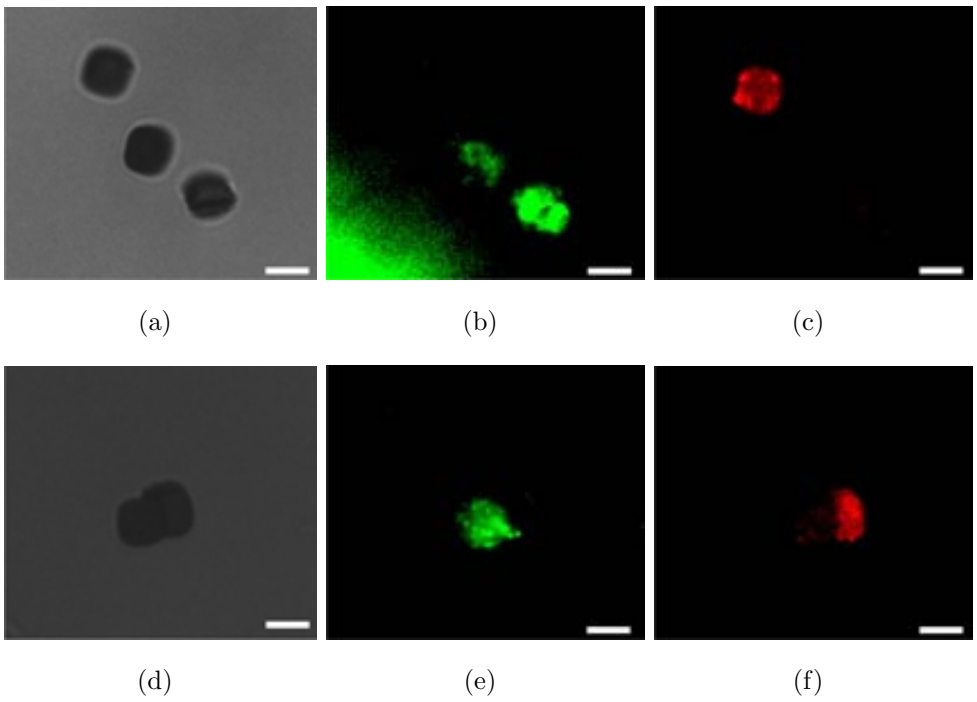

Figure 4.14: **Fluorescence microscopy images of released polysilicon-chromium-gold chips orthogonally functionalized with F-ConA (green) and TR-WGA (red)**. (a-c) Microscopy images of several polysilicon-chromium-gold chips and its correspondings a) optical, b) green and c) red fluorescence microscopy images. (d-f) Overlapping polysilicon-chromium-gold chips and its respectives d) optical, e) green and f) red fluorescence images.

These images evidence the homogenous immobilization of both lectins onto the polysilicon-chromium-gold chips, and prove the possibility of preparing chemically bifunctional microchips.

4.6.5 Validation of Polysilicon-Chromium-Gold Chips as intracellular multi-material devices: Cell-viability tests

(Performed by Department of Cellular Biology, Physiology and Immunology, Universitat Autònoma de Barcelona)

In figure 4.15a and b it can be seen that most of the cells were alive (green fluorescence) when were observed under the fluorescent microscope and that scarce death cells (red cells) can be observed. See section 4.5.4 for further details related to the preparation of the samples.

In order to determine the location of these chips (i.e. if they are attached to the cell membrane or inside the cell), scanning electron microscopy analysis were carried out. SEM images showed that the multi-material chips were successfully phagocyted by macrophages. A macrophage in the process of engulfing a chip, by membrane evaginations, and some phagocyted chips can be seen in figure 4.15c. In addition, cells exposed to chips conserved their normal morphology and membrane integrity. Finally, some cells were analyzed by CLSM to confirm cell internalization. Even the phagocytosis of several chips (macrophages with 3 or more phagocyted chips were observed) did not interfere cell viability (Figure 4.15d and e).

Furthermore, no significant differences were found between macrophage cultures incubated with polysilicon-chromium-gold chips during 1, 3 and 7 days and control cultures (Figure 4.15f), indicating that the incubation of macrophages in presence of polysilicon-chromium-gold chips did not affect significantly cell viability.

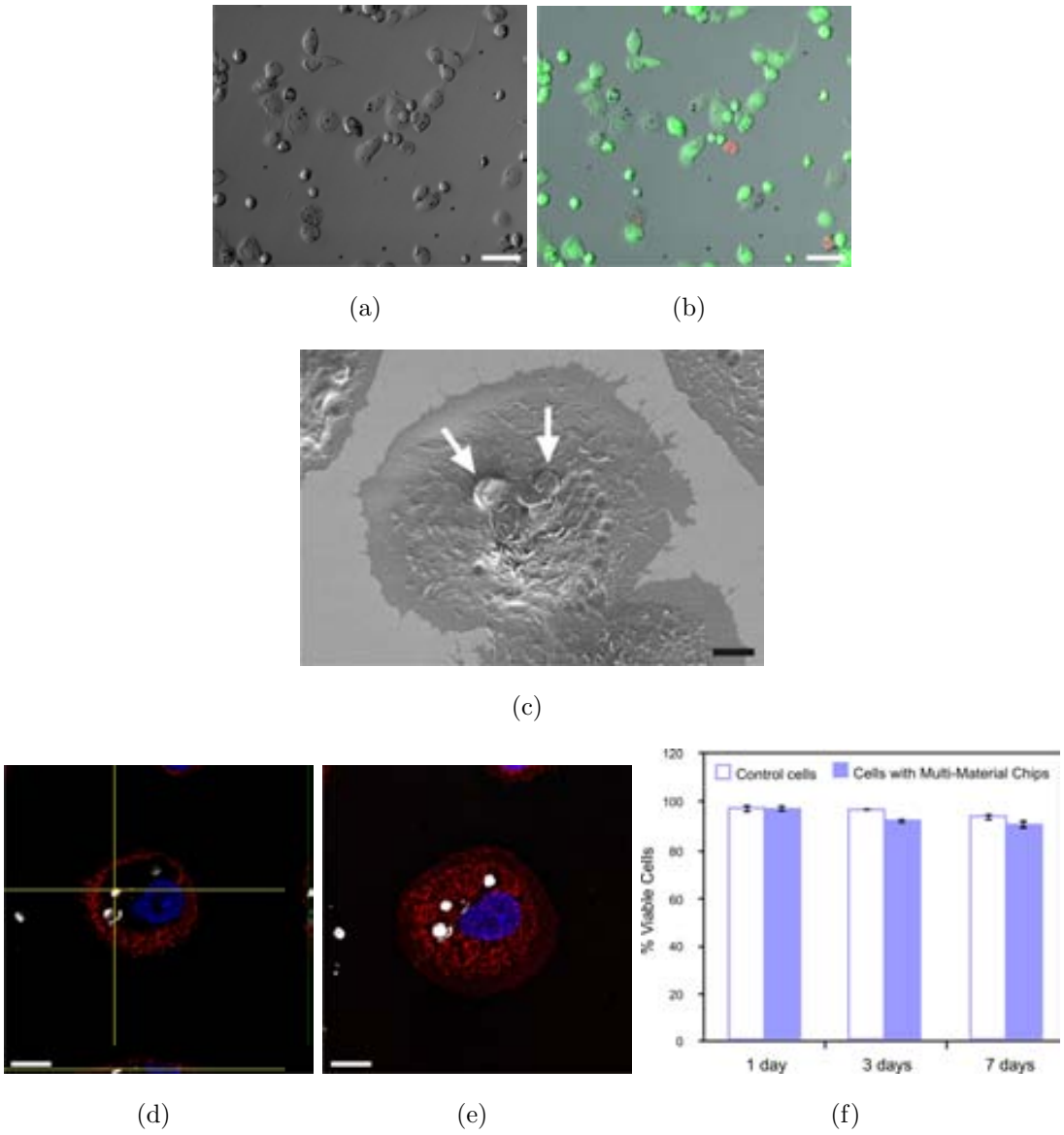

Figure 4.15: **Cell-viability assays with internalized polysilicon-chromium-gold chips**. a) Inverted microscope images of macrophages incubated with polysilicon-chromium-gold chips. b) The same image observed under an inverted fluorescence microscope shows that most of the cells are live (green fluorescence) while scare ones are death (red fluorescence). Scale bars = 50 μm. c) SEM image of a cell with several internalized polysilicon-chromium-gold chips. Arrows indicate zones, where intracellular chips are situated. Scale bar = 5 μm. d) Orthogonal projection of the z-stack reconstructions of consecutive focal planes with several internalized chips. Chips appear as white spots in confocal laser images. e) Maximal confocal projection of the same cell taken with CLSM. Scale bars = 10 μm. f) Percentage of viable cells in the presence or absence (control) of multi-material chips (Mean $\pm$ Standard error of the mean), n = 750.

4.7 Conclusions

In this chapter the fabrication of chemically multi-functionalized Polysilicon-Chromium-Gold chips for intracellular applications has been presented. These devices can be successfully fabricated using semiconductor technologies based on photolithographic techniques.

Polysilicon and gold as device materials were selected because of their high versatility and orthogonal chemistry. However, the well-known weak adhesion of metallic gold to silicon substrates limits its use in this type of devices. To circumvent this fabrication issue, a chromium interlayer was selected to be deposited in between, due to its adherent properties and its high resistance to HF-wet etchings. As a previous step and to confirm the possibility of using metallic chromium to manufacture cell-internalizable devices, chips entirely made of this material were manufactured and their cell-viability was evaluated and confirmed. In the light of these results, an ultra-thin (30 nm) chromium interlayer was deposited in between polysilicon and gold device layers causing a notably increased in the adherence. Finally, robust and perfectly defined polysilicon-chromium-gold chips were fabricated.

In order to provide the multi-material devices with bi-functional capabilities, two different lectins were immobilized. This doubled functionalization was successfully performed using orthogonal chemistry. Fluoresceinamine labelled Concanavalin and the Texas red labeled Wheat Germ Agglutinin were used to selectively bi-functionalize gold and polysilicon layers, respectively, through self-assembled monolayers. Fluorescence microscopy was used for unambiguous characterization of the bi-functionalized chips. Internalization and cell-viability tests with the fabricated chips were also performed to ensure their future applications in cell biology. The obtained results showed high cell viability when they were compared with control cell cultures.

In summary, a simple but effective method to manufacture Polysilicon-Chromium-Gold devices was provided, testing their capability to be chemically multi-functionalized and their cell-viability inside living macrophages.

Bibliography

[1] J. El-Ali, P. K. Sorger, and K. F. Jensen, Cells on chips, *Nature*, vol. 442, pp. 403 411, July 2006. (cited on page(s) 42, 129, 161)

[2] D. B. Weibel, W. R. Diluzio, and G. M. Whitesides, Microfabrication meets microbiology., *Nature reviews. Microbiology*, vol. 5, pp. 209 18, Mar. 2007. (cited on page(s) 129)

[3] A. K. Shalek, J. T. Robinson, E. S. Karp, J. S. Lee, D. R. Ahn, M. H. Yoon, A. Sutton, M. Jorgolli, R. S. Gertner, T. S. Gujral, G. MacBeath, E. G. Yang, and H. Park, Vertical silicon nanowires as a universal platform for delivering biomolecules into living cells, *PNAS*, vol. 107, pp. 1870 1875, Feb. 2010. (cited on page(s) 44, 129, 161, 162, 176, 189)

[4] Y. Hu, D. H. Fine, E. Tasciotti, A. Bouamrani, and M. Ferrari, Nanodevices in diagnostics, *Wiley interdisciplinary reviews. Nanomedicine and nanobiotechnology*, vol. 3, no. 1, pp. 11 32, 2011. (cited on page(s) 129)

[5] K. R. Kam and T. A. Desai, Nano- and microfabrication for overcoming drug delivery challenges, *Journal of Materials Chemistry B.*, vol. 1, pp. 1878 1884, 2013. (cited on page(s) 40, 129)

[6] S. E. Cross, Y. S. Jin, J. Rao, and J. K. Gimzewski, Nanomechanical analysis of cells from cancer patients, *Nature Nanotechnology*, vol. 2, pp. 780 783, Dec. 2007. (cited on page(s) 129, 161)

[7] S. Ferrati, A. Mack, C. Chiappini, X. Liu, A. J. Bean, M. Ferrari, and R. E. Serda, Intracellular trafficking of silicon particles and logic-embedded vectors., *Nanoscale*, vol. 2, pp. 1512 20, Aug. 2010. (cited on page(s) 129)

[8] R. E. Serda, J. Gu, R. C. Bhavane, X. Liu, C. Chiappini, P. Decuzzi, and M. Ferrari, Biomaterials The association of silicon microparticles with endothelial cells in drug delivery to the vasculature, *Biomaterials*, vol. 30, no. 13, pp. 2440 2448, 2009. (cited on page(s) 37, 129)

[9] A. Fulati, S. M. U. Ali, M. H. Asif, N. U. H. Alvi, M. Willander, C. Brannmark, P. Strå lfors, S. I. Borjesson, F. Elinder, and B. Danielsson, An intracellular glucose biosensor based on nanoflake ZnO, *Sensors and Actuators B: Chemical*, vol. 150, pp. 673 680, Oct. 2010. (cited on page(s) 129)

[10] T. F. Otero and J. G. Martinez, Biomimetic intracellular matrix (ICM) materials, properties and functions. Full integration of actuators and sensors, *Journal of Materials Chemistry B*, vol. 1, no. 1, p. 26, 2013. (cited on page(s) 129)

[11] E. Fernández-Rosas, R. Gómez-Martínez, E. Ibanez, L. Barrios, M. Duch, J. Esteve, C. Nogués, and J. A. Plaza, Intracellular polysilicon barcodes for cell tracking, *Small*, vol. 5, pp. 2433 2439, Nov. 2009. (cited on page(s) 49, 53, 54, 69, 97, 129, 161, 178)

[12] R. Gómez-Martínez, A. M. Hernández-Pinto, M. Duch, P. Vázquez, K. Zinoviev, E. J. de la Rosa, J. Esteve, T. Suárez, and J. A. Plaza, Silicon chips detect intracellular pressure changes in living cells, *Nature Nanotechnology*, vol. 8, pp. 517 521, July 2013. (cited on page(s) 129, 161, 176, 178, 179)

[13] R. Gómez-Martínez, P. Vázquez, M. Duch, A. Muriano, D. Pinacho, N. Sanvicens, F. Sánchez-Baeza, P. Boya, E. J. de la Rosa, J. Esteve, T. Suárez, and J. A. Plaza, Intracellular silicon chips in living cells, *Small*, vol. 6, pp. 499 502, Feb. 2010. (cited on page(s) 50, 51, 130, 132, 161, 165, 176, 178, 179)

[14] O. Penon, D. Siapkas, S. Novo, S. Durán, G. Oncins, A. Errachid, L. Barrios, C. Nogués, M. Duch, J. A. Plaza, and L. Pérez-García, Optimized immobilization of lectins using self-assembled monolayers on polysilicon encoded materials for cell tagging, *Colloids and Surfaces B: Biointerfaces*, vol. 116, pp. 104 113, Apr. 2014. (cited on page(s) 130, 201)

[15] S. Novo, R. Morató, O. Penon, and S. Duran, Identification of bovine embryos cultured in groups by attachment of barcodes to the zona pellucida, *Reproduction, Fertility and Development*, vol. 25, no. 1, pp. 218 219, 2013. (cited on page(s) 97, 130, 201, 215, 227)

[16] S. Novo, O. Penon, L. Barrios, C. Nogués, J. Santaló, S. Durán, R. Gómez-Matínez, J. Samitier, J. A. Plaza, L. Pérez-García, and E. Ibánez, Direct embryo tagging and identification system by attachment of biofunctionalized polysilicon barcodes to the zona pellucida of mouse embryos, *Human Reproduction*, vol. 28, pp. 1519 1527, June 2013. (cited on page(s) 84, 85, 86, 97, 130, 201, 215, 227)

[17] S. Novo, C. Nogués, O. Penon, L. Barrios, J. Santaló, R. Gómez-Martínez, J. Esteve, A. Errachid, J. A. Plaza, L. Pérez-García, and E. Ibánez, Barcode tagging of human oocytes and embryos to prevent mix-ups in assisted reproduction technologies, *Human Reproduction*, vol. 29, pp. 18 28, Jan. 2014. (cited on page(s) 97, 130, 201, 215)

[18] S. S. Kelkar and T. M. Reineke, Theranostics: combining imaging and therapy., *Bioconjugate chemistry*, vol. 22, pp. 1879 903, Oct. 2011. (cited on page(s) 130)

[19] O. Crespo-Biel, B. J. Ravoo, D. N. Reinhoudt, and J. Huskens, Noncovalent nanoarchitectures on surfaces: from 2D to 3D nanostructures, *Journal of Materials Chemistry*, vol. 16, no. 41, p. 3997, 2006. (cited on page(s) 130)

[20] P. S. Cremer, Surface Patterning : More than Just Scratching the Surface, *Journal of American Chemical Society*, vol. 133, no. 21, pp. 167 169, 2011. (cited on page(s) 130)

[21] L. Nebhani and C. Barner-Kowollik, Orthogonal Transformations on Solid Substrates: Efficient Avenues to Surface Modification, *Advanced Materials*, vol. 21, pp. 3442 3468, Sept. 2009. (cited on page(s) 130)

[22] H.-Y. Xie, C. Zuo, Y. Liu, Z.-L. Zhang, D.-W. Pang, X.-L. Li, J.-P. Gong, C. Dickinson, and W. Zhou, Cell-targeting multifunctional nanospheres with both fluorescence and magnetism., *Small*, vol. 1, pp. 506 509, May 2005. (cited on page(s) 130)

[23] M. Veiseh, M. H. Zareie, and M. Zhang, Highly Selective Protein Patterning on Gold - Silicon Substrates for Biosensor Applications, *Langmuir*, vol. 14, no. 7, pp. 6671 6678, 2002. (cited on page(s) 130)

[24] E. Briand, V. Humblot, J. Landoulsi, S. Petronis, C.-M. Pradier, B. Kasemo, and S. Svedhem, Chemical modifications of Au/SiO2 template substrates for

patterned biofunctional surfaces., *Langmuir : the ACS journal of surfaces and colloids*, vol. 27, pp. 678 85, Jan. 2011. (cited on page(s) 130)

[25] L. Tang and J. Cheng, Nonporous Silica Nanoparticles for Nanomedicine Application., *Nano today*, vol. 8, pp. 290 312, June 2013. (cited on page(s) 130)

[26] M. Nordstrom, A. Johansson, E. S. Noguerón, B. Clausen, M. Calleja, and A. Boisen, Investigation of the bond strength between the photo-sensitive polymer SU-8 and gold, *Microelectronic Engineering*, vol. 78-79, pp. 152 157, Mar. 2005. (cited on page(s) 130)

[27] J. Fan and P. K. Chu, Group IV nanoparticles: synthesis, properties, and biological applications, *Small*, vol. 6, pp. 2080 2098, Oct. 2010. (cited on page(s) 130, 178)

[28] T. Shirman, R. Kaminker, D. Freeman, and M. E. van der Boom, Halogen-bonding mediated stepwise assembly of gold nanoparticles onto planar surfaces., *ACS nano*, vol. 5, pp. 6553 63, Aug. 2011. (cited on page(s) 130)

[29] P. Pyykko, Theoretical chemistry of gold., *Angewandte Chemie*, vol. 43, pp. 4412 56, Aug. 2004. (cited on page(s) 130)

[30] E. Fernández-Rosas, R. Gómez-Martínez, E. Ibanez, L. Barrios, M. Duch, J. Esteve, J. A. Plaza, and C. Nogués, Internalization and cytotoxicity analysis of silicon-based microparticles in macrophages and embryos, *Biomedical Microdevices*, vol. 12, pp. 371 379, June 2010. (cited on page(s) 50, 51, 70, 84, 97, 130, 132, 183)

[31] D. Wilson, S. Hoyt, J. Janata, K. Booksh, and L. Obando, Chemical sensors for portable, handheld field instruments, *IEEE Sensors Journal*, vol. 1, no. 4, pp. 256 274, 2001. (cited on page(s) 130)

[32] M. A. George, W. S. Glaunsinger, T. Thundat, and S. M. Lindsay, Electrical, spectroscopic, and morphological investigation of chromium diffusion through gold films, vol. 189, pp. 59 72, 1990. (cited on page(s) 130, 135)

[33] R. Audino, G. Destefanis, F. Gorgellino, E. Pollino, and S. Tamagno, Interface behaviour evaluation in Au/Cr, Au/Ti and Au/Pd/Ti thin films by means of resistivity and stylus measurements, *Thin Solid Films*, vol. 36, no. 1916, pp. 343 347, 1975. (cited on page(s) 130, 135)

[34] K. D. Kang, R. R. Burgess, M. G. Coleman, J. G. K. Ieee, and T. Electron, A Cr - Ag - Au metalization system, *IEEE Transactions on Electron Devices*, vol. 16, pp. 356 360, 1969. (cited on page(s) 130, 135)

[35] N. R. Moody, D. P. Adams, D. Medlin, T. Headley, and N. Yang, Effects of diffusion on interfacial fracture of gold-chromium hybrid microcircuit films, *International Journal of Fracture*, vol. 119, pp. 407 419, 2003. (cited on page(s) 130)

[36] O. Penon, S. Novo, S. Durán, E. Ibanez, C. Nogués, J. Samitier, M. Duch, J. A. Plaza, and L. Pérez-García, Efficient biofunctionalization of polysilicon barcodes for adhesion to the zona pellucida of mouse embryos, *Bioconjugate chemistry*, vol. 23, pp. 2392 2402, Dec. 2012. (cited on page(s) 71, 87, 132, 161, 178, 201)

[37] D. G. Barceloux, Chromium toxicity, *Clinical Toxicology*, vol. 2, no. 37, pp. 173 194, 1999. (cited on page(s) 140)

[38] L. Kanerva and A. Aitio, Dermatotoxicological aspects of metallic chromium, *European Journal of Dermathology*, vol. 7, no. 2, pp. 79 84, 1997. (cited on page(s) 140)

[39] J. C. Love, L. a. Estroff, J. K. Kriebel, R. G. Nuzzo, and G. M. Whitesides, *Self-assembled monolayers of thiolates on metals as a form of nanotechnology.*, vol. 105. Apr. 2005. (cited on page(s) 147)

[40] C. Haensch, S. Hoeppener, and U. S. Schubert, Chemical modification of self-assembled silane based monolayers by surface reactions., *Chemical Society reviews*, vol. 39, pp. 2323 34, June 2010. (cited on page(s) 147)

[41] L. S. Wong, F. Khan, and J. Micklefield, Selective covalent protein immobilization: strategies and applications., *Chemical Reviews*, vol. 109, pp. 4025 53, Sept. 2009. (cited on page(s) 46, 147)

[42] H. Lis and N. Sharon, Lectins : Carbohydrate-Specific Proteins That Mediate Cellular Recognition †, *Chemical Reviews*, vol. 98, pp. 637 674, 1998. (cited on page(s) 147)

Chapter 5

Nanowire Silicon Chips for intracellular applications

Contents

5.1 Abstract

In this chapter, a technology for the integration of silicon nanowires on cell-internalizable polysilicon chips for future advanced intracellular devices is presented. Micrometer-sized silicon chips have been demonstrated to be cell-internalizable and more importantly to be cell-viable, offering the possibility of incorporating even smaller features at the nanoscale for intracellular advanced applications. Conversely, silicon nanowires integrated on extracellular devices have been widely reported as biosensors or drug delivering systems. The presented intracellular devices will combine the functional features of both approaches fabricating silicon nanowire chips. After fabrication, the cellular uptake in HeLa cells of silicon nanowire-based chips with two different morphologies (micro and nanosizes) is investigated and the results are compared with those of non-nanostructured chips. A positive chip-internalization without affecting cell viability is achieved in all cases, however, important cell behavior differences are observed. In particular, the first stage of cell-internalization is favored by silicon nanowire interfaces in contrast to bulk silicon.

5.2 Introduction

Increasingly, advances in miniaturization technologies are providing new tools to study fundamental issues in cell biology.[1–4] For instance, integrated microdevices with nanosized parts offer a huge potential to develop extracellular sensors for cell mechanics[5] or invasive biomolecular tools for drug delivery and diagnosis.[6, 7] However, micro and nanochips have revealed too an enormous potential for intracellular applications, as they are small enough to allow their cell-internalization.

Thanks to the capability of silicon technologies to produce nanostructured chips smaller than cells, our group have previously demonstrated that intracellular chips can be used for single-cell labelling,[8, 9] biomolecular recognition,[10] and more recently, for cell mechanics.[11] But on the other hand, the incorporation of semiconductor nanowires on different devices[12–14] have a vast range of potential uses, for instance, in advanced field effect transistor applications,[15–17] or nanomechanics.[18, 19] Furthermore, nanowire devices have been proved to transduce chemical and biological binding events into electronics suggesting the potential for a highly sophisticated interface

for biological information.[20–23] Accordingly, extracellular or invasive devices with integrated silicon nanowires have demonstrated their capability in many potential applications in cell biology. As relevant examples, they have been used for delivering biomolecules into living cells by using the ability of vertical silicon nanowires to penetrate the cell membrane,[6, 7] as efficient capturer of circulating tumor cells by nanopillar arrays[24, 25] or for localized single-cell electroporation,[26] or even it has been reported that individual and disaggregated silicon nanowires can be internalized inside cells.[27, 28] However, the small size of isolated nanowires limits their prospective application inside living cells due to their difficult intracellular visualization, its small surface-area for molecular delivery and the fact that it is difficult to implement a real transduction principle for sensing applications. In contrast, silicon nanowires integrated on planar silicon chips have been demonstrated to offer innovative possibilities for a wide range of applications.[29] Thus, the prospect of obtaining silicon nanowire chips smaller than cells will open new opportunities in intracellular biology.

In this chapter a technology for the fabrication of two different designs of silicon nanowire chips based on standard semiconductor techniques combined with a vapor-liquid-solid mechanism (VLS) for the nanowires growth is showed. To demonstrate the cell-viability and cellular uptake of these polysilicon chips we use a combination of correlative light and electron microscopy techniques. The results also show the fact that the morphology of the chips can affect the initial stage of their cell-internalization as the basis for future applications.

5.3 Design of Silicon Nanowire Chips and Isolated Silicon Nanowire Meshes as nano-patterned devices for intracellular applications

Two revolutionary designs of silicon nanowire chips were performed to improve the functional features of our traditional polysilicon chips (see section 4.3 and figure 4.2). In these new designs we complemented the mono-material polysilicon chips with a random mesh of silicon nanowires directly grown on the chip´s surface. Randomly oriented nanowires are obtained because of the roughness of the polysilicon surface. Polysilicon is composed of silicon crystals (nanocluters at the initial stage of polysilicon deposition and subsequently grains as time goes by) which have random crystallographic orientations and will affect the direction of the grown nanowires afterwards. In addition, taking advantage of the polysilicon nucleation at nanometer-scale which allows the formation of small nanoclusters at the initial stage of the deposition,[30] two types of silicon nanowires devices are devised. First, we reproduce the same conditions followed to obtain our tradition polysilicon chips combined with the nanowire growth, but in addition we explore the possibility of obtaining a brand new design completely into the nanoscale. Hence, we will shorten the polysilicon deposition time as much as possible. Thus, a nanometric polysilicon nanocluster mesh is obtained and it will be used as nano-platform for the nanowire growth. See figure 5.1a for the nanoplatform formation and 5.1b for the micro one.

The main advantage of having silicon nanowires featuring polysilicon chips is a broad number of applications, such as intracellular sensing through the chemical functionalization of the silicon nanowires or the operation of silicon nanowire chips as intracellular drug delivery systems. In the first presented design (Silicon Nanowire Chips) the main material was a layer of polysilicon, where the external dimensions were fixed to 3.0 μm length, 3.0 μm width and 500 nm thickness (Figure 5.2a). While in the second one (Isolated Silicon Nanowire Meshes) the polysilicon main layer was reduced to the minimum possible thickness and only a 65 nm-thick polysilicon layer (formed by hundreds of polysilicon nanoclusters) was used as a platform for the posterior silicon nanowire growth (Figure 5.2b). These two tools were also fabricated with the main objective of comparing their different fabrication results and cell-internalizations, both depending on the shape and size of the devices.

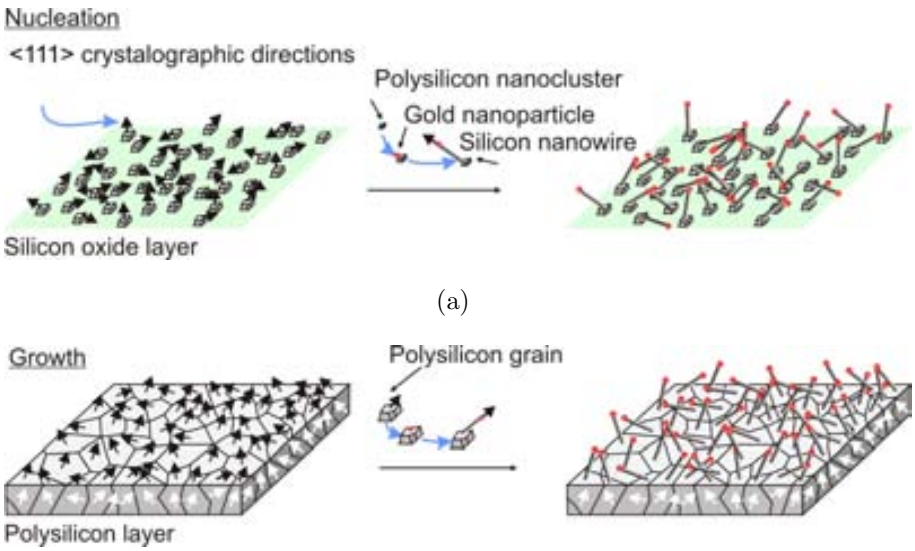

Figure 5.1: **Polysilicon film formation: Nucleation and growth**. a) At the initial stage of the polysilicon deposition a mesh formed of polysilicon nanoclusters is obtained. The different orientations of the nanoclusters induce a random growth of the silicon nanowires. b) However if the deposition process continues the nanoclusters will become into grains forming a continuous layer. And what occurs with the nanoclusters, the different orientation of the grains induces a random growth of the nanowires. Black arrows indicate crystallographic orientations.

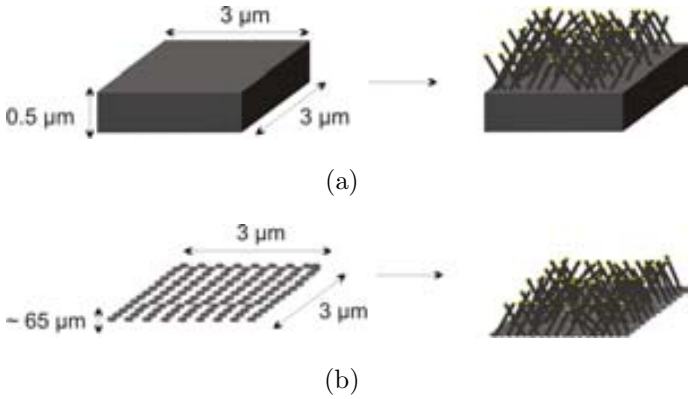

Figure 5.2: **Design of Silicon Nanowire Chips and Isolated Silicon Nanowire Meshes**. Design and dimensions of a) silicon nanowire chips and b) isolated silicon nanowire meshes.

5.4 Polysilicon Chips

5.4.1 Technological development of Polysilicon Chips

Firstly, a fabrication technology to obtain polysilicon chips (SiμC) without nanowires as non-nanostructured control devices is developed.[10] A 1 μm-thick silicon oxide layer on a silicon wafer defined the initial substrate (Figure 5.3a). 500 nm-thick polysilicon layer deposition as main material was carried out (Figure 5.3b). A photolithographic step (Figure 5.3c and d) combined with a polysilicon dry etching (Figure 5.3e) were performed to obtain the devices. A photoresist removal was carried out to finally obtain an array of 3 μm x 3 μm chips separated 3 μm (Figure 5.3f). Eventually, chips were released by a 40 min-sacrificial etching of the silicon oxide layer in vapors of 49% HF (See Figure 5.3g), suspended in 96% ethanol, centrifuged at 14000 g for 5 minutes (MiniSpin Plus) and collected in eppendorfs for posterior cell studies.

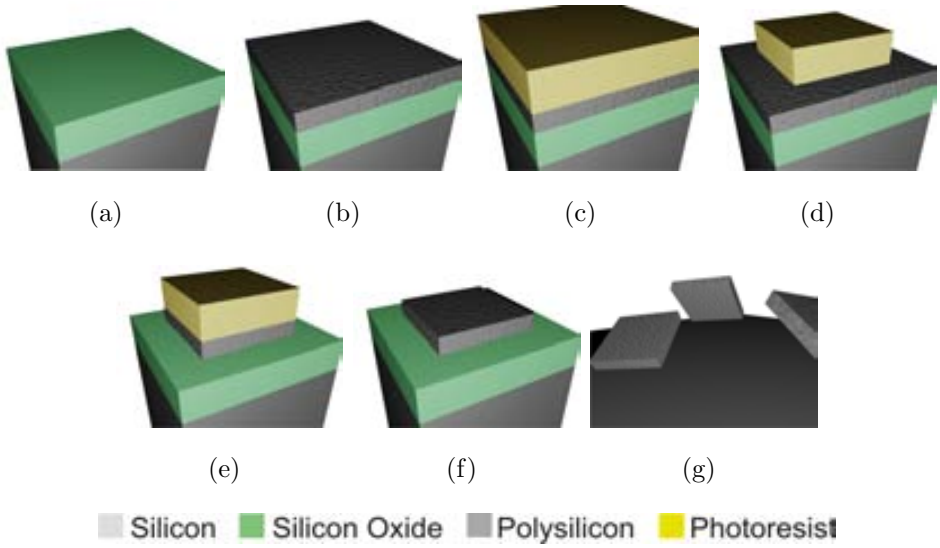

Figure 5.3: **Fabrication of the polysilicon chips**. a) A 1 μm-thick silicon oxide layer was grown as sacrificial layer. b) A 500 nm-thick polysilicon layer was deposited by chemical vapor deposition. c) A 1.2 μm-thick positive photoresist was spun onto the wafers. d) The photolithographic step defined the lateral dimensions of the chips. e) Etching away the exposed polysilicon defined the engineered particles. f) Photoresist stripping. g) The sacrificial etching in 49% HF vapors released the SiμCs from the wafer.

5.4.2 Characterization of fabricated Polysilicon Chips

After a successfully fabrication process non-nanostructured polysilicon chips were obtained. As it can be seen in figure 5.4, right-side-up and bottom-side-up sides of SiμCs did not reveal any relevant morphological difference between them. This fact is relevant, as I describe later, for their cell-internalization.

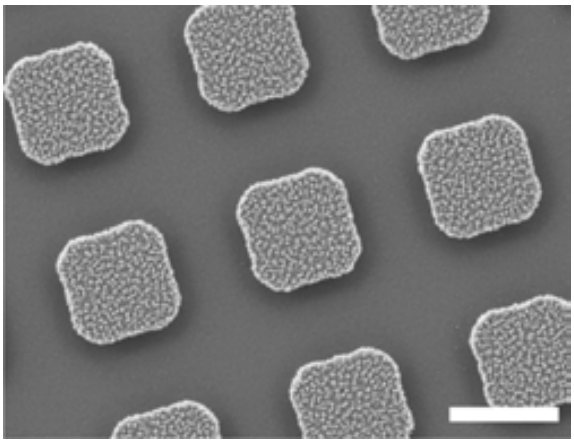

(a)

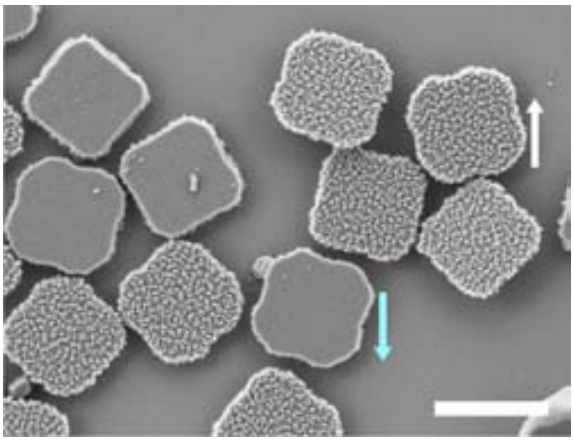

(b)

Figure 5.4: **Fabrication results of the polysilicon chips**. Scanning electrom microscopy images of the fabricated chips (a) still on the wafer and (b) after their release. Arrows indicated the chip orientation (white: right-side up, blue: down-side up). Scale bars = 3 μm.

5.5 Silicon Nanowire Chips

5.5.1 Technological development of Silicon Nanowire Chips

In this section a fabrication technology to obtain silicon nanowire chips (SiμC+SiNWs) with well-controlled dimensions is shown. These chips were fabricated using semiconductor technologies based on photolithographic techniques, in combination with a bottom-up silicon nanowire growth for a high aspect ratio nanostructure. The first steps of the SiuμC+SiNWs fabrication process were similar to those performed for SiμC. A 1 μm-thick silicon oxide layer on a 100 mm p-type silicon wafer defined the sacrificial layer (Figure 5.5a). A 500 nm-thick polysilicon layer deposition (Figure 5.5b), a photolithographic step (Figure 5.5c and d) and a polysilicon dry etching (Figure 5.5e) define the devices. An array of 3 μm x 3 μm chips separated 3 μm was obtained (Figure 5.5f). Later, a nanowire growth process *(Performed by NEMS and Nanofabrication Group, IMB-CNM, CSIC)* was performed by taking advantage of the galvanic displacement deposition method that ensures gold catalyst nanoparticle deposition only at silicon surfaces (Figure 5.5g).[31] Gold nanoparticles were selectively deposited on the polysilicon chips surfaces by immersing the substrates in a reverse micellar microemulsion. The microemulsion was synthetized by mixing an aqueous plating solution with n-heptane and a surfactant, sodium bis(2-ethylhexyl) sulfosuccinate (AOT, $C_{20}H_{37}O_7SNa$). The aqueous solution consists of 0.2 M HF and 0.01 M $KAuCl_4$, while the AOT/heptane solution is made by dissolving 0.33 M AOT in n-heptane. Micellar diameter is determined by the water-to-surfactant molar ratio, R = $[H_2O]$/[AOT] according to the empiric law Rm = 0.175R + 1.5.[31] A molar ration of R = 20 and an immersion time of 10 s - 30 s were used. Silicon nanowires were grown via the vapor liquid solid mechanism (VLS) (Figure 5.5h), which is one of the most commonly used route for semiconductor nanowire production.[32] The growth process was performed in a homemade CVD at 750°C - 800°C and atmospheric pressure. A 10% H_2 in Ar was used as both diluent and carrier gas. Flow rates of 270 sccm and 40 sccm - 50 sccm were used, respectively. The carrier gas was passed through a liquid $SiCl_4$ bubbler kept at 0°C to maintain constant vapor pressure. Lastly, chips were released by a 40 min-sacrificial etching of the silicon oxide layer in vapors of 49% HF (Figure 5.5i), suspended in 96% ethanol, centrifuged at 14000 g for 5 minutes (MiniSpin Plus) and collected in eppendorfs for posterior cell studies.

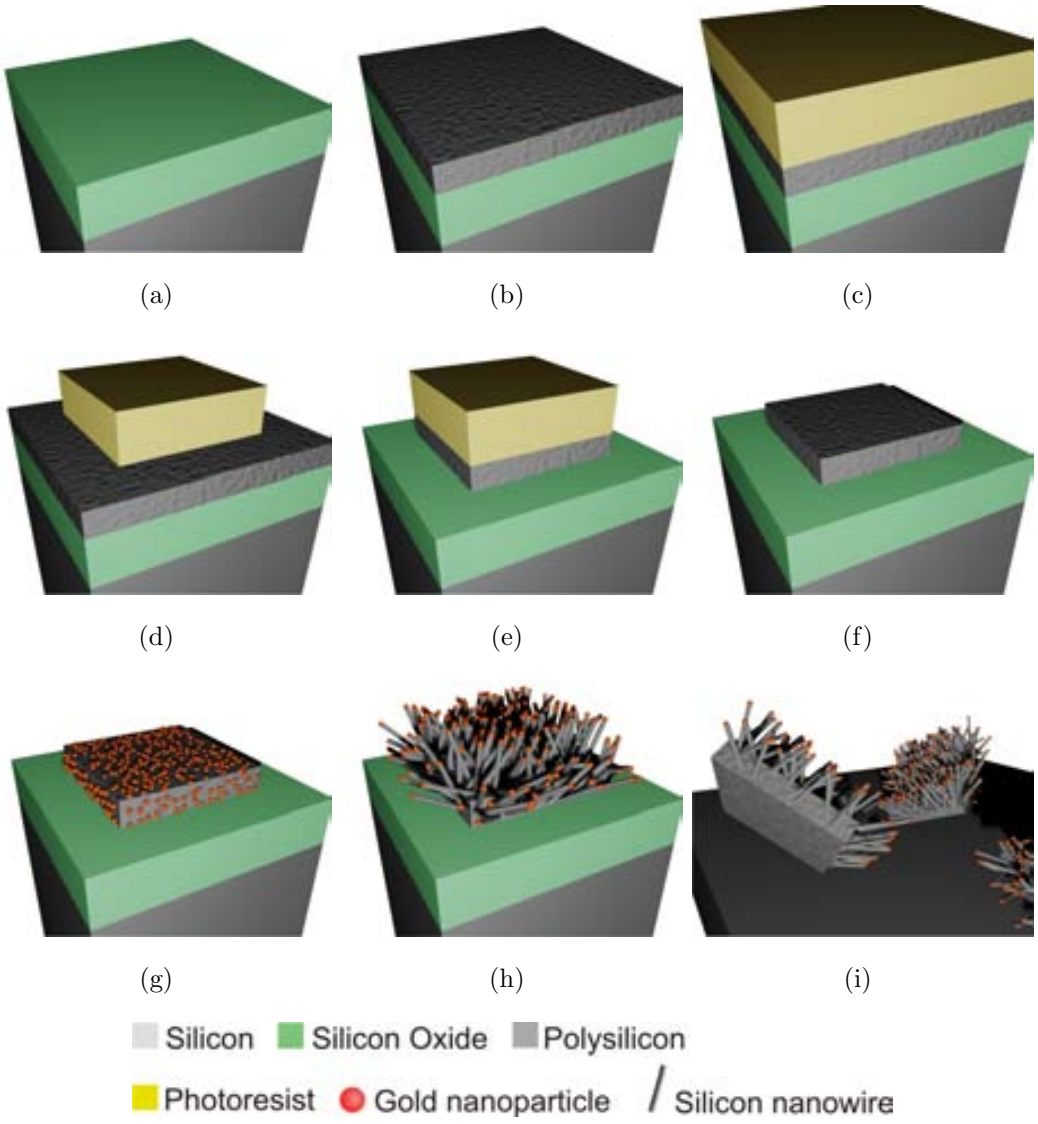

Figure 5.5: **Fabrication process of silicon nanowire chips**. a) A 1 μm-thick silicon oxide layer was grown as sacrificial layer. b) A 500 nm-thick polysilicon layer was deposited by chemical vapor deposition. c) A 1.2 μm-thick positive photoresist was spun onto the wafers. d) The photolithographic step defined the lateral dimensions of the chips. e) A polysilicon etching defined the particles. f) Photoresist removal. g) A galvanic displacement deposition of gold nanoparticles were deposited on the SiμC. h) Silicon nanowires were grown by the VLS method. i) A sacrificial etching in 49% HF vapors was performed to release the SiμCs+SiNW from the wafer.

5.5.2 Characterization of fabricated Silicon Nanowire Chips

After a successful fabrication process the obtained SiμCs+SiNW were analized by scanning electron microscopy. And it can be seen in figure 5.6, the right-side-up and bottom-side-up sides of the chips revealed relevant morphological differences, as one of side was nano-structured and the other one not. And as what occurs with the SiμCs this fact will be relevant for their posterior cell-internalization due to their different shape and size.

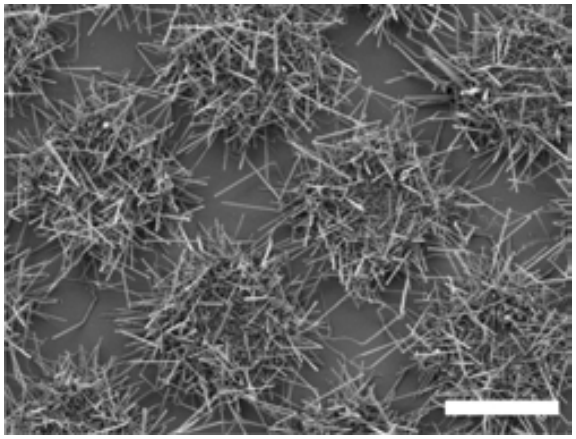

(a)

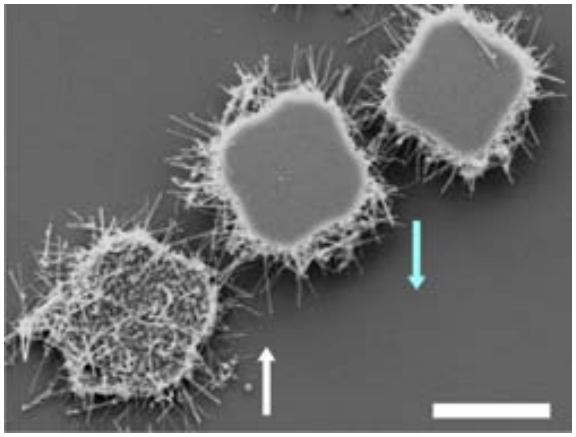

(b)

Figure 5.6: **Fabrication results of the silicon nanowire chips**. Scanning electrom microscopy images of the fabricated chips. SiuC+SiNWs (a) still on the wafer and (b) after their release. Arrows indicated the chip orientation (white: right-side up, blue: down-side up). Scale bars = 3 μm.

5.6 Isolated Silicon Nanowire Meshes

5.6.1 Technological development of Isolated Silicon Nanowire Meshes

The isolated silicon nanowire meshes (SiNW-Meshes) were trickier to produce due to the shortening of the polysilicon main layer, as in this case this layer was reduced to the minimum possible thickness and only a 65 nm-thick polysilicon nanoclusters were used as a platform for the posterior silicon nanowire growth.

A 1 μm-thick silicon oxide layer on a 100 mm p-type silicon wafer defined the sacrificial layer (Figure 5.7a). A 65 nm-thick polysilicon nanoclusters were deposited. The diameter and density of the nanoclusters were fixed by the deposition conditions (temperature 580°C, pressure 350 mTorr and a SiH_4 flow rate of 40 sccm). After nanoclusters formation, a photolithographic step (Figure 5.7c and d) defined the lateral dimensions of the chips (3 μm x 3 μm). Later, a polysilicon dry etching was performed (Figure 5.7e) and after the photoresist removal an array of 3 μm x 3 μm chips separated 3 μm was obtained (Figure 5.7f).

Later, a nanowire growth process *(Performed by NEMS and Nanofabrication Group, IMB-CNM, CSIC)* was performed by taking advantage of the galvanic displacement deposition method (Figure 5.7g). For further details about the nanowire growth see section 5.5.1. As in the SiuC+SiNW case, randomly oriented nanowires were obtained because of the random crystallographic orientations of the polysilicon grains (Figure 5.7h).

Lastly, isolated silicon nanowire meshes were released by a 40 min-sacrificial etching of the silicon oxide layer in vapors of 49% HF (Figure 5.7i), suspended in 96% ethanol, centrifuged at 14000 g for 5 minutes (MiniSpin Plus) and collected in eppendorfs for posterior cell studies.

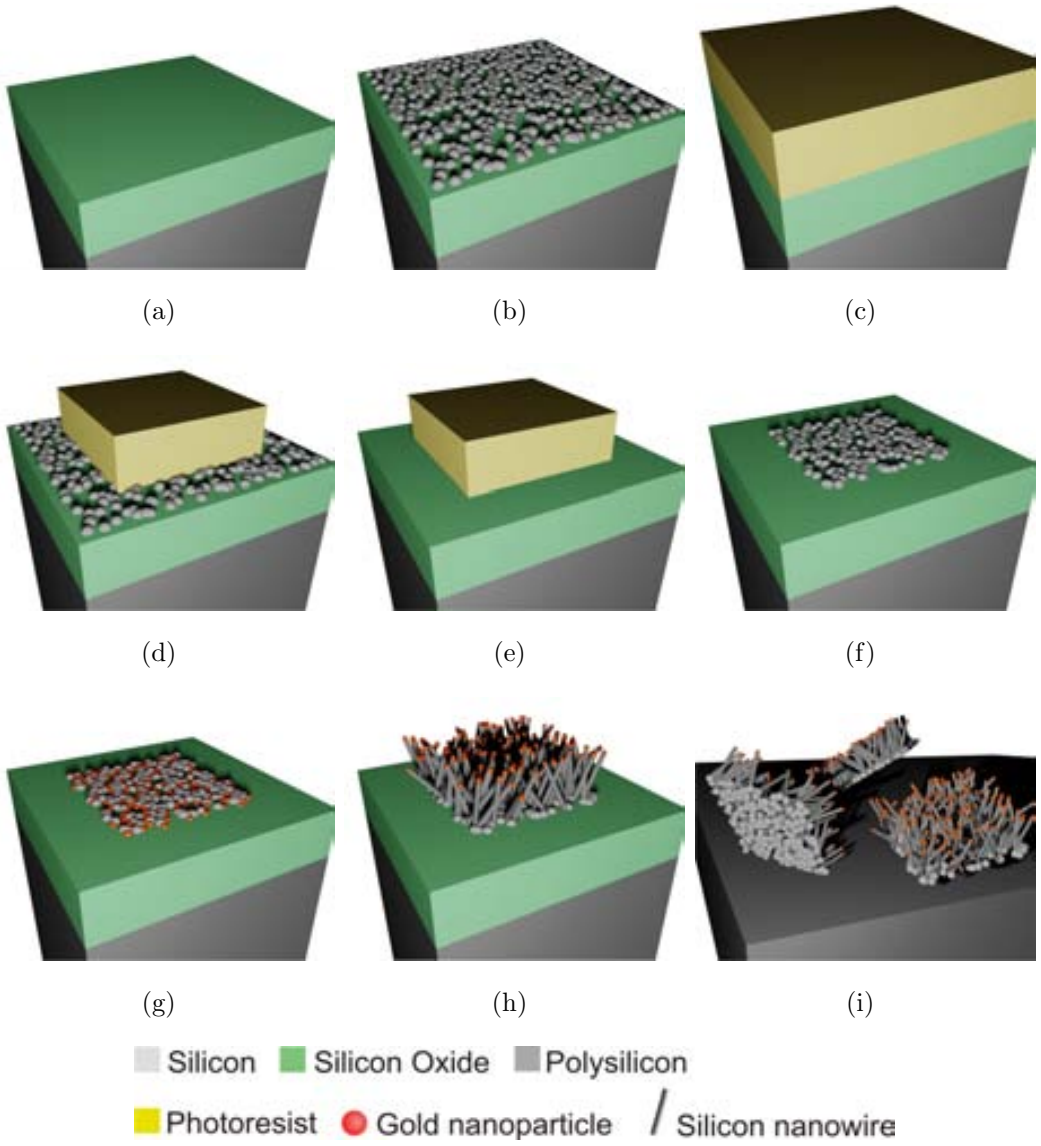

Figure 5.7: **Fabrication process of isolated silicon nanowire meshes**. a) A 1 μm-thick silicon oxide layer was grown as sacrificial layer. b) A 65 nm-thick polysilicon nanoclusters were deposited by chemical vapor deposition. c) A 1.2 μm-thick positive photoresist was spun onto the wafers. d) The photolithographic step defined the lateral dimensions of the chips. e) A polysilicon dry etching process was carried out for the removal of unnecessary polysilicon areas. f) Photoresist was removed. g) A galvanic displacement deposition of gold nanoparticles were deposited on the nanoclusters. h) Silicon nanowires were grown by the VLS method. i) A sacrificial etching in 49% HF vapors was performed to release the SiNW-Meshes from the wafer.

5.6.2 Characterization of Isolated Silicon Nanowire Meshes

After a successful fabrication process the obtained SiNW-Meshes were analized by scanning electron microscopy. The isolated silicon nanowire meshes show different nanostructured morphologies at the two sides, polysilicon nanoclusters on the bottom-side-up and silicon nanowires on the right-side-up (Figure 5.8). As what occurs with the silicon nanowire chips, this fact is relevant, as I describe later, for their cell-internalization due to their different shape and size.

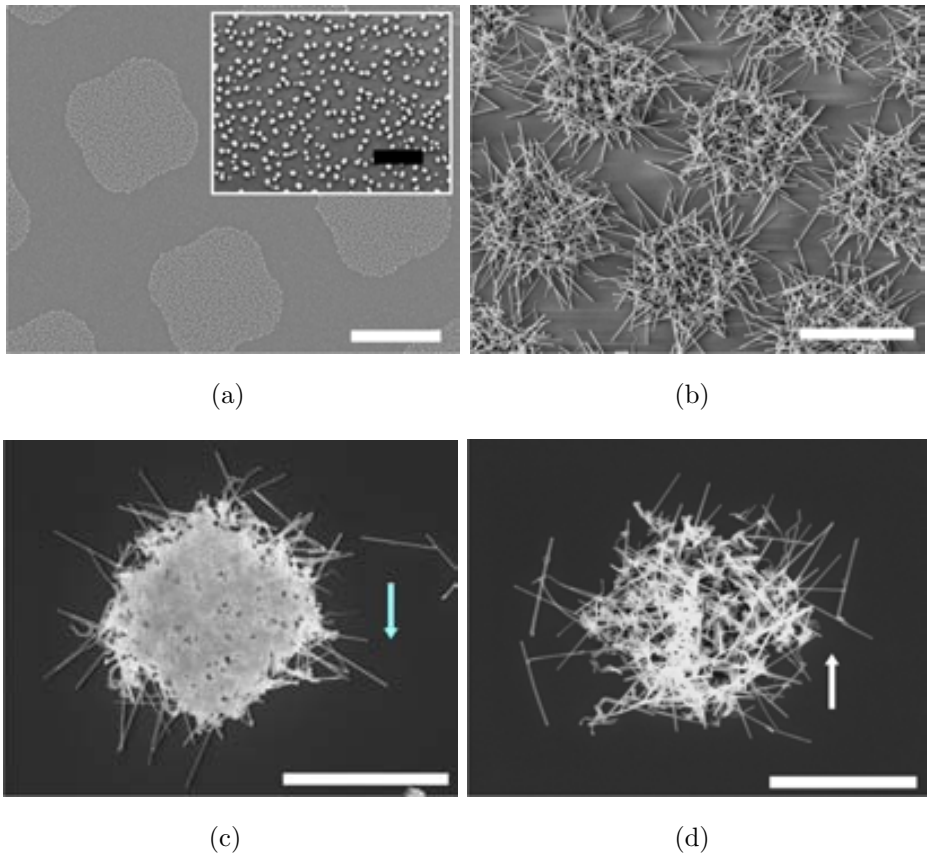

(a) (b)

(c) (d)

Figure 5.8: **Fabrication results of the isolated silicon nanowire meshes**. Scanning electron microscopy images of the fabricated chips. a) Polysilicon nanoclusters before the nanowire growth (Inset, image zoom). b) Isolated silicon nanowire meshes still on the wafer. c, d) After the meshes release. Arrows indicated the chip orientation (white: right-side up, blue: down-side up). White scale bars = 3 μm. Black scale bar = 500 nm.

5.7 Characterization of Polysilicon Nanoclusters and Silicon Nanowires

Several morphological features of the silicon nanowire chips and for the obtained silicon nanoclusters were studied and analyzed in order to obtain a clear idea of the growth and deposition conditions for future fabrication processes. The obtained data are shown in figure 5.9.

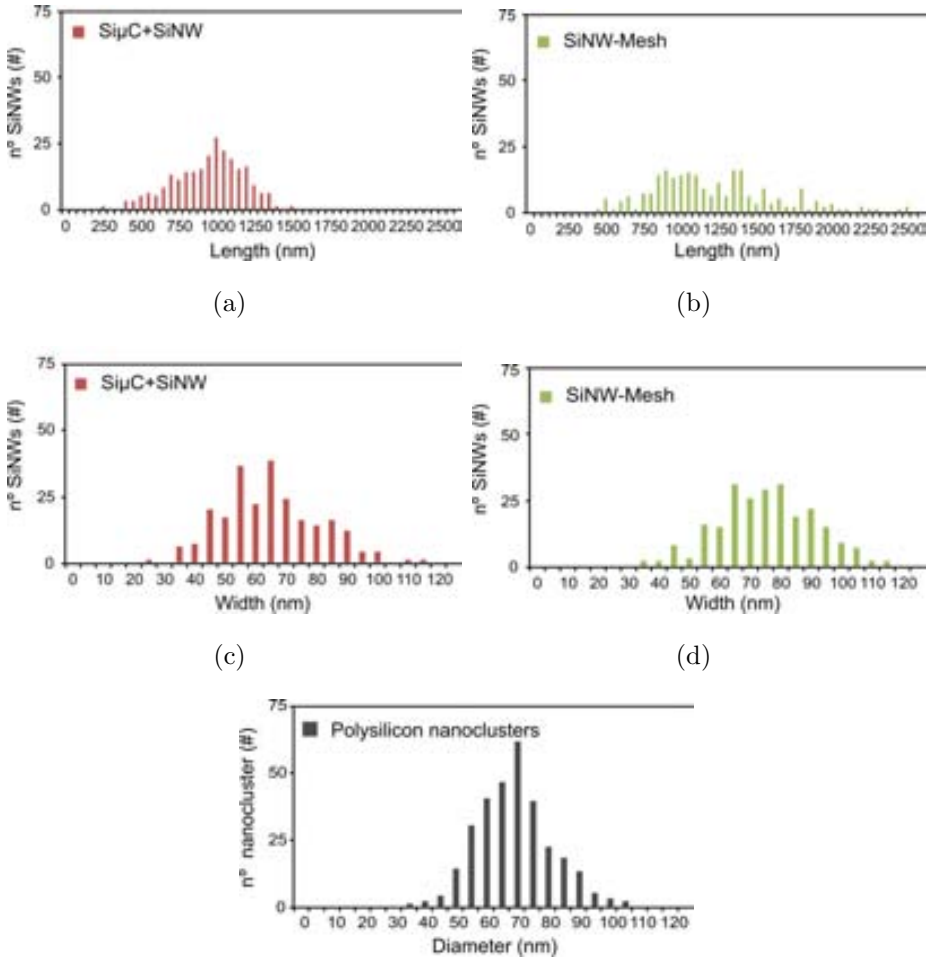

Figure 5.9: **Silicon nanowires and polysilicon nanoclusters morphology**. The plots show the distribution of nanowire (a, b) length, (c, d) width and (e) polysilicon nanocluster diameter obtained from the SiμC+SiNWs and SiNW-Meshes, respectively. Nanowire count, n, of: SiμC+SiNWs $n = 1500$ and SiNW-Mesh $n = 2300$. Polysilicon nanoclusters count, n: $n = 6000$.

Nanowire growth time were fixed at 60 s and 90 s for the SiμC+SiNWs and SiNW-Meshes, respectively. Longer growth time was selected for the meshes in order to obtain longer wires and ensure the nanowire entanglement, as in this case there was no 500 nm-thick polysilicon platform (SiμC) to ensure the structural integrity of the chips (Table 5.1).

Device	Length (nm)	Width (nm)	Density (SiNWs/μm^2)
SiμC+SiNW	885 ± 231	60 ± 19	28 ± 2
SiNW-Mesh	1124 ± 405	71 ± 16	47 ± 2

Table 5.1: **Density, length and width values of the obtained silicon nanowires**. Nanowire count, n, of: SiμC+SiNWs $n = 1500$ and SiNW-Mesh $n = 2300$.

The fact that the density of the nanowires in SiNW-Meshes was smaller than the density of the polysilicon nanoclusters indicates that the process was dominated in fact by the number of the gold particles (Table 5.2).

Device	Diameter (nm)	Density (clusters/μm^2)
Polysilicon nanoclusters	65 ± 12	128 ± 8

Table 5.2: **Diameter and density values of the obtained polysilicon nanoclusters.** Polysilicon nanocluster count, n: $n = 6000$

It should also take into account that an excessive wire growth time can ruin the posterior chip collection, as nanowire junctions between neighboring chips can be originated. Different times of growth it can be observed in figure 5.10.

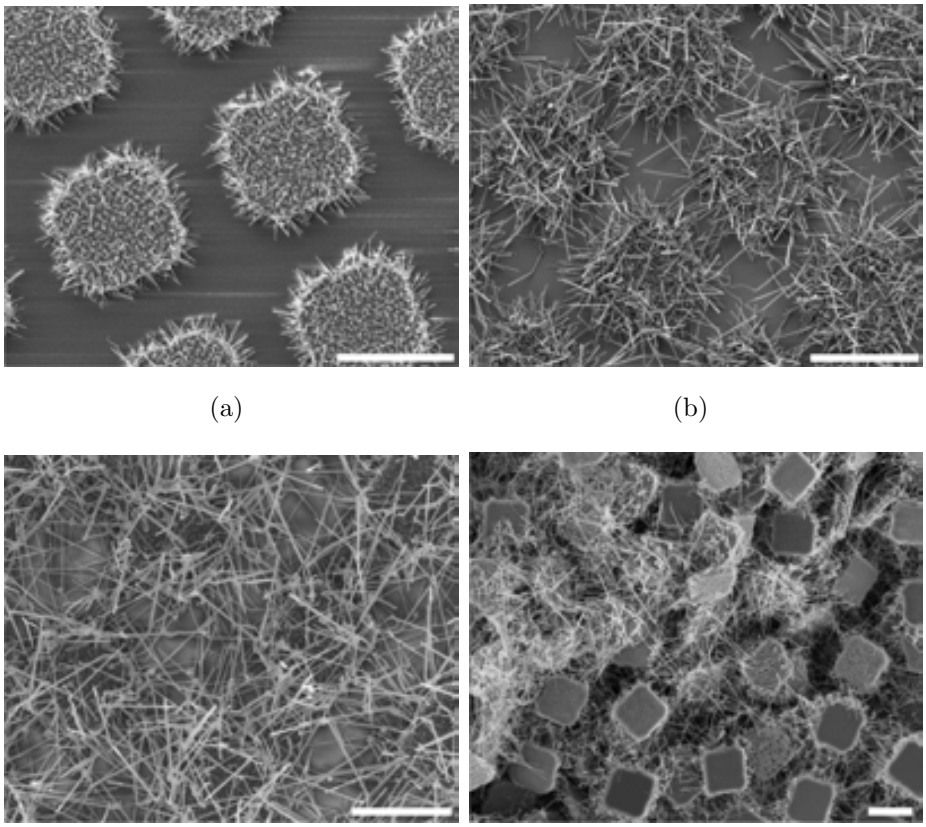

(a) (b)

(c) (d)

Figure 5.10: **Nanowire length controlled by growth time**. (a-c) Images show SiμC decorated with silicon nanowires grown during 45 s, 60 s and 90 s, respectively. (d) Longer growth-times created nanowires junctions between neighboring chips which ruined the device collection. Scale bars = 3 μm.

5.8 Biological studies: Silicon Nanowire Chips and Isolated Silicon Nanowire Meshes cell-viability tests

(Performed by CELLTEC UB, Department of Cellular Biology, Universitat de Barcelona)

The previous works performed in our group showed that the internalization of SiμCs and silicon-based pressure sensors with similar dimensions were possible.[10, 11] Thus, in this chapter we evaluated the internalization of chips with integrated silicon nanostructures. HeLa cells were lipofected with FuGene , which is a non-liposomal transfection reagent (Fugent LLC, Wisconsin, USA) and the fabricated chips. We selected HeLa cells because this kind of cells are widely used as a simple model for more complex biological systems.[2, 6, 10, 11, 21]

HeLa cells were cultured in Dulbeccos modified Eagle medium (DMEM) containing 1 g/L glucose and supplemented with 10% foetal calf serum, 2 mM glutamine, 5 U/ml penicillin, and 5 μg/ml streptomycin. The cultures were maintained at 37°C in a 5% CO_2 - 95% air atmosphere. Upon reaching 80% confluence cells were detached using 0.25 mg/ml trypsin/EDTA solution and seeded at a density of 50.000 cells/cm^2 in the specified support for each experiment. After 24 hours, media was replaced by an internalization solution containing silicon chips (SiμC, SiμC+SiNWs and SiNW-Meshes), in a relation of 10 silicon chips/cell, and FuGene6 in Opti-MEM medium. After 24 hours, the internalization solution was removed and cells were washed for three times with Opti-MEM and processed for observation.

Our tests showed HeLa cells viability after 24 h exposure to SiμC, SiμC+SiNWs and SiNW-Meshes using the Calcein-AM method (Invitrogen Corporation). Calcein-AM is a non-fluorescent hydrophobic compound that easily permeates intact live cells. The hydrolysis of Calcein-AM by intracellular esterases produces Calcein, a hydrophilic strongly fluorescent compound that is well-retained in the cell cytoplasm and that can be measured as viability indicator. To assess cell viability, the membrane-permeable dye calcein acetoxymethyl ester was prepared as a stock solution of 2 mM in dimethylsulfoxide, stored at -20°C and used at final concentration of 5 μM in Opti-MEM. Cells seeded in 8-wells Nunc Lab-Tek II chambered cover glass

and incubated with the internalization solution as described above, were rinsed with Opti-MEM and incubated with 50 μL Calcein-AM working solution at 37°C in a CO_2 atmosphere. After 1 hour, Calcein-AM solution was removed and cells were washed for three times. Cells were maintained for 20 minutes at room temperature for a complete de-esterification of the dye prior their observation. Images for quantification were obtained using a confocal laser scanning Microscope (CLSM) Leica TCS SP2 (Leica Lasertechnik GmbH, Mannheim, Germany) adapted to an inverted Leitz DMIRBE microscope and using a HC Plan Apochromatic x20/0.70 oil immersion objective (Figure 5.11a-d).

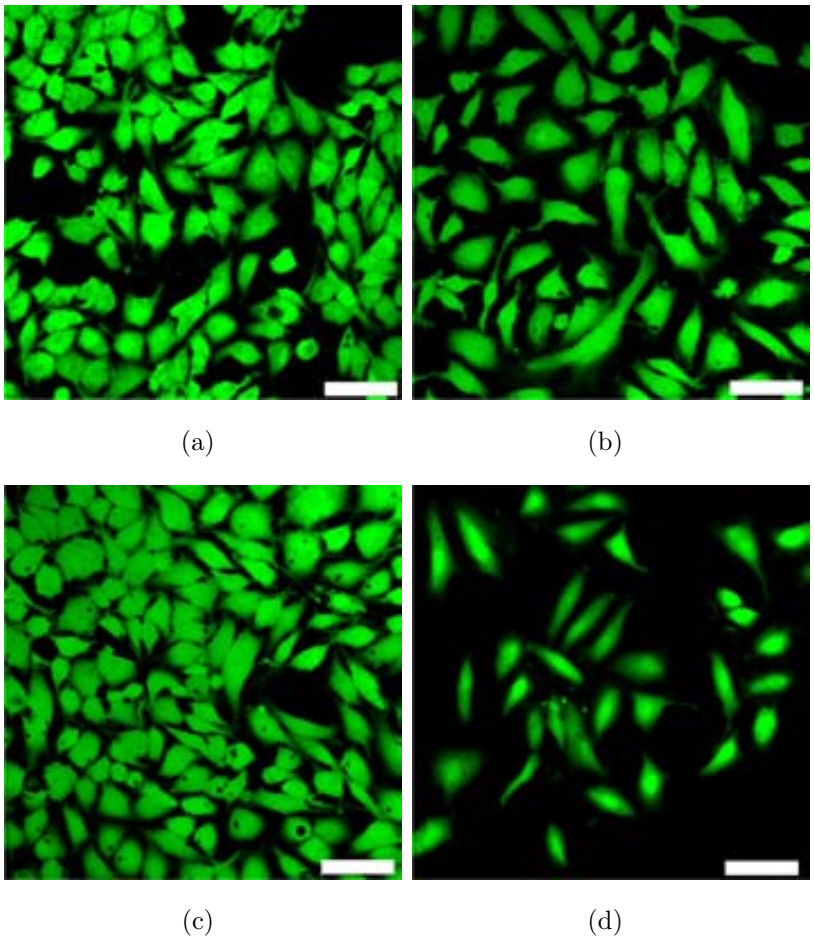

(a) (b)

(c) (d)

Figure 5.11: **Viability assays of cells with and without polysilicon chips**. Confocal images of (a) control cells and cells with internalized (b) SiμC, (c) SiμC+SiNWs and (d) SiNW-Meshes. Scale bar = 50 μm.

To obtain the fluorescence images from Calcein, cells were excited with the 488-nm line of an argon-ion laser and the emission light of 500 nm - 600 nm was acquired. Silicon chips were simultaneously localized with the reflection mode of the same excitation line in each image. Fluorescence density of Calcein was measured using ImageJ software (NIH, http://imagej.nih.gov/ij/). Regions of interest were set for each cell and the presence or absence of silicon chips in cells was set by the observation of dark spots and checked with the refection mode image of each section. Experiments were performed by triplicate and at least 20 cells of each condition were measured in each experiment.

In figure 5.12 it can be seen that the viability of the cells that have internalized silicon chips is practically unaffected in comparison with those that have not. This fact was in good agreement with the well-known silicon biocompatibility[33] and with our previous viability tests obtained with polysilicon chips in different cell types.[8–11]

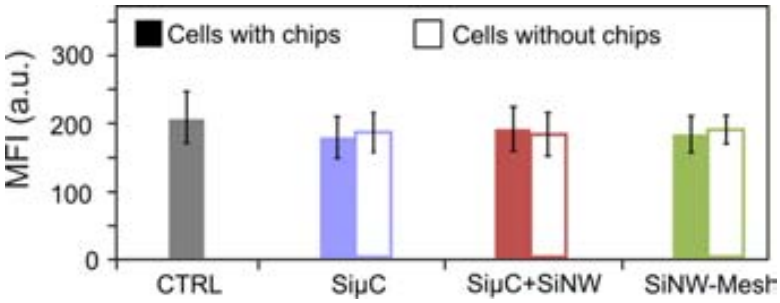

Figure 5.12: **Graph of the viability values of HeLa cells with and without polysilicon chips**. Cell viability measured as the mean fluorescence intensity (MFI) obtained by the Calcein method. Cell count, n: Control $n = 209$, SiμC $n = 366$, SiμC+SiNWs $n = 377$, SiNW-Meshes $n = 375$. Error bars: $\pm$ 1SD.

5.9 Validation of Silicon Nanowire Chips and isolated Silicon Nanowire Meshes as nano-patterned intracellular devices.

5.9.1 Correlative light and electron microscopy characterization

Many researchers worldwide have already proved the capabilities of single nanowires to perform as nanosensors and actuators using fluorescence dyes.[2, 10, 11, 34] However, the fact that we have 3D complex structures instead of isolated nanowires and because of non-transparency of silicon, limits the use of this technique. Hence, tests without any kind of functionalization were carried out and bright field optical microscopy (BFOM), scanning electron microscopy (SEM), focused ion beam (FIB) correlative inspections and a detailed cell mapping were used to confirm chip internalization (Figure 5.13).

Chips appeared as opaque areas in BFOM images because of the low optical transmission of silicon (Figure 5.13a). However, the information of these images was not enough to unambiguously determine whether the chips were inside or outside the cells. In addition, SEM inspection only revealed chips partially or totally outside the cells, but not those chips which are totally internalized (Figure 5.13b). Thus, we used a detailed cell mapping and a correlative optical and SEM inspections to identify the chip-localization. A complementary Focused Ion Bean (FIB) nanomilling was also performed to evidence and reveal chips that were completely internalized and preserved inside the cell (Figure 5.13c and d). This methodology allows us to obtain high-resolution images and the study of cell interactions with fluorescence-dye-free silicon structures. The preparation of the samples was performed by *CELLTEC UB, Department of Cellular Biology in the Universitat de Barcelona*. HeLa cells were plated on squared home-made gridded glass pieces (1 cm x 1 cm) and incubated with internalization solution as described before. Later on, samples were fixed with 2.5% glutaraldehyde, dehydrated through a graded series of ethanol-water mixtures to 100% ethanol, and dried by the critical-point method. Then, the cells of interest were mapped on the gridded glass pieces.

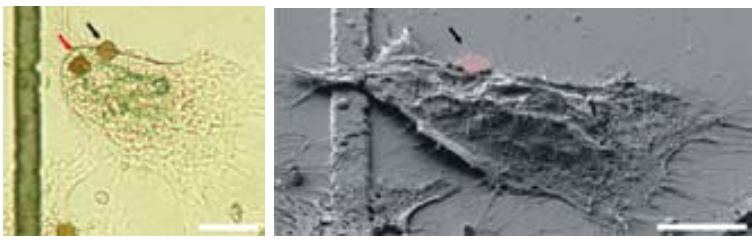

(a) (b)

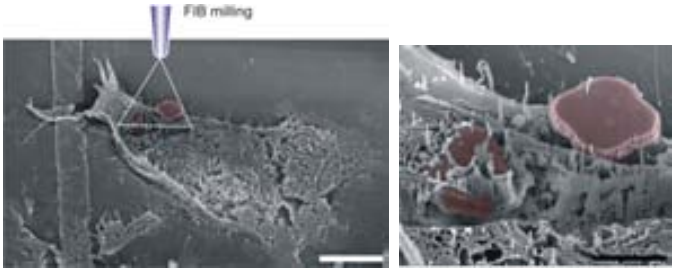

(c) (d)

Figure 5.13: **BFOM, SEM and FIB correlative inspections of internalized chips**. (a) Silicon chips were clearly identified on bright field optical microscope due to the low optical transmission of silicon. However, the localization of the chips inside (red arrow) or outside (black arrow) the cell cannot be determined. (b) On the contrary, SEM inspection of the same cell only showed the chip outside the cell. (c, d) Hence, FIB nanomachining was used to section the cell. White scale bars = 10 μm. Black scale bar = 3 μm.

Eventually, we used this correlative light and electron microscopy characterization method in order to prove cell internalizations of the three designs (SiμCs, SiμCs+SiNWs and SiNW-Meshes). The cellular uptake was probed using a transmission BFOM, using an Eclipse ME600 upright optical microscope (Nikon) with a $\times$100 magnification, (Figure 5.14a-c, left column). Afterwards, the interested cells were localized and observed by SEM (Carl Zeiss Auriga - Microscope GmbH, Germany) (Figure 5.14a-c, second column from the left). And finally, the same cells were studied by FIB using Ga^+ ions in a dual-beam instrument (Carl Zeiss 1560XB Cross Beam - Microscopy GmbH, Germany) to evidence and reveal the chips that were completely internalized and preserved inside the cells (Figure 5.14, two right columns). Although, internalization depends on the particle morphology and shape,[35] we found positive chip-internalization in HeLa cells for the three different morphologies.

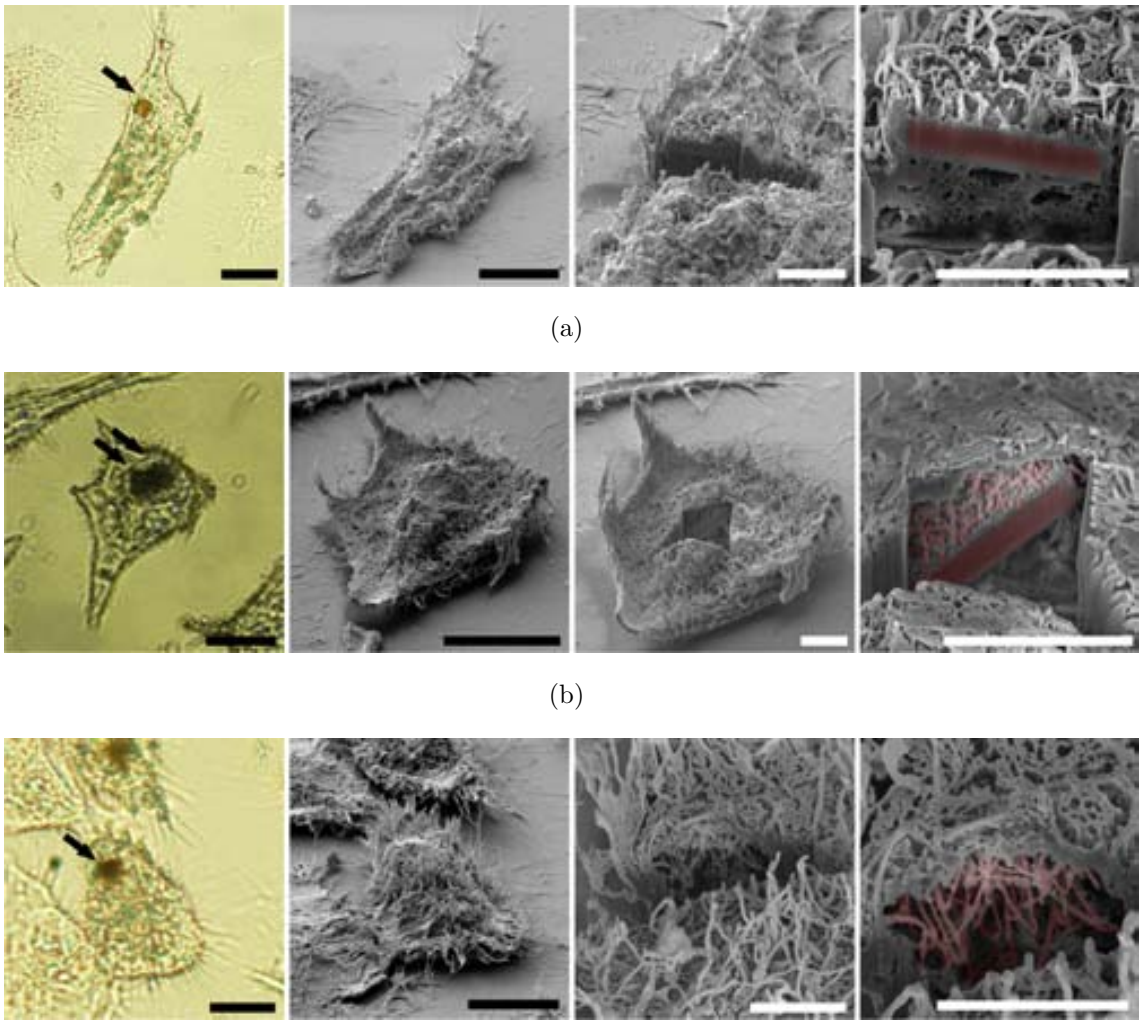

Figure 5.14: **Chip internalization in HeLa cells**. HeLa cells with internalized (a) SiμCs, (b) SiμCs+SiNWs and (c) SiNW-Meshes. Panel from left to right shows: BFOM, SEM, SEM after FIB milling and pseudo-colored detailed image (pink color indicates silicon). Black arrows point out chip position. Black scale bars = 10 μm. White scale bars = 3 μm.

1287 cells were analyzed and 827 chips were localized by the correlative inspection method. The major part of the chips were cell-internalized with values between 59.2%-74.8% (Figure 5.15a), and a lower proportion was partially internalized or adhered at the cell membrane, 21.6%-36.7%. Although, the major part of the cells, 25%, with internalized chips carried only one chip (Figure 5.15b), cells carrying up to 6 chips were found. These results show a large cell-capacity to internalize silicon chips, and remarkably, no significant differences in these results were found between chips with micro- and nanomorphologies.

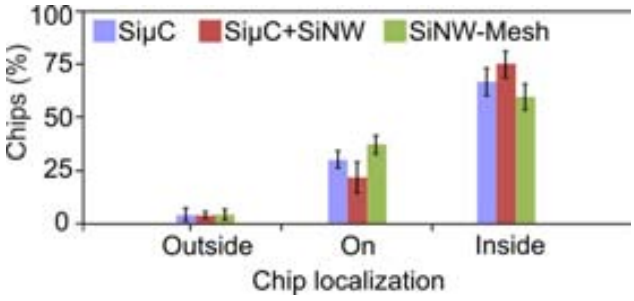

(a)

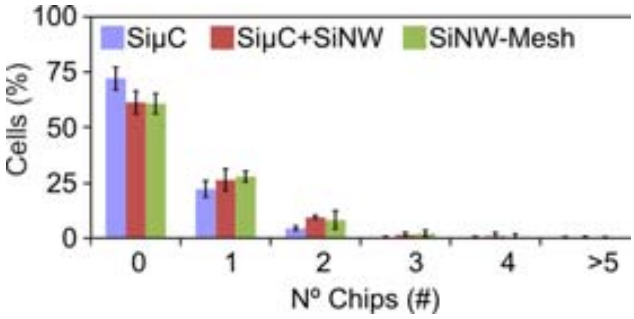

(b)

Figure 5.15: **Graph of the silicon chips internalization values in HeLa cells**. a) Graph showing the proportion of chips laying on the substrate outside the cells, on the cell membrane and inside cells. b) Graph showing the proportion of cells with internalized chips. Chips and cells count, n: SiμC $n = 170$ and cells $n = 345$, SiμC+SiNWs $n = 360$ and cells $n = 524$, SiNW-Meshes $n = 297$ and cells $n = 418$. Error bars: $\pm$ 1SD.

5.9.2 Energy-dispersive X-ray spectroscopy characterization

SEM inspection of cell sections and energy-dispersive X-ray (EDX) analysis were used to confirm the presence of silicon inside the cells.

The preparation of the samples was performed by *CELLTEC UB, Department of Cellular Biology, Universitat de Barcelona*. HeLa cells seeded in 60 mm-diameter dishes and incubated with the internalization solution as described above were fixed with 2.5% (v/v) glutaraldehyde (EM grade; Sigma) in 100 mM phosphate buffer (PB, pH 7.0) for 1.5 h at 4°C. The fixed cells were harvested and pelleted, followed by three washes with 100 mM PB. The cells were then postfixed in 1% (w/v) osmium tetroxide for 2 h at 4°C and washed an additional three times with 100 mM PB.

The cells were dehydrated through a graded acetone series; infiltrated at room temperature in several increasing Epon12 - acetone mixtures and, finally, embedded in fresh Epon12 resin (EM Ltd.) for 5 h and polymerized for 48 h at 60°C. A Reichert ultramicrotome was used to produce sections about 150 nm-thick that were collected over Formvar-carbonated copper grids and stained with uranyl acetate (7%) and lead citrate.

EDX analysis was performed on cell pellets sections. Images were captured by an Oxford Instruments IncaX-act SEM and the EDX spectrums were obtained using a PentaFET-Precision attached to the SEM equipment. Previous works in the Micro and Nanotools group demonstrated that SiμCs could be found in a tight association with endosomal membranes (Figure 5.16a).[36]

On the contrary, images of internalized SiμCs+SiNWs and SiNW-Meshes revealed that they could be encircled by a lax membrane-bound compartment (Figure 5.16b and 5.14c right panel). This could open new opportunities in a large variety of fields, such as intracellular nanosensing or intracellular drug delivery.

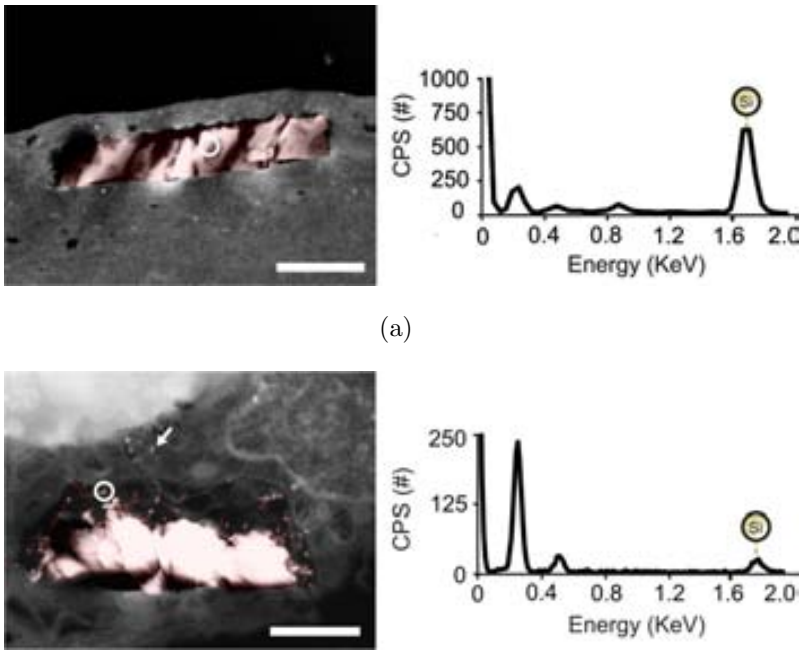

Figure 5.16: **EDX analysis of polysilicon chips within HeLa cells**. Pseudo-colored images showing an internalized (a) SiμC and (b) a SiμC+SiNWs. Right panel shows their respective EDX spectrums. White encircled areas show the spot, where the EDX analysis was performed. Counts per second (CPS). Scale bar = 1 μm.

5.10 Silicon morphological dependence at the initial stage of chip-internalization

We also explored the initial stage of chip-internalization of 827 chips. The top and bottom sides of the SiμCs have equivalent morphologies (Figure 5.4) and consistently, SEM images do not reveal any preferred chip orientation (Figure 5.17a, top panel). On the contrary, the strong morphological-asymmetry of SiμC+SiNWs (Figure 5.6) results in a favored orientation during the cell internalization, which corresponds to that of the nanowire-side is in contact with the cell membrane (Figure 5.17b, top panel). This fact suggests that HeLa cells prefer silicon nanowire interfaces at the first stage of cell internalization. Finally, SiNW-Meshes did not present statistical differences in chip-orientation during cell-internalization (Figure 5.17c, top panel), in agreement with the small morphological differences between top and bottom nanostructured sides (Figure 5.8).

Sedimentation tests with only silicon chips were also carried out to discard any fluid-dynamic effects in chip orientation during deposition (Figure 5.17a-c, bottom panels). The SiμCs, SiμC+SiNWs and SiNW-Meshes were suspended by ultrasounds in 96% ethanol, centrifuged at 14000 g for 5 minutes (MiniSpin Plus) and collected in three eppendorfs, respectively. Next, the three samples were pipetted and 2 μl-drops were deposited on a clean silicon substrate. After solvent evaporation the substrates were observed on a scanning electron microscope (Carl Zeiss Auriga - Microscope GmbH, Germany). A number of devices in a right-side up and bottom-side up position were counted and analyzed using ImageJ software (NIH, http://imagej.nih.gov/ij/). For each type of devices, three sets of 100 devices were counted for statistics. No significant differences were observed for SiμCs (Figure 5.17a, bottom panel), or SiNW-Meshes (Figure 5.17c, bottom panel). Conversely, significant differences were observed for SiμC+SiNWs (Figure 5.17b, bottom panel). Regardless of their initial orientation, it seems that chips settle down with the flat micropart turned down and the nanowire side turned up, and remained in this orientation, similar to a shuttlecock. The fact that a majority of SiμC+SiNWs were deposited with the micropart down while these chips were found with the nanowire side down on the cell membranes (Figure 5.17b, top panel) supports the fact that HeLa cells prefer the silicon nanowires at the initial stage of chip-internalization.

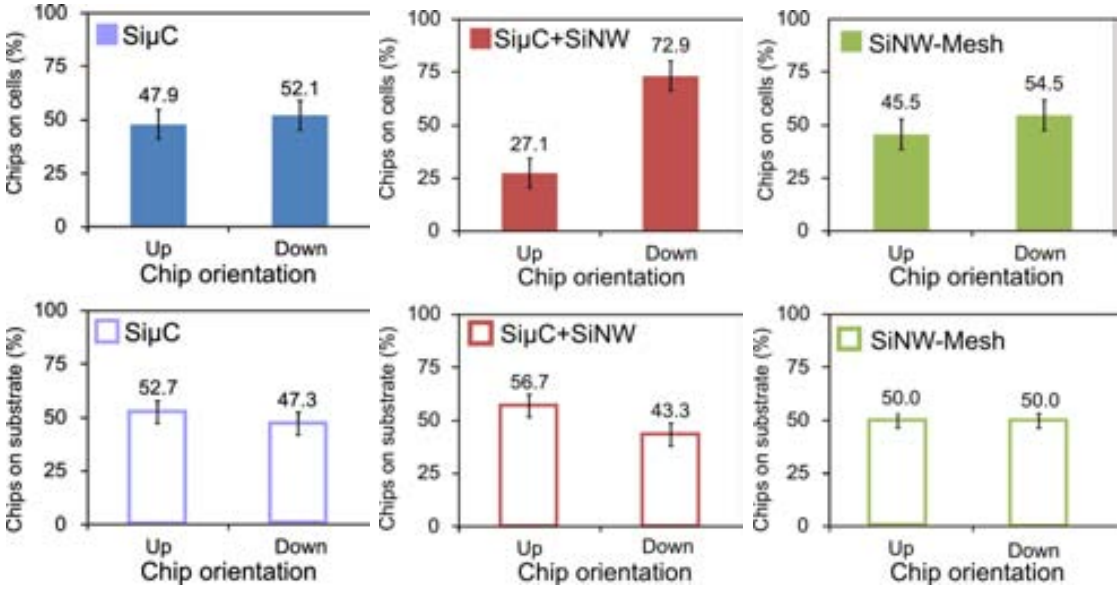

Figure 5.17: **Silicon morphological dependence at the initial stage of internalization**. (a-c) Graphs showing the proportion of chips on the cell membrane (top panels) and on the silicon substrate after sedimentation tests (bottom panels) with the topside facing upwards or downwards for SiμCs, SiμC+SiNWs and SiNW-Meshes, respectively. Chips count, n, for (a-c, top panel): SiμC $n = 170$, SiμC+SiNWs $n = 360$, SiNW-Meshes $n = 297$. Chips count, n, for (a-c, bottom panel): SiμCs count $n = 300$, SiμC+SiNWs $n = 300$, SiNW-Meshes $n = 300$. Error bars: $\pm$ 1SD.

At this point, considering that the percentage of chips inside cells was similar for all the types of chips (Figure 5.15), we speculate that the SiμC+SiNWs were indeed turned upside down by the cells. This idea is in good agreement with the fact that particles of different shape and size could be internalized by different pathways[37] and cellular uptake kinetics could depend on particle size.[35] These results indicate that initial cell contact-sites were facilitated by nano-structured silicon (Figure 5.18a and b) in contrast to micro-structured silicon. This observation is in good agreement with other works focused on 3D nanostructured platforms for cell trapping.[25] The combination of SEM images and EDX analysis (Figure 5.18c) revealed a contact site between a silicon nanowire and a cell. The detection of the silicon EDX signal (Figure 5.18c, points 1-3) and the fact that the silicon signal disappeared 200 nm from the nanowire (Figure 5.18b, point 4) validated the EDX technique for nanowire detection in spite of their small diameter.

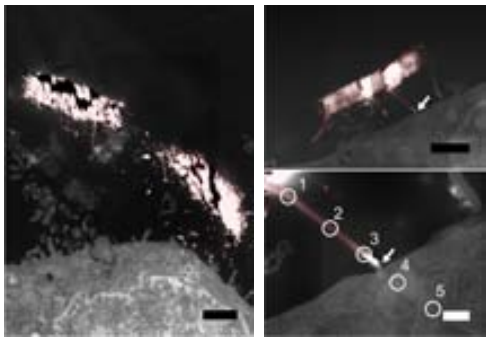

(a) (b)

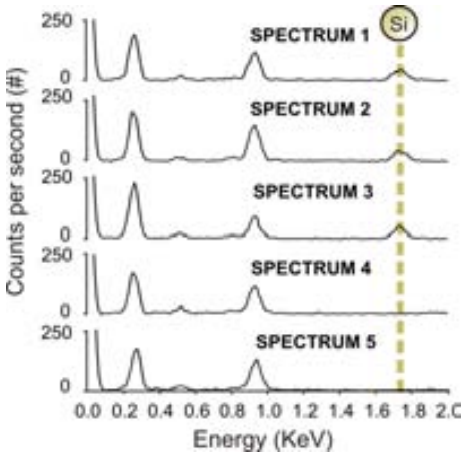

(c)

Figure 5.18: **EDX analysis of silicon morphological dependence at the initial stage of internalization**. a, b) Pseudo-colored SEM images showing the initial contact between several SiμC+SiNWs and a HeLa cell (pink color indicates silicon). (b-bottom panel) Detailed image of a nanowire on the cell membrane. White arrows indicate nanowire-cell contact-sites. White circles indicate EDX spectrum points. c) EDX spectrums confirmed silicon presence. Black scale bars = 1 μm. White scale bar = 200 nm.

The inspection also showed that SiNWs and cellular surface components, like filopodia,[38] have similar size and shape (Figure 5.19). However, thanks to a EDX analysis we can easily recognize the silicon signal at 1.739 KeV. In addittion the analysis showed a characteristic gold signal at 2.120 KeV, due to the previous gold metallization to enhance the image quality.

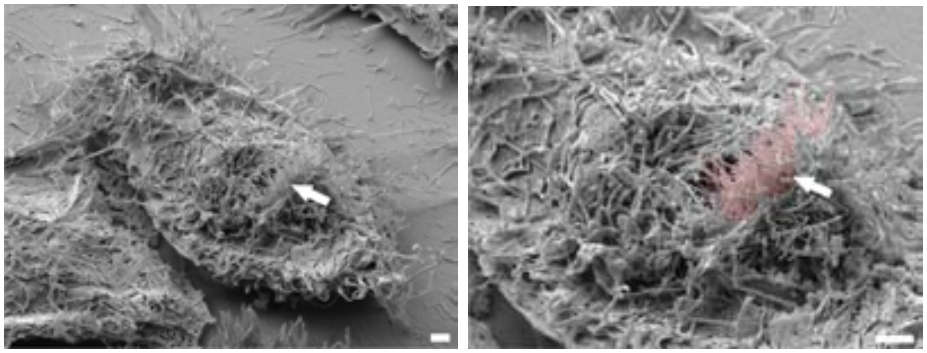

(a) (b)

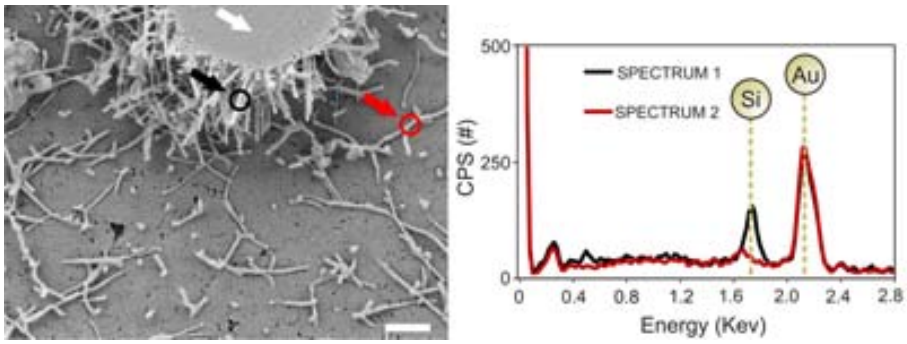

(c)

Figure 5.19: **Silicon nanowires at the scale of cell surface structures**. a) SEM image of a HeLa cell with a semi-internalized SiNW-Mesh. b) The same cell revealing the silicon nanowires (pink color). c) SEM image of a SiμC+SiNWs on a HeLa membrane. Right panel: EDX spectroscopy was used to probe the presence of silicon. White arrows indicate chip localization. Red and black arrows indicate the selected filopodia and SiNW for the EDX analysis, respectively. Counts per second (CPS). Scale bars = 1 μm.

5.11 Conclusions

In this chapter a technology for the fabrication of nanowire silicon chips with controlled dimensions to be cell-internalizable was developed. These devices can be collected and suspended for their posterior use on cell-cultures, so that isolated devices at microscale were obtained, in contrast with previous studies where experiments were performed at surface platforms.[6, 7, 21] Bright field optical microscopy (BFOM), scanning electron microscopy (SEM) and focused ion beam (FIB) correlative inspections and a detailed cell mapping were used to confirm chip internalization. And SEM inspections of cell sections and energy-dispersive X-ray (EDX) analysis were used to confirm the presence of silicon inside the cells. Cell viability assays with micro and nanostructured chips were performed in HeLa cells and did not reveal any significant differences when compared with control cells studies. Thus, these devices can be considered as biocompatibles for this cell line.

On the other hand, understanding how the geometry and size material affect the cell internalization processes is a crucial issue for the development of future intracellular tools. Hence, in this work we fabricated nanowire chips entirely made of unique material, silicon, and fluorescence-dye-free to discern morphological and size effects in cell internalization. Our experiments showed that the internalization ratio for silicon chips with integrated SiNWs and SiNWs entangled meshes was similar to the results for non-nanostructured chips. However, the main difference was revealed at the initial stage of chip-internalization. HeLa cells prefer SiNWs sides (nano- instead of microstructured silicon) for initial uptake. This could be related to the fact that particles of different size could be internalized by different pathways with different kinetics.[37]

In addition, the ability to produce chips decorated with a large amount of silicon nanowires and a high area-volume ratio, which allows a large payload, opens new opportunities for intracellular drug delivery.[39] Additionally, nanowire intracellular devices have potential use in sensing applications,[7, 40] as chemical functionalization of the nanowires will produce valuable devices for biomolecular recognition.[21, 34] Finally, the implementation of SiNWs on intracellular chips as nanomechanical sensors[41] will provide invaluable information of intracellular forces involved in many fundamental cellular processes.

Bibliography

[1] G. M. Whitesides, The right size in nanobiotechnology, *Nature Biotechnology*, vol. 21, pp. 1161 1165, Oct. 2003. (cited on page(s) 161)

[2] R. Singhal, Z. Orynbayeva, R. V. Kalyana Sundaram, J. J. Niu, S. Bhattacharyya, E. A. Vitol, M. G. Schrlau, E. S. Papazoglou, G. Friedman, and Y. Gogotsi, Multifunctional carbon-nanotube cellular endoscopes, *Nature Nanotechnology*, vol. 6, pp. 57 64, Jan. 2011. (cited on page(s) 161, 176, 179)

[3] B. Tian and C. M. Lieber, Synthetic nanoelectronic probes for biological cells and tissues, *Annual review of analytical chemistry*, vol. 6, pp. 31 51, Jan. 2013. (cited on page(s) 161)

[4] J. El-Ali, P. K. Sorger, and K. F. Jensen, Cells on chips, *Nature*, vol. 442, pp. 403 411, July 2006. (cited on page(s) 42, 129, 161)

[5] S. E. Cross, Y. S. Jin, J. Rao, and J. K. Gimzewski, Nanomechanical analysis of cells from cancer patients, *Nature Nanotechnology*, vol. 2, pp. 780 783, Dec. 2007. (cited on page(s) 129, 161)

[6] A. K. Shalek, J. T. Robinson, E. S. Karp, J. S. Lee, D. R. Ahn, M. H. Yoon, A. Sutton, M. Jorgolli, R. S. Gertner, T. S. Gujral, G. MacBeath, E. G. Yang, and H. Park, Vertical silicon nanowires as a universal platform for delivering biomolecules into living cells, *PNAS*, vol. 107, pp. 1870 1875, Feb. 2010. (cited on page(s) 44, 129, 161, 162, 176, 189)

[7] W. Kim, J. K. Ng, M. E. Kunitake, B. R. Conklin, and P. Yang, Interfacing silicon nanowires with mammalian cells, *Journal of the American Chemical Society*, vol. 129, pp. 7228 7229, June 2007. (cited on page(s) 44, 45, 161, 162, 189, 201)

[8] E. Fernández-Rosas, R. Gómez-Martínez, E. Ibanez, L. Barrios, M. Duch, J. Esteve, C. Nogués, and J. A. Plaza, Intracellular polysilicon barcodes for cell tracking, *Small*, vol. 5, pp. 2433 2439, Nov. 2009. (cited on page(s) 49, 53, 54, 69, 97, 129, 161, 178)

[9] O. Penon, S. Novo, S. Durán, E. Ibanez, C. Nogués, J. Samitier, M. Duch, J. A. Plaza, and L. Pérez-García, Efficient biofunctionalization of polysilicon barcodes for adhesion to the zona pellucida of mouse embryos, *Bioconjugate chemistry*, vol. 23, pp. 2392 2402, Dec. 2012. (cited on page(s) 71, 87, 132, 161, 178, 201)

[10] R. Gómez-Martínez, P. Vázquez, M. Duch, A. Muriano, D. Pinacho, N. Sanvicens, F. Sánchez-Baeza, P. Boya, E. J. de la Rosa, J. Esteve, T. Suárez, and J. A. Plaza, Intracellular silicon chips in living cells, *Small*, vol. 6, pp. 499 502, Feb. 2010. (cited on page(s) 50, 51, 130, 132, 161, 165, 176, 178, 179)

[11] R. Gómez-Martínez, A. M. Hernández-Pinto, M. Duch, P. Vázquez, K. Zinoviev, E. J. de la Rosa, J. Esteve, T. Suárez, and J. A. Plaza, Silicon chips detect intracellular pressure changes in living cells, *Nature Nanotechnology*, vol. 8, pp. 517 521, July 2013. (cited on page(s) 129, 161, 176, 178, 179)

[12] H. J. Fan, P. Werner, and M. Zacharias, Semiconductor nanowires: from self-organization to patterned growth, *Small*, vol. 2, pp. 700 717, June 2006. (cited on page(s) 161)

[13] K. Yin, H. Lin, Q. Cai, Y. Zhao, S. T. Lee, F. Hu, and M. Shao, Silicon nanowires nanogenerator based on the piezoelectricity of alpha-quartz, *Nanoscale*, vol. 5, pp. 12330 12334, Dec. 2013. (cited on page(s) 161)

[14] Y. Cui, Q. Wei, H. Park, and C. M. Lieber, Nanowire nanosensors for highly sensitive and selective detection of biological and chemical species, *Science*, vol. 293, pp. 1289 1292, Aug. 2001. (cited on page(s) 161)

[15] V. Schmidt, H. Riel, S. Senz, S. Karg, W. Riess, and U. Gosele, Realization of a silicon nanowire vertical surround-gate field-effect transistor, *Small*, vol. 2, pp. 85 88, Jan. 2006. (cited on page(s) 161)

[16] J. Goldberger, A. I. Hochbaum, R. Fan, and P. Yang, Silicon Vertically Integrated Nanowire Field Effect Transistors, *Nano Letters*, vol. 6, pp. 973 977,

May 2006. (cited on page(s) 161)

[17] B. Tian, T. Cohen-Karni, Q. Qing, X. Duan, P. Xie, and C. M. Lieber, Three-dimensional, flexible nanoscale field-effect transistors as localized bioprobes, *Science*, vol. 329, pp. 830 834, Aug. 2010. (cited on page(s) 43, 161)

[18] E. Gil-Santos, D. Ramos, J. Martínez, M. Fernández-Regúlez, R. García, A. San Paulo, M. Calleja, and J. Tamayo, Nanomechanical mass sensing and stiffness spectrometry based on two-dimensional vibrations of resonant nanowires, *Nature Nanotechnology*, vol. 5, pp. 641 645, Sept. 2010. (cited on page(s) 161)

[19] A. San Paulo, N. Arellano, J. a. Plaza, R. He, C. Carraro, R. Maboudian, R. T. Howe, J. Bokor, and P. Yang, Suspended mechanical structures based on elastic silicon nanowire arrays, *Nano Letters*, vol. 7, pp. 1100 1104, Apr. 2007. (cited on page(s) 161)

[20] G. Zheng, F. Patolsky, Y. Cui, W. U. Wang, and C. M. Lieber, Multiplexed electrical detection of cancer markers with nanowire sensor arrays, *Nature Biotechnology*, vol. 23, pp. 1294 1301, Oct. 2005. (cited on page(s) 44, 45, 162)

[21] F. Mumm, K. M. Beckwith, S. Bonde, K. L. Martinez, and P. Sikorski, A transparent nanowire-based cell impalement device suitable for detailed cell-nanowire interaction studies, *Small*, vol. 9, pp. 263 272, Jan. 2013. (cited on page(s) 44, 162, 176, 189)

[22] L. De Vico, M. H. Sorensen, L. Iversen, D. M. Rogers, B. S. Sorensen, M. Brandbyge, J. Nygard, K. L. Martinez, and J. H. Jensen, Quantifying signal changes in nano-wire based biosensors, *Nanoscale*, vol. 3, pp. 706 717, Mar. 2011. (cited on page(s) 44, 162)

[23] N. S. Ramgir, Y. Yang, and M. Zacharias, Nanowire-based sensors, *Small*, vol. 6, pp. 1705 1722, Aug. 2010. (cited on page(s) 44, 162)

[24] S. Hou, H. Zhao, L. Zhao, Q. Shen, K. S. Wei, D. Y. Suh, A. Nakao, M. A. Garcia, M. Song, T. Lee, B. Xiong, S. C. Luo, H. R. Tseng, and H. H. Yu, Capture and stimulated release of circulating tumor cells on polymer-grafted silicon nanostructures, *Advanced Materials*, vol. 25, pp. 1547 1551, Mar. 2013. (cited on page(s) 44, 45, 162)

[25] S. Wang, H. Wang, J. Jiao, K.-J. Chen, G. E. Owens, K.-i. Kamei, J. Sun, D. J. Sherman, C. P. Behrenbruch, H. Wu, and H.-R. Tseng, Three-dimensional nanostructured substrates toward efficient capture of circulating tumor cells, *Angewandte Chemie*, vol. 48, pp. 8970 8973, Jan. 2009. (cited on page(s) 44, 162, 186)

[26] N. Jokilaakso, E. Salm, A. Chen, L. Millet, C. D. Guevara, B. Dorvel, B. Reddy, A. E. Karlstrom, Y. Chen, H. Ji, R. Sooryakumar, and R. Bashir, Ultra-localized single cell electroporation using silicon nanowires, *Lab on a chip*, vol. 13, pp. 336 339, Feb. 2013. (cited on page(s) 162)

[27] R. Wierzbicki, C. Kobler, M. R. B. Jensen, J. Lopacinska, M. S. Schmidt, M. Skolimowski, F. Abeille, K. Qvortrup, and K. Molhave, Mapping the complex morphology of cell interactions with nanowire substrates using FIB-SEM, *PLOS one*, vol. 8, pp. 1 12, Jan. 2013. (cited on page(s) 162)

[28] W. Zhang, L. Tong, and C. Yang, Cellular binding and internalization of functionalized silicon nanowires, *Nano Letters*, vol. 12, pp. 1002 1006, Feb. 2012. (cited on page(s) 162)

[29] Y. Cui, Z. Zhong, D. Wang, W. U. Wang, and C. M. Lieber, High performance silicon nanowire field effect transistors, *Nano Letters*, vol. 3, pp. 149 152, Feb. 2003. (cited on page(s) 162)

[30] T. Kamins, Polycrystalline silicon for integrated circuit applications, *Kluwer Academic Publishers, Springer US, Norwell, Massachusetts*, vol. 45, pp. 1 249, 1988. (cited on page(s) 163)

[31] L. Magagnin, V. Bertani, P. L. Cavallotti, R. Maboudian, and C. Carraro, Selective deposition of gold nanoclusters on silicon by a galvanic displacement process, *Microelectronic Engineering*, vol. 64, pp. 479 485, 2002. (cited on page(s) 167, 204)

[32] R. G. Hobbs, N. Petkov, and J. D. Holmes, Semiconductor nanowire babrication by bottom-up and tTop-down paradigms, *Chemistry of Materials*, vol. 24, pp. 1975 1991, June 2012. (cited on page(s) 167)

[33] J. Fan and P. K. Chu, Group IV nanoparticles: synthesis, properties, and biological applications, *Small*, vol. 6, pp. 2080 2098, Oct. 2010. (cited on

page(s) 130, 178)

[34] J. T. Robinson, M. Jorgolli, A. K. Shalek, M. H. Yoon, R. S. Gertner, and H. Park, Vertical nanowire electrode arrays as a scalable platform for intracellular interfacing to neuronal circuits, *Nature Nanotechnology*, vol. 7, pp. 180 184, Mar. 2012. (cited on page(s) 179, 189)

[35] S. E. A. Gratton, P. A. Ropp, P. D. Pohlhaus, J. C. Luft, V. J. Madden, M. E. Napier, and J. M. De Simone, The effect of particle design on cellular internalization pathways, *PNAS*, vol. 105, pp. 11613 11618, Aug. 2008. (cited on page(s) 180, 186)

[36] E. Fernández-Rosas, R. Gómez-Martínez, E. Ibanez, L. Barrios, M. Duch, J. Esteve, J. A. Plaza, and C. Nogués, Internalization and cytotoxicity analysis of silicon-based microparticles in macrophages and embryos, *Biomedical Microdevices*, vol. 12, pp. 371 379, June 2010. (cited on page(s) 50, 51, 70, 84, 97, 130, 132, 183)

[37] S. D. Conner and S. L. Schmid, Regulated portals of entry into the cell, *Nature*, vol. 422, pp. 37 44, Mar. 2003. (cited on page(s) 186, 189)

[38] H. W. Fisher and T. W. Cooper, Electron microscope studies of the microvilli of HeLa cells, *The Journal of Cell Biology*, vol. 34, pp. 569 576, Aug. 1967. (cited on page(s) 187)

[39] K. E. Fischer, A. Jayagopal, G. Nagaraj, R. H. Daniels, E. M. Li, M. T. Silvestrini, and T. A. Desai, Nanoengineered surfaces enhance drug loading and adhesion, *Nano Letters*, vol. 11, pp. 1076 1081, Mar. 2011. (cited on page(s) 189)

[40] T. Berthing, S. Bonde, C. B. Sø rensen, P. Utko, J. Nygå rd, and K. L. Martinez, Intact mammalian cell function on semiconductor nanowire arrays: new perspectives for cell-based biosensing, *Small*, vol. 7, pp. 640 647, Mar. 2011. (cited on page(s) 189, 201)

[41] X. Xie, A. M. Xu, M. R. Angle, N. Tayebi, P. Verma, and N. A. Melosh, Mechanical model of vertical nanowire cell penetration, *Nano Letters*, vol. 13, pp. 6002 8, Dec. 2013. (cited on page(s) 189)

Chapter 6

Nanowire Silicon Barcodes for extracellular tagging of living mouse embryos

Contents

6.1 Abstract

In the last chapter we have succeeded in combining the advanced features of our polysilicon barcodes as single cell labels and the adhesion capabilities of silicon nanowires. So, here I report the design, technological development and characterization of polysilicon microbarcodes featuring, in this case, silicon nanowires as extracellular physical attachment labels to identify and track living mouse embryos. Although some typical applications of silicon nanowires integrated in microsystems are focused on achieving a Cell-on-a-Chip strategy, we are interested in obtaining Chip-on-a-Cell systems. Chips are attached to the outer surface of a mouse embryo to avoid the direct contact between the chip and the inner cell membrane. Two attachment methodologies, Rolling and Pushpin, which allow two entirely different levels of applied forces to attach the chips to living embryos are evaluated. The former consists of rolling the mouse embryos over one barcode with the silicon nanowires facing upwards, while in the latter the barcode is pushed against the embryo with a micropipette. The effect on *in vitro* embryo development and the retention rate related to the calculated applied forces are stated. Scanning electron microscopy inspection, which allowed a high resolution imaging, also confirms the physical attachment of the nanowires with some of them piercing or wrapped by the zona pellucida (the cover membrane that surrounds embryos). The behavior of the silicon nanowires attached to the embryo membrane is also investigated. For instance, parameters such as the radii of curvature and stresses reached by the nanowires are exhaustively studied, as highly bent silicon nanowires are observed during the attachment experiments.

6.2 Introduction

In this chapter the adhesive capabilities of silicon nanowires to be used as physical nanovelcros to attach polysilicon barcodes to living mouse embryos for their individual identification is explored. As stated in the former chapters, (Chapters 1, 2 and 3) bio-labeling and tracking show relevant scientific and commercial applications.[1–3] Our line of research is focused, specifically, in one of these possible bio-applications, the assisted reproductive technologies (ART) (Chapter 2). Successful development of embryos cultured in groups has been extensively recognized in several species,[4] but then, efficient embryo identifications are required allowing the collective culture of embryos while their identification is preserved. Therefore, single embryo labeling and tracking, is still a challenge in such applications. Many different approaches from the fields of micro- and nanotechnologies have been proposed for cell labeling.[1, 5–9] However, many of them show complex fabrication technologies, can be harmful for living cells, or are designed to discriminate subpopulations of cells mixed in the same culture but not for individual cell labeling.

Along these lines, our group has a strong background (as it can be observed in the last chapters) in single embryo-labeling and tracking using both extra- and intracellular micron-sized polysilicon barcodes through microelectronic-based technologies.

Taking advantage of the existence of the zona pellucida (ZP) (an external glycoprotein coat the embryo is surrounded by) (Figure 6.1a), our group first investigated whether silicon-based polysilicon barcodes could be microinjected into the perivitelline space (area between the ZP and the plasma membrane) of mouse embryos.[10–12] In these experiments mouse embryo labeling was demonstrated, however, an important limitation for individual embryo identification consists in avoiding a direct contact between the membrane of the embryo and the microbarcodes, as in case the embryo is subsequently transferred to a recipient female the microbarcodes could interfere with its implantation on the uterine wall.

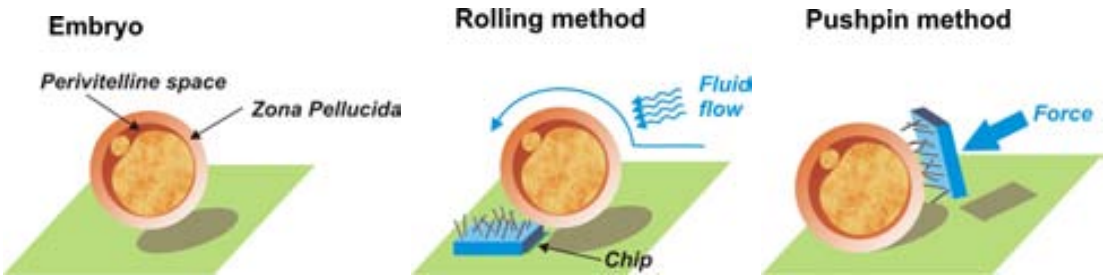

(a) (b) (c)

Figure 6.1: **Schematic drawing of an embryo and the two different methods of attachment, Rolling and Pushpin.** a) A schematic representation of the mouse embryo. The embryo is surrounded by a glycoprotein coat called Zona Pellucida (ZP). The perivitelline space is the space between the ZP and the cell membrane of the embryo. b) Rolling method. The embryos are rolled by a gentle fluid flow to overpass the barcode with the nanowires facing upwards. c) Pushpin method. A barcode with the nanowires facing the embryo is pushed towards the ZP using an external force.

Consequently, from that moment, our strategy was focused on locating our labels on the external part of the ZP. Thus, a chemical functionalization of the barcodes to attach them to the ZP surface was positively tested (see Chapter 2).[13, 14] Wheat germ agglutinin (WGA) was demonstrated to chemically bind the polysilicon barcodes to the external surface of the ZP, rich in specific carbohydrates, avoiding direct contact between the barcodes and the living eggs. In all cases, the studied embryos were developed until the blastocyst stage and a high retention and identification rates without showing negative effects on the embryo development were observed.[10, 15–17]

Although the chemical adhesion of barcodes to the ZP was successfully demonstrated, in the present work we explored the possibility of a physical attachment between the polysilicon barcodes and the living embryos through silicon nanowires, avoiding a chemical functionalization. Micro- and nanostructured substrates have been widely reported to enhance cell adhesion.[18, 19] For instance, nanowires have been widely used to deliver specific compounds directly in the intracellular medium or as sensing platforms, where nanowire surfaces are responsible to attach cells on a chip.[20, 21] In this sense, silicon nanowires have been reported to be interesting for biological applications because of their slow degradation, their variety of

well-characterized nanowire fabrication techniques and remarkably they could be integrated into other silicon-based chips, such as Microelectromechanical Systems (MEMS).[22]

Summarizing, in this chapter we develop a Chip-on-an-Cell strategy, as free-standing polysilicon microbarcodes decorated with hundreds of silicon nanowires attached physically to the ZP of mouse embryos is developed. In order to discern this assumption, two different attachment methods with two different levels of applied forces between the barcode and the embryo are investigated: Rolling and Pushpin methods (Figure 6.1b and c). Differences in retention rates of the anchored barcodes by the two methods, their effects on embryo *in vitro* development and on the nature of the silicon nanowires are studied.

6.3 Design of Nanowire Silicon Barcodes as physical extracellular labels to identify and track living embryos

In this chapter a novel device which combines our polysilicon barcode design (see section 2.3.2 in Chapter 2) with a controlled growth of silicon nanowires on the surface of the barcode is presented.

In refering to the polysilicon barcode and as noted in chapters 2 and 3, the design of barcode type D is the most robust, the easiest to identify and is alone dealt with in the involved experiments in this chapter (see figure 2.3).

Furthermore, in this case we go one step forward and a novel line of polysilicon barcodes featured silicon nanowires is showed (Figure 6.3). The main advantage of having silicon nanowires featuring our polysilicon barcodes is a broad number of applications, such as future intracellular sensing through the chemical functionalization of the silicon nanowires or the operation of silicon nanowire chips as intracellular drug delivery systems.

These devices can be used as single cell labels taking advantage of the adhesion capabilities of nanowires, as they will act as a kind of physical nanovelcro (random nanowires will be obtained due to the rough surface of polysilicon, see figure 5.1) to attach the polysilicon barcodes to the zona pellucida to identify and track living embryos.

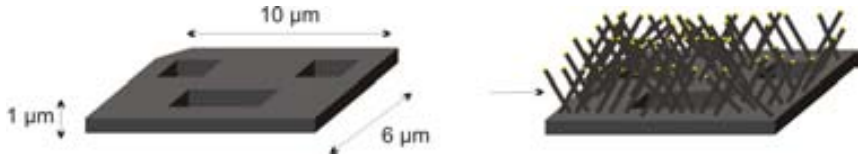

Figure 6.2: **Design of silicon nanowire barcodes**. Design and dimensions of silicon nanowire barcodes

6.4 Technological development of Nanowire Silicon Barcodes

Silicon nanowire barcodes technology was based on the deposition of a polysilicon structural layer combined with a vapor-liquid-solid deposition process for the silicon nanowire growth. A 100 mm p-type silicon wafers were used as substrates, where a 1 μm-thick silicon oxide layer and a 1 μm-thick polysilicon layer were deposited as sacrificial and device layers, respectively (Figure 6.3a). A photolithographic process covering the wafer with photoresist by spin coating (Figure 6.3b), combined with a polysilicon dry etching process were performed to define the polysilicon barcodes (Figure 6.3c). Afterwards, the photoresist was removed. Silicon nanowires were grown via the vapor-liquid-solid mechanism (VLS) along the $< 111 >$ crystallographic directions *(Performed by NEMS and Nanofabrication Group, IMB-CNM, CSIC)*. Gold nanoparticles were selectively deposited on the polysilicon surfaces of the wafer by a galvanic displacement process (Figure 6.3d), as they were used as catalytic seeds for the nanowire synthesis.[23] This method ensures catalyst nanoparticle deposition only at silicon surfaces but not on silicon oxide, i.e. in our case silicon nanowires will only grow over the polysilicon barcodes and not over the silicon oxide underneath. For galvanic displacement deposition of the gold catalyst nanoparticles, the devices were immersed in a microemulsion formed by an aqueous solution which contains potassium gold (III) chloride (0.01 M $KAuCl_4$) and a low concentration of hydrofluoric acid (0.2 M HF) with a mixture of n-heptane and dioctyl sodium sulfosuccinate (AOT). The mixture of this two components results in a microemulsion of inverse micelles. The diameter of the resulting gold nanoparticles is directly proportional to the diameter of the micelles, providing a way of controlling the diameter of the nanowires. The silicon nanowires were grown in a chemical vapor deposition tube furnace at 750 - 850^{o}C by a mixture of $SiCl_4$ precursor gas (30 sccm - 80 sccm), BBr_3 dopant gas (0 sccm - 1 sccm) and Ar - 10% H_2 carrier gas (250 sccm - 300 sccm) for 60 seconds (Figure 6.3e). The length of the nanowires was fixed to $\sim$ 3 μm and the range of their radius was from 20 nm to 70 nm. Finally, devices were released by silicon oxide sacrificial layer etching in vapors of 49% HF for 40 minutes (Figure 6.3f). The released barcodes were suspended by ultrasounds in ethanol, collected and centrifuged at 14000 rpm for 5 minutes (MiniSpin Plus).

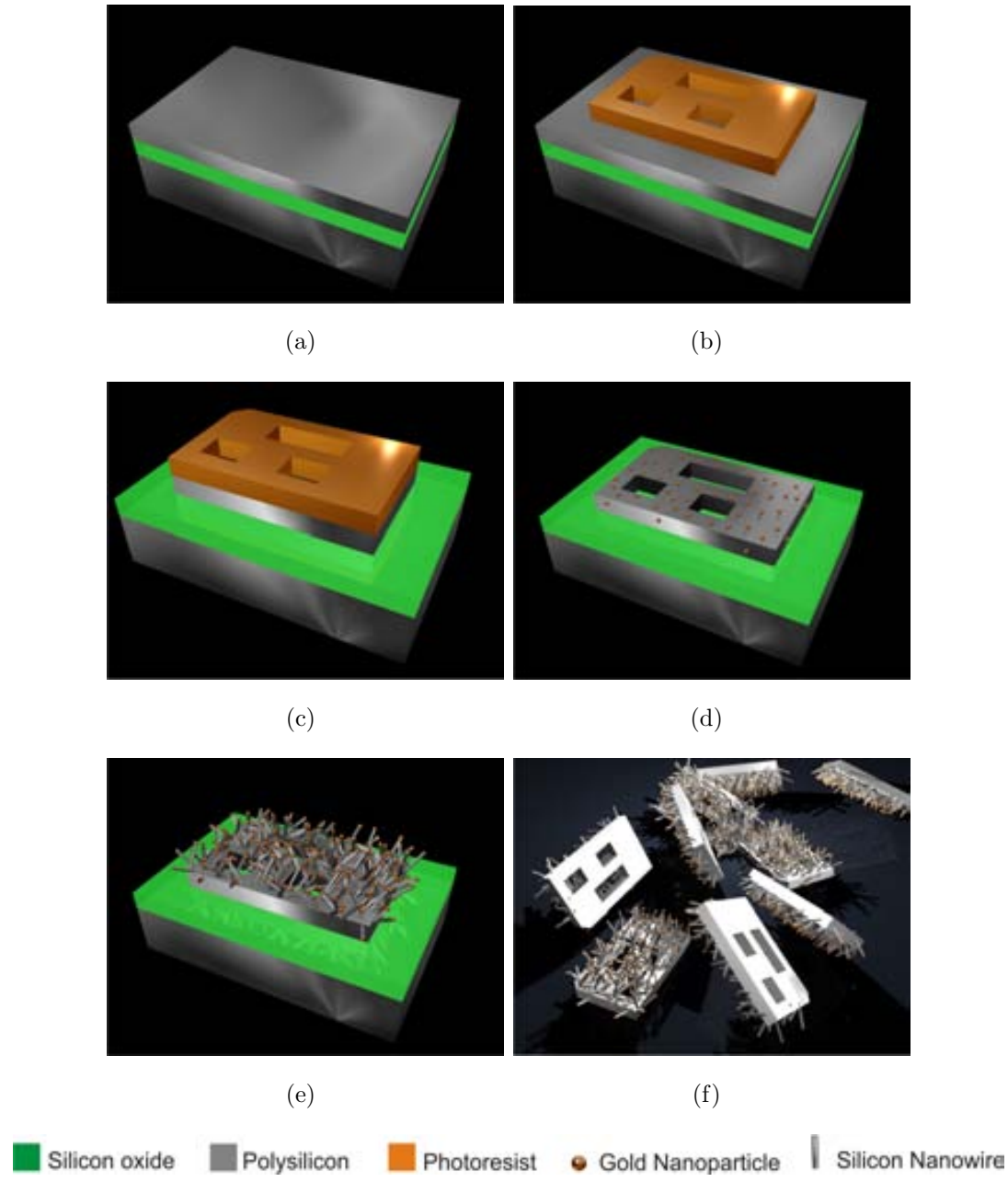

Figure 6.3: **Fabrication of the polysilicon barcodes decorated with silicon nanowires.** a) A 1 μm-thick polysilicon layer deposited on a 1 μm-thick silicon oxide. b) Photolithographic step to define the barcode dimensions. c) Polysilicon dry etching to pattern the chips. d) Selective gold nanoparticle deposition on the polysilicon layer. e) Silicon nanowire growth via vapor-liquid-solid mechanism (VLS). f) Release of the silicon nanowire barcodes from the wafer by wet etching.

6.5 Characterization of fabricated Nanowire Silicon Barcodes

A 2 μl-drop of 96% ethanol with barcodes in suspension was dried and inspected using scanning electron microscopy (Auriga Zeiss, Germany). A manufactured device, still on the wafer and before silicon nanowire growth, is shown in figure 6.4a. Images after the silicon nanowire growth are shown in figure 6.4b and c, before and after the sacrificial etching, respectively. Zoom images of released barcodes facing upwards and downwards are presented in figure 6.4d and e. In these conditions, polysilicon barcodes decorated with straight silicon nanowires were obtained (Figure 6.4f).

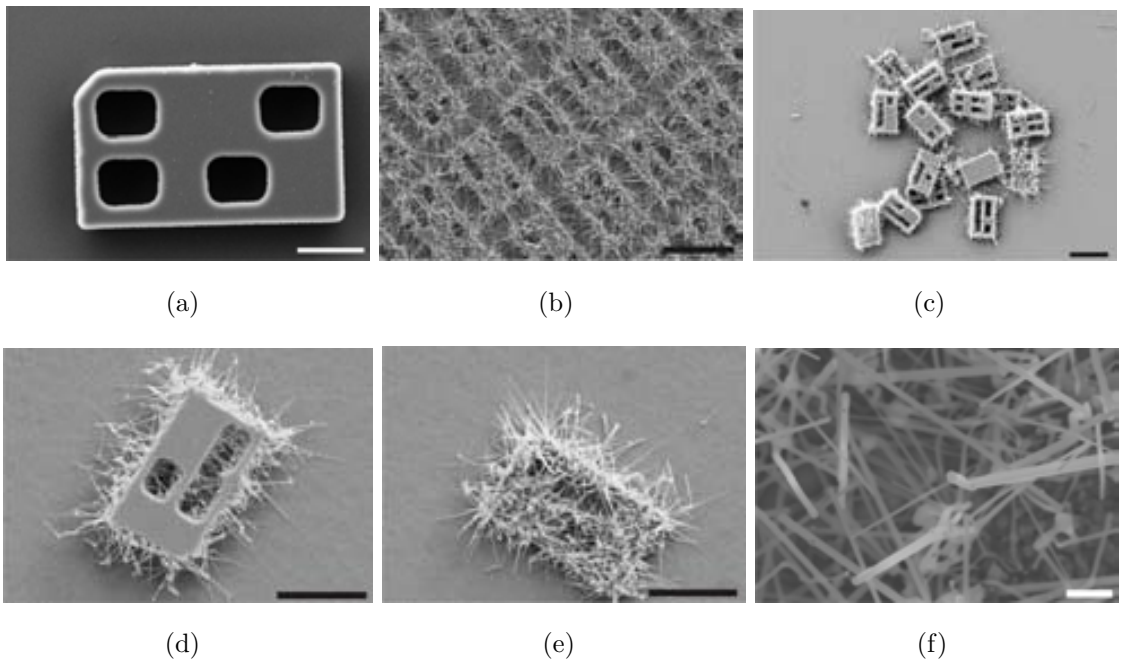

Figure 6.4: **Scanning electron microscopy images of the fabricated barcodes.** a) A polysilicon barcode before the nanowire growth. Scale bar = 2.5 μm. b) Polysilicon barcodes after the nanowire growth at wafer level and (c) after their release. Scale bars = 10 μm. d) A zoom image of a polysilicon barcode facing downwards and e) upwards. Scale bars = 5 μm. f) A detailed SEM image of straight nanowires on the barcode top surface. Scale bar = 500 nm.

6.6 Nanowire Silicon Barcode attachment to living mouse embryos

Two methods, Rolling and Pushpin, to attach silicon nanowiere barcodes to the outer surface of each mouse embryo ZP were tested. Mouse embryo collection and bio-experiments were performed by *Department of Cellular Biology, Physiology and Immunology, Universitat Autònoma de Barcelona*.

Animal care and procedures required in this study were carried out according to the protocols approved by the Ethics Committee on Animal and Human Research of the Universitat Autònoma de Barcelona and by the Departament d Agricultura, Ramaderia i Pesca of the Generalitat de Catalunya.

Pronuclear (PN) embryos from superovulated female mice (age, 8-12 weeks) were employed in this study. PN embryos were collected and incubated during 5 - 10 min at 37°C in Hepes-buffered potassium simplex optimized medium (H-KSOM.)[24] After denudation, PN embryos were washed twice in fresh H-KSOM.

6.6.1 Rolling method

i Nanowire Silicon Barcode attachment during Rolling Method

In the Rolling method barcodes were placed by micromanipulation, a technique commonly used in fertilization, in a drop of KSOM-H with the silicon nanowires oriented upwards.

Then, embryos were individually rolled over one barcode under a stereoscopic microscope using a mouth-controlled aspiration system with a glass capillary with 150 μm of inner diameter. The flow generated by the micropipette was responsible for making the embryo roll (Figure 6.5).

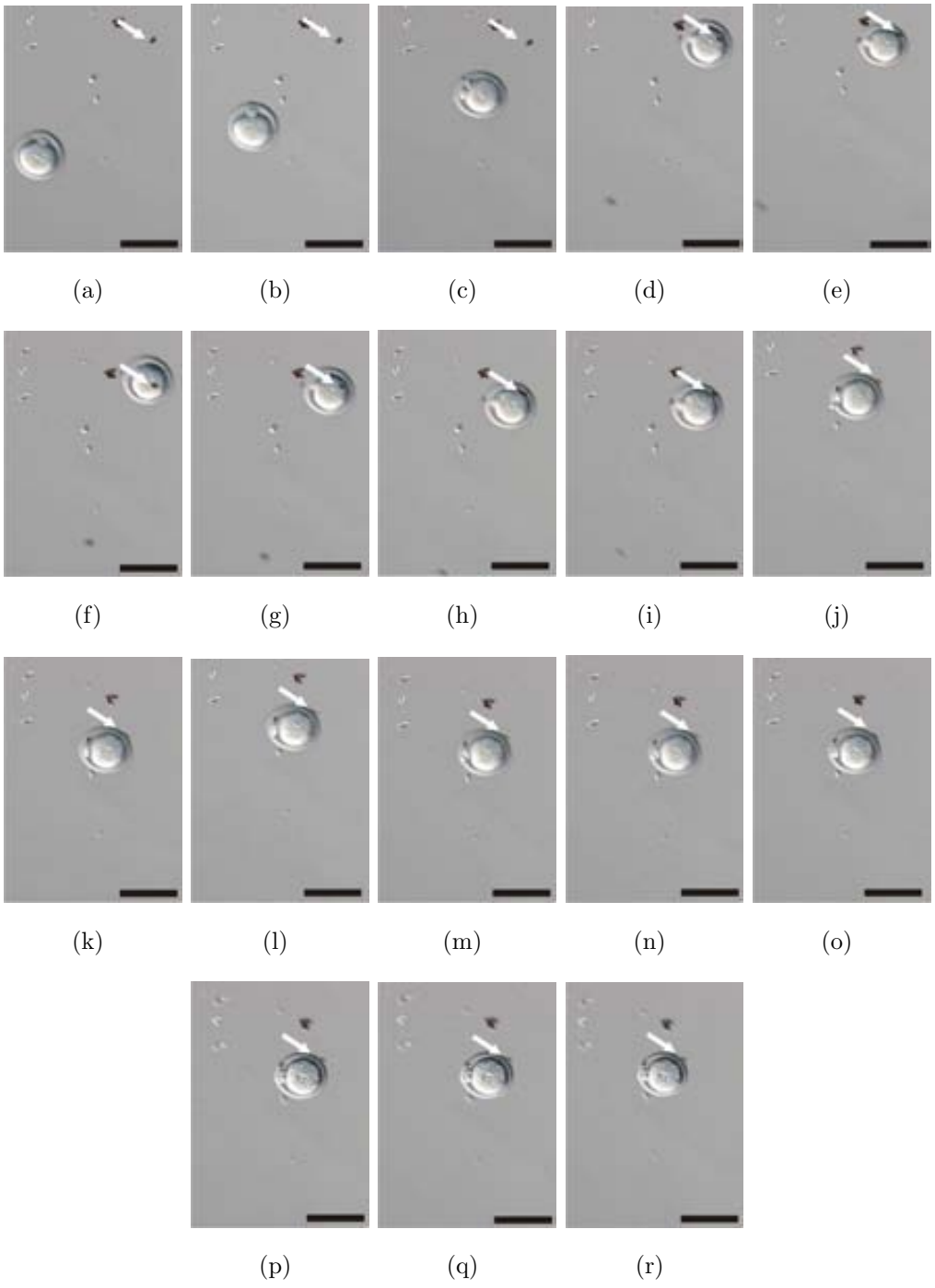

Figure 6.5: **Rolling method.** Optical images of the Rolling method taken with an inverted optical microscope showing an embryo overpassing a barcode (white arrows) with the nanowires facing upwards at (a) 0.00 s, (b) 1.01 s, (c) 2.01 s, (d) 2.03 s, (e) 3.27 s, (f) 3.89 s, (g) 4.99 s, (h) 6.06 s, (i) 7.18 s, (j) 7.25 s, (k) 8.32 s, (l) 9.39 s, (m) 9.45 s, (n) 10.51 s, (o) 10.54 s, (p) 11.57 s, (q) 11.61 s, (r) 11.63 s. Scale bars = 50 μm.

ii Calculation of the applied force reached during the Rolling method

The maximum force between the embryo and the barcode during the Rolling method was calculated on the basis of the embryo mass and the upward buoyant force that is exerted on the embryo immersed in the fluid (culture medium) (Figure 6.6).

Figure 6.6: **Schematic representation of the participating forces during the Rolling method.** Two forces are applied to the embryo: gravity, due to embryo weight (orange arrow) and the buoyant force due to the medium (blue arrow).

Firstly, we should have calculated the weight of the mouse embryos by determining the volumen of a mouse embryo on an optical microscope, where r_{Emb} is the radius of the embryo.

$$Weight_{Emb} = V_{Emb} \cdot \rho_{Emb} \cdot \mathrm{g}$$

$$V_{Emb} = 4/3 \cdot \pi \cdot r_{Emb}^3$$

The embryo density (ρ_{Emb}) of the mouse embryo was calculated by using a method equivalent to the falling sphere viscometers (performed by *Department of Cellular Biology, Physiology and Immunology, Universitat Autònoma de Barcelona*) and applying the following formula given by the Stoke´s law. 8 embryos (so-called spherical particles) were placed in a PBS medium and allowed to descend through the liquid until they reached terminal velocity (*vel*). The terminal velocity was calculated by the time they took to descend 10 mm (Table 6.1).

$$\rho_{Emb} = \frac{9 vel \mu_{PBS}}{2 r_{Emb}^2 g} + \rho_{PBS}$$

Where μ_{PBS} was the viscosity of the PBS (0.001002 Kg/m·s), ρ_{PBS} was the density of the PBS (1007.7571 Kg/m^3) and g was the gravitational acceleration.

Embryo (n)	Time (s)	Length (m)	Velocity (m/s)	Radius of the Embryo (m)	Density of the Embryo (Kg/m^3)	Volume of the Embryo (m^3)	Mass of the Embryo (Kg)
1	19.32	0.01	$5.18{\cdot}10^{-4}$	$5.19{\cdot}10^{-5}$	1096	$5.87{\cdot}10^{-13}$	$6.43{\cdot}10^{-10}$
2	18.10	0.01	$5.52{\cdot}10^{-4}$	$5.01{\cdot}10^{-5}$	1109	$5.25{\cdot}10^{-13}$	$5.83{\cdot}10^{-10}$
3	20.04	0.01	$4.99{\cdot}10^{-4}$	$5.18{\cdot}10^{-5}$	1093	$5.82{\cdot}10^{-13}$	$6.37{\cdot}10^{-10}$
4	24.18	0.01	$4.14{\cdot}10^{-4}$	$5.28{\cdot}10^{-5}$	1076	$6.16{\cdot}10^{-13}$	$6.63{\cdot}10^{-10}$
5	20.79	0.01	$4.81{\cdot}10^{-4}$	$5.16{\cdot}10^{-5}$	1091	$5.76{\cdot}10^{-13}$	$6.28{\cdot}10^{-10}$
6	25.94	0.01	$3.86{\cdot}10^{-4}$	$5.03{\cdot}10^{-5}$	1078	$5.33{\cdot}10^{-13}$	$5.74{\cdot}10^{-10}$
7	18.37	0.01	$5.44{\cdot}10^{-4}$	$5.03{\cdot}10^{-5}$	1107	$5.34{\cdot}10^{-13}$	$5.91{\cdot}10^{-10}$
8	19.00	0.01	$5.26{\cdot}10^{-4}$	$5.06{\cdot}10^{-5}$	1102	$5.44{\cdot}10^{-13}$	$5.99{\cdot}10^{-10}$
Average	20.72	0.01	$4.90{\cdot}10^{-4}$	$5.12{\cdot}10^{-5}$	1094	$5.62{\cdot}10^{-13}$	$6.15{\cdot}10^{-10}$
Error (±)	2.85*	0.001	$0.83{\cdot}10^{-4}$	$0.99{\cdot}10^{-5*}$	15	$0.33{\cdot}10^{-13}$	$0.37{\cdot}10^{-10}$

Table 6.1: **Embryo weight values obtained from the falling experiments.** *Standard deviation

Eventually, the calculated density for a mouse embryo was $\rho_{Emb} = 1094\ Kg/m^3$, the volume of a mouse embryo was $V_{Emb} = 5.62{\cdot}10^{-13}\ m^3$ and its calculated weight was $m_{Emb} = 6.15{\cdot}10^{-10}$ Kg.

Then, the force between the embryos and the barcodes was calculated by subtracting the buoyancy force, from the weight of the embryo.

$$F_{Bouyant} = Volume_{Emb} \cdot \rho_{KSOM-H} \cdot \mathrm{g}$$

$$F_{Rolling} = Weight_{Emb} - F_{Bouyant}$$

Considering the size and density of the embryos a maximum force of $F_{Max.Rolling}$ = $5.63 \cdot 10^{-10}$ N between the embryo and the barcode was calculated (Figure 6.7). Although we did not appreciate any observable deformation of the embryo, these tiny forces were high enough to attach the barcode, through the nanowires, to the living embryos in less than a second.

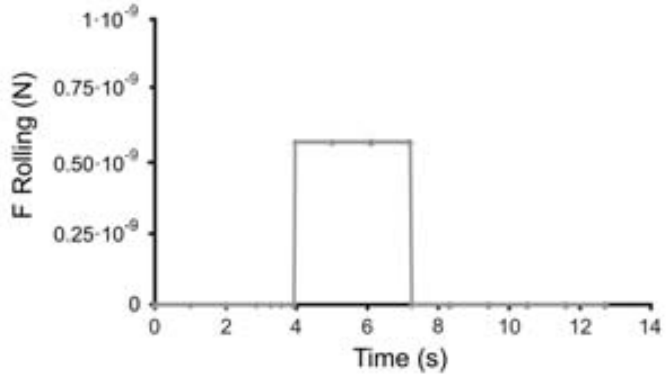

Figure 6.7: **Applied force between the embryo and the silicon nanowire barcode during the Rolling method.** A step function was assumed for the applied force between the embryo and the barcode, as the force was only applied while the embryo was over the barcode.

6.6.2 Pushpin method

i Nanowire Silicon Barcode attachment by Pushpin method

In the pushpin method, barcodes were attached to embryos by micromanipulation techniques. An embryo was held with a holding micropipette using gentle suction. Then, a barcode was firmly subjected at the tip of the transfer micropipette (5 µm of inner diameter) with the nanowires facing the embryo. The transfer micropipette with the barcode was oriented uniaxially to the holding micropipette, and it was carefully pushed against the ZP (Figure 6.8). This experiment was performed by *Department of Cellular Biology, Physiology and Immunology, Universitat Autònoma de Barcelona.*

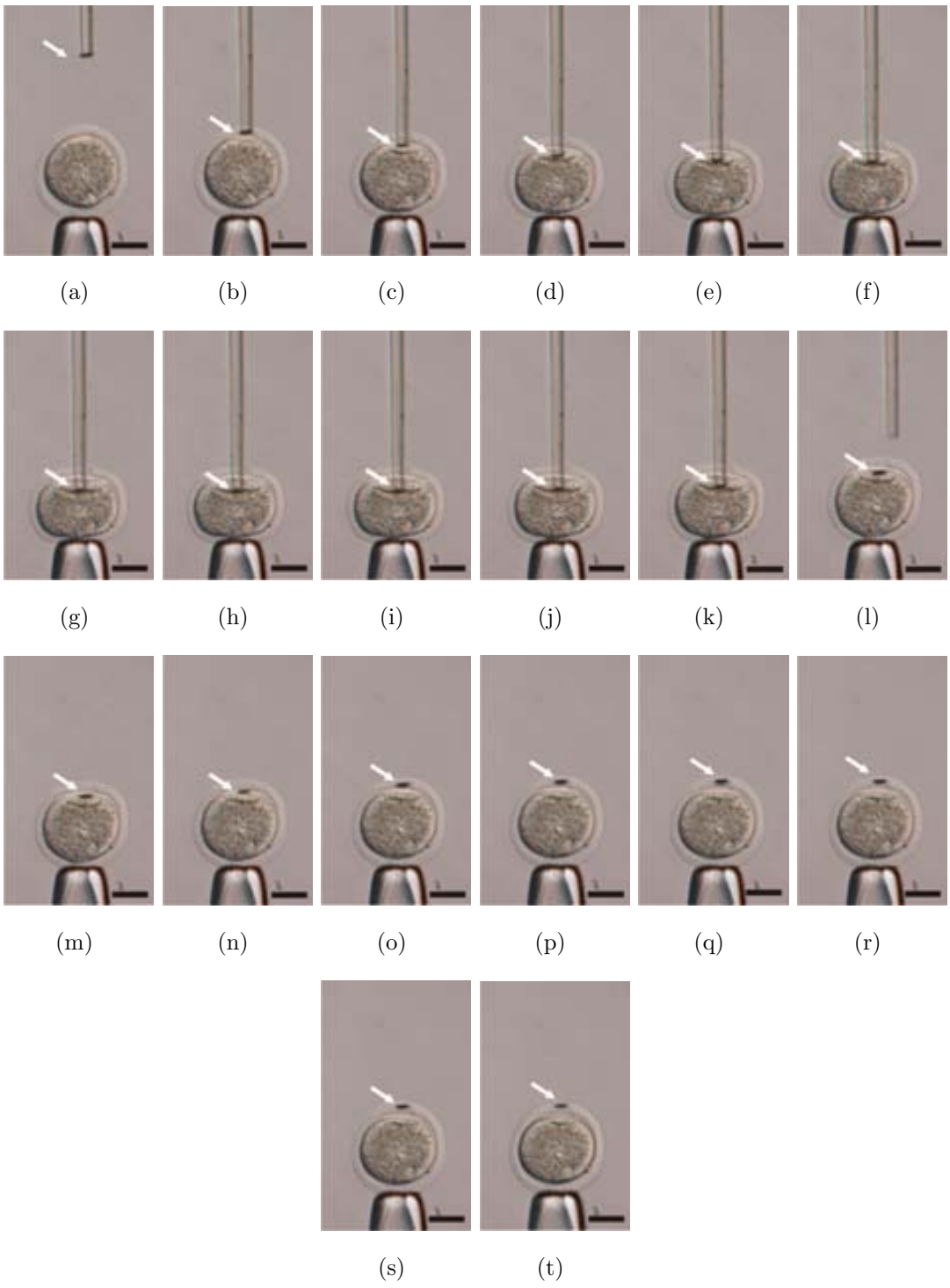

Figure 6.8: **Pushpin method.** Images of the Pushpin method, taken on an optical microscope, showing a barcode (white arrow) with the nanowires towards the embryo and fixed at the tip of a pipette pushing the ZP at (a) 0.00 s, (b) 4.61 s, (c) 5.04 s, (d) 5.27 s, (e) 5.74 s, (f) 6.07 s, (g) 6.42 s, (h) 7.39 s, (i) 8.03 s, (j) 8.59 s, (k) 9.18 s, (l) 9.57 s, (m) 9.96 s, (n) 10.38 s, (o) 10.99 s, (p) 11.35 s, (q) 11.70 s, (r) 12.36 s, (s) 12.94 s, (t) 14.09 s. Scale bars = 25 μm.

ii Calculation of the applied force reached during the Pushpin method

The maximum force between the embryo and the barcode during the Pushpin method was calculated starting from the basis of the reported Young s modulus of the ZP in mouse embryos at PN stage (Y_{ZP} = 42200 Pa) and the measured embryo-deformation caused by the applied force (Figure 6.9a). Then, we were able to estimate the applied force by the formula reported by Sun et al (Figure 6.9b),[25] which considers the ZP as a thin film and assumes that the inner cytoplasm provides a hydrostatic pressure on the membrane.[25, 26]

The estimated maximum applied force between the embryo and the barcodes using the Pushpin method was $F_{Max.Pushpin} = 9.36{\cdot}10^{-6}$ N (Figure 6.10). Using this method we observed a large deformation of the embryo, comparable with deformations obtained during artificial fertilization procedures.

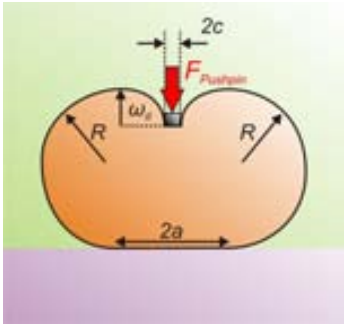

(a)

$$F_{Pushpin} = \frac{2\cdot\pi\cdot Y_{ZP}\cdot h\cdot\omega_d^3}{a^2(1-\upsilon_{ZP})}\left[\frac{3-4\left(\frac{c}{a}\right)^2+\left(\frac{c}{a}\right)^4+2\cdot\ln\left(\frac{c}{a}\right)^2}{\left(1-\left(\frac{c}{a}\right)^2\right)\left(1-\left(\frac{c}{a}\right)^2+\ln\left(\frac{c}{a}\right)^2\right)^3}\right]$$

(b)

Figure 6.9: **Schematic representation of the participating forces during the Pushpin method.** a) Embryo-deformation caused by the applied force, where the geometric parameter, ϖd, was measured from the optical images in figure 6.8. The constant values were h = 6.6 μm for the thickness of the ZP and c = 5 μm as effective indenter radius. b) The applied force between the barcode and the embryo was approximated by the biomechanical membrane model described by Sun et al.[25] Elastic modulus (Y_{ZP}) and the Poisson ratio (ν_{ZP}) were set to 42200 Pa[25] and 0.5[27] respectively. The constant value a was measured from the optical images in figure 6.8.

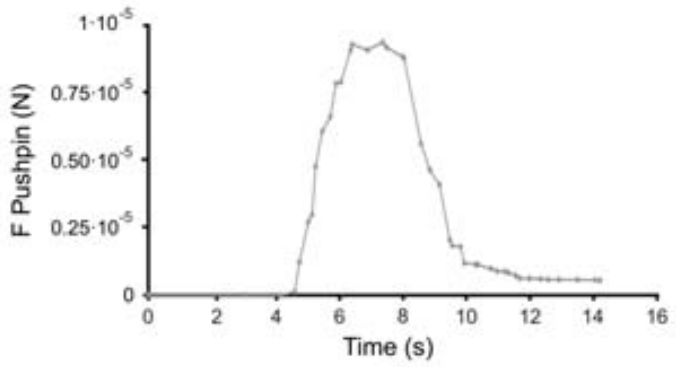

Figure 6.10: **Applied force between the embryo and the silicon nanowire barcode during the Pushpin method.** In this case a so-called gaussian function was obtained, as force tendency was almost symmetric. Although no force was applied after the second 9.57, a remaining pushin force between the seconds 10.32 - 14.09 was observed. This fact can be easily explained, as the calculation of the pushpin force was directly related to the embryo deformation and after the applied force a remaining deformation was clearly observed.

6.7 Biological studies: Embryo development

(Performed by Department of Cellular Biology, Physiology and Immunology, Universitat Autònoma de Barcelona).

Our previous studies demonstrated that the polysilicon microbarcodes do not interfere with the embryo development in mouse,[10, 15] bovine[16] and human embryos.[17] In this case we wanted to examine if the silicon nanowires integrated in polysilicon barcodes follow the same tendency. Optical images of the labeled mouse embryos were obtained to discard any effect in the embryonic process. In figure 6.11a it can be observed that the presence of attached barcodes on the ZP during the Rolling method do not affect in any significant manner their development. Consequently, the development of embryos labeled during the Pushpin method followed the same tendency and as in the previous method, we observed that the attached barcode does not affect the embryo development (Figure 6.11b).

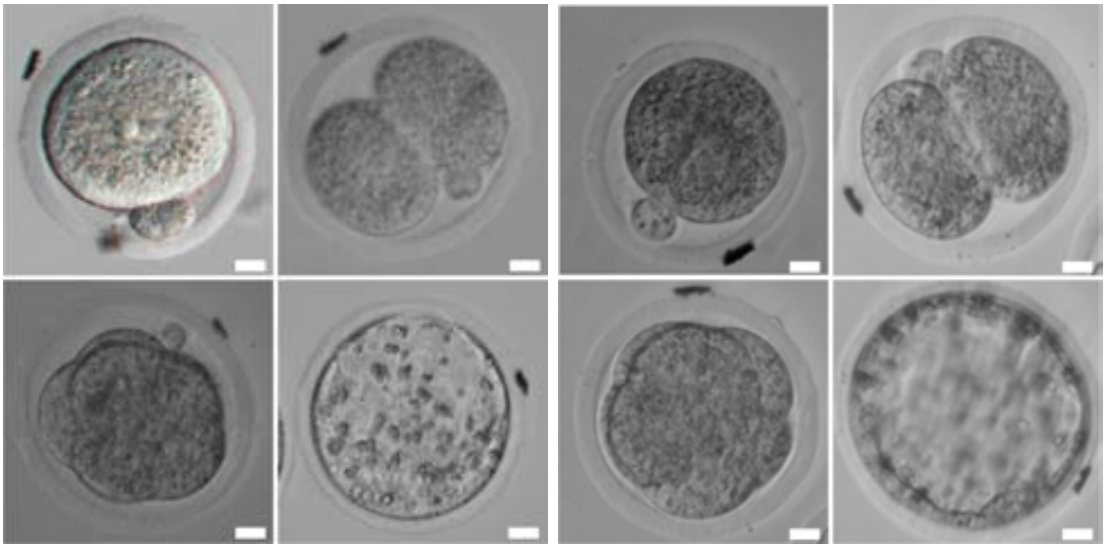

(a) (b)

Figure 6.11: ***In vitro* development of a mouse embryo with an attached silicon nanowire on its ZP.** a) Rolling method and (b) Pushpin method. (Top left: one-cell. Top right: 2-cell. Bottom left: Morula. Bottom right: Blastocyst). Scale bars = 10 μm.

We also quantified the effect of the attached barcodes on the embryo development. 50 embryos were cultured for 96 hours (blastocyst stage) in standard conditions (37^{o}C and 5% CO_2) in KSOM culture medium. The PN embryos, divided in three experiments, were used for each barcode attachment method and 42 embryos were used as controls. The obtained values (Rolling: 88.0%; Pushpin: 92.0%; control: 88.1%) suggested that neither the presence of the barcodes with integrated nanowires nor its attachment method affects the embryo developmental potential (Figure 6.12).

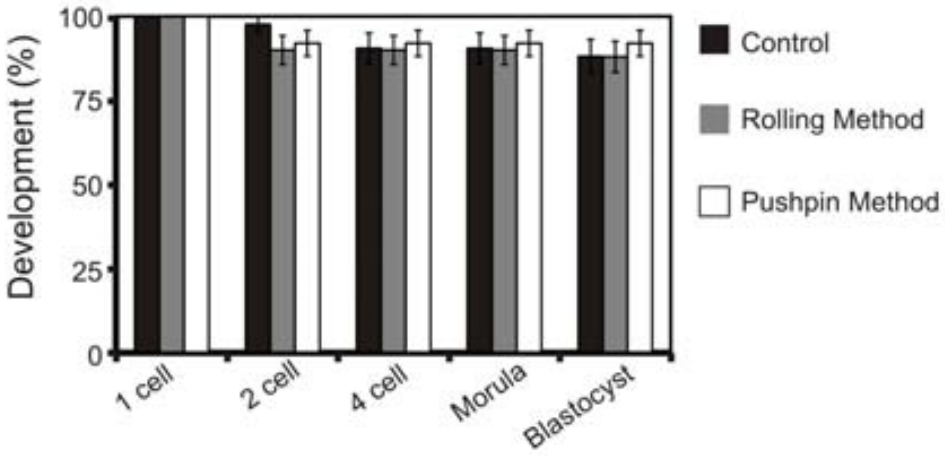

Figure 6.12: ***In vitro* development rates of mouse embryos with attached barcodes.** No significant differences from one-cell to blastocyst attachment rates were found among groups.

6.8 Validation of Silicon Nanowire Barcodes as physical extracellular embryo labels: Retention studies

In addition to the demonstration that the barcodes did not affect embryo viability, the capability of these methods for embryo labeling is evaluated. Every 24 hours embryos labelled with a unique barcode were inspected to assess the number of embryos that retained a barcode (retention rate) (Figure 6.13). Remarkably, an initial 100% retention rate was obtained for the two methods. After the initial stage, the barcode retention rate was higher for the Pushpin method compared to the Rolling method at all observation. The retention rate decreased following embryo development.

These results could be related to the reported fact that ZP becomes softer as the embryo matured.[28] At the end of the embryo culture (96 hours) $\sim$ 40% of the embryos from the Pushpin method still presented the barcode attached to their ZP, a value significantly higher than the 16% obtained for the Rolling method. Thus, there was a strong relation between the applied forces and the retention rate as the force was more than 10^4 times larger in the case of the Pushpin method ($F_{Max.Pushpin} = 9.36{\cdot}10^{-6}$ N) compared with the case of the Rolling method ($F_{Max.Rolling} = 5.63{\cdot}10^{-10}$ N).

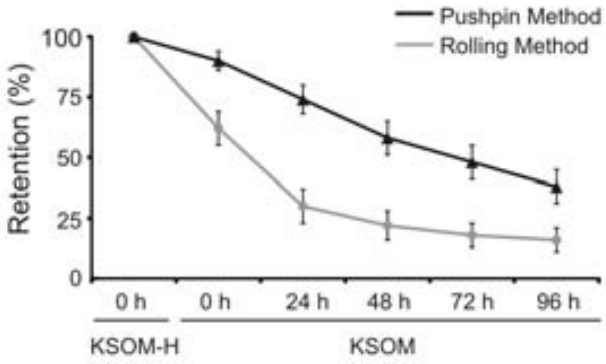

Figure 6.13: **Barcode retention rates for mouse embryos labeled with a silicon nanowire barcode by the Rolling and Pushpin methods.** The barcode retention rate was higher for the Pushpin method compared to the Rolling method at all observation.

Next the barcode bind to the ZP under a scanning electron microscope is investigated. Pronuclear embryos with barcodes attached to their ZP were dehydrated in a series of increasing ethanol concentrations until 100%. Finally, they were critical point-dried using CO_2 (CPD 030 critical point dryer Bal-Tec) and mounted onto aluminum stub. The samples were observed under a field emission scanning electron microscope (Merlin Zeiss, Germany).

The obtained images (Figure 6.14) clearly indicated that the attachment by both methods was mediated by the penetration of silicon nanowires inside the ZP. Images a-d in figure 6.14 show an attached barcode after the Rolling method. Meanwhile, images e-f were obtained after the Pushpin method. The images also show that the silicon nanowires extended underneath of the ZP (Figure 6.14f). Some of the nanowires pierced the ZP, figure 6.14e, in concordance with the puncture pressure for a tip pipette with a 5 μm diameter reported by Sun et al.,[25] considering the value of the applied forces in our experiments and the extraordinary small section of our nanowire (30 nm - 65 nm). As expected, our results showed that inorganic silicon nanowires can penetrate the ZP by force and being even more interesting, we did not observe any observable damage of the ZP.

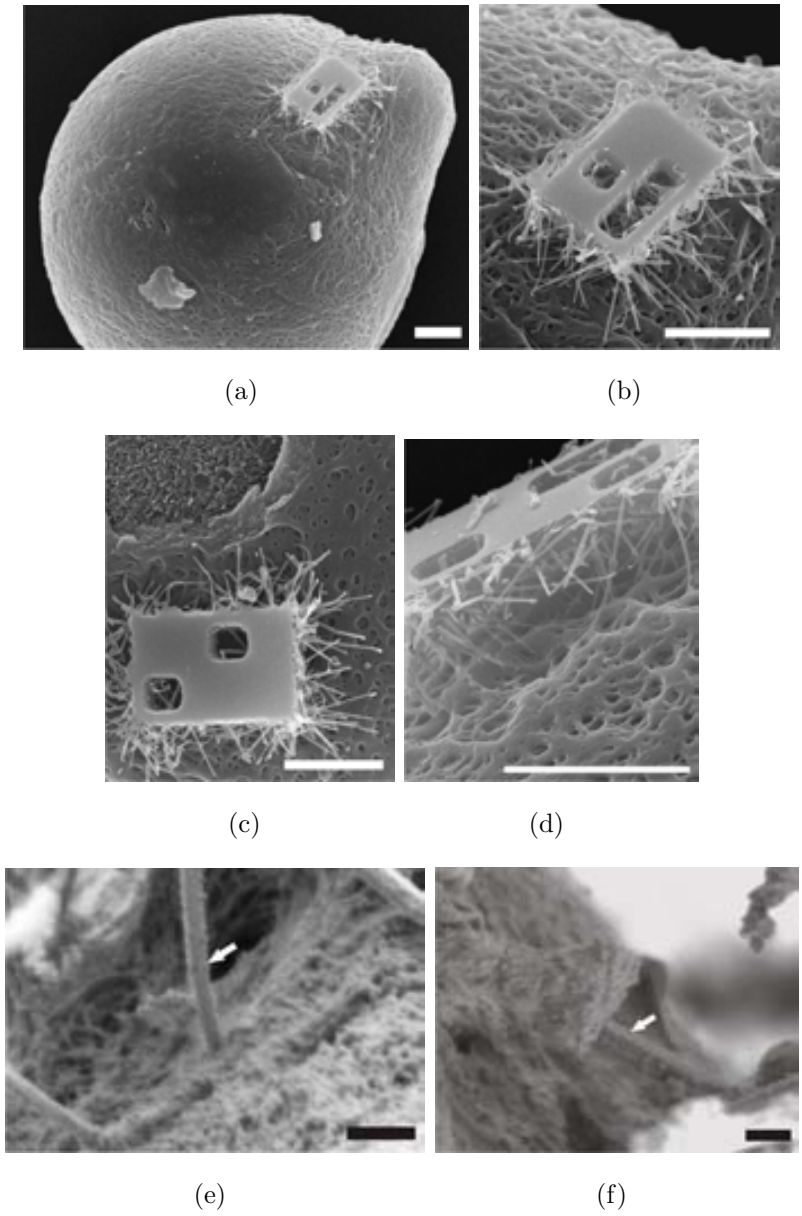

Figure 6.14: **Detailed scanning electron microscopy images of silicon nanowires attached to the Zona Pellucida.** SEM images of a) a barcode attached to the ZP of a mouse embryo by Rolling method and (b-d) detailed SEM images of attached barcodes performed by the same method. SEM images of attached barcodes performed by Pushpin method. e) Nanowire piercing the ZP. f) Nanowire wrapped by the ZP. White arrows point at interesting nanowires. White scale bars = 5 μm. Black scale bars = 200 nm.

6.9 Silicon Nanowire physical studies: Radii of curvature and stresses reached by the Silicon Nanowires during the Rolling and Pushpin methods

The SEM inspection also allowed us to perform a detailed observation of the silicon nanowires in contact with the ZP. In spite of very brittle nature of silicon, the images revealed nanowires showing an extraordinary bending (Figure 6.14). The deformation of the nanowire could have originated during the attachment and/or during the dehydration process of the embryos required for the SEM inspection. Nevertheless, at least dehydrated ZP can withstand the extraordinary forces needed to bend nanostructures with a high Young´s modulus ($Y_{Si(111)}$) = 188 GPa), to a radius of curvature that induce stresses up to the theoretical ultimate strength limit of silicon ($\sigma_{Si(111)}$ = 21GPa).[29]

The ideal strength of a specific material is defined as the critical level of external stress under which a lattice becomes structurally unstable and often this limit is far beyond the experimental reach, due to the presence of defects on the material.[29] However, when the defect density is made sufficiently small (such as in nanostructures), the strength of this material can approach the ideal strength. This is the reason why several works have been focused on finding the ultimate silicon strength by the study of the fracture of silicon nanowires. Tabid-Azar et al. reported a maximum bending stress 0.21 - 0.83 GPa for 140 - 200 nm-thick silicon nanowires,[30] Hoffmann et al. reported a maximum strength of 12 GPa for 100 - 200 nm-thick nanowires before fracture.[31] Recently Stan et al. reported fracture strength from 12 - 18 GPa (close to the ideal strength of Si) on 40 - 120 nm-thick silicon nanowires held by adhesion on flat surfaces and bent by AFM manipulations.[32]

Along these lines, our SEM images allowed us to observe a frozen state of many bent nanowires. Thus, we could calculate the value of the maximum stress (σ_{Max}) (Figure 6.15a) of some studied nanowires and the experimental determination of their radii of curvature (R) (Figure 6.15b). The absolute maximum stress ($\mid \sigma_{Max} \mid$) experienced in the nanowire section is located at the furthest points (r) from the neutral axis of the beam.

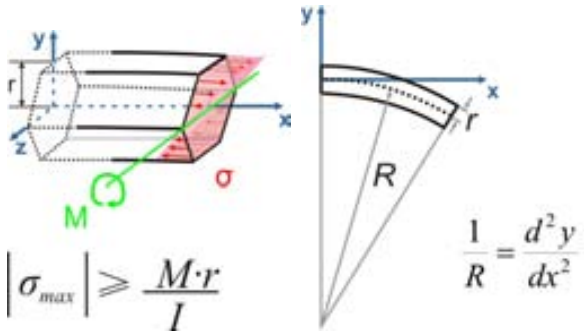

(a) (b)

Figure 6.15: **Schematic view of bending stress distribution and definition of the radius of curvature.** a) Bending stress distribution (σ) on a silicon nanowire, where M is the moment about the neutral axis (bending moment), I is the second moment of area about the neutral axis x (moment of inertia) and r is the perpendicular distance to the neutral axis (radius). b) Definition of the radius of curvature (R) of a bent nanowire.

In figure 6.16 it can be observed 25 types of shape-deformed silicon nanowires analyzed in this study.

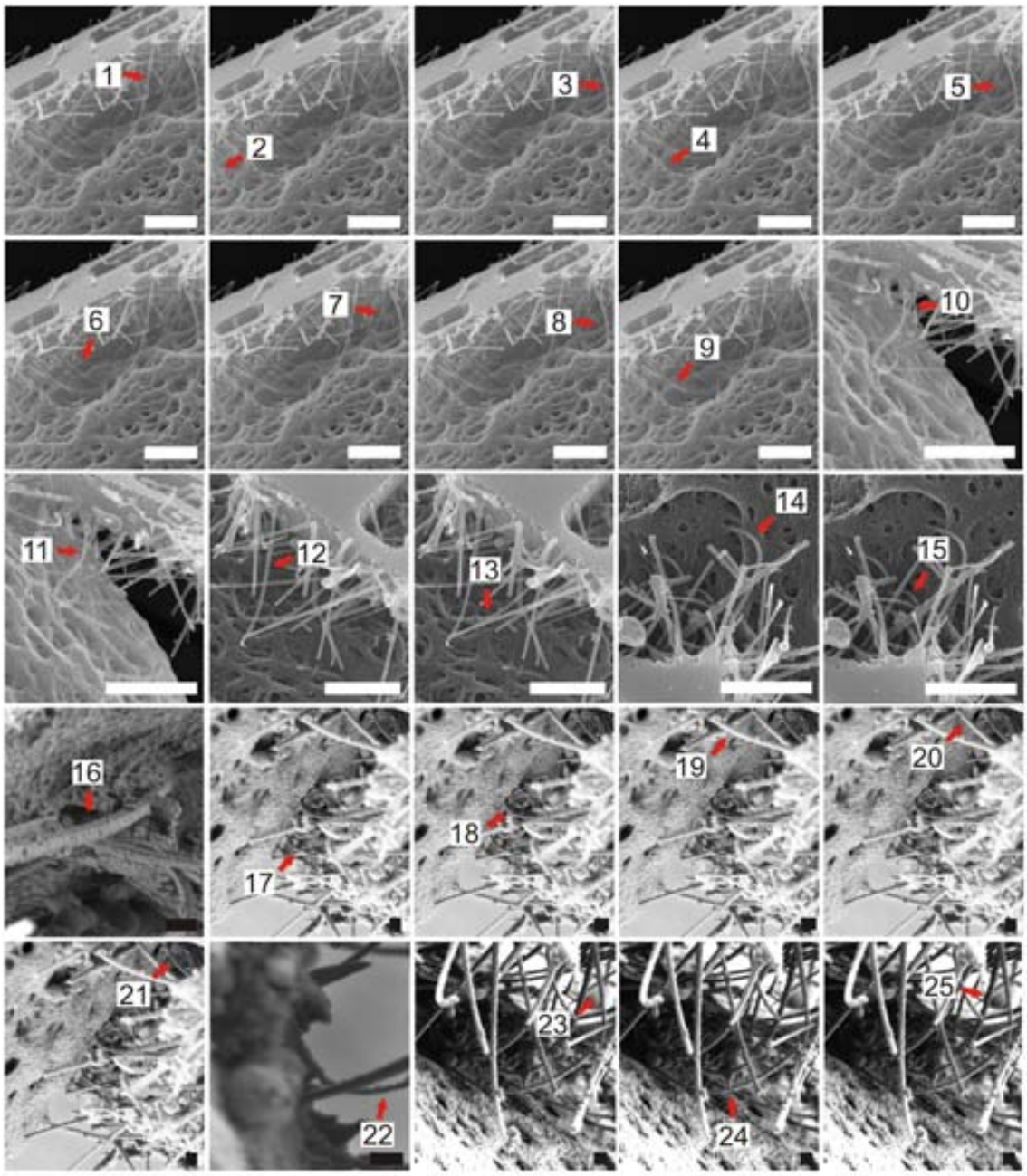

Figure 6.16: **Analyzed silicon nanowires during the studies of strength and radius of curvature.** From nanowire 1 to nanowire 15 correspond to those during Rolling method. While from nanowire 16 to nanowire 25 correspond to Pushpin method. White scale bar = 2 μm. Black scale bar = 200 nm.

The position of the studied silicon nanowires can be approximated by a 6^{th} degree polynomial with the help of a mathematical software and in addition can be used to obtain the length of the nanowire (x), the vertical displacement (y) and even the nanowire rotation (z). Using this metrology we could reproduce (using Finite Element Modelling, FEM) the deformation of the nanowire and obtained its distribution of bending stress (Figure 6.17)

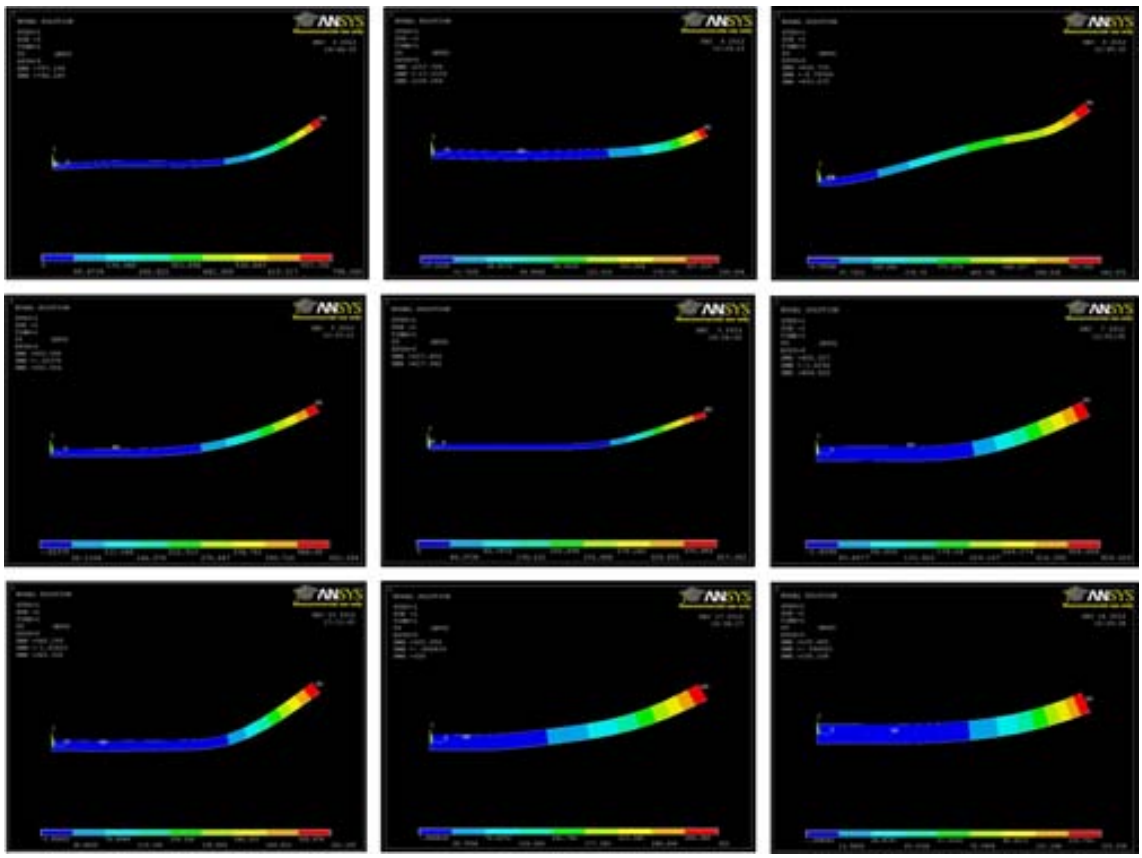

Figure 6.17: **Some simulated silicon nanowires using FEM.**

We can also simulate a specific silicon nanowire using finite element modelling and after that overlap the simulation over the scanning electron miscroscopy image of the same nanowire (Figure 6.18).

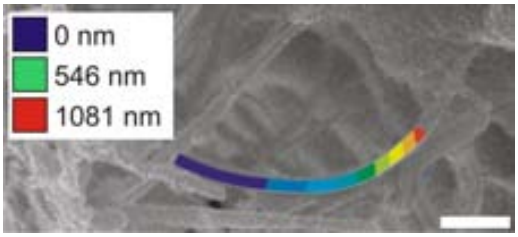

(a)

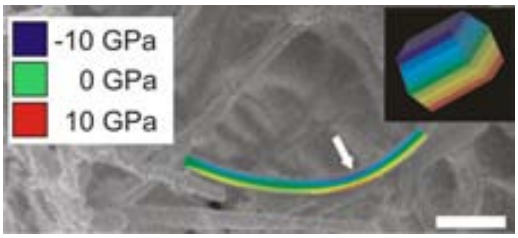

(b)

Figure 6.18: **Shape and stress simulation of bent silicon nanowires by FEM.** Scanning electron microscopy images where a bent nanowire and an overlay of the simulated result can be observed. a) Silicon nanowire simulation can perfectly reproduce the nanowire position and the same nanowire deformation. b) SEM image showing the bending stress along the nanowire. The bending stress was maximum at the point where the radius of curvature is smaller (white arrow) and the modulus of the stress is maximum at the top and bottom surface of the nanowire. Inset image is a zoom image of the FEM simulation where the stress value is maximum. Scale bars = 500 nm.

Next, we determined (from the SEM images) the maximum radii of curvature (R) of the bent nanowires (Figure 6.19a). Radii from few to hundreds of nanometers were observed. Although, the bending stress depends on the radius of curvature it also depends on the radii of the nanowires. Therefore, it was also interesting to calculate the factor R/r (Figure 6.19b). In this case only bent nanowires which acomplish the condition R/r>10 can be considered, as large bending considerations should be implemented when the bending radius (R) is smaller than ten section heights (r). A detailed image is shown in figure 6.20, describing the followed procedure to calculate the radii of curvature of silicon nanowires from a SEM image.

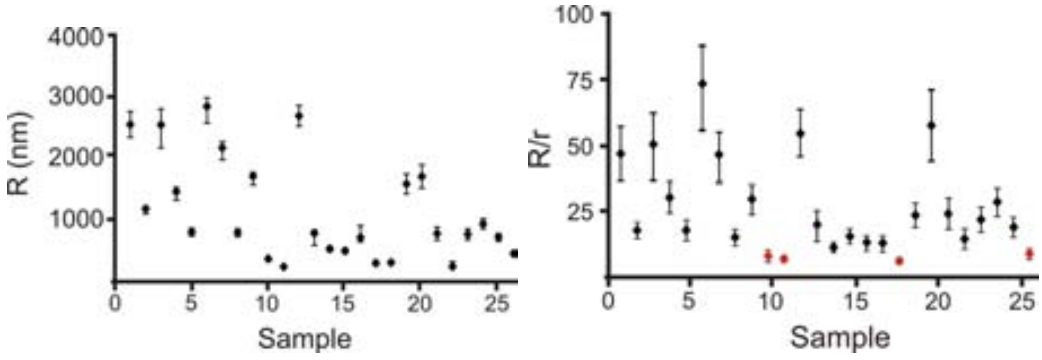

(a) (b)

Figure 6.19: **Calculated radii of curvature of silicon nanowires.** a) Maximum radii of curvature for the 25 studied nanowires. Values were extracted by image processing. b) Representation of R/r (red points show values below the condition R/r>10 which are the limit to long deformations. c) SEM image showing the process followed to calculate the maximum radius of curvature of a bent silicon nanowire.

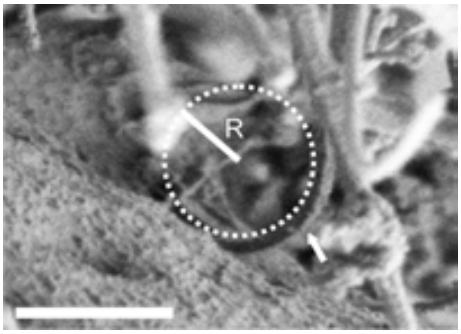

Figure 6.20: **Followed method to calculate the radii of curvature of silicon nanowires.** SEM image showing the process to calculate the maximum radius of curvature of a bent silicon nanowire. Scale bar = 500 nm.

Using these values the maximum strain on the nanowires was also calculated (Figure 6.21a). This methodology showed maximum stress values ($\sigma_{Exp.Si(111)} \sim 14$ GPa) for 60 - 130 nm-thick nanowires, close to the theoretically ultimate strength limit of silicon ($\sigma_{Si(111)} = 21$ GPa). These values are in the order of the obtained by other groups, previously referenced. The maximum stress of the 4 nanowires, that did not satisfy R/r > 10 and hence were in a large bending regime, were larger than the shown on (Figure 6.21a) ($\sigma_{Exp.Si(111)} \sim 26$ GPa). The calculated strain for bent nanowires under the condition R/r > 10 is also shown in figure 6.21b. Accordingly

with recent works which demonstrated a considerably plasticity of silicon nanowires for large strains.[33]

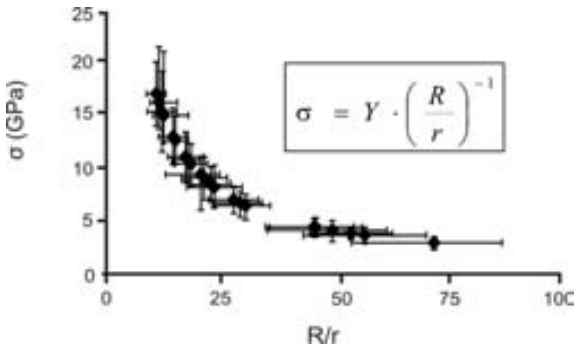

(a)

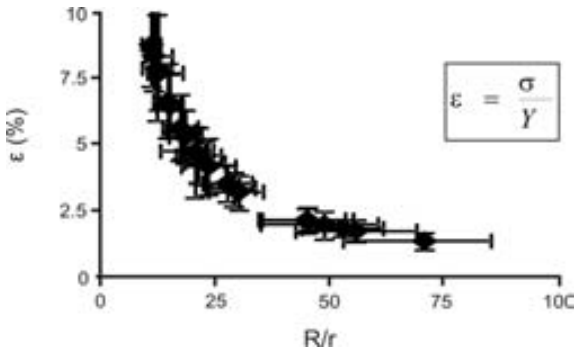

(b)

Figure 6.21: **Maximun stress and strain of bent silicon nanowires.** Calculated maximum (a) stress (σ) and (b) strain (ϵ) for the nanowires under the condition R/r > 10. Silicon Young s modulus $= Y_{Si}$

6.10 Conclusions

In this context, the design, fabrication and collection of suspended polysilicon barcodes decorated with hundreds of silicon nanowires to be used as physical embryo labels to identify and track living mouse embryos are presented. Two different methods to adhere these devices to the Zona Pellucida, Rolling and Pushpin have been tested. In the Rolling method the mouse embryos were individually rolled over one barcode, while in the Pushpin method the living embryo was held with a micropipette, while a barcode was subjected with a transfer micropipette with the silicon nanowires facing the embryo. The micropipette with the barcode was oriented to the holding micropipette and it was carefully pushed against the ZP. In spite of large differences in the applied forces between the two methods ($> 10^4$), we obtained slight differences in the retention rates during the experiments, where Pushpin method was only 2 orders of magnitude bigger than Rolling method. In the future, these retention rates can easily be increased, as this attachment issue could be circumvented by adding more than one code to the same embryo, a technique that we used routinely for the chemical adhesion.[15, 16] In addition, our results also show no significant effects of polysilicon barcodes with silicon nanowires in mouse embryo development. Furthermore, an exhaustive physical characterization for several silicon nanowires was performed and highly bent silicon nanowires were observed during the attachment experiments. The mechanical study revealed that stresses reached by silicon nanowires were close to the ultimate strength of silicon.

Summarizing, silicon nanowire barcodes were successfully obtained as extracellular physical labels for embryo identification and tracking.

Bibliography

[1] S. R. Nicewarner-Pena, R. G. Freeman, B. D. Reiss, L. He, D. J. Pena, I. D. Walton, R. Cromer, C. D. Keating, and M. J. Natan, Submicrometer metallic barcodes., *Science*, vol. 294, pp. 137 141, Oct. 2001. (cited on page(s) 52, 69, 200)

[2] D. J. Lockhart and M. O. Trulson, Multiplex metallica Molecular tag made of small metal rods may enable parallel and, *Nature Biotechnology*, vol. 19, pp. 1122 1123, 2001. (cited on page(s) 52, 69, 200)

[3] S. E. Brunker, K. B. Cederquist, and C. D. Keating, Metallic barcodes for multiplexed bioassays., *Nanomedicine*, vol. 2, pp. 695 710, Oct. 2007. (cited on page(s) 52, 69, 200)

[4] K. S. Richter, The importance of growth factors for preimplantation embryo development and in-vitro culture ., *Current Opinion in Obstetrics and Gynecology*, vol. 20, no. 3, pp. 292 304, 2008. (cited on page(s) 200)

[5] N. George, H. Pick, H. Vogel, N. Johnsson, and K. Johnsson, Specific labeling of cell surface proteins with chemically diverse compounds., *Journal of the American Chemical Society*, vol. 126, pp. 8896 8897, July 2004. (cited on page(s) 200)

[6] W. J. Rogers, C. H. Meyer, and C. M. Kramer, Technology insight: in vivo cell tracking by use of MRI., *Nature clinical practice. Cardiovascular medicine*, vol. 3, pp. 554 562, Oct. 2006. (cited on page(s) 69, 200)

[7] J. Gao and B. Xu, Applications of nanomaterials inside cells, *Nano Today*, vol. 4, pp. 37 51, Feb. 2009. (cited on page(s) 30, 31, 200)

[8] M. Han, X. Gao, J. Z. Su, and S. Nie, Quantum-dot-tagged microbeads for multiplexed optical coding of biomolecules., *Nature Biotechnology*, vol. 19, pp. 631 635, July 2001. (cited on page(s) 33, 69, 200)

[9] O. Faklaris, D. Garrot, V. Joshi, F. Druon, J.-P. Boudou, T. Sauvage, P. Georges, P. a. Curmi, and F. Treussart, Detection of single photoluminescent diamond nanoparticles in cells and study of the internalization pathway., *Small (Weinheim an der Bergstrasse, Germany)*, vol. 4, pp. 2236 2239, Dec. 2008. (cited on page(s) 200)

[10] S. Novo, L. Barrios, J. Santaló, R. Gómez-Martínez, M. Duch, J. Esteve, J. A. Plaza, C. Nogués, and E. Ibánez, A novel embryo identification system by direct tagging of mouse embryos using silicon-based barcodes, *Human Reproduction*, vol. 26, pp. 96 105, Jan. 2011. (cited on page(s) 53, 54, 70, 72, 73, 84, 97, 200, 201, 215)

[11] D. P. Green, Three-dimensional structure of the zona pellucida., *Reviews of Reproduction*, vol. 2, pp. 147 156, Sept. 1997. (cited on page(s) 200)

[12] P. M. Wassarman, Welcome to the fold, vol. 456, no. 4, pp. 1 2, 2008. (cited on page(s) 200)

[13] O. Penon, S. Novo, S. Durán, E. Ibanez, C. Nogués, J. Samitier, M. Duch, J. A. Plaza, and L. Pérez-García, Efficient biofunctionalization of polysilicon barcodes for adhesion to the zona pellucida of mouse embryos, *Bioconjugate chemistry*, vol. 23, pp. 2392 2402, Dec. 2012. (cited on page(s) 71, 87, 132, 161, 178, 201)

[14] O. Penon, D. Siapkas, S. Novo, S. Durán, G. Oncins, A. Errachid, L. Barrios, C. Nogués, M. Duch, J. A. Plaza, and L. Pérez-García, Optimized immobilization of lectins using self-assembled monolayers on polysilicon encoded materials for cell tagging, *Colloids and Surfaces B: Biointerfaces*, vol. 116, pp. 104 113, Apr. 2014. (cited on page(s) 130, 201)

[15] S. Novo, O. Penon, L. Barrios, C. Nogués, J. Santaló, S. Durán, R. Gómez-Matínez, J. Samitier, J. A. Plaza, L. Pérez-García, and E. Ibánez, Direct embryo tagging and identification system by attachment of biofunctionalized polysilicon barcodes to the zona pellucida of mouse embryos, *Human Reproduction*, vol. 28, pp. 1519 1527, June 2013. (cited on page(s) 84, 85, 86, 97, 130, 201, 215, 227)

[16] S. Novo, R. Morató, O. Penon, and S. Duran, Identification of bovine embryos cultured in groups by attachment of barcodes to the zona pellucida, *Reproduction, Fertility and Development*, vol. 25, no. 1, pp. 218 219, 2013. (cited on page(s) 97, 130, 201, 215, 227)

[17] S. Novo, C. Nogués, O. Penon, L. Barrios, J. Santaló, R. Gómez-Martínez, J. Esteve, A. Errachid, J. A. Plaza, L. Pérez-García, and E. Ibánez, Barcode tagging of human oocytes and embryos to prevent mix-ups in assisted reproduction technologies, *Human Reproduction*, vol. 29, pp. 18 28, Jan. 2014. (cited on page(s) 97, 130, 201, 215)

[18] M. T. Yang, N. J. Sniadecki, and C. S. Chen, Geometric Considerations of Micro- to Nanoscale Elastomeric Post Arrays to Study Cellular Traction Forces, *Advanced Materials*, vol. 19, pp. 3119 3123, Oct. 2007. (cited on page(s) 201)

[19] L. Wang, W. Asghar, U. Demirci, and Y. Wan, Nanostructured substrates for isolation of circulating tumor cells, *Nano Today*, vol. 8, pp. 374 387, Aug. 2013. (cited on page(s) 201)

[20] T. Berthing, S. Bonde, C. B. Sø rensen, P. Utko, J. Nygå rd, and K. L. Martinez, Intact mammalian cell function on semiconductor nanowire arrays: new perspectives for cell-based biosensing, *Small*, vol. 7, pp. 640 647, Mar. 2011. (cited on page(s) 189, 201)

[21] W. Kim, J. K. Ng, M. E. Kunitake, B. R. Conklin, and P. Yang, Interfacing silicon nanowires with mammalian cells, *Journal of the American Chemical Society*, vol. 129, pp. 7228 7229, June 2007. (cited on page(s) 44, 45, 161, 162, 189, 201)

[22] K. E. Fischer, B. J. Alemán, S. L. Tao, R. Hugh Daniels, E. M. Li, M. D. Bunger, G. Nagaraj, P. Singh, A. Zettl, and T. a. Desai, Biomimetic nanowire coatings for next generation adhesive drug delivery systems., *Nano Letters*, vol. 9, pp. 716 720, Feb. 2009. (cited on page(s) 202)

[23] L. Magagnin, V. Bertani, P. L. Cavallotti, R. Maboudian, and C. Carraro, Selective deposition of gold nanoclusters on silicon by a galvanic displacement process, *Microelectronic Engineering*, vol. 64, pp. 479 485, 2002. (cited on page(s) 167, 204)

[24] J. D. Biggers, L. K. McGinnis, and M. Raffin, Amino acids and preimplantation development of the mouse in protein-free potassium simplex optimized medium., *Biology of Reproduction*, vol. 63, pp. 281 293, July 2000. (cited on page(s) 207)

[25] Y. Sun, K.-T. Wan, K. P. Roberts, J. C. Bischof, and B. J. Nelson, Mechanical property characterization of mouse zona pellucida., *IEEE transactions on nanobioscience*, vol. 2, pp. 279 286, Dec. 2003. (cited on page(s) 213, 218)

[26] Y. Sun, Investigating Protein Structure Change in the Zona Pellucida with a Microrobotic System, *The International Journal of Robotics Research*, vol. 24, pp. 211 218, Feb. 2005. (cited on page(s) 213)

[27] A. Vinckier and G. Semenza, Measuring elasticity of biological materials by atomic force microscopy., *FEBS letters*, vol. 430, pp. 12 16, June 1998. (cited on page(s) 213)

[28] Y. Murayama, J. Mizuno, H. Kamakura, Y. Fueta, H. Nakamura, K. Akaishi, K. Anzai, A. Watanabe, H. Inui, and S. Omata, Mouse zona pellucida dynamically changes its elasticity during oocyte maturation, fertilization and early embryo development., *Human Cell*, vol. 19, pp. 119 125, Nov. 2006. (cited on page(s) 217)

[29] S. M.-M. Dubois, G.-M. Rignanese, T. Pardoen, and J.-C. Charlier, Ideal strength of silicon: An ab initio study, *Physical Review B*, vol. 74, pp. 23520301 23520307, Dec. 2006. (cited on page(s) 220)

[30] M. Tabib-Azar, M. Nassirou, R. Wang, S. Sharma, T. I. Kamins, M. S. Islam, and R. S. Williams, Mechanical properties of self-welded silicon nanobridges, *Applied Physics Letters*, vol. 87, no. 11, p. 113102, 2005. (cited on page(s) 220)

[31] S. Hoffmann, I. Utke, B. Moser, J. Michler, S. H. Christiansen, V. Schmidt, S. Senz, P. Werner, U. Gosele, and C. Ballif, Measurement of the bending strength of vapor-liquid-solid grown silicon nanowires., *Nano letters*, vol. 6, pp. 622 625, Apr. 2006. (cited on page(s) 220)

[32] G. Stan, S. Krylyuk, A. V. Davydov, and R. F. Cook, Bending manipulation and measurements of fracture strength of silicon and oxidized silicon nanowires by atomic force microscopy, *Journal of Materials Research*, vol. 27, pp. 562 570, Nov. 2012. (cited on page(s) 220)

[33] D.-M. Tang, C.-L. Ren, M.-S. Wang, X. Wei, N. Kawamoto, C. Liu, Y. Bando, M. Mitome, N. Fukata, and D. Golberg, Mechanical properties of Si nanowires as revealed by in situ transmission electron microscopy and molecular dynamics simulations., *Nano Letters*, vol. 12, pp. 1898 1904, Apr. 2012. (cited on page(s) 226)

Chapter 7

General Conclusions

The work developed during this PhD project allows us to extract several conclusions that are summarised below:

First Two-dimensional polysilicon barcodes have been designed and fabricated with a perfect shape and homogenous surface. Several functionalization tests have been performed in order to ensure their efficiency as functionalization platforms at cell scale. Biological tests have been also carried out with the objective of demonstrating the non-toxicity of the polysilicon barcodes. Retention studies of the devices to the outer membrane of mouse embryos have been also developed. The obtained results clearly validate our polysilicon barcodes as appropiated microtools for embryo tagging.

Second The electrodeposition setup for the obtaining of CoNi thin films has been optimized. Magnetic CoNi barcodes have been designed as magnetic labels for micro and nanoapplications. Several parameters such as time and temperature of deposition have been studied to obtain the optimal barcode thickness. Several etching tests have been also performed in order to find the most suitable process to successfully release the CoNi barcodes from the wafer. And almost well-defined barcodes have been fabricated.

Third Polysilicon-Chromium-Gold chips have been successfully fabricated after some preliminary tests. The efficiency of a thin layer of chromium as adherent interlayer between the two main device materials (polysilicon and gold) for the obtaining of more robust devices has been tested. Two different fluorescent

proteins have been immobilized on both chip surfaces in order to provide the chip with bi-functional capabilities. A fluorescence microscopy test has been used for an unambiguous characterization of the bi-functionalized chips. Internalization and cell-viability tests with the fabricated chips have been also performed too and the obtained results have shown high cell viability.

Fourth Nanowire silicon chips and silicon nanowire entangled meshes have been successfully designed and fabricated. Cell viability assays with micro- and nanostructured chips have been performed and have not revealed cell-toxicity. The initial stage of chip-internalization has been also analyzed and the obtained results showed that HeLa cells prefer silicon nanowire sides for their chip-uptake.

Fifth Silicon nanowire barcodes have been successfully designed and fabricated. Two different methods to adhere these devices to mouse living embryos, Rolling and Pushpin, have been tested. Although different values of force have been applied, slight differences in the retention rates have been observed. An exhaustive silicon nanowire physical characterization has been also performed and the radius of curvature and stress values reached by silicon nanowires have been analyzed. The obtained values have demonstrated that silicon nanowires are a powerful tool for advanced micro and nanoapplications.

As general conclusion and because of everything said so far, we can conclude that all the mentioned features added to our devices can provide them with the ability of being used for countless bioapplications. We hope that the results obtained during this PhD project will help somehow in a near future improve fields like medicine, cell biology and micro and nanotechnologies.

Scientific contributions

Publications

1. S. Durán, M. Duch, R. Gómez-Martínez, M. Fernández-Regúlez, M. Reina, C. Muller, A. San Paulo, J. Esteve, S. Castel, J. A. Plaza. C*ontrolled fabrication of nanowire silicon chips for cell internalization in HeLa cells.* In preparation (Expected submission in December 2014).

2. S. Durán, S. Novo, M. Fernández-Regúlez, M. Duch, R. Gómez-Martínez, A. San Paulo, E. Ibánez, J. Esteve, J. A. Plaza. *Silicon-nanowire based attachment of silicon chips to living embryos unexpectedly reveals the ultimate strength of silicon.* In preparation (Expected submission in October 2014).

3. S. Durán, M. Duch, T. Patino, A. Torres, O. Penon, R. Gómez-Martínez, L. Barrios, J. Esteve, Carme Nogués, L. Pérez-García, J. A. Plaza. *Technological development of intracellular Polysilicon-Chromium-Gold chips for orthogonal chemical functionalization.* Under review in Sensors and Actuators B. Chemical (SNB-S-14-01828).

4. O. Penon, D. Siapkas, S. Novo, S. Durán, G. Oncins, A. Errachid, L. Barrios, C. Nogués, M. Duch, J. A. Plaza, L. Pérez-García. *Optimized immobilization of lectins using self-assembled monolayers on polysilicon encoded materials for cell tagging.* Colloids and Surfaces B: Biointerfaces, **2014**, 116, 104-113

5. S. Novo, R. Morató, O. Penon, S. Durán, L. Barrios, C. Nogués, J.A. Plaza, L. Pérez-García, T. Mogas, E. Ibánez. *Identification of bovine*

embryos cultured in groups by attachment of barcodes to the zona pellucida. Reproduction fertility and development, **2013**, 25 (1) 218-219

6. S. Novo, O. Penon, L. Barrios, C. Nogués, J. Santaló, S. Durán, R. Gómez-Martínez, J. Samitier, J. A. Plaza, L. Pérez-García, E. Ibánez. *Direct embryo tagging and identification system by attachment of biofunctionalized polysilicon barcodes to the zona pellucida of mouse embryos.* Human Reproduction, **2013**, 28 (6) 1519-1527

7. O. Penon, S. Novo, S. Durán, E. Ibánez, C. Nogués, J. Samitier, M. Duch, J. A. Plaza, L. Pérez-García. *Efficient biofunctionalization of polysilicon barcodes for adhesion to the zona pellucida of mouse embryos.* Bioconjugate Chemistry. **2012**, 23 (12) 2392-2402.

Conferences

1. S. Durán, M. Duch, T. Patino, A. Torres, O. Penon, R. Gómez-Martínez, L. Barrios, J. Esteve, Carme Nogués, L. Pérez-García, J. A. Plaza. *Bifunctional polysilicon-chromium-gold microchips as intracellular platforms for bioapplications.* Fourth International Conference on Multifunctional, Hybrid and Nanomaterials, HYMA2015. Sitges, Barcelona, Spain. March 9th - 13th, **2015**. *Abstract submitted*

2. D. Limón, A. Torres, O. Penon, L. Rodríguez, S. Durán, M. Duch, J. A. Plaza, L. Pérez-García. *Functionalization of microparticles for skin diseases therapy.* VI Jornada del Institut de Nanociència i Nanotecnologia, IN2UB. Barcelona, Spain. June 5th, **2014**. *Poster presentation*

3. A. Kadambi, S. Durán, M. Duch, R. Gómez-Martínez, J. Esteve, J. A. Plaza. *Technology and Characterization of Magnetic CoNi MicroBarcodes.* VI Jornada del Institut de Nanociència i Nanotecnologia, IN2UB. Barcelona, Spain. June 5th, **2014**. *Poster presentation*

4. O. Penon, S. Novo, S. Durán, E. Ibánez, C. Nogués, J. Samitier, M. Duch, J. A. Plaza, L. Pérez-García. *Optimized immobilization of lectins using self-assembled monolayers on polysilicon encoded materials for cell tagging.* EC COST Thematic Workshop. Leipzig, Germany. October 8th - 9th, **2013**. *Poster presentation*

5. S. Durán, I. Santana, T. Patino, M. Duch, O. Penon, L. Barrios, R. Gómez-Martínez, J. Esteve, C. Nogués, L. Pérez-García, J. A. Plaza. *Intracellular Multi-Material Chips in Living Cells.* The 39th International Conference on Micro and Nano Engineering, MNE 2013, London, England. September 16th - 19th, **2013**. *Poster presentation*

6. T. Patino, L. Barrios, E. Ibánez, S. Durán, M. Duch, J. A. Plaza, C. Nogués. *Cytotoxicity, Uptake and Immunogenicity of Novel Multi-Material Intracellular Chips.* 25th European Conference on Biomaterials, ESB2013. Madrid, Spain. September 8th - 12th, **2013**. *Poster presentation*

7. S. Novo, O. Penon, L. Barrios, C. Nogués, J. Santaló, S. Durán, R. Gómez-

Martínez, J. Samitier, J. A. Plaza, L. Pérez-García, E. Ibánez. *Direct embryo tagging and identification system by attachment of biofunctionalized polysilicon barcodes to the zona pellucida of mouse embryos.* Annual Meeting of the European Society of Human Reproduction and Embryology, London, UK. July 1st - 10th, **2013**. *Poster presentation*

8. S. Durán, M. Duch, R. Gómez-Martínez, R. P. del Real, J. Esteve, J. A. Plaza. *Technology Development of Magnetic CoNi MicroParticles: Barcoding and Sorting the Microworld.* The 3rd Jornades Doctorals del Departament de Química de la UAB. Barcelona, Spain. May 15th - 27th, **2013**. *Oral contribution*

9. T. Patino, L. Barrios, E. Ibánez, S. Durán, M. Duch, J. A. Plaza, C. Nogués. *Cytotoxicity and cellular uptake assessment of multi-material intracellular chips by the use of correlative microscopy.* Focus on Microscopy. Maastricht, The Netherlands. March 24th - 27th, **2013**. *Poster presentation*

10. O. Penon, S. Novo, S. Durán, E. Ibánez, C. Nogués, J. Samitier, M. Duch, J. A. Plaza, L. Pérez-García. *Lectin immobilization on encoded silicon microtools for individual cell tagging.* Third International Conference on Multifunctional, Hybrid and Nanomaterials. Sorrento, Italy. March 3rd - 4th, **2013**. *Poster presentation*

11. O. Penon, S. Novo, S. Durán, E. Ibánez, C. Nogués, J. Samitier, M. Duch, J. A. Plaza, L. Pérez-García. *Lectin immobilization on encoded silicon microtools for individual cell tagging.* Magnyfico 2013 Workshop. Barcelona, Spain. February 20th - 22th, **2013**. *Poster presentation*

12. S. Novo, R. Morató, O. Penon, S. Durán, L. Barrios, C. Nogués, M. Duch, Ll. Pérez-García, E. Ibánez, T. Mogas. *Zona Pellucida tagging with barcodes allows the traceability of bovine embryos cultured in group.* 39th Annual Conference of the IETS, IETS 2013. Hannover, Germany. January 19th - 22th, **2013**. *Poster presentation*

13. O. Penon, S. Novo, S. Durán, E. Ibánez, C. Nogués, J. Samitier, M. Duch, J. A. Plaza, L. Pérez-García. *Design of micronanotools for cell tagging and sensing in living cells.* V Jornada del Institut de Nanociència

i Nanotecnologia (IN2UB). Barcelona, Spain. November 2nd, **2012**. *Oral communication*

14. S. Durán, M. Duch, R. Gómez-Martínez, R. P. del Real, J. Esteve, J. A. Plaza. *Technology Development of Magnetic CoNi MicroParticles: Barcoding and Sorting the Microworld.* The 38th International Conference on Micro and Nano Engineering. MNE 2012, Toulouse, France. September 16th - 20th, **2012**. *Poster presentation*

15. S. Novo, R. Morató, O. Penon, S. Durán, L. Barrios, C. Nogués, M. Duch, Ll. Pérez-García, T. Mogas, E. Ibánez. *Identification of bovine embryos cultured in group by attachment of barcodes to the zona pellucida.* 28th Scientific Meeting of the European Embryo Transfer Association, AETE 2012. Saint Malo, France. September 06th - 08th, **2012**. *Poster presentation*

16. S. Novo, R. Morató, O. Penon, S. Durán, L. Barrios, C. Nogués, M. Duch, L. Pérez-García, T. Mogas, E. Ibánez. *Identificació d'embrions bovins cultivats en grup mitjancant l'adhesió de codis a la zona pel.lúcida.* Global questions on advanced biology I. Congrés International de Biologia de Catalunya, CIBICAT 2012. Barcelona, Spain. July 09th - 12th, **2012**. *Poster presentation*

17. S. Durán, S. Novo, M. Fernández-Regúlez, M. Duch, R. Gómez-Martínez, A. San Paulo, E. Ibánez, J. Esteve, J. A. Plaza. *Silicon Nanovelcro to attach inorganic microdevices to biological material.* The 14th International Conference on Miniaturized Systems for Chemistry and Life Sciences, MicroTAS 2010. Groningen, The Netherlands. October 03th - 07th, **2010**. *Poster presentation*

Projects

1. **MINAHE3:** Design and fabrication of MicroNanoTools to study and identify living cells (TEC2008-06883-C03-01). Granted by: Spanish Ministry of Science and Innovation. Term: January 2009 - December 2011.
2. **MINAHE4:** Design and fabrication of MicroNanoTools for Life Sciences (TEC2011-29140-C03-01). Granted by: Spanish Ministry of Science and Innovation. January 2012 - December 2014.

Future work

The most important aspects to cover from now on within the investigation described in this thesis are:

1. In reference to the functionalized polysilicon barcodes, different natures of living embryos (besides mouse and bovine embryos) will be interesting to label and track. For instance, human embryos can be (in the near future) identified inside their own culture for applications in fertility clinics.

2. In reference to the magnetic CoNi barcodes, we should optimize the barcode release from the wafer, as our traditional method (HF wet etching) has proven to be too aggressive for CoNi layers. Furthermore, sorting proves would be interesting to develop. In fact, we have already planned the fabrication of a suitable microfluidic system to achieve the separation of polysilicon barcodes (not magnetic) from CoNi barcodes (magnetic) using guide magnetic fields. In the near future our intention is to internalize our magnetic barcodes (cell toxicity tests will be previously needed) into living cells or embryos and achieve a magnetic controlled sorting process. Therefore, we will be able to manipulate cells with internalized CoNi barcodes, while the ones which do not carry any device will remain into the cell culture.

3. In reference to the polysilicon-chromium-gold multi-material chips, the functionalization of both surfaces with a specific actuator would be interesting. For instance, we can functionalize the chip surface with a specific antibody, so that the antigen joins it and indirectly attaches itself to the chip. Hence, we can induce an immune response inside the cell.

4. Along the line of multi-material chips, we are also working on the design of

a new line of multi-material misaligned chips. With this new device we will be able to observe both materials (polysilicon and gold) simultaneously, as the material observation in the aligned chips, depends on the faces facing upwards or downwards. With the misaligned chips we solve this issue, as both surfaces into the same chip will be equal. This improvement also allows us the bi-functionalization in the same surface of the same chip, in contrast to the bi-functionalization in the aligned chips which was performed in both surfaces of the same device.

5. In reference to the silicon nanowire chips, our purpose is the functionalization of the silicon nanowire surfaces with different proteins (for instance, WGA) to provide the chips with sensing capabilities. Or also in the near future, we could functionalize the silicon nanowire surfaces with, for instance, some of the nanoparticles explained in Chapter 1, taking advantage of the nanostructured silicon surfaces and performing some tests of intracellular drug delivery. In addition, we are planning to carry out a degradation study of the silicon nanowires into several mediums, such as culture mediums, different pH buffers or into simulated body fluid.

6. And last but not least, in reference to the silicon nanowire barcodes and after a careful analysis of the mechanical properties of the silicon nanowires during the Rolling and Pushpin methods, we are planning to perform an additional mechanical study growing silicon nanowires on top of a home-made rounded microscopic tip *(performed in the Instituto de Microelectrónica de Barcelona, IMB-CNM, CSIC)*. So that, we can analyze, in a highly controlled way, the attachment of the silicon nanowire tip over different bio-entities, such as molecules, proteins or cell membranes. And along this line, we can also functionalize the surface of our home-made rounded tip with several molecules and perform, in the same way of that with the silicon nanowires, attachment studies over different bio-entities.

Annexes

List of Figures

Page

List of Tables

Page